EXHUMED FLUVIAL DEPOSITS: NEW PALEOHYDROLOGICAL TOOLS INDICATE LONG-DURATION FLUVIAL ACTIVITY ON EARLY MARS

Thesis by

Alistair Thompson Hayden

In Partial Fulfillment of the Requirements for the

degree of

Doctor of Philosophy in Geology

CALIFORNIA INSTITUTE OF TECHNOLOGY

Pasadena, California

2020

(Defended June 3, 2020)

Alistair Thompson Hayden
ORCID: 0000-0003-3540-7807

Before you can be an [internationalist] you have first to be a naturalist and feel the ground under you making a whole circle…The planet is everybody's. All it offers is the grass, the sky, the water, and the ineluctable dream of peace and fruition.

E.B. White, writing on December 11, 1941

ACKNOWLEDGEMENTS

This thesis results from the incredible education I have received from a list of people and organizations too long to fully include. Thanks (and sorry!) go also to many not listed here.

Thanks to my whole family, who instilled in me the importance of education, a love of the outdoors, and curiosity about and care for the world. In particular, I thank my parents, Andreas Hayden and Emily Thompson, for ensuring I attended good schools and providing extra learning opportunities, and my sisters, Elspeth and Kristen Hayden, for their love and support.

Thanks to Ann Arbor Public Schools, University of Michigan, and Caltech for being excellent academic institutions, filled with interesting opportunities and people of diverse backgrounds who have greatly enriched my personal and professional life. I thank AAPS and UM friends including Seth Buchsbaum, Alex Carney, Jamie Fogel, DJ Heebner, Tao Li, Jeff Liu, Ethan Shirley, and Bob Teixeira for over a decade of friendship and exemplifying excellence and initiative in a wide variety of fields. I thank Anna Ho and other Caltech friends, including my housemates, the Caltech Dining (and art) crew, my officemates, the Lamb-group members and alumni, the Graduate Student Council, and the Triathlon Club for years of inspiration, collaboration, and support.

Numerous people have provided scientific mentorship that built my interest and skillset in geology and planetary science—I thank Matt Linke for hiring me to the planetarium where I became excited about planets, and Keith Riles and Daniel Fisher for mentoring me on undergraduate research. I thank my PhD advisor, Mike Lamb, for the significant training he provided over the years, and his dedication to my success. I also thank my committee for their mentorship and collaboration over my time at Caltech—Bethany Ehlmann, Woody Fischer, and John Grotzinger. Finally, I thank Jay Dickson for additional mentorship and Becky Williams for frequent collaboration.

ABSTRACT

Fluvial sinuous ridges are common landforms on Mars that have been used for interpreting the history of ancient martian rivers. They are typically interpreted as eroded casts of an ancient river at a snapshot in time. However, some ridges might instead be channel belts that preserve river history, leading to significant differences in interpretation of paleohydrology, including flow direction, duration, and discharge. In this thesis, I used analog sites on Earth and techniques from fluvial sedimentology and fluvial geomorphology to determine that many ridges are exhumed channel belts, and to create and apply new tools for measuring bankfull discharge and duration of river flow from remote-sensing observations of these sedimentary deposits. I found evidence that rivers on ancient Mars were comparable in size to those on Earth today, and that they flowed for at least millions of years.

I examined sinuous ridges in three terrestrial sites to better understand ridges on Mars: the Cretaceous Cedar Mountain Formation and Jurassic Morrison Formation of Eastern Utah, and the Miocene Caspe Formation of Northeast Spain. Ridges at all sites are capped with sandy units rich with dune and bar strata atop a mudstone pedestal and they cross each other at different stratigraphic levels, observations that together indicate that ridges are channel belts exhumed from floodplain sediments—the most common arrangement of fluvial stratigraphy. By compiling measurements of hundreds of terrestrial channel belts and their associated channels, I found that the best methods to reconstruct paleochannel bankfull geometry from such deposits are to use thickness of channel belts (1-4 times paleochannel depth) or radius of curvature of lateral accretion sets (half the channel width). Ridge width and planview wavelength, common proxies for paleochannel width, are significantly more uncertain due to channel amalgamation and ridge erosion by scarp retreat, which

I quantified with geometry and a new erosion model. Intermittency factor converts bankfull discharge to average discharge, enabling measurement of duration of river flow. I calculated the intermittency factor for 206 fluvial deposits and USGS streamgages, and found that it ranges between 0.003-0.7 with a median of 0.10, with values depending on the ratio of catchment-averaged erosion rate to average precipitation but independent of timescale, river size, climate, or grainsize.

Throughout the work, I applied the methods to sinuous ridges on Mars to demonstrate their applicability. I found that many ridges are likely channel belts, and that the ancient rivers they represent are likely smaller but longer- than previously studies have indicated. Altogether, this contribution enables new quantitative analyses of ancient rivers on Earth and Mars, and provides evidence that ancient Martian climate was capable of supporting liquid water at many locations across the surface for at least millions of years.

PUBLISHED CONTENT AND CONTRIBUTIONS

Hayden, A. T., Lamb, M. P., & Carney, A. J. (submitted to *Geology*). Similar Curvature-to-Width Ratios for Channels and Channel Belts: Implications for Paleo-Hydraulics of Fluvial Ridges on Mars.

ATH led the conception of the project, data analysis, and writing.

Hayden, A. T., & Lamb, M. P. (in press). Fluvial Sinuous Ridges of the Morrison Formation, USA: Meandering, Scarp Retreat, and Implications for Mars. In press at *JGR: Planets*.

ATH participated in the conception of the project, and led the fieldwork, analysis, and writing.

Hayden, A. T., Lamb, M. P., Fischer, W. W., Ewing, R. C., McElroy, B., & Williams, R. M. E. (2019). Formation of sinuous ridges by inversion of river-channel belts in Utah, USA, with implications for Mars. *Icarus, 332*, 92-110. doi:10.1016/j.icarus.2019.04.019

ATH participated in the conception of the project, and led the fieldwork, analysis, and writing.

TABLE OF CONTENTS

LIST OF ILLUSTRATIONS AND TABLES

TABLES

FIGURES

NOMENCLATURE

Channel. Conduit through which river flows. Note that this term in some sedimentary geology and mining literature refers to sand bodies, which is closer to how I use "channel belt".

Channel belt. Deposit built as a channel migrates laterally and aggrades vertically over long durations. Typically comprises coarser-grained bed material (sand and gravel).

Channel fill. Material that fills in a channel, usually in reference to fluvial sediments, though lava fills also are observed in the case of inverted channels. Channel fills preserve the channel geometry and typically fill it with fine-grained material representative of overbank floods. Note that some sedimentary geology literature uses this term to mean fluvial-origin sand bodies, similar to how I use "channel belt".

CTX. Context Camera.

DEM. Digital elevation model.

Exhumed channel belt. Channel belt exhumed by preferential erosion, forming a fluvial ridge.

HiRISE. High Resolution Imaging Science Experiment.

Inverted channel. Channel fill exhumed by preferential erosion, forming a fluvial ridge.

Intermittency factor. A theoretical representation of the fraction of time where a river does work. Defined by Paola et al. (1992) as the ratio of mean sediment flux to bankfull sediment flux. Note that this formulation lacks information about frequency of large flows (see instead *recurrence interval*).

MOLA. Mars Orbiter Laser Altimeter.

MRO. Mars Reconnaissance Orbiter.

Point bar. The lateral accretion sets from a river migrating laterally. Typically comprises bed-material sediment accumulated in the subsurface.

Recurrence interval. The average time between flows exceeding a certain value, typically bankfull. Note that this formulation lacks information about flow duration (see instead *intermittency factor*).

Scroll bar. Ridge-and-swale-topography representing prior levee positions from a river migrating laterally. Scroll bars differ from point bars in that they occur on the surface, atop the point-bar deposit, and typically comprise overbank muds.

Chapter 1

1 THESIS INTRODUCTION

I do not know any other profession more beneficial than extraction of hidden water
as it flourishes and cultivates lands, improves people's welfare, and grants ample profits
Abubakr Mohammad Al-Karaji (The Extraction of Hidden Waters, 11th century)

1.1. Water is life, and the search for both on Mars

Mars has always held a unique position among the planets; in antiquity when planets were bright specks wandering through the nighttime sky, Mars' red hue tied it to a destroyer god in many cultures. In modernity, however, its allure is linked to the possibility of past or present extraterrestrial life, and Mars is currently a main target in the ongoing search for biosignatures beyond Earth (Planetary Science Decadal Survey, 2011). Speculation about observational evidence of water and life on Mars was first fueled in the public imagination by the common mistranslation of *canali* (Schiaparelli, 1877) as *canals* (e.g., New York Times, 1882), instead of Schiaparelli's intended meaning of *channels* (e.g., Lane, 2006). Subsequent telescopic observations at higher resolution, including some conducted nearby at the Mt. Wilson Observatory by E. E. Barnard in the early 1900s, indicated that there were no engineered canals on Mars, but the idea did not recede from public imagination until pole-to-pole photographs during the Mariner program in the 1960s and 1970s showed a planet devoid of macroscopic life and in-situ experiments performed by the Viking landers were unable to detect microscopic life (e.g., Arvidson et al., 1989).

However, orbital images from Mariner, and later, Viking did indeed show abundant remnants of ancient rivers, with numerous striking images of fluvial valleys and outflow channels (e.g., Masursky, 1973; Milton, 1973; Sharp and Malin, 1975). Because liquid water is crucial to life as we know it, finding landforms carved by water led the search for martian biosignatures to be reframed as "Follow the water", a mantra that has guided much of Mars science up to the present. Extensive mapping efforts revealed that rivers spanned Mars, but were mostly confined to the first major period of Mars history, known as the Noachian, with almost no river activity through the later Hesperian and Amazonian periods (Tanaka, 1986). Images with significantly improved resolution from the later Mars Global Surveyor and Mars Reconnaissance Orbiter missions revealed a high density of river networks indicative of precipitation-fed river systems (e.g., Craddock and Howard, 2002; Hynek et al., 2010), presenting the possibility of a developed water cycle like on Earth. High-resolution orbital images also enabled additional characterization of layered sedimentary deposits (e.g., Malin and Edgett, 2000; Grotzinger and Milliken, 2012), deltas (e.g., Moore et al., 2003), crater-lakes (Fassett and Head, 2008), and a putative ocean or large sea (Parker et al., 1989). Together the erosional valleys and deposits represent a set of potentially previously habitable locations—high priority targets for exploration.

Over the last two decades, rover exploration has supplemented orbiter observations, enabling specific tests of hypotheses related to water flow. The Opportunity rover characterized Arabia Terra, and found sedimentary structures and mineral deposits indicating an ancient dune field with a water table near the surface (Squyres et al., 2004; Grotzinger et al., 2005; Arvidson et al., 2006). The Curiosity rover on the other hand did find significant evidence of liquid water at the surface of Mars, including sedimentary structures indicating river flow, lake deposits indicating long-lived (up to 10^7

years) standing water, and mud cracks indicating cyclic wetting and drying (e.g., Grotzinger et al., 2014; Stein et al., 2017; Rivera-Hernandez et al., 2020). Importantly, Curiosity's geochemical, mineral, sedimentological analyses indicated that the water was close to neutral pH, had salinity similar to terrestrial freshwater, and had variable redox states (McLennan et al., 2014; Vaniman et al., 2014), which together indicate an ancient lake that would have been habitable for life as we know it. Together, the complementary approaches—geomorphological and mineralogical, orbital and rover—presented clear evidence of liquid water that could represent habitable conditions.

Building on a combined 39 years of mission elapsed time from the surface of Mars and approaching 10^6 images from orbit, the next chapter of Mars exploration seeks to answer remaining questions about the history of martian water and habitability. In particular, robust debate continues over the nature of Mars' early climate (Wordsworth et al., 2018). A major goal is to understand the geologic evidence of significant river erosion and deposition 3-4 billion years ago because it represents a climate significantly different from the cold and arid environment of modern Mars (e.g., Hoke et al., 2011; Grotzinger et al., 2014; Wordsworth 2016). Proposed endmember hypotheses for the observed river record reflect fundamentally different interpretations of habitability, ranging from long-lived greenhouse conditions (e.g., Halevy and Head, 2012) to transient greenhouse conditions (e.g., Segura et al., 2002) to just locally wet conditions (e.g., Fairen, 2010; Wordsworth et al., 2013). Fundamental aspects of surface-water flow that could help constrain these hypotheses have been analyzed from orbit based on geomorphological evidence but still remain uncertain, including total volumes of water (current estimates of the minimum volume range from 3 m to 5 km global equivalent layer; Rosenberg and Head, 2015; Luo et al., 2017), size of rivers (e.g., Kite et al., 2019), and how frequently flows occurred (Buhler et al., 2014; Lapôtre and Ielpi, 2020). Constraining flow

parameters, in particular duration and discharge of fluvial systems, will help better understand the ancient hydrologic system.

A major opportunity to improve our understanding of ancient Mars is to analyze its sedimentary deposits. Sedimentary deposits have been observed globally across Mars (e.g., Malin and Edgett, 2000; Dickson et al., in rev.), but detailed study of their hydrological significance at that scale is scarce, which represents a major opportunity to improve our understanding of the planet – depositional tracts represent at least half of terrestrial fluvial systems (Somme et al., 2009; Nyberg et al., 2015), and the sedimentary record has been used to build most of our understanding of Earth's history of climate, tectonics, and life (e.g., Miall, 2013).

In this thesis, I studied exhumed channel belts, a class of fluvial sedimentary deposit present globally across Mars (Dickson et al., in rev.; Fig. 1.1), and present at the landing sites of the Perseverance and Rosalind Franklin rovers (e.g., Goudge et al., 2018; Balme et al., 2020) and near the landing site of the Curiosity rover (e.g., Palucis et al., 2014). My goal was to use orbital observations of exhumed channel belts to complement ongoing and future in-situ rover exploration of fluvial deposits in order to learn more about river discharge and duration on ancient Mars and thereby better understand the hydrologic system and potential habitability of early Mars. I combined common methods of fluvial geomorphology with field observations of the sedimentology of exhumed channel belts on Earth to create new tools for understanding exhumed channel belts from Mars orbit, and then I applied those tools to make quantitative estimates of the duration and discharge of rivers on ancient Mars. My results support interpretations of long-lived ($>10^6$ years) terrestrial-sized rivers on early Mars, which represent potentially habitable conditions.

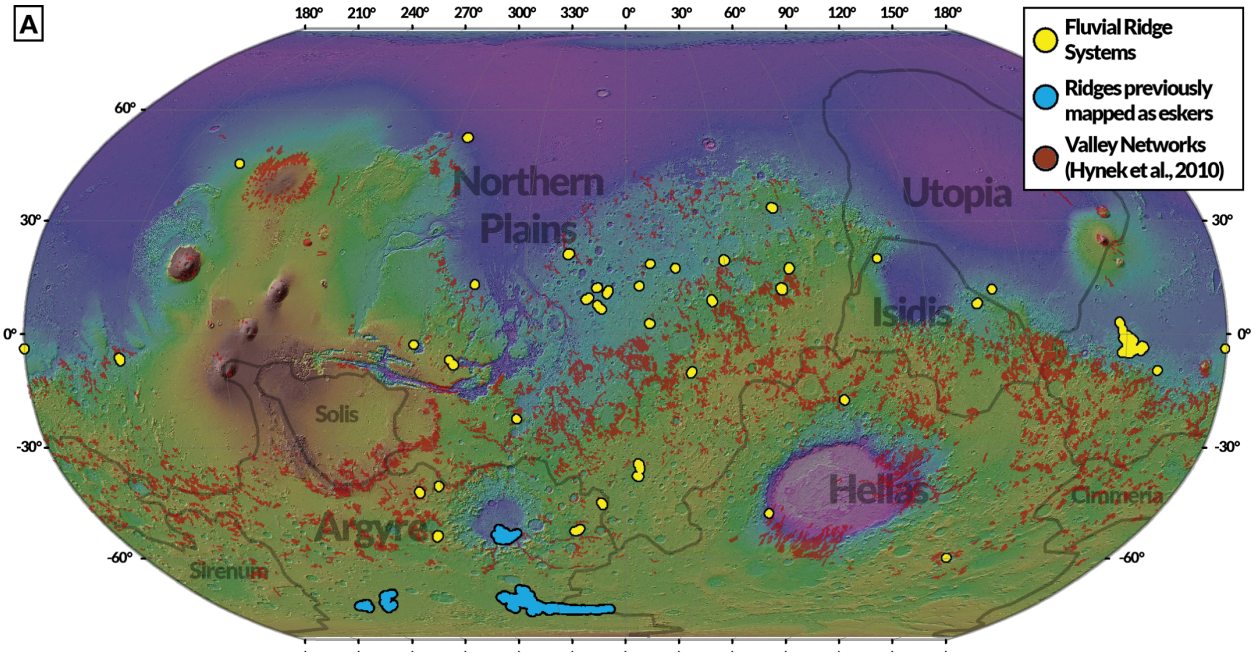

Figure 1.1—Map of fluvial ridges in relationship to valley networks from Dickson, Lamb, Williams, Hayden, and Fischer (in rev.). Ridges are globally distributed like the valley networks, but tend to be at lower elevations. Unlike other fluvial sedimentary deposits, fluvial ridges are commonly found in inter-crater plains, potentially indicating large regional depositional rivers (Dickson, Lamb, Williams, Hayden, and Fischer, in rev.). Background is MOLA data. Esker identifications from Head and Pratt (2001) and Banks et al. (2009). Background is MOLA data.

1.2. Quantitative analysis of the veins of the Earth and their fossils

Rivers have been recognized as the "veins of the Earth" for millennia, including notably by al-Karaji in what is considered to be the oldest extant hydrology text (11th century). Indeed, rivers are the main conduit for transporting water, sediment, and nutrients, so understanding that transport has been of vital importance to not just understanding Earth and other planets, but also to the infrastructure that underpins human civilization. Engineers in ancient Persia built "qanat" irrigation tunnels to deliver water across arid regions, and in the process discovered that the rate of flow depends on the width, depth, and slope of the conduit (al-Karaji reports on this in the 11th century

CE, but the earliest qanat predate 1000 BCE). European canal engineers in the late 1800s developed equations relating the flow rate of channels to their geometry (e.g., Gauckler, 1863; Manning, 1890). At a similar time, the United States founded the U.S. Geological Survey (USGS) to study territorial acquisitions for economic use, and USGS surveyors began trying to quantitatively understand how rivers transport water and sediment based on their observations of the American West (e.g., Gilbert, 1877). Theoretical and experimental work to improve airplane capabilities for the U.S. and Germany through World War II built an understanding of fluid mechanics that was subsequently applied to river channels (e.g., Prandtl, 1925; von Kármán, 1937; Keulegan, 1938; Nikuradse, 1950). These investigative threads were drawn together mid-century by researchers trying to understand how to manage rivers and the impacts of rivers on the built environment (e.g., Wolman et al., 1960), which also necessitated introduction of frameworks for studying sediment transport (e.g., Einstein, 1950; Engelund and Hansen, 1967) and incorporating time into the analysis (e.g., Wolman and Miller, 1960; Paola et al., 1992).

Rivers can become fossilized and just as with fossils, we can study river remnants and extant analogs to learn about ancient worlds and ancient life. Research since the 1960s has sought to apply the knowledge from hydrological engineers and geomorphologists to the rock record (e.g., Jopling, 1966; Baker, 1974; Dury, 1976; Ethridge et al., 1977). Small scales preserve structures that correspond to features in the original channel, including bar clinoforms that preserve bar geometry and therefore preserve bank geometry (e.g., Allen, 1965; Mohrig et al., 2000; Fig. 1.2), and dune cross-strata that are truncated remnants of dunes (Paola and Borgmann, 1991; Fig. 1.2) that had heights that scale with channel depth (Bradley and Venditti, 2017). Larger scales preserve a history of channel organization, with a common deposit architecture comprising coarse-grained channel

belts representing locations of channel deposition, encased in fine-grained deposits representing locations of floodplain (i.e., non-channel) deposition (e.g., Leeder, 1977; Fig. 1.2). Channel belts form by river deposition as channels migrate laterally and aggrade vertically, and therefore also contain surfaces representing erosion and deposition from throughout that process. At the largest scale, spanning entire formations, changes in structures of all smaller scales are investigated to study changes in ancient channels as a proxy for changes in ancient conditions (e.g., Foreman et al., 2012).

In this thesis, I link small-scale structures that can only be observed by visiting rock outcrops with large-scale structures that can be observed from orbital imagery in order to use orbital observations to constrain duration and discharge of ancient rivers on Mars from their deposits.

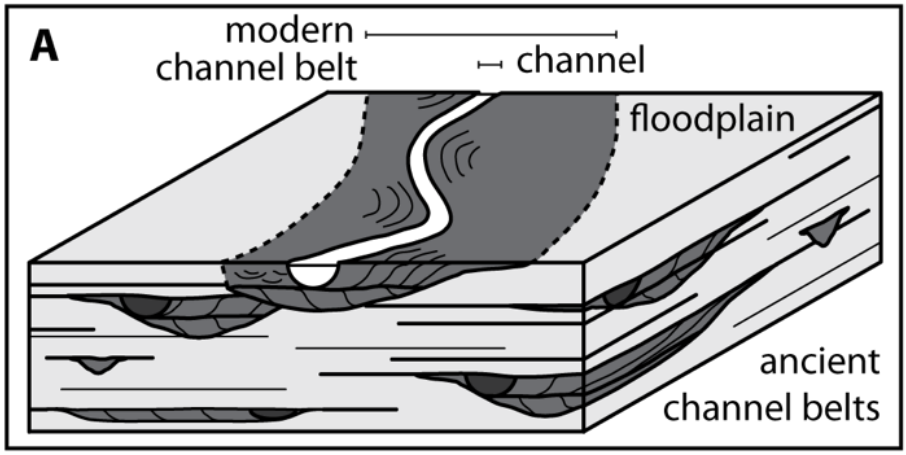

Figure 1.2—Schematic of a channel building stratigraphy as it migrates laterally and aggrades vertically across its floodplain (figure from Hayden et al., 2019; see Fig. 3.3 for additional context). Lateral migration builds scroll bars out of mud on the surface (black arcs in planview) and builds point bars out of sand and gravel in the subsurface (black s-shapes in cross-section). Flow also builds dune cross-strata (black arcs in top channel belt in cross-section). Vertical aggradation builds multiple stories (horizontal lines separating point bars). Together, the sediments deposited during lateral accretion and vertical aggradation form channel belts (dark gray), which are encased in mudstone (light gray)—together these form the bulk of fluvial stratigraphy. Also present are channel fills (darkest gray), which are the remnants after a channel undergoes avulsion and occupies a new channel location. Over time, avulsions create a thick stratigraphy filled with channel belts of different sizes that amalgamate in places.

1.3. Understanding (river) fossils on Mars

Analysis of fossil rivers has been in increasing use for the study of not just Earth, but Mars as well, where relict rivers have been widely observed as valleys (e.g., Hynek et al., 2010) and also, unexpectedly, as sinuous ridges (e.g., Pain et al., 2007). These fluvial sinuous ridges occur in branching networks that resemble river networks, except the ridges stand in positive relief. They occur globally across Mars (Dickson, Lamb, Williams, Hayden, and Fischer, in rev.; Fig. 1.1), with the greatest concentrations in Aeolis Dorsa (e.g., Burr et al., 2009; 2010) and Arabia Terra (Davis et al., 2016; 2019), and specific examples occur near the landing site of the Curiosity rover (e.g., Palucis et al., 2014) as well as within the landing ellipses for the upcoming Perseverance and Rosalind Franklin Rovers (e.g., Goudge et al., 2018; Balme et al., 2020).

Sinuous ridges have proven useful to reconstruct ancient hydrology because they are fluvial features that can be observed from orbit, but uncertainty remains in interpreting them. For example, observation of fluvial ridges has yielded calculated flow durations at individual sites, but they vary by orders of magnitude (e.g., Eberswalde Delta has duration interpretations ranging 10 to 10,000 years; Jerolmack et al., 2004; Irwin et al., 2015); some ridges provide evidence for global oceans or large-scale seas, though none of it is conclusive (e.g., DiBiase et al., 2013; Hughes et al., 2019; Adler et al., 2018); and the width of some ridges compared to the contributing catchment areas implies of exceptionally large rivers, though this finding has yet to be corroborated (Kite et al., 2019). Even parameters as fundamental as flow direction remain enigmatic; for example, flow has been interpreted in opposite directions for features in Aeolis Dorsa (Lefort et al., 2012; 2015; DiBiase et al., 2013), likely because rivers can have slopes that are almost flat (e.g., the Mississippi River has gradient of 10^{-5}) that can easily be obscured by any form of post-emplacement deformation.

A main source of uncertainty is whether ridges represent inverted channels, casts of channels that preserve channel geometries and ancient topography at a snapshot in time (e.g., Pain and Ollier, 1995; Pain et al., 2007), or instead are exhumed channel belts, the amalgamated deposits left behind as a channel migrates and aggrades over geologic time (e.g., DiBiase et al., 2013). Discerning inverted channels from exhumed channel belts is critical to interpreting flow direction, dimension, and duration from observations of fluvial ridges. These uncertainties in understanding fluvial sinuous ridges represent a major hindrance to interpreting ancient hydrology.

In this thesis, I created and applied tools to measure the discharge and duration of ancient rivers from simple remote-sensing measurements of fluvial ridges. I followed three lines of inquiry: 1) re-assessing methods for discerning inverted channels from exhumed channel belts; 2) creating new methods to relate measurements of fluvial ridges to the water discharge, sediment flux, and duration of their associated river; and 3) applying the methods to fluvial ridges on Mars to improve understanding of global fluvial history of Mars.

First, I evaluated a common method of distinguishing inverted channels from exhumed channel belts, which assumes that channels and channel belts have distinct values of ratio of curvature to width, and I found that the ratios are nonunique due to geometric effects (Chapter 2). I then developed new criteria to identify exhumed channel belts based on field observations from ridges at three terrestrial analog sites (Chapters 3-5) -- the Cretaceous Cedar Mountain Formation (Eastern Utah, USA), Jurassic upper Morrison Formation (Eastern Utah, USA), and the Miocene Guadalope-Matarranya Fan (Southern Ebro Basin, Spain). Based on the new criteria, all the terrestrial analogues I examined represent exhumed channel belts. Furthermore, I also found that some of the existing confusion between inverted channels and exhumed channel belts stems from

differing use of the word “channel”, much as for Mars in the 1800s—in this case a “channel” to the mining engineer is a generic sandstone body, which is a “channel belt” to the geomorphologist.

Once a fluvial ridge is correctly interpreted as an inverted channel or exhumed channel belt, the hydrology of its parent paleochannel can be more accurately quantified. I examined existing methods for this hydrologic reconstruction and then created new methods. I found that the width, radius of curvature, and wavelength of a ridge are unreliable as indicators of paleohydrology for exhumed channel belts due to lateral amalgamation (Chapters 2 and 3), and show that the radius of curvature of any observed point bars is more accurate (Chapter 4). I developed a new erosion model that accurately represents the erosion extent of the studied ridges and found that the dominant form of erosion is scarp retreat, which preferentially modifies ridge width (Chapter 4). Caprock thickness on the other hand is less modified because channel belts typically aggrade to a thickness slightly more than the depth of the paleochannel, and scarp-retreat erosion leaves caprock thickness relatively unmodified (Chapters 3 and 4). I also developed equations for water discharge and sediment flux using nondimensional forms of typical river equations so that they can be applied in Mars gravity (Chapters 3-5), and quantified values for river intermittency by analyzing USGS stream gauge data and bankfull survey data for over 200 rivers and sediment deposits (Chapter 5). Intermittency factors are critical for accurately reconstructing durations because they account for natural river variability. Intermittency factor is found to be relatively invariant with slope, grainsize, aridity, timescale of study, or whether a river or its deposit is studied, so the values I found are expected to apply to Mars. A main control instead appears to be shear stress; for example, for rivers with beds coarser than gravel the intermittency factor can be approximated by the fraction of days where shear stress exceeds critical and moves sediment. At the landscape scale, the main control appears to be the ratio

between sediment generation, measured from catchment-averaged denudation rates, and precipitation.

Throughout the work, I applied all these tools to sedimentary deposits on Mars to calculate discharge and duration of rivers on ancient Mars and thereby better understand what the hydrologic system might have looked like. I found that rivers were generally smaller but flowed for longer than previously thought, suggesting that Mars may have indeed maintained a habitable climate early in its history.

Altogether, this contribution enables new quantitative analyses of ancient rivers on both Earth and Mars, resolves longstanding questions about intermittency in sedimentary deposits, and demonstrates that ancient Mars likely had widespread and long-lived liquid water. This thesis can be read as a how-to guide for quantitative river reconstructions from observations of their deposits, with instructions for reconstructing discharge of long-gone rivers in Chapters 3 and 4 and for calculating duration of river activity in Chapter 5. The methods are meant to apply equally well to any planet, provided information about sediment density and planetary gravity. The intermittency factor calculated in Chapter 5 in particular is likely to be of greatest use for Earth applications because it is commonly included in landscape-evolution models.

This thesis also highlights several areas where future work will be fruitful. First, river science on both Earth and Mars will benefit greatly from further improvement of the morphodynamics equations used in Chapters 3-5, such as experiments that validate the role of parameters like gravity and viscosity, and explanation of the physical underpinnings of as-yet unexplained empiricisms like the relationship between Shields shear stress and Reynolds number. Furthermore, the framework for analyzing intermittency factors based on streamgage data presented in Chapter 5 is novel, and

presents a new dataset of intermittency factors along with surveyed bankfull data and USGS hydrographs for future workers to analyze. Morphodynamics advances such as these will improve understanding of both Earth and Mars, and prove useful to river engineers as well. New discoveries of large sedimentary deposits will likely require additional HiRISE-resolution images, perhaps from autonomous flying vehicles. Combining new observations of sedimentary deposits with new tools to study them will greatly benefit our ability to follow the water and thereby search for biosignatures on Mars.

1.4. Works cited

(1882). Canals on the Planet Mars. New York Times.

Adler, J. B., J. F. Bell, P. Fawdon, J. Davis, N. H. Warner, E. Sefton-Nash and T. N. Harrison (2018). "Hypotheses for the Origin of the Hypanis Fan-Shaped Deposit at the Edge of the Chryse Escarpment, Mars: Is it a Delta?" Icarus.

Allen, J. R. (1965). "A review of the origin and characteristics of recent alluvial sediments." Sedimentology **5**(2): 89-191.

Arvidson, R. E., J. L. Gooding and H. J. Moore (1989). "The Martian surface as imaged, sampled, and analyzed by the Viking landers." Reviews of Geophysics **27**(1): 39-60.

Arvidson, R. E., F. Poulet, R. V. Morris, J. P. Bibring, J. F. Bell, S. W. Squyres, P. R. Christensen, G. Bellucci, B. Gondet, B. L. Ehlmann, W. H. Farrand, R. L. Fergason, M. Golombek, J. L. Griffes, J. Grotzinger, E. A. Guinness, K. E. Herkenhoff, J. R. Johnson, G. Klingelhöfer, Y. Langevin, D. Ming, K. Seelos, R. J. Sullivan, J. G. Ward, S. M. Wiseman and M. Wolff (2006). "Nature and origin of the hematite-bearing plains of Terra Meridiani based on analyses of orbital and Mars Exploration rover data sets." Journal of Geophysical Research: Planets **111**(E12): E12S08.

Ataie-Ashtiani, B. and C. T. Simmons (2020). "The millennium-old hydrogeology textbook The Extraction of Hidden Waters by the Persian mathematician and engineer Abubakr Mohammad Karaji (953 CE–1029 CE)." Hydrology and Earth System Sciences **24**(2): 761-761.

Baker, V. R. (1974). "Paleohydraulic interpretation of Quaternary alluvium near Golden, Colorado." Quaternary Research **4**(1): 94-112.

Balme, M. R., S. Gupta, J. M. Davis, P. Fawdon, P. M. Grindrod, J. C. Bridges, E. Sefton-Nash and R. M. E. Williams (2020). "Aram Dorsum: An Extensive Mid-Noachian Age Fluvial Depositional System in Arabia Terra, Mars." Journal of Geophysical Research: Planets **125**(5): e2019JE006244.

Banks, M. E., N. P. Lang, J. S. Kargel, A. S. McEwen, V. R. Baker, J. A. Grant, J. D. Pelletier and R. G. Strom (2009). "An analysis of sinuous ridges in the southern Argyre Planitia, Mars using HiRISE and CTX images and MOLA data." Journal of Geophysical Research: Planets **114**(E9).

Board, S. S. and N. R. Council (2012). Vision and voyages for planetary science in the decade 2013-2022, National Academies Press.

Bradley, R. W. and J. G. Venditti (2017). "Reevaluating dune scaling relations." Earth-Science Reviews **165**: 356-376.

Buhler, P. B., C. I. Fassett, J. W. Head and M. P. Lamb (2014). "Timescales of fluvial activity and intermittency in Milna Crater, Mars." Icarus **241**: 130-147.

Burr, D. M., M.-T. Enga, R. M. E. Williams, J. R. Zimbelman, A. D. Howard and T. A. Brennand (2009). "Pervasive aqueous paleoflow features in the Aeolis/Zephyria Plana region, Mars." Icarus **200**(1): 52-76.

Burr, D. M., R. M. E. Williams, K. D. Wendell, M. Chojnacki and J. P. Emery (2010). "Inverted fluvial features in the Aeolis/Zephyria Plana region, Mars: Formation mechanism and initial paleodischarge estimates." Journal of Geophysical Research: Planets **115**(E07011).

Craddock, R. A. and A. D. Howard (2002). "The case for rainfall on a warm, wet early Mars." Journal of Geophysical Research: Planets **107**(E11): 21-21-21-36.

Davis, J. M., M. Balme, P. M. Grindrod, R. M. E. Williams and S. Gupta (2016). "Extensive Noachian fluvial systems in Arabia Terra: Implications for early Martian climate." Geology **44**(10): 847-850.

Davis, J. M., S. Gupta, M. Balme, P. M. Grindrod, P. Fawdon, Z. I. Dickeson and R. M. E. Williams (2019). "A Diverse Array of Fluvial Depositional Systems in Arabia Terra: Evidence for mid-Noachian to Early Hesperian Rivers on Mars." Journal of Geophysical Research: Planets **124**(7): 1913-1934.

DiBiase, R. A., A. B. Limaye, J. S. Scheingross, W. W. Fischer and M. P. Lamb (2013). "Deltaic deposits at Aeolis Dorsa: Sedimentary evidence for a standing body of water on the northern plains of Mars." Journal of Geophysical Research: Planets **118**(6): 1285-1302.

Dickson, J. L., M. P. Lamb, R. M. E. Williams, A. T. Hayden and W. W. Fischer (in rev.). "The Global Distribution of Depositional Rivers on Early Mars." Nature Geoscience.

Dury, G. H. (1976). "Discharge prediction, present and former, from channel dimensions." Journal of Hydrology **30**(3): 219-245.

Einstein, H. A. (1950). The bed-load function for sediment transportation in open channel flows, United States Department of Agriculture. **1026**.

Engelund, F. and E. Hansen (1967). A monograph on sediment transport in alluvial streams, Tekniskforlag Skelbrekgade 4, Copenhagen V, Denmark.

Ethridge, F. G. and S. A. Schumm (1977). "Reconstructing paleochannel morphologic and flow characteristics: methodology, limitations, and assessment." Fluvial Sedimentology **Memoir 5**(Paleohydraulics).

Fairén, A. G. (2010). "A cold and wet Mars." Icarus **208**(1): 165-175.

Fassett, C. I. and J. W. Head (2008). "Valley network-fed, open-basin lakes on Mars: Distribution and implications for Noachian surface and subsurface hydrology." Icarus **198**(1): 37-56.

Foreman, B. Z., P. L. Heller and M. T. Clementz (2012). "Fluvial response to abrupt global warming at the Palaeocene/Eocene boundary." Nature **491**(7422): 92-95.

Gauckler, P. (1863). Etudes Théoriques et Pratiques sur l'Ecoulement et le Mouvement des Eaux, Dunod.

Gilbert, G. K. (1877). Geology of the Henry mountains, Government Printing Office.

Goudge, T. A., D. Mohrig, B. T. Cardenas, C. M. Hughes and C. I. Fassett (2018). "Stratigraphy and paleohydrology of delta channel deposits, Jezero crater, Mars." Icarus **301**: 58-75.

Grotzinger, J. P., R. E. Arvidson, J. F. Bell Iii, W. Calvin, B. C. Clark, D. A. Fike, M. Golombek, R. Greeley, A. Haldemann, K. E. Herkenhoff, B. L. Jolliff, A. H. Knoll, M. Malin, S. M. McLennan, T. Parker, L. Soderblom, J. N. Sohl-Dickstein, S. W. Squyres, N. J. Tosca and W. A. Watters (2005). "Stratigraphy and sedimentology of a dry to wet eolian depositional system, Burns formation, Meridiani Planum, Mars." Earth and Planetary Science Letters **240**(1): 11-72.

Grotzinger, J. P. and R. E. Milliken (2012). "The sedimentary rock record of Mars: Distribution, origins, and global stratigraphy." Sedimentary Geology of Mars **102**: 1-48.

Grotzinger, J. P., D. Y. Sumner, L. Kah, K. Stack, S. Gupta, L. Edgar, D. Rubin, K. Lewis, J. Schieber and N. Mangold (2014). "A habitable fluvio-lacustrine environment at Yellowknife Bay, Gale Crater, Mars." Science **343**(6169): 1242777.

Halevy, I. and J. W. Head III (2014). "Episodic warming of early Mars by punctuated volcanism." Nature Geoscience **7**(12): 865-868.

Hayden, A. T., M. P. Lamb, W. W. Fischer, R. C. Ewing, B. McElroy and R. M. E. Williams (2019). "Formation of sinuous ridges by inversion of river-channel belts in Utah, USA, with implications for Mars." Icarus **332**: 92-110.

Head III, J. W. and S. Pratt (2001). "Extensive Hesperian-aged south polar ice sheet on Mars: Evidence for massive melting and retreat, and lateral flow and ponding of meltwater." Journal of Geophysical Research: Planets **106**(E6): 12275-12299.

Heller, P. L. and C. Paola (1996). "Downstream changes in alluvial architecture: an exploration of controls on channel-stacking patterns." Journal of Sedimentary Research **66**(2).

Hoke, M. R., B. M. Hynek and G. E. Tucker (2011). "Formation timescales of large Martian valley networks." Earth and Planetary Science Letters **312**(1-2): 1-12.

Hughes, C. M., B. T. Cardenas, T. A. Goudge and D. Mohrig (2019). "Deltaic Deposits Indicative of a Paleo-Coastline at Aeolis Dorsa, Mars." Icarus **317**: 442-4534.

Hynek, B. M., M. Beach and M. R. Hoke (2010). "Updated global map of Martian valley networks and implications for climate and hydrologic processes." Journal of Geophysical Research: Planets **115**(E9).

Irwin, R. P., K. W. Lewis, A. D. Howard and J. A. Grant (2015). "Paleohydrology of Eberswalde crater, Mars." Geomorphology **240**: 83-101.

Jerolmack, D. J., D. Mohrig, M. T. Zuber and S. Byrne (2004). "A minimum time for the formation of Holden Northeast fan, Mars." Geophysical Research Letters **31**(21).

Jopling, A. V. (1966). "Some principles and techniques used in reconstructing the hydraulic parameters of a paleo-flow regime." Journal of Sedimentary Research **36**(1).

Keulegan, G. H. (1938). Laws of turbulent flow in open channels, National Bureau of Standards US.

Kite, E. S., D. P. Mayer, S. A. Wilson, J. M. Davis, A. S. Lucas and G. S. de Quay (2019). "Persistence of intense, climate-driven runoff late in Mars history." Science Advances **5**(3): eaav7710.

Lane, K. M. D. (2006). "Mapping the Mars canal mania: Cartographic projection and the creation of a popular icon." Imago Mundi **58**(2): 198-211.

Lapôtre, M. G. A. and A. Ielpi (2020). "The Pace of Fluvial Meanders on Mars and Implications for the Western Delta Deposits of Jezero Crater." AGU Advances **1**(2): e2019AV000141.

Leeder, M. (1977). "A quantitative stratigraphic model for alluvium, with special reference to channel deposit density and interconnectedness." Fluvial Sedimentology **Memoir 5**: 587-596.

Lefort, A., D. M. Burr, R. A. Beyer and A. D. Howard (2012). "Inverted fluvial features in the Aeolis-Zephyria Plana, western Medusae Fossae Formation, Mars: Evidence for post-formation modification." Journal of Geophysical Research: Planets **117**(E3).

Lefort, A., D. M. Burr, F. Nimmo and R. E. Jacobsen (2015). "Channel slope reversal near the Martian dichotomy boundary: Testing tectonic hypotheses." Geomorphology **240**: 121-136.

Luo, W., X. Cang and A. D. Howard (2017). "New Martian valley network volume estimate consistent with ancient ocean and warm and wet climate." Nature Communications **8**: 15766.

Malin, M. C. and K. S. Edgett (2000). "Sedimentary rocks of early Mars." Science **290**(5498): 1927-1937.

Manning, R. (1890). On the flow of water in open channels and pipes.

Masursky, H. (1973). "An overview of geological results from Mariner 9." Journal of Geophysical Research **78**(20): 4009-4030.

McLennan, S. M., R. Anderson, J. Bell, J. Bridges, F. Calef, J. L. Campbell, B. Clark, S. Clegg, P. Conrad and A. Cousin (2014). "Elemental geochemistry of sedimentary rocks at Yellowknife Bay, Gale crater, Mars." science **343**(6169).

Miall, A. D. (2013). Principles of sedimentary basin analysis, Springer Science & Business Media.

Milton, D. J. (1973). "Water and processes of degradation in the Martian landscape." Journal of Geophysical Research **78**(20): 4037-4047.

Mohrig, D., P. L. Heller, C. Paola and W. J. Lyons (2000). "Interpreting avulsion process from ancient alluvial sequences: Guadalope-Matarranya system (northern Spain) and Wasatch Formation (western Colorado)." Geological Society of America Bulletin **112**(12): 1787-1803.

Moore, J. M., A. D. Howard, W. E. Dietrich and P. M. Schenk (2003). "Martian layered fluvial deposits: Implications for Noachian climate scenarios." Geophysical Research Letters **30**(24).

Nikuradse, J. (1950). Laws of flow in rough pipes. N. T. Memorandum. Washington, D.C.

Nyberg, B. and J. A. Howell (2015). "Is the present the key to the past? A global characterization of modern sedimentary basins." Geology **43**(7): 643-646.

Pain, C., J. Clarke and M. Thomas (2007). "Inversion of relief on Mars." Icarus **190**(2): 478-491.

Pain, C. F. and C. D. Ollier (1995). "Inversion of relief — a component of landscape evolution." Geomorphology **12**(2): 151-165.

Palucis, M. C., W. E. Dietrich, A. G. Hayes, R. M. E. Williams, S. Gupta, N. Mangold, H. Newsom, C. Hardgrove, F. Calef and D. Y. Sumner (2014). "The origin and evolution of the Peace Vallis fan system that drains to the Curiosity landing area, Gale Crater, Mars." Journal of Geophysical Research: Planets **119**(4): 705-728.

Paola, C. and L. Borgman (1991). "Reconstructing random topography from preserved stratification." Sedimentology **38**(4): 553-565.

Paola, C., P. L. Heller and C. L. Angevine (1992). "The large-scale dynamics of grain-size variation in alluvial basins, 1: Theory." Basin research **4**(2): 73-90.

Parker, T. J., R. S. Saunders and D. M. Schneeberger (1989). "Transitional morphology in west Deuteronilus Mensae, Mars: Implications for modification of the lowland/upland boundary." Icarus **82**(1): 111-145.

Prandtl, L. (1925). "7. Bericht über Untersuchungen zur ausgebildeten Turbulenz." ZAMM-Journal of Applied Mathematics and Mechanics/Zeitschrift für Angewandte Mathematik und Mechanik **5**(2): 136-139.

Rivera-Hernández, F., D. Y. Sumner, N. Mangold, S. G. Banham, K. S. Edgett, C. M. Fedo, S. Gupta, S. Gwizd, E. Heydari and S. Maurice (2020). "Grain Size Variations in the Murray Formation: Stratigraphic Evidence for Changing Depositional Environments in Gale Crater, Mars." Journal of Geophysical Research: Planets **125**(2): e2019JE006230.

Rosenberg, E. N. and J. W. Head III (2015). "Late Noachian fluvial erosion on Mars: cumulative water volumes required to carve the valley networks and grain size of bed-sediment." Planetary and Space Science **117**: 429-435.

Schiaparelli, G. V. (1878). Osservazioni astronomiche e fisiche sull'asse di rotazione e sulla topografia del pianeta Marte...: Memoria, Salviucci.

Segura, T. L., O. B. Toon, A. Colaprete and K. Zahnle (2002). "Environmental effects of large impacts on Mars." Science **298**(5600): 1977-1980.

Sharp, R. P. and M. C. Malin (1975). "Channels on mars." Geological Society of America Bulletin **86**(5): 593-609.

Sømme, T. O., W. Helland-Hansen, O. J. Martinsen and J. B. Thurmond (2009). "Relationships between morphological and sedimentological parameters in source-to-sink systems: A basis for predicting semi-quantitative characteristics in subsurface systems." Basin Research **21**(4): 361-387.

Squyres, S. W., J. P. Grotzinger, R. E. Arvidson, J. F. Bell, W. Calvin, P. R. Christensen, B. C. Clark, J. A. Crisp, W. H. Farrand, K. E. Herkenhoff, J. R. Johnson, G. Klingelhöfer, A. H. Knoll, S. M. McLennan, H. Y. McSween, R. V. Morris, J. W. Rice, R. Rieder and L. A. Soderblom (2004). "In Situ Evidence for an Ancient Aqueous Environment at Meridiani Planum, Mars." Science **306**(5702): 1709-1714.

Stein, N., J. P. Grotzinger, J. Schieber, N. Mangold, B. Hallet, H. Newsom, K. M. Stack, J. A. Berger, L. Thompson, K. L. Siebach, A. Cousin, S. Le Mouélic, M. Minitti, D. Y. Sumner, C. Fedo, C. H. House, S. Gupta, A. R. Vasavada, R. Gellert, R. C. Wiens, J. Frydenvang, O. Forni, P. Y. Meslin, V. Payré and E. Dehouck (2018). "Desiccation cracks provide evidence of lake drying on Mars, Sutton Island member, Murray formation, Gale Crater." Geology **46**(6): 515-518.

Tanaka, K. L. (1986). "The stratigraphy of Mars." Journal of Geophysical Research: Solid Earth **91**(B13): E139-E158.

Vaniman, D., D. Bish, D. Ming, T. Bristow, R. Morris, D. Blake, S. Chipera, S. Morrison, A. Treiman and E. Rampe (2014). "Mineralogy of a mudstone at Yellowknife Bay, Gale crater, Mars." Science **343**(6169).

von Karman, T. (1937). "The fundamentals of the statistical theory of turbulence." Journal of the Aeronautical Sciences **4**(4): 131-138.

Wolman, M. G. and J. P. Miller (1960). "Magnitude and frequency of forces in geomorphic processes." The Journal of Geology: 54-74.

Wordsworth, R., B. Ehlmann, F. Forget, R. Haberle, J. Head and L. Kerber (2018). "Healthy debate on early Mars." Nature Geoscience **11**(12): 888-888.

Wordsworth, R., F. Forget, E. Millour, J. W. Head, J. B. Madeleine and B. Charnay (2013). "Global modelling of the early martian climate under a denser CO2 atmosphere: Water cycle and ice evolution." Icarus **222**(1): 1-19.

Wordsworth, R. D. (2016). "The climate of early Mars." Annual Review of Earth and Planetary Sciences **44**: 381-408.

Chapter 2

2 SIMILAR CURVATURE-TO-WIDTH RATIOS FOR CHANNELS AND CHANNEL BELTS: IMPLICATIONS FOR PALEO-HYDRAULICS OF FLUVIAL RIDGES ON MARS

Hayden, A.T., Lamb, M. P., Carney, A. J. Submitted to *Geology*.

Abstract

The surface of Mars contains abundant sinuous ridges that appear similar to river channels in planform, but they stand as topographic highs. Ridges have similar curvature-to-width ratios as terrestrial meandering rivers, which has been used to support the hypothesis that ridges are inverted channels that directly reflect channel geometry. Anomalously wide ridges, in turn, have been interpreted as evidence for larger rivers on Mars compared to Earth. However, an alternate hypothesis is that ridges are exhumed channel-belt deposits—a larger zone of relatively coarse-grained deposits formed from channel lateral migration and aggradation. Here we measured landform wavelength, radius of curvature and width to evaluate whether they can be used to distinguish channels, channel belts, and martian ridges. We found that all three landforms follow similar scaling relations, in which radius of curvature-to-width ratios ranges from 1.7-7.3, and wavelength-to-width ratios range from 5.8-13. We interpret this similarity to be a geometric consequence of a sinuous curved line of finite width. Combined with observations of ridge-stacking patterns, our results suggest that wide ridges on Mars more likely indicate fluvial channel-belts that formed over significant time, rather than anomalously large rivers.

2.1 Introduction

The hydrology of ancient Mars remains poorly constrained, with major questions remaining about the discharge and duration of ancient river flows (e.g., Wordsworth et al., 2018; Kite, 2019). One important landform class used to reconstruct the hydraulics of rivers is fluvial ridges (Burr et al., 2010; Williams et al., 2013) (Fig. 2.1). Fluvial ridges are topographic highs that have often have a sinuous or branching planform pattern that appears similar to river channels or deltas. Consequently, fluvial ridges are often interpreted as *inverted channels* (Fig. 2.1A); that is, the topographic inversion of a channel-filling deposit that was more resistant to erosion than the surrounding material, and was exhumed to produce a ridge that reflects the geometry of the original channel (e.g., Pain et al., 1995, 2007; Burr et al., 2009; 2010). The inverted channel hypothesis has been used to infer the discharge of ancient rivers on Mars (Burr et al., 2010; Williams et al., 2013) and interpret flow direction from the branching pattern of ridges (Lefort et al., 2012). By comparing martian fluvial ridges to terrestrial river channels of the same catchment area, Kite et al. (2019) found that martian ridges are wider, and interpreted that rivers on ancient Mars must also have been larger than those on Earth today.

The inverted-channel hypothesis, however, is not the only possible interpretation of fluvial ridges. Alternatively, fluvial ridges could be eroded remnants of channel-belt deposits (DiBiase et al., 2013). Channel belts are fluvial deposits built over time as rivers migrate laterally and aggrade vertically; they are often much wider than the channel width (e.g., Robinson and McCabe, 1997; Fernandes et al., 2016). Exhumation of these deposits, with preferential erosion of the mudstone and juxtaposition of channel-belts at different stratigraphic levels, has produced terrestrial ridges and ridge networks that appear similar to examples on Mars (e.g., Williams et al., 2009; Hayden et al., 2019; Cardenas et al., 2020).

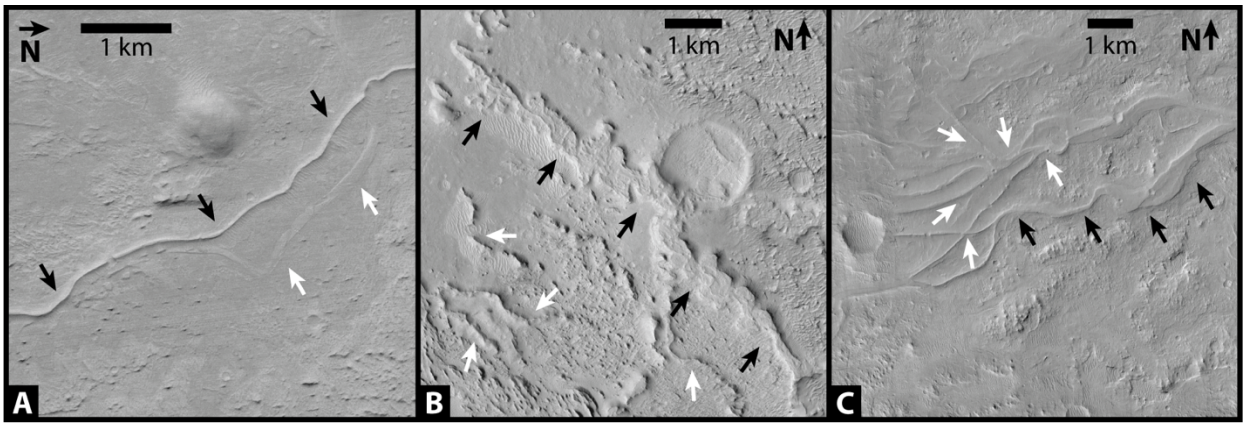

Figure 2.1-- Sinuous ridges in Aeolis Dorsa, Mars, shown in CTX mosaic (Dickson et al., 2019). A) Sinuous ridge (black arrows; "Mars Ridge 3" in Table 2.1) classified as "thin" and interpreted as an inverted channel (Burr et al., 2009; 2010), and stacked on a low-relief ridge (white arrows). Location: 5.63°S, 152.67°E. B) Sinuous ridge classified as "flat" and interpreted as an exhumed channel belt (Burr et al., 2009; Hughes et al., 2019). Location: 6.34°S, 154.15°E. C) Sinuous ridge classified as an inverted channel (black arrows; "Mars Ridges 1 and 2" in Table 2.1) and used to support the observation that rivers on ancient Mars were wider than modern terrestrial rivers (Kite et al., 2019). Other ridges (white arrows) are stacked beneath the main ridge. Location: 3.03°S, 151.68°E.

Because ridge stratigraphy cannot easily be observed on Mars, it is difficult to distinguish these two formation mechanisms. Support for the inverted channel hypothesis has come from a comparison of ridge geometry to that of terrestrial meandering rivers (e.g., Burr et al., 2010; Kite et al., 2015; 2019). In particular, meandering rivers follow scaling relations between channel-bend radius of curvature, R, or channel-bend wavelength, λ, and channel width, W,

$$\lambda = aW^b, \qquad \text{Eq. 2.1}$$

$$R = cW^d, \qquad \text{Eq. 2.2}$$

where $a = 7.5$, $b = 1.12$, $c = 1.5$, and $d = 1.12$ are empirical constants (Williams, 1988). Many ridges on Mars follow the same scaling relations, which has been used to argue that ridges are inverted channels and reflect channel dimensions (Burr et al., 2010; Kite et al., 2015; 2019). Similar arguments also have been made for interpreting ancient river deposits observed in reflectance

seismology on Earth (e.g., Martin et al., 2018; Payenberg et al., 2019). However, it is yet to be tested whether channel-belt curvature also scales with landform width.

2.2 Methods

We digitized landform outlines (shapefiles) from 16 river channels, 7 channel belts, and 10 sinuous ridges on Mars (Fig. 2.2; Table 2.1) to test whether channel-belts follow similar scaling relations as channels. The channel-belt dataset contains all published shapefiles of channel belts we could find, including the Mississippi River (Fernandes et al., 2016), three belts on the Rhine-Meuse Delta (Digitaal Basisbestand Paleogeografie van de Rijn-Maas Delta; Cohen and Stouthamer, 2012), and three river corridors in Vermont (Vermont Department of Environmental Conservation). Channels were selected to pair with the channel belts (Mississippi, Meuse, Nederrijn, and Waal Rivers), rivers in the Williams (1986) compilation ($n = 10$), and two additional large North American Rivers from an Esri database (Assiniboine and MacKenzie Rivers). European river channels were obtained from OpenStreetMap using its Overpass API downloading function; North American channels were obtained from the North America Water Polygons dataset (Class=1 for rivers) from Esri; and the remainder (all from the Williams, 1986, compilation) were digitized by hand on imagery in Google Earth. Ridges on Mars were selected from those analyzed by Kite et al. (2019) ($n = 5$), and by Burr et al. (2009; 2010) ($n = 5$). Selections were made based on finding well-defined caprocks in Context Camera (CTX) imagery, and ridge outlines were traced manually on those images.

We extracted centerlines and landform width measured perpendicular to the centerline from the landform shapefiles using the RivMap package (Schwenk et al., 2017). Both manual (e.g., Williams, 1986) and automated methods (e.g., Ferguson, 1975; Kite et al., 2015; Vermeulen et al., 2016) require manually digitized centerlines, which are difficult to trace precisely or consistently. To overcome these issues, we manually outlined landforms at a resolution finer than half the

estimated landform width, converted it to a high-resolution binary image mask, and used RivMap (Shwenk et al., 2017) to obtain a skeletonized centerline (see Supplementary Methods; Fig. 2.4). The centerline was resampled at increments equal to the median landform width, *W*, to avoid bias in comparisons across scales (e.g., Nikora, 1991), and to be consistent with manual measurements (Williams, 1986). To resample, we found the intersection of the skeletonized centerline and a circle of radius *W*, drawn around the centerline start point, defined the next node in the new centerline at that intersection, and repeated the process along the landform length (Supplementary Methods).

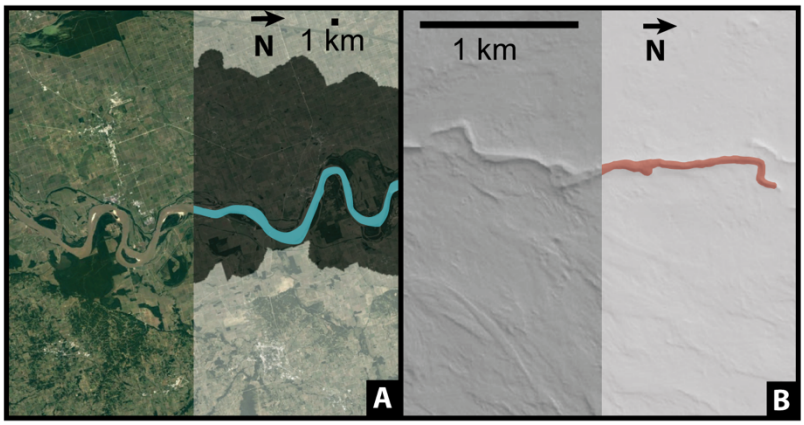

Figure 2.2-- Example results of landform width and curvature extraction (right side of each image). A) Mississippi River with extracted channel (blue) and channel belt (grey), USA (36.1°N, 89.5°W; Google Earth). B) Sinuous ridge in Roddy Crater, Mars (Mars Ridge 4, Table 2.1). Note an additional ridge in the upper right. (21.66°S, 39.74°W).

We measured radius of curvature and wavelength on the centerline for each bend. Curvature was calculated at each centerline node following Vermeulen et al. (2016) (Supplementary Methods, Section 2.7.2). Zero-crossings in curvature defined the boundaries between individual bends (Ferguson, 1975), and we calculated meander wavelength as twice the straight-line distance in planview between each crossing (e.g., Kite et al., 2015). The radius of curvature was calculated as by the inverse of the maximum curvature for each bend because it approximates prior methods of fitting circles to the tightest bend (e.g., Vermeulen et al., 2016). We took the median values of radius

of curvature, R, and wavelength, λ, for each landform. Our method compares within a factor of three of W, R, and λ values measured manually by Williams (1986) (Supplementary Methods, Fig. 2.5).

2.3 Results

We analyzed in total 1336 bends from river channels, 312 from channel belts, and 193 from martian fluvial ridges. Channels have median widths of 18 - 2000 m, channel belts have widths of 210 – 25,000 m, and ridges have widths of 6.4 - 210 m (Figs. 2.3A and 2.3B). The channel-belts are on average larger than the channels, as expected, and they both follow a similar scaling relation with channel width. Wavelength and radius of curvature follow similar power-law relations (Eq. 2.1 and 2.2) for all three landforms with best-fit (using reduced-major-axis fitting to the data in log space) b and d values equal to 0.97 and 1.06 for channels, 1.03 and 1.1 for channel belts, and 1.14 and 0.92 for ridges. The data follow the relation proposed by Williams (1986) for smaller landforms (their channels had $W < 1975$ m), but not for cases with $W > 300$ m (Figs. 2.3A and 2.3B). We also calculated the ratios λ/W and R/W because b and d are near one. The median and interquartile range of λ/W are 10.8 (8.8-12) for channels, 6.4 (6.1-7.3) for channel belts, and 8.4 (7.8-9.5) for martian ridges (Fig. 2.3C). The median and interquartile range of R/W are 3.2 (2.4-4.0) for channels, 2.4 (2.3-2.6) for channel belts, and 3.4 (1.9-3.9) for ridges (Fig. 2.3D). Although channels tend to have slightly larger values of λ/W and R/W compared to channel-belts, the distributions overlap making these metrics undiagnostic of whether ridges are channels or channel belts.

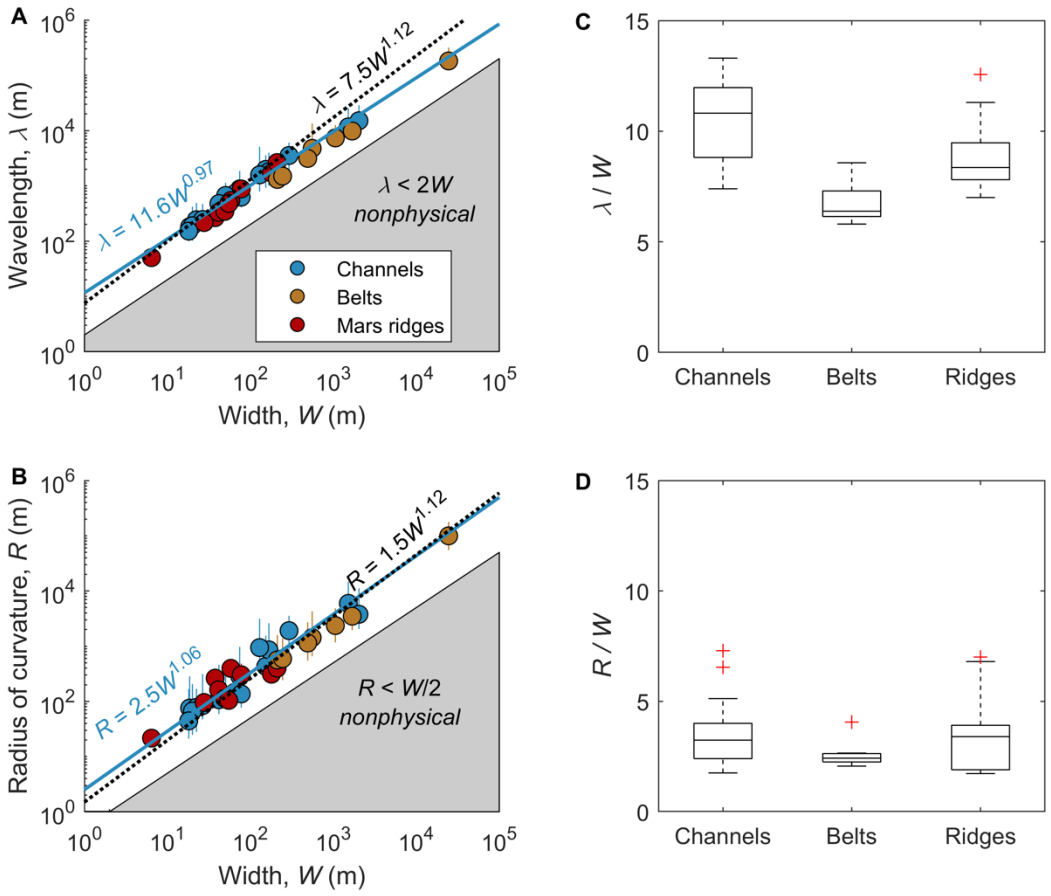

Figure 2.3-- Comparison of landform wavelength and radius of curvature to width (Table 2.1). A&B) Each dot represents the median values for one landform, with error bars (usually smaller than the dot) representing the 5-95 percentile range. The solid blue lines are the reduced-major-axis best-fits to terrestrial river channel data, and the dashed black lines are the Williams (1986) relations. Gray area is nonphysical by Eqs. (2.3) and (2.4). C&D) Box-and-whisker plots of the ratio between wavelength or radius of curvature and width.

The reason for similar scaling between river channels, channel belts, and ridges is that, geometrically, they all are sinuous lines with a finite width, which places lower limits on λ/W and R/W (Fig. 2.3). For instance, if radius of curvature of the centerline is lower than half the width, the edges would contact each other and there would no longer be a recognizable centerline, such that

$$R \geq W/2. \qquad \text{Eq. 2.3}$$

Similarly, the edges contact when the straight-line distance between bend endpoints ($\lambda/2$ by definition) decreases to the width, such that

$$\lambda/2 \geq W. \quad \text{Eq. 2.4}$$

If bends along the landforms were all identical to the lower limits given by Eqs. (2.3) and (2.4), then the landforms would be tight, repeating curves. In reality, the curvature of rivers and channel belts is fractal (e.g., Nikora, 1991; Data Repository) and therefore the wavelength and curvature values occur at many scales above the cutoff scale (Vermeulen et al., 2016) (Figs. 2.4, 2.7-2.14), which increases the median values away from the lower bounds. However, the fractal nature also means that each large curve comprises many smaller curves (Vermeulen et al., 2016), so the abundance of small curves weights the median values towards the lower bounds.

2.4 Discussion

Our results show that channel belts and channels follow similar scaling relations with landform width, and both are similar to relations for martian ridges. Although two-factor Kolmogorov-Smirnov tests (see Data Repository for explanation) can distinguish the distributions of channels and channel belts for λ/W, they do not for R/W, and the similarity between the distributions, nonetheless, makes them ambiguous metrics for discerning whether ridges are channels or channel belts. This result necessitates reevaluation of interpretations where the similarity was used to interpret martian ridges as direct proxies for fluvial channels.

Ridges examined by Kite et al. (2019) (e.g., Figs. 2.1C and 2.2B) are wider by a factor of up to twenty compared to terrestrial channels with similar catchment areas, which they interpreted to represent rivers with extraordinary discharges, as compared to Earth. We propose that a simpler explanation is that these landforms are exhumed channel belts (e.g., DiBiase et al., 2013; Cardenas et al., 2018; Davis et al., 2019). Because channel belts form over time due channel lateral migration,

they can be up to 30-fold wider than their associated channels (Hayden et al., 2019). Moreover, stacked coarse-grained channel belts within a fine-grained floodplain matrix define the typical stratigraphic architecture of fluvial sedimentary basins (e.g., Allen, 1978; Bridge and Leeder, 1979), such that channel belts should be the null hypothesis (DiBiase et al., 2013). On Mars, stacking has been observed (DiBiase et al., 2013; Cardenas et al., 2017; Davis et al., 2019), often in association with "flat" ridges (e.g., Burr et al., 2009; 2010; Kite et al., 2015), and many of the ridges that we analyzed are also stacked (Figs. 2.1A, 2.1C, and 2.2B), supporting a channel-belt interpretation. In contrast, channel fills that preserve channel geometry are rare in terrestrial fluvial stratigraphy; they tend to be fine-grained as a result of overbank sedimentation into an abandoned channel (e.g., Nichols and Fisher, 2007), and are therefore unlikely to be resistant to erosion to form ridges. Non-fluvial channel fills, such as lava flows, are also plausible, but these typically fill valleys or canyons (e.g., Stearns, 1936), rather than channels, such that they also would yield ridges that are wider than the channels.

If martian ridges are indeed exhumed channel belts, rather than inverted channels, then ridge width and wavelength should reflect channel-belt geometry rather than the channel geometry. In this case, the bankfull discharge of ancient martian rivers would be significantly smaller than calculations that have assumed that ridge width and wavelength reflect the channel properties (e.g., Burr et al., 2010; Williams et al., 2013; Kite et al., 2015). The error is compounded in estimates of discharge because of the nonlinear relation between discharge and channel width (e.g., Hayden et al., 2019). Furthermore, while ridges are interpreted to be a preserved fluvial landscape at a snapshot in time under the inverted-channel hypothesis, channel belts represent fluvial deposits accumulated over thousands of years (e.g., Tornqvist et al., 1996). Moreover, thick sequences of fluvial deposits with stacked channel belts, similar to those on Mars (e.g., Kite et al., 2015; DiBiase et al., 2013), form on Earth over hundreds of thousands to millions of years (e.g., Johnson et al., 1985).

2.5 Conclusions

River channels, channel belts and martian ridges are all sinuous landforms with a finite width, and they all have similar scaling relations between radius of curvature, R, and landform width, W, and wavelength, λ, and width. Our results indicate that R-W and λ-W scaling relations should not be used to interpret whether martian ridges represent inverted channels or exhumed channel belts. Channel belts are larger than channels because they form over time due to river lateral migration, and their deposits are a fundamental element of fluvial stratigraphic architecture. Therefore, large martian ridges might represent exhumed channel belts representing river activity over substantial time, rather than extraordinarily large rivers.

2.6 Works cited

Allen, J. (1978). "Studies in fluviatile sedimentation: an exploratory quantitative model for the architecture of avulsion-controlled alluvial suites." Sedimentary Geology **21**(2): 129-147.

Bridge, J. S. and M. R. Leeder (1979). "A simulation model of alluvial stratigraphy." Sedimentology **26**(5): 617-644.

Burr, D. M., M.-T. Enga, R. M. E. Williams, J. R. Zimbelman, A. D. Howard and T. A. Brennand (2009). "Pervasive aqueous paleoflow features in the Aeolis/Zephyria Plana region, Mars." Icarus **200**(1): 52-76.

Burr, D. M., R. M. E. Williams, K. D. Wendell, M. Chojnacki and J. P. Emery (2010). "Inverted fluvial features in the Aeolis/Zephyria Plana region, Mars: Formation mechanism and initial paleodischarge estimates." Journal of Geophysical Research: Planets **115**(E07011).

Cardenas, B. T., D. Mohrig and T. A. Goudge (2018). "Fluvial stratigraphy of valley fills at Aeolis Dorsa, Mars: Evidence for base-level fluctuations controlled by a downstream water body." GSA Bulletin **130**(3-4): 484-498.

Cardenas, B. T., D. Mohrig, T. A. Goudge, C. M. Hughes, J. S. Levy, T. Swanson, J. Mason and F. Zhao (2020). "The anatomy of exhumed river-channel belts: Bedform to belt-scale river kinematics of the Ruby Ranch Member, Cretaceous Cedar Mountain Formation, Utah, USA." Sedimentology **n/a**(n/a).

Cohen, K., E. Stouthamer, H. Pierik and A. Geurts (2012). "Digitaal Basisbestand Paleogeografie van de Rijn-Maas Delta." Dept. Fysische Geografie. Universiteit Utrecht. Digitale Dataset.

Conservation, V. D. o. "River Corridor and Floodplain Maps." Retrieved September 2019, from https://dec.vermont.gov/watershed/rivers/river-corridor-and-floodplain-protection/river-corridor-and-floodplain-maps.

Davis, J. M., S. Gupta, M. Balme, P. M. Grindrod, P. Fawdon, Z. I. Dickeson and R. M. E. Williams (2019). "A Diverse Array of Fluvial Depositional Systems in Arabia Terra: Evidence for mid-Noachian to Early Hesperian Rivers on Mars." Journal of Geophysical Research: Planets **124**(7): 1913-1934.

DiBiase, R. A., A. B. Limaye, J. S. Scheingross, W. W. Fischer and M. P. Lamb (2013). "Deltaic deposits at Aeolis Dorsa: Sedimentary evidence for a standing body of water on the northern plains of Mars." Journal of Geophysical Research: Planets **118**(6): 1285-1302.

Ferguson, R. I. (1975). "Meander irregularity and wavelength estimation." Journal of Hydrology **26**(3-4): 315-333.

Fernandes, A. M., T. E. Tornqvist, K. M. Straub and D. Mohrig (2016). "Connecting the backwater hydraulics of coastal rivers to fluvio-deltaic sedimentology and stratigraphy." Geology **44**(12): 979-982.

Hayden, A. T., M. P. Lamb, W. W. Fischer, R. C. Ewing, B. McElroy and R. M. E. Williams (2019). "Formation of sinuous ridges by inversion of river-channel belts in Utah, USA, with implications for Mars." Icarus **332**: 92-110.

Johnson, N. M., J. Stix, L. Tauxe, P. F. Cerveny and R. A. Tahirkheli (1985). "Paleomagnetic chronology, fluvial processes, and tectonic implications of the Siwalik deposits near Chinji village, Pakistan." The Journal of Geology **93**(1): 27-40.

Kite, E. S. (2019). "Geologic Constraints on Early Mars Climate." Space Science Reviews **215**(1): 10.

Kite, E. S., A. D. Howard, A. Lucas and K. W. Lewis (2015a). "Resolving the era of river-forming climates on Mars using stratigraphic logs of river-deposit dimensions." Earth and Planetary Science Letters **420**: 55-65.

Kite, E. S., D. P. Mayer, S. A. Wilson, J. M. Davis, A. S. Lucas and G. S. de Quay (2019). "Persistence of intense, climate-driven runoff late in Mars history." Science Advances **5**(3): eaav7710.

Lefort, A., D. M. Burr, R. A. Beyer and A. D. Howard (2012). "Inverted fluvial features in the Aeolis-Zephyria Plana, western Medusae Fossae Formation, Mars: Evidence for post-formation modification." Journal of Geophysical Research: Planets **117**(E3).

Malin, M. C., J. F. Bell, B. A. Cantor, M. A. Caplinger, W. M. Calvin, R. T. Clancy, K. S. Edgett, L. Edwards, R. M. Haberle, P. B. James, S. W. Lee, M. A. Ravine, P. C. Thomas and M. J. Wolff (2007). "Context Camera Investigation on board the Mars Reconnaissance Orbiter." Journal of Geophysical Research **112**(E5).

Martin, J., A. M. Fernandes, J. Pickering, N. Howes, S. Mann and K. McNeil (2018). "The Stratigraphically Preserved Signature of Persistent Backwater Dynamics in a Large Paleodelta System: The Mungaroo Formation, North West Shelf, Australia." Journal of Sedimentary Research **88**(7): 850-872.

Montgomery, K. (1996). "Sinuosity and Fractal Dimension of Meandering Rivers." Area **28**(4): 491-500.

Nichols, G. J. and J. A. Fisher (2007). "Processes, facies and architecture of fluvial distributary system deposits." Sedimentary Geology **195**(1): 75-90.

Nikora, V. I. (1991). "Fractal structures of river plan forms." Water resources research **27**(6): 1327-1333.

Pain, C., J. Clarke and M. Thomas (2007). "Inversion of relief on Mars." Icarus **190**(2): 478-491.

Pain, C. F. and C. D. Ollier (1995). "Inversion of relief — a component of landscape evolution." Geomorphology **12**(2): 151-165.

Robinson, J. W. and P. J. McCabe (1997). "Sandstone-body and shale-body dimensions in a braided fluvial system: Salt Wash Sandstone Member (Morrison Formation), Garfield County, Utah." AAPG bulletin **81**(8): 1267-1291.

Schwenk, J., A. Khandelwal, M. Fratkin, V. Kumar and E. Foufoula-Georgiou (2017). "High spatiotemporal resolution of river planform dynamics from Landsat: The RivMAP toolbox and results from the Ucayali River." Earth and Space Science **4**(2): 46-75.

Stearns, H. T. (1936). "Origin of the large springs and their alcoves along the Snake River in southern Idaho." The Journal of Geology **44**(4): 429-450.

Törnqvist, T. E., T. R. Kidder, W. J. Autin, K. van der Borg, A. F. de Jong, C. J. Klerks, E. M. Snijders, J. E. Storms, R. L. van Dam and M. C. Wiemann (1996). "A revised chronology for Mississippi River subdeltas." Science **273**(5282): 1693-1696.

Vermeulen, B., A. J. F. Hoitink, G. Zolezzi, J. D. Abad and R. Aalto (2016). "Multiscale structure of meanders." Geophysical Research Letters **43**(7): 3288-3297.

Williams, G. P. (1986). "River meanders and channel size." Journal of Hydrology **88**(1-2): 147-164.

Williams, G. P. (1988). Paleofluvial estimates from dimensions of former channels and meanders. Flood Geomorphology. V. R. Baker, R. C. Kochel and P. C. Patton. New York, John Wiley & Sons**:** 321-334.

Williams, R. M. E., R. P. Irwin, D. M. Burr, T. Harrison and P. McClelland (2013). "Variability in martian sinuous ridge form: Case study of Aeolis Serpens in the Aeolis Dorsa, Mars, and insight from the Mirackina paleoriver, South Australia." Icarus **225**(1): 308-324.

Williams, R. M. E., R. P. Irwin and J. R. Zimbelman (2009). "Evaluation of paleohydrologic models for terrestrial inverted channels: Implications for application to martian sinuous ridges." Geomorphology **107**(3-4): 300-315.

Wordsworth, R., B. Ehlmann, F. Forget, R. Haberle, J. Head and L. Kerber (2018). "Healthy debate on early Mars." Nature Geoscience **11**(12): 888-888.

2.7 Supplemental material

This data repository contains description of previous work, our methods for curvature determination, a fractal geometry description of channel belts, martian ridge descriptions, and the measured data.

2.7.1 Prior methods for measuring curvature

The typical method to measure the planform geometry of a river channel has previously begun with manual definition of a line (Ferguson, 1976; Martin et al., 2018; Payenberg et al., 2019; Jacobsen and Burr, 2018). To capture river geometry efficiently, the line is typically digitized with

a spacing between centerline points comparable to the channel width, though some studies use variable point spacing (e.g., Basher et al., 2018) and at least one study uses point spacing significantly smaller than channel width in their analysis of scroll-bar geometry (Jacobsen and Burr, 2018). Individual bends are defined either visually or algorithmically by places where the centerline changes direction (e.g., Ferguson, 1971 Williams, 1986; Kite et al., 2015). Meander half-wavelength, $\lambda/2$, is measured as the straight-line distance between bend termini, and arc wavelength (λ_a) is measured along the centerline. Within each bend, the radius of curvature is obtained by fitting a circle to the tightest point, which is known to have some variation between users (Williams, 1986) so sometimes measurements are repeated with different users (e.g., Kite et al., 2015; Jacobsen and Burr, 2018). Automated methods applied to these manually defined centerlines have also been used, including use of zero-crossings in planform geometry to determine ends of meander bends (Ferguson, 1976; Howard and Hemberger, 1991; Kite et al., 2015; Martin et al., 2018; Payenberg et al., 2019), and an automated circle-fitting algorithm (Jacobsen and Burr, 2018).

2.7.2 New method for measuring curvature

We developed a new method to analyze planform geometry that minimizes impact from the biases of manual centerline selection because channel belts have sinuous, non-parallel boundaries, and also minimizes impact from scale-dependent measurements that result from fractal geometry of river channels (e.g., Nikora, 1991) and channel belts.

The new method used a high-resolution trace of the landform outline as the input for all its analyses (Fig. 2.4). The point spacing on the outline was smaller than the width of the landform by a factor 2 - 4 in order to reduce scale-dependent biases. The outline was then converted to a binary image mask and skeletonized to a centerline using RivMap, which employs Matlab image-processing tools to equally erode the shape laterally to find the centerline and discard any spurs that occur off the centerline (Schwenk et al., 2017). Widths were analyzed at every tenth pixel along the

centerline by dividing the landform area parallel to that section of centerline by the length of that section of centerline (Schwenk et al., 2017), and then the median width, *W*, was taken for the whole landform.

The resulting high-resolution centerline was pixelated; to get a smoother centerline we generated a new centerline by resampling. To get the new centerline at arbitrary point spacing, η, we found the intersection of the original pixelated centerline and a circle of radius η drawn around the centerline start point, defined the next node in the new centerline at that intersection, and repeated the process along the entire length. We selected $\eta = W$ for our main scale of analysis.

Curvature (*C*) was calculated from its definition at each centerline node, using partial derivatives of latitude (*y*) and longitude (*x*) (where $x' = dx/\eta$ and $y'' = d^2y/\eta^2$, and each measurement is discrete) at each centerline position using actual coordinates and a η value (Vermeulen et al., 2016)

$$C = (x'y\text{-}x''y') / (x'^2 + y'^2)^{3/2}. \qquad \text{Eq. 2.5}$$

Note that the line is made of discrete line segments, and so any method for determining curvature is limited. Schwenk et al. (2015) documented three different methods for determining curvature; the method we selected is their method 1. While they preferred method 3 for its built-in smoothing, it does this by approximating meander segments as circular arcs with constant curvature. We chose method 1 as it instead produces the maximal curvature at the apex of a second-order approximation, better aligning with prior work that manually fitted a circle to the tightest part of each bend.

With a series of curvature values at each centerline point, we then used zero-crossings in curvature to define the boundaries of bends, following prior methods (e.g., Vermeulen et al., 2016). For each bend, we took the inverse of the maximum curvature to get radius of curvature, *R*, for that bend, and found the straight-line distance between the bend termina as the meander half-wavelength,

which we doubled to get wavelength, λ, similar to prior work (e.g., Kite et al., 2015). Automated methods detect many small-scale bends (e.g., Vermeulen et al., 2016), and we excluded bends made of one or two segments (along-centerline length $\leq 2\eta$) because such bends would be ignored in a visual analysis. This approach is similar to some prior work (e.g., Kite et al., 2015), which included a sinuosity threshold below which near-straight bends were incorporated into adjacent bends. We then took the median values of W, R, and λ from all included bends on the landform.

To assess the accuracy of our new method we compared it to the earlier manual method (Fig. 2.5). We used the data from Williams (1986) for comparison, and applied our method to the listed rivers by tracing the river channels in Google Earth at the locations near the towns listed by Williams (1986). Discrepancies likely result because our method averages over a number of bends, and it is unclear which bends Williams (1986) specifically studied. Furthermore, the tendency towards overestimating radius of curvature is likely due to the tendency of the algorithm to identify bends that are straighter than humans visually would include (Fig. 2.4).

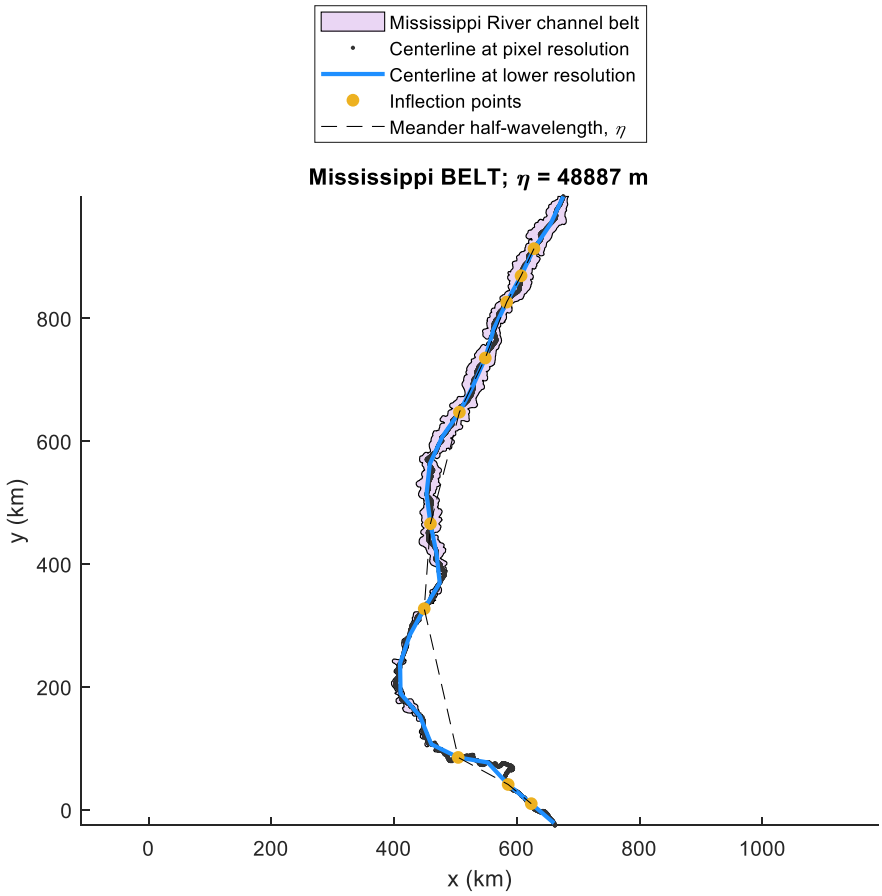

Figure 2.4--Automated analysis on the channel belt of the Mississippi River (blue shape) captures the centerline at a variety of scales and calculates wavelength for all bends at each scale. The solid black line is all the points recognized by the RivMap algorithm (Schwenk et al., 2017) as the centerline at pixel-scale resolution, while the blue line is the centerline resampled at lower resolution, η. The resampling loses details finer than η but captures larger-scale features. Yellow points are the bend inflection points detected on the blue line, and the dashed black lines connect them and thereby represents the half-wavelength of each bend.

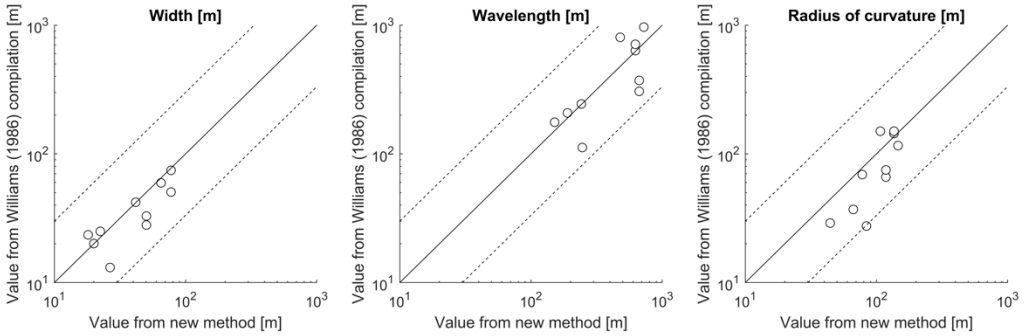

Figure 2.5--Comparison between values from Williams (1986) and values from our new method, using $\eta = W$ to emulate the manual methods. Dashed lines represent a factor of three difference.

2.7.3 Kolmogorov-Smirnov similarity testing

To evaluate the similarity of the distributions of wavelength-width and radius-of-curvature-width ratio, we used two-factor Kolmogorov-Smirnov tests (*kstest2* in Matlab). This analysis computes the difference between the cumulative distribution functions (CDFs) of each parameter and uses the maximum difference between the CDFs to evaluate the probability that each set of values were drawn from the same distribution. We used 5% significance level as the threshold to reject the null hypothesis that values were drawn from the same distribution.

2.7.4 Fractal nature of channels, channel belts, and ridges

River channel planview curvature can be described using fractal geometry (Mandelbrot, 1982; Nikora, 1991; Montgomery, 1996), and we hypothesized that fractal geometry plays a role in setting the wavelength and radius of curvature for channels and channel belts. Here, we tested the hypothesis that channel belts are fractal like river channels.

The fractal equation relates the straight-line distance between endpoints (L_0) to the length of the curve (L_η) measured at arbitrary node spacing η (Mandelbrot, 1982)

$$\frac{L_\eta}{\eta} = \left(\frac{L_0}{\eta}\right)^F, \qquad \text{Eq. 2.6}$$

in which F is the fractal dimension. A non-fractal plane curve will have F=1, and F>1 is indicative of fractal behavior. We determined F using a Richardson plot, which relates the length of a sinuous line to the scale at which is measured (centerline node spacing, η), in which the slope of the best-fit line is equal to 1-F (Fig. 2.6).

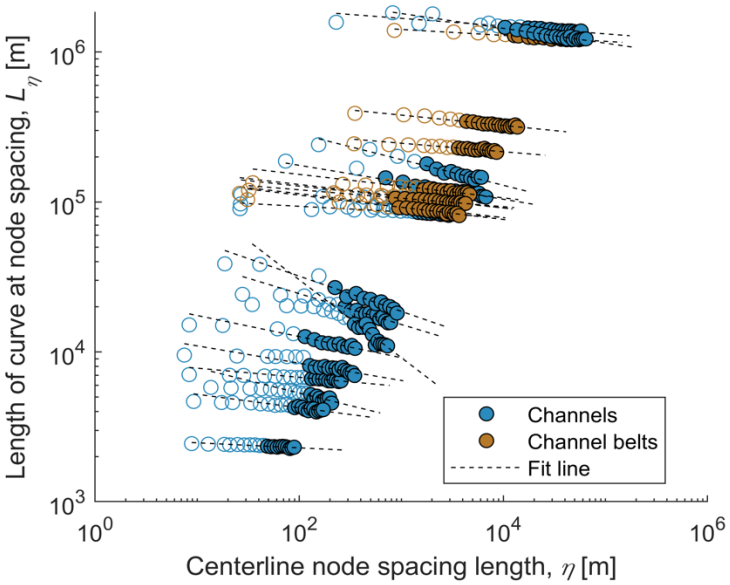

Figure 2.6–Richardson plots for each terrestrial location analyzed. Each data has a section where L_η is mostly independent of η (empty circles) and a section where L_η scales as η to a negative power (filled circles). The scale-dependence of length is a fractal property, so any feature that shows this dependence is fractal. Slope of the best-fit line (i.e., the exponent of a power-law fit; dashed line) is equal to $1 - F$. Small scales are non-fractal. Steepest line is Murrumbudgee River, which has the highest fractal dimension ($F = 1.52$).

We found that channels in our database have fractal dimensions between 1.03-1.52, similar to previous work 1.1-1.5 (Montgomery, 1996). We detected rollover points from the data on Fig. 2.6 using the *findchangepts* command in Matlab, which determines which subset of points have a stable mean value and which points destabilize that mean. The rollover observed with this method (open circles in Fig. 2.6) indicates a minimum scale of fractal geometry, which Nikora (1991) predicted to be near the channel width. However, unlike the predictions of Nikora (1991), we did not observe

any rollover at large scale on the Richardson plot that would indicate upper limits on the fractal behavior of channels, such as bounds from a confining valley.

Channel belts also follow fractal scaling, but have generally smaller fractal dimensions of 1.04-1.08 (Fig. 2.6). Similar to our observations of the river channels, the fractal behavior of channel belts also is bounded at the smallest scales. The low values of fractal dimension for channel belts are likely related to the relatively low sinuosity of channel belts compared to channels because sinuosity and fractal dimension are related (Montgomery, 1996).

Because individual channels and channel belts exhibit fractal dimensions $F>1$ down to a scale near that of their width, both exhibit curves at scales down to the width. Thus, both have ratios of wavelength-to-width and radius of curvature-to-width near the lower bounds defined by Eqs. (2.3) and (2.4). It may be possible in some instances to identify channel belts by their lower fractal dimensions, but the wide range of dimensions for channels make this metric ambiguous.

2.7.5 Mars ridges analyzed

Martian ridges included in the study are shown below (Figs. 2.7-2.14). In all images, the background is the CTX mosaic (Dickson et al., 2019), analyzed ridge(s) are traced in red, prior centerline sketch of Kite et al. (2019) is in orange when available, and coordinate of location from Burr et al., (2009) is also given. In the numerous cases where other ridges are present they are indicated with arrows. Illustrations of the measurement are also provided; in all illustrations the red shape is the traced landform from CTX images, black solid line is the skeletonized centerline at pixel resolution, light blue line is the centerline rescaled to node spacing of $\eta = W$, yellow dots are the inflection points identified by the curvature analysis, and black dashed line is the meander half-wavelength. In some cases, the algorithm finds so many inflection points that the whole line appears yellow; these occur when the landform is made of many segments, and the algorithm detects the

many small curves rather than focusing on the large curves that are visually prominent, which is due to the fractal or multiscale.

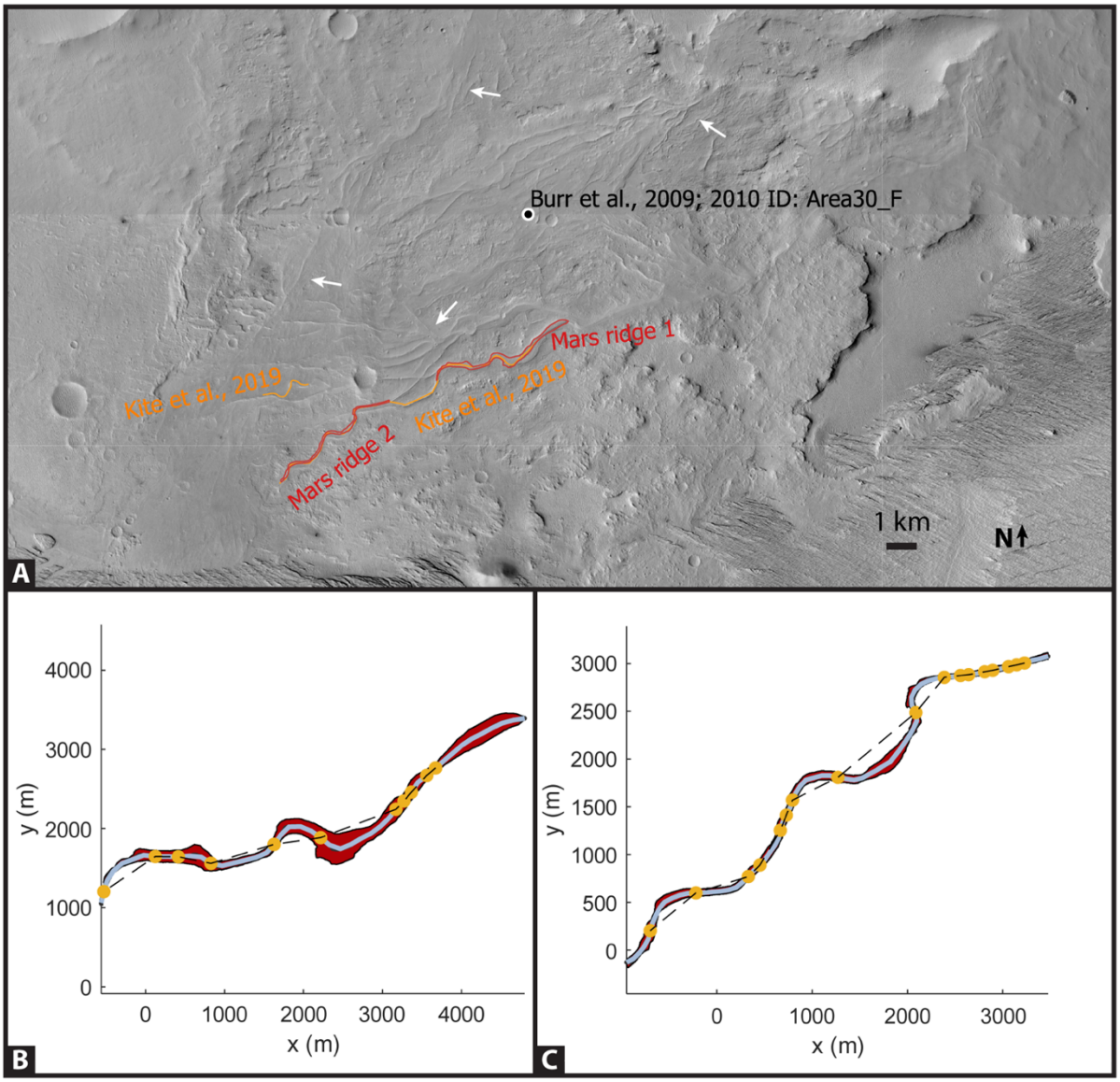

Figure 2.7 – Mars Ridges 1 and 2, which were noted by Burr et al. (2009) and previously analyzed by Kite et al. (2019). A) Numerous ridges are present in northeast Aeolis Dorsa (152.7°E, -4.10°S). We studied one ridge studied by Kite et al. (2019), but we split it into two because the ridge width changes visibly at a bifurcation that occurs between our two segments. Numerous other ridges are present (white arrows), and stacking patterns are clear (see also Fig. 2.1). B) Ridge 1, analyzed at $\eta = 146$ m. C) Ridge 2, analyzed at $\eta = 86$ m.

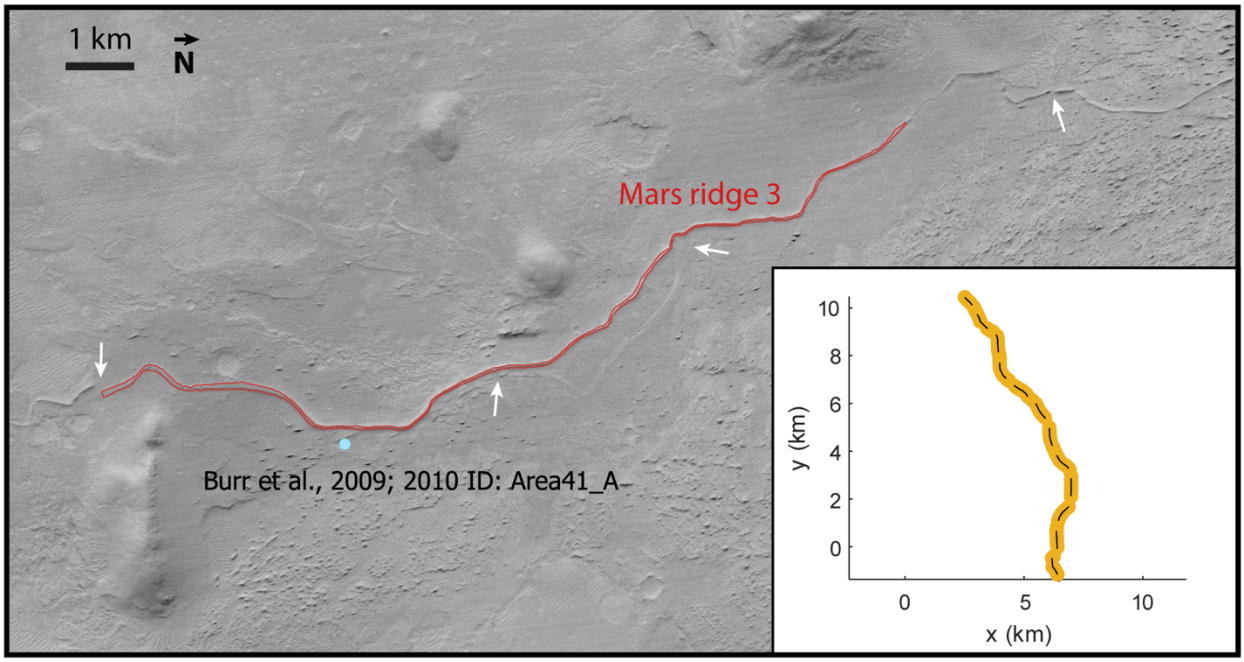

Figure 2.8 – Mars Ridge 3, which was noted and analyzed by Burr et al. (2009; 2010) in central Aeolis Dorsa (152.7°E, 5.7°S). Other ridges are present, and white arrows here indicate locations where stacked ridges cross (see also Fig. 2.1). Inset: sketch of Ridge 3, analyzed at $\eta = 38$ m.

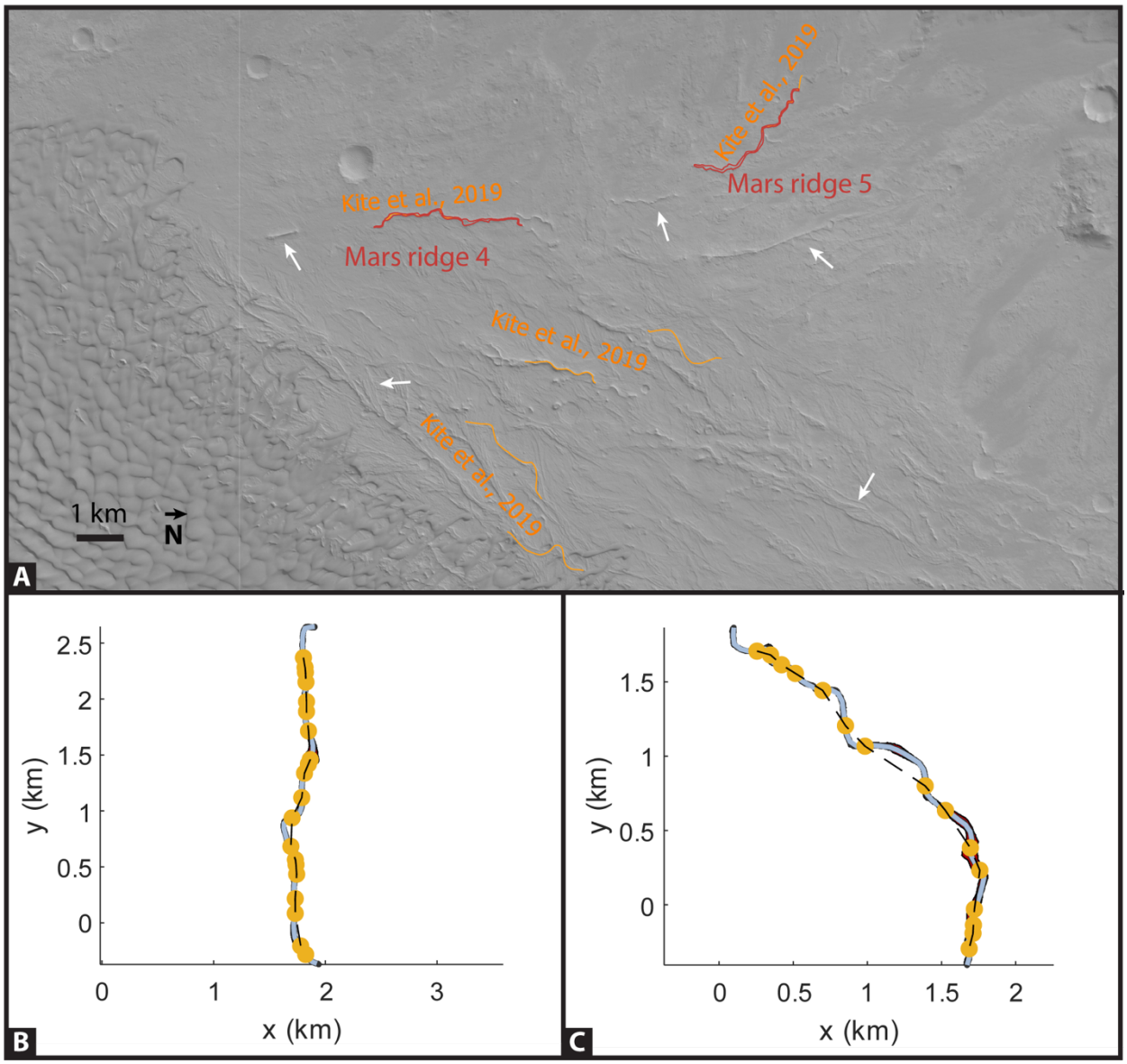

Figure 2.9 – Mars Ridges 4 and 5, which were previously analyzed by Kite et al. (2019). A) Numerous ridges are present in Roddy Crater (39.76°W, 21.65°S). We studied two ridges previously studied by Kite et al. (2019), and numerous other ridges are present (white arrows). Stacking patterns are clear. B) Ridge 4, analyzed at $\eta = 44$ m. C) Ridge 5, analyzed at $\eta = 56$ m.

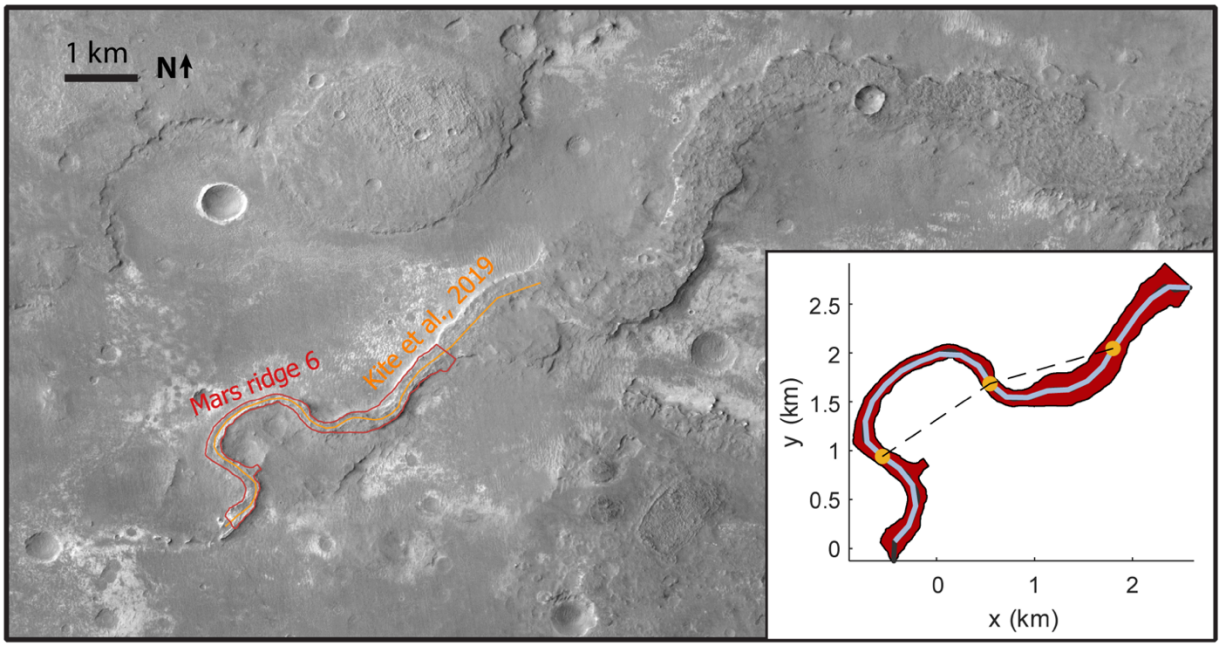

Figure 2.10 – Mars Ridge 6, which was noted and analyzed by Kite et al. (2019) in northern Greely Crater (2.8°E, 34.2°S). The ridge extends further to the right in the image, but becomes complicated by impact craters so we only analyzed a subset, like Kite et al. (2019). Inset: sketch of Ridge 6, analyzed at $\eta = 215$ m.

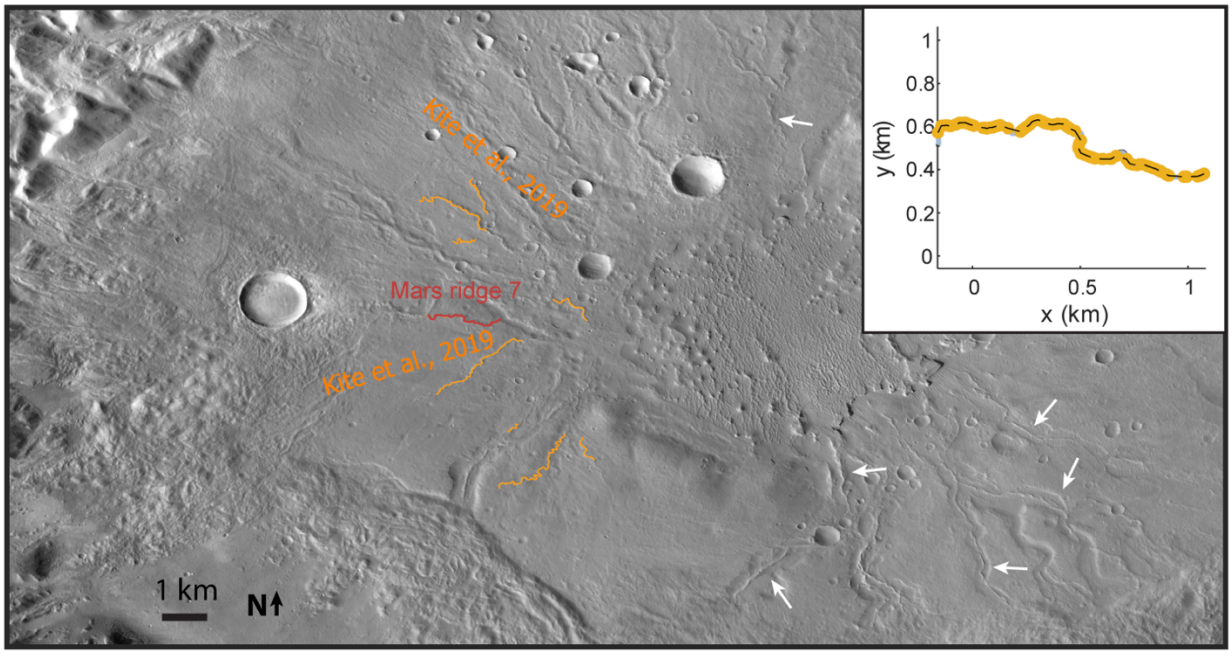

Figure 2.11 – Mars Ridge 7, which was noted and analyzed by Kite et al. (2019) in Chukhung Crater (72.58°W, 38.46°N). Other ridges are present (white arrows). Inset: sketch of Ridge 7, analyzed at $\eta = 7$ m.

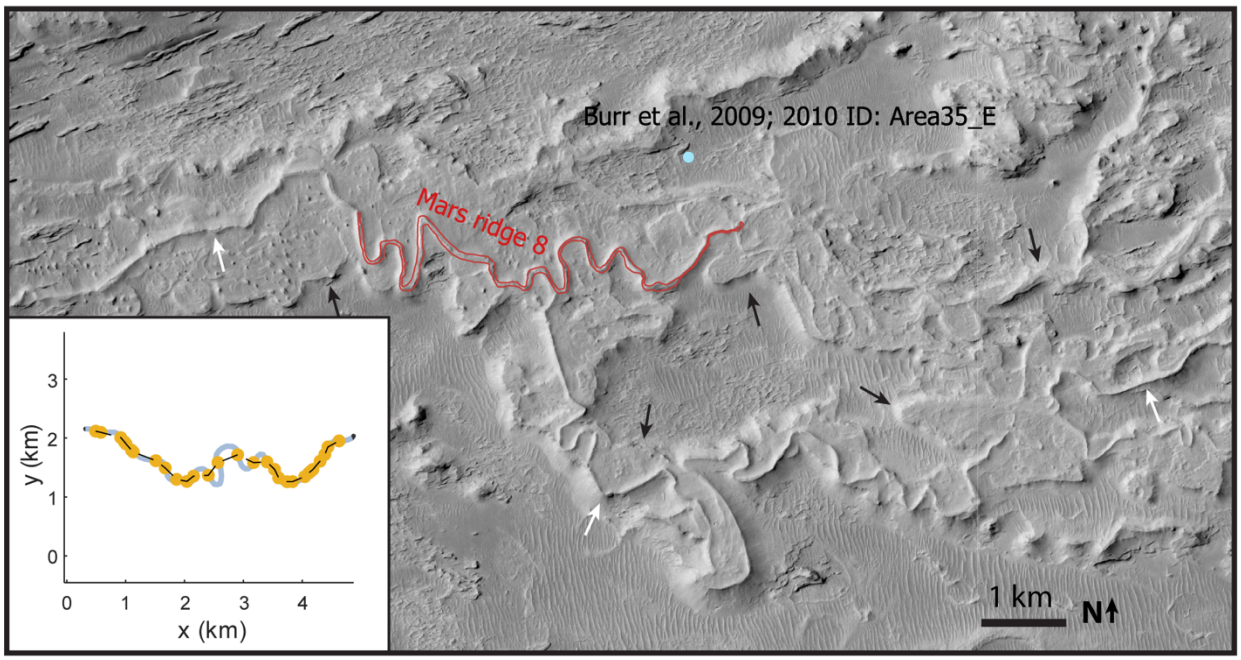

Figure 2.12 – Mars Ridge 8, which was noted and analyzed by Burr et al. (2009; 2010) in eastern Aeolis Dorsa (154.9°E, 4.92°S). Numerous other ridges are present, and white arrows here indicate those that were interpreted as inverted channels while black arrows indicate those interpreted as exhumed channel belts (Burr et al., 2009; 2010). Inset: sketch of Ridge 8, analyzed at $\eta = 60$ m.

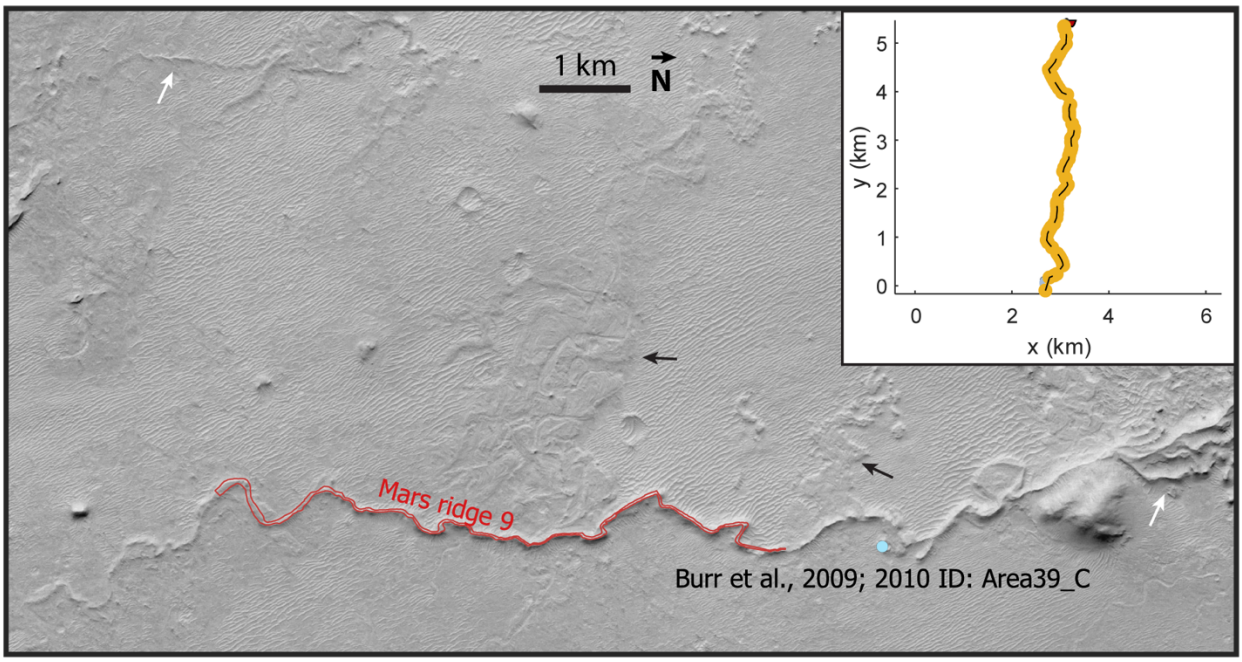

Figure 2.13– Mars Ridge 9, which was noted and analyzed by Burr et al. (2009; 2010) in southeastern Aeolis Dorsa (153.6°E, 6.3°S). A few other ridges are present (white arrows), and

there appear to be lateral accretion sets indicating channel belts (black arrows). Inset: sketch of Ridge 9, analyzed at $\eta = 28$ m.

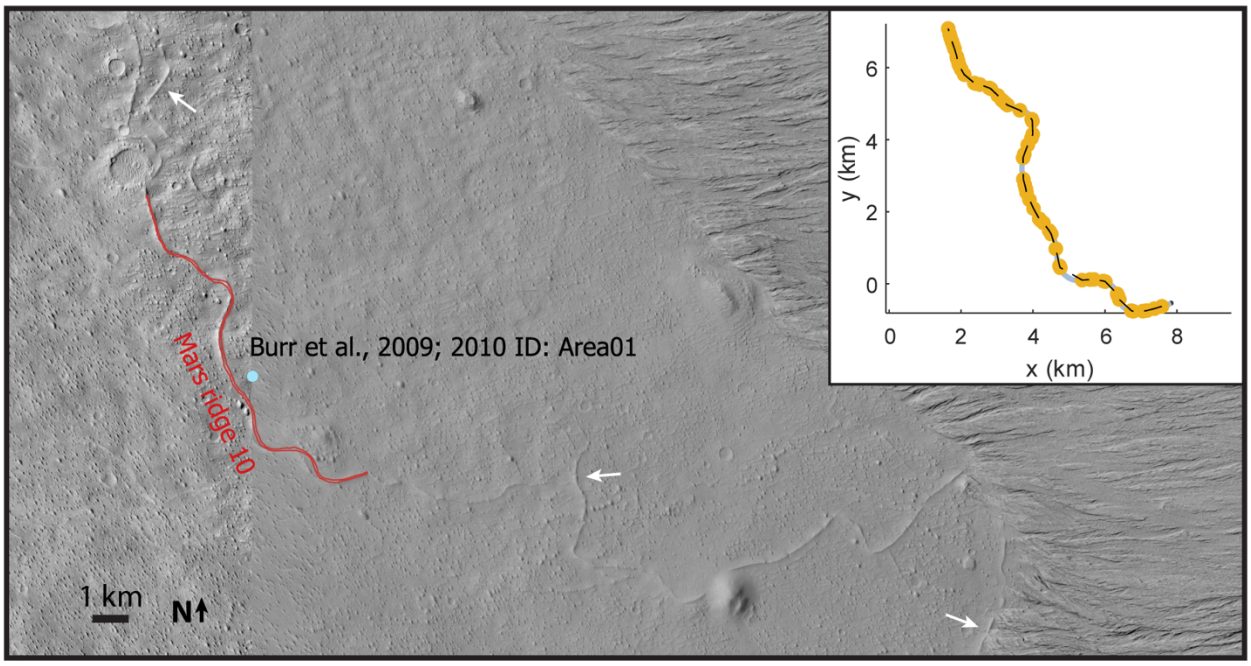

Figure 2.14– Mars Ridge 10, which was noted and analyzed by Burr et al. (2009; 2010) in northeast Aeolis Dorsa (151.9°E, 2.9°S). Other ridges are present (white arrows). Inset: sketch of Ridge 10, analyzed at $\eta = 55$ m.

Landform Name	Location	Original centerline node spacing, η (m)	Node spacing at analysis scale, $\eta \approx W$ (m)	Width, W (m)	Half-wavelength, $\lambda/2$ (m)	Meander arc length (m)	Radius of curvature, R (m)	Sinuosity, S (-)	Length, L_η, measured at $\eta = W$ (m)	Fractal dimension, F	Number of bends analyzed
Assiniboine River [a]	50.04N, 97.88W	3.67	73.5	74.3	440	515	287	1.94	187000	1.11	259
Desna [b]	51.0N, 30.9E	17.9	155	153	991	1240	431	1.82	241000	1.17	154
Emån [b]	57.41N, 15.62E	1	18.5	18.5	90.8	92.3	75.6	1.32	2420	1.03	17
Lagan [b]	57.19N, 14.05E	4.23	21.5	22.4	121	139	77.9	1.71	5750	1.17	32
Lesser Slave River [b]	55.2N, 114.1W	3.3	65.6	65	362	525	146	1.69	24000	1.21	42
Ljusnan [b]	62.55N, 12.57E	0.886	28.5	26.6	123	142	83.9	1.36	6980	1.06	37
Logdealven [b]	65.14N, 20.73E	0.849	48.9	50.3	334	538	118	2.01	9330	1.12	16
MacKenzie River [a]	65.5N, 127.7W	26.2	1490	1520	5830	5950	5960	1.32	1550000	1.05	175
Mississippi BELT [c]	33N, 91W	237	24900	24500	91000	99500	99600	1.23	1240000	1.04	6
Mississippi CHANNEL [c]	33N, 91W	236	2030	2040	7530	10100	3780	1.75	1800000	1.1	153
Murrumbidgee River [b]	34.5S, 144.8E	9.86	75.3	77.5	312	452	136	2.36	20300	1.52	39
Rhine Belt 1 [d]	52.00N, 5.10E	100	1050	1060	3670	4220	2360	1.74	382000	1.07	65
Rhine Belt 1 CHANNEL [b]	52.00N, 5.10E	3.56	170	167	901	935	857	1.19	109000	1.07	74
Rhine Belt 2 [d]	51.87N, 6.01E	50	1660	1690	4890	4990	3490	1.16	238000	1.06	24

Rhine Belt 2 CHANNEL [b]	51.87N, 6.01E	3.57	297	292	1770	1780	1910	1.16	92500	1.08	34
Rhine Belt 3 [d]	51.83N, 5.55E	3.57	636	556	2380	2860	1430	1.25	111000	1.08	28
Rhine Belt 3 CHANNEL [b]	51.83N, 5.55E	3.57	132	129	790	793	942	1.23	89000	1.04	61
Svagan [b]	61.90N, 16.52E	1.07	22.2	20	94.8	111	66.6	1.41	4600	1.09	28
Swan River [b]	55.3N, 115.4W	2.15	41.1	41.7	239	329	107	2.79	38400	1.23	96
Tomichi Creek [b]	38.53N, 106.93W	2.45	17.8	18.1	75.7	88.9	44.4	1.65	15000	1.14	119
Vermont Belt 1 BELT [e]	43.84N, 73.15W	9.44	446	491	1570	1780	1140	1.21	130000	1.08	47
Vermont Belt 2 BELT [e]	44.4N, 73.0W	9.41	218	211	653	871	562	1.47	115000	1.06	81
Vermont Belt 3 BELT [e]	44.65N, 72.94W	4.09	247	244	749	989	593	1.33	99900	1.08	61
Mars ridge 1 [fg]	4.10S, 153.79E	3.9	179	180	850	894	311	1.11	6440	1.04	3
Mars ridge 10 [g]	2.9S, 151.99E	3.91	54.6	58.2	271	273	396	1.21	12000	1.03	28
Mars ridge 2 [fg]	4.17S, 153.65E	3.9	76.4	77.7	439	459	303	1.13	6110	1.02	11
Mars ridge 3 [g]	5.7S, 152.7E	1.95	38.3	37.6	133	134	263	1.13	14100	1.07	46
Mars ridge 4 [f]	21.65S, 39.76W	1.95	39.6	41.4	165	198	162	1.11	3320	1.03	11
Mars ridge 5 [f]	21.54S, 39.79W	3.75	43.1	49.3	172	194	113	1.22	3360	1.04	10
Mars ridge 6 [f]	34.23S, 2.77E	3.58	215	210	1320	1830	399	1.46	5800	1.02	2
Mars ridge 7 [f]	38.465N, 72.58W	0.792	16	15.8	63.3	64.1	38.4	1.28	2040	1.12	21
Mars ridge 8 [g]	4.92S, 154.878E	3.88	49.1	52.2	215	295	99.3	1.85	9340	1.14	24

Mars ridge 9 [g]	6.3S, 153.59E	1.95	27.7	27.7	108	111	95.4	1.22	6870	1.06	38

Table 2.1--Data from study. Mask pixel size and point spacing are user-specified; all other values result from the automated analyses. Data are plotted in Fig. 3. Data sources: [a] shapefiles North American Water Polygons (Esri; downloaded from arcgis.com), rivers selected for their large size; [b] shapefiles downloaded from OpenStreetMap (www.openstreetmap.org) using the "overpass turbo" application of Overpass API (http://overpass-turbo.eu); [c] Shapefile from Fernandes et al. (2016); [d] shapefiles from Digitaal Basisbestand Paleogeografie van de Rijn-Maas Delta (Cohen and Stouthamer, 2012); [e] shapefiles from Vermont Department of Environmental Quality maps of "river corridors", which they define as including "the width of the meander belt of a river and an additional 50' buffer" (https://dec.vermont.gov/watershed/rivers/river-corridor-and-floodplain-protection/river-corridor-and-floodplain-maps); [f] shapefile traced on Context Camera imagery in Google Mars, selected from ridges interpreted as inverted channels in Kite et al. (2019); [g] shapefile traced on Context Camera imagery in Google Mars, selected from ridges interpreted as inverted channels in Burr et al. (2009, 2010), specifically, their areas 01, 30_F, 35_E, 39_C, and 41_A

2.8 Works cited in supplementary materials

Basher, Z., A. J. Lynch and W. W. Taylor (2018). "New global high-resolution centerlines dataset of selected river systems." Data in brief **20**: 1552-1555.

Burr, D. M., M.-T. Enga, R. M. E. Williams, J. R. Zimbelman, A. D. Howard and T. A. Brennand (2009). "Pervasive aqueous paleoflow features in the Aeolis/Zephyria Plana region, Mars." Icarus **200**(1): 52-76.

Burr, D. M., R. M. E. Williams, K. D. Wendell, M. Chojnacki and J. P. Emery (2010). "Inverted fluvial features in the Aeolis/Zephyria Plana region, Mars: Formation mechanism and initial paleodischarge estimates." Journal of Geophysical Research: Planets **115**(E07011).

Dickson, J. L., L. A. Kerber, C. I. Fassett and B. L. Ehlmann (2018). A global, blended CTX mosaic of Mars with vectorized seam mapping: a new mosaicking pipeline using principles of non-destructive image editing. Lunar and Planetary Science Conference.

Ferguson, R. I. (1975). "Meander irregularity and wavelength estimation." Journal of Hydrology **26**(3-4): 315-333.

Howard, A. D. and A. T. Hemberger (1991). "Multivariate characterization of meandering." Geomorphology **4**(3-4): 161-186.

Jacobsen, R. E. and D. M. Burr (2018). "Errors in Martian paleodischarges skew interpretations of hydrologic history: Case study of the Aeolis Dorsa, Mars, with insights from the Quinn River, NV." Icarus **302**: 407-417.

Kite, E. S., A. D. Howard, A. Lucas and K. W. Lewis (2015a). "Resolving the era of river-forming climates on Mars using stratigraphic logs of river-deposit dimensions." Earth and Planetary Science Letters **420**: 55-65.

Kite, E. S., D. P. Mayer, S. A. Wilson, J. M. Davis, A. S. Lucas and G. S. de Quay (2019). "Persistence of intense, climate-driven runoff late in Mars history." Science Advances **5**(3): eaav7710.

Malin, M. C., J. F. Bell, B. A. Cantor, M. A. Caplinger, W. M. Calvin, R. T. Clancy, K. S. Edgett, L. Edwards, R. M. Haberle, P. B. James, S. W. Lee, M. A. Ravine, P. C. Thomas and M. J. Wolff (2007). "Context Camera Investigation on board the Mars Reconnaissance Orbiter." Journal of Geophysical Research **112**(E5).

Mandelbrot, B. B. (1983). The fractal geometry of nature, WH freeman New York.

Martin, J., A. M. Fernandes, J. Pickering, N. Howes, S. Mann and K. McNeil (2018). "The Stratigraphically Preserved Signature of Persistent Backwater Dynamics in a Large Paleodelta System: The Mungaroo Formation, North West Shelf, Australia." Journal of Sedimentary Research **88**(7): 850-872.

Montgomery, K. (1996). "Sinuosity and Fractal Dimension of Meandering Rivers." Area **28**(4): 491-500.

Nikora, V. I. (1991). "Fractal structures of river plan forms." Water resources research **27**(6): 1327-1333.

Schwenk, J., A. Khandelwal, M. Fratkin, V. Kumar and E. Foufoula-Georgiou (2017). "High spatiotemporal resolution of river planform dynamics from Landsat: The RivMAP toolbox and results from the Ucayali River." Earth and Space Science **4**(2): 46-75.

Schwenk, J., S. Lanzoni and E. Foufoula-Georgiou (2015). "The life of a meander bend: Connecting shape and dynamics via analysis of a numerical model." Journal of Geophysical Research: Earth Surface **120**(4): 690-710.

Chapter 3

3 FORMATION OF SINUOUS RIDGES BY INVERSION OF RIVER-CHANNEL BELTS IN UTAH, USA, WITH IMPLICATIONS FOR MARS

Hayden, A. T., Lamb, M. P., Fischer, W. W., Ewing, R. C., McElroy, B., & Williams, R. M. E. (2019). Formation of sinuous ridges by inversion of river-channel belts in Utah, USA, with implications for Mars. *Icarus*, 332, 92-110. doi:10.1016/j.icarus.2019.04.019

Abstract

Sinuous ridges are important landforms on the surface of Mars that show promise for quantifying ancient Martian surface hydrology. Morphological similarity of these ridges to river channels in planform led to a hypothesis that ridges are topographically inverted river channels, or "inverted channels," formed due to an erosion-resistant channel-filling material that preserved a snapshot of the channel geometry in inverted relief due to differential erosion. An alternative deposit-inversion hypothesis proposes that ridges represent exhumed river-channel belts, with geometries that reflect the lateral migration and vertical aggradation of rivers over significant geologic time, rather than the original channel geometry. To investigate these hypotheses, we studied sinuous ridges within the Cretaceous Cedar Mountain Formation near Green River, Utah, USA. Ridges in Utah extend for hundreds of meters, are up to 120m wide, and stand up to 39m above the surrounding plain. Ridges are capped by sandstone bodies 3–10m thick that contain dune and bar-scale inclined stratification, which we interpret as eroded remnants of channel belts that record the migration and aggradation of single-thread, sand-bedded rivers, rather than channel fills that can preserve the original channel geometry. Caprocks overlie mudstones and thinner sandstone beds that are interpreted as floodplain deposits, and in cases additional channel-belt sandstones are present lower

in the ridge stratigraphy. Apparent networks from branching ridges typically represent discrete sandstone bodies that cross at different stratigraphic levels rather than a coeval river network. Ridge-forming sandstone bodies also have been narrowed during exhumation by cliff retreat and bisected by fluvial erosion. Using a large compilation of channel-belt geometries on Earth and our measurements of ridges in Utah, we propose that caprock thickness is the most reliable indicator of paleo-channel geometry, and can be used to reconstruct river depth and discharge. In contrast, channel lateral migration and caprock erosion during exhumation make ridge breadth an uncertain proxy for channel width. An example in Aeolis Dorsa, Mars, illustrates that river discharge estimates based solely on caprock width may differ significantly from estimates based on caprock thickness. Overall, our study suggests that sinuous ridges are not inverted channel fills, but rather reflect exhumation of a thick stratigraphic package of stacked channel belts and overbank deposits formed from depositional rivers over significant geologic time.

3.1 Introduction

Sinuous topographic ridges are abundant landforms on the surface of Mars, and they are important for reconstructing the history of surface water on early Mars (e.g.; Williams, 2007; Burr et al., 2010; Moore et al., 2003; Palucis et al., 2014; Fassett and Head, 2005; Kite et al., 2015a, 2015b; Cardenas et al., 2017; Goudge et al., 2018; Fig. 3.1A–B). Some sinuous ridges have been interpreted to be igneous wrinkle ridges, glacial moraines, eskers, or exhumed igneous and sedimentary dikes (Kargel and Strom, 1992), but the most common interpretation is that they reflect—in some fashion—topographically inverted river channels, owing to their similarity to river channels in planform (Pain and Ollier, 1995; Pain et al., 2007) (Fig. 3.1). The inverted-channel hypothesis suggests that river channels were filled with a more resistant material, such as a lava flow (e.g., Stanislaus Table Mountain described in Burr et al., 2010), or a coarse or well-cemented

sediment (e.g., Maizels, 1987, 1990), and that subsequent deflation of the neighboring land left the channel fill as a topographic high (Fig. 3.2A). Because of their putative connection to river processes, sinuous ridges on Mars have been used to infer paleo-hydrology (Fassett and Head, 2005; Burr et al., 2010; Irwin et al., 2015), global history of water (Kite et al., 2015a, 2015b), tectonics (Lefort et al., 2015), and large oceans or seas (DiBiase et al., 2013; Cardenas et al., 2017). In addition to being detectable and measurable from orbital data, they also are valuable to rover missions due to their presence in Gale Crater, the site of the Mars Science Laboratory rover (Anderson and Bell, 2010; Le Deit et al., 2013; Palucis et al., 2014), and in several sites of interest for future missions (e.g., Eberswalde crater (Irwin et al., 2015), Holden crater (Grant and Wilson, 2012), Jezero Crater (Goudge et al., 2018), Mawrth Valles (Loizeau et al., 2015), Melas Chasma (Williams and Weitz, 2014), and Aram Dorsum (Balme et al., 2016)).

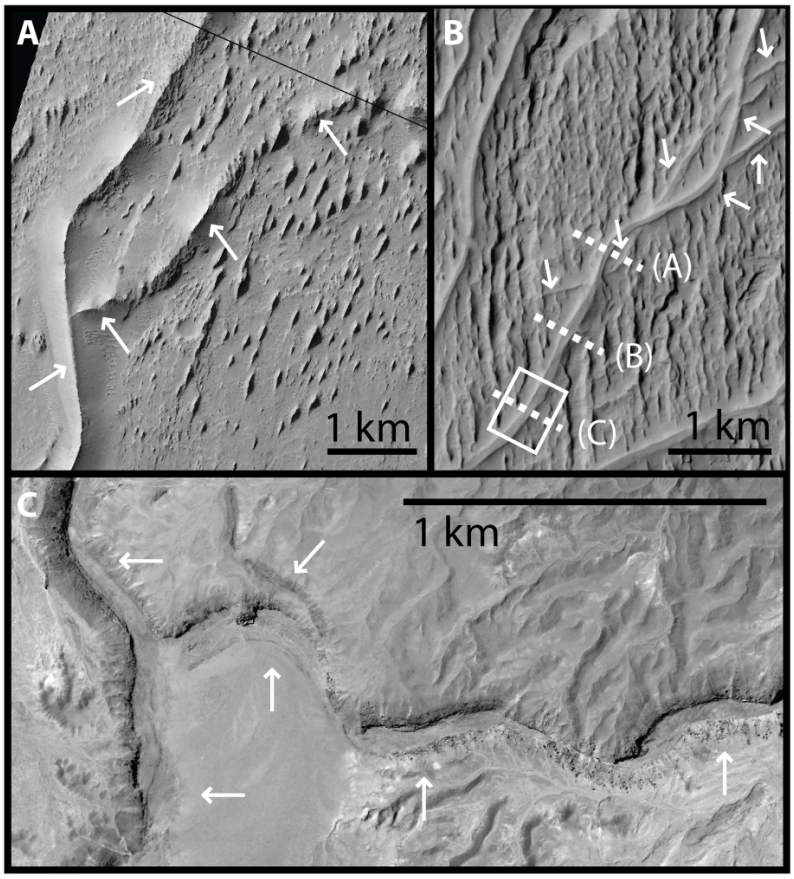

Figure 3.1–Examples of sinuous ridges from Mars and Earth. Arrows point to ridges. A) Long ridge with a single branch in Aeolis Dorsa, Mars. Small parallel bumps are yardangs (Coordinates -4.67, 151.13; HiRISE image PSP_010533_1755; credit: NASA/JPL/University of Arizona). B) At least two sets of stratigraphically distinct ridges on Mars with superposed yardangs. This is part of a larger ridge network that has been interpreted both as convergent flow to the lower left based on channel inversion and divergent flow to the upper right on the basis of deposit inversion (Lefort et al., 2012; 2015; DiBiase et al., 2013). White box indicates section shown in Fig. 3.15A, dotted lines denote cross section locations in Fig. 3.15B. (Coordinates -6.105, 151.479; Aeolis Dorsa, Mars; CTX image B18_016691_1740_XN_06S208W; credit: NASA/JPL/Malin Space Science Systems). C) Branching, segmented ridges in our field area, south of Green River, Utah (38.876, -110.271; National Agriculture Image Program 2014 image).

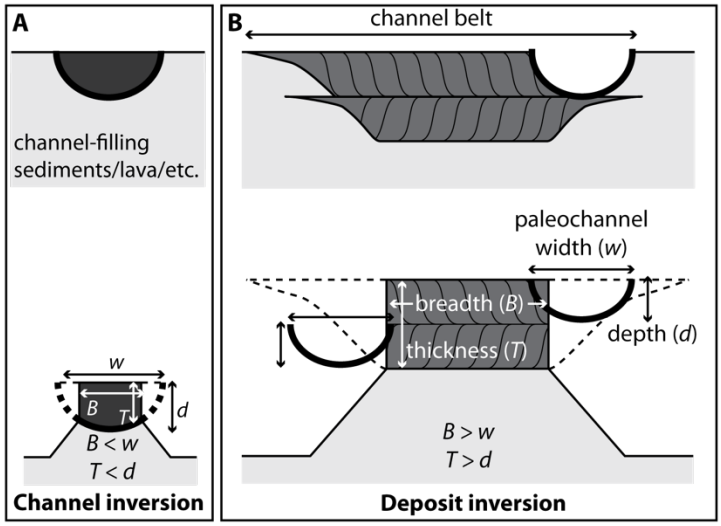

Figure 3.2–Schematic hypotheses for the formation of fluvial sinuous ridges. A) Schematic of the topographic-inversion hypothesis: a channel (black semi-circle) has been filled with a resistant material (dark gray) and is subsequently exhumed to form a ridge with caprock dimensions (breadth, *B*, and thickness, *T*) that are slightly smaller than the original channel dimensions (width, *w*, depth, *d*) due to erosion. B) Schematic of the deposit-inversion hypothesis: a channel (black semi-circle) aggrades and migrates across the floodplain (light gray) building a channel-belt sandstone body (medium gray) that is larger than the original channel. During exhumation, erosion modifies the channel-belt sandstone primarily by lateral backwasting reducing the ridge breadth. The channel fill may not be preserved in the caprock sandstone, as indicated.

Although the inverted-channel hypothesis is commonly assumed on Mars, little work has been done to evaluate it. Part of the issue is that outcrop-scale observations are needed to confirm the nature of the ridge material and whether the ridges represent true casts of channels, and these observations are not readily available on Mars. Many studies assume that ridge geometries, such as width and planform curvature, closely approximate the corresponding river channel geometries (Fig. 3.2A), and use these parameters in empirical formulas developed from terrestrial meandering rivers to calculate river discharge (e.g., Burr et al., 2010; Williams et al., 2013; Palucis et al., 2014; Kite et al., 2015b). However, another possibility is that the sinuous ridges represent exhumed river-channel belts (Figs. 3.2B & 3.3) (DiBiase et al., 2013; Matsubara et al., 2015; Kite et al., 2015a; Irwin et al., 2015), which DiBiase et al. (2013) termed deposit inversion. For instance, it is well known that the

stratigraphic architecture of depositional fluvial systems typically shows discrete tabular bodies of sandstone or conglomerate that are interspersed within a finer grained mudstone floodplain facies (e.g., Friend et al., 1979; Gibling, 2006; Heller and Paola, 1996), which could lead to differential erosion and exhumation of the coarser bodies (Fig. 3.3A). Fluvial sandstone and conglomerate bodies are typically far wider and thicker than the original river channels because the bodies formed from lateral migration, aggradation, and abandonment and reoccupation of the river channel within its channel belt (e.g., Mohrig et al., 2000; Fig. 3.3). The bend wavelength for an entire channel belt also is typically different than the bend wavelength of the channel (Fig. 3.3), which can be observed in examples for both modern and ancient systems (e.g., Fernandes et al., 2016; Martin et al., 2018; Chapter 2). On Mars, supporting observations for deposit inversion include ridges at distinct stratigraphic levels and ridges comprised of amalgamated channel deposits (Malin and Edgett, 2003; Moore et al., 2003; Burr et al., 2009, 2010; DiBiase et al., 2013; Kite et al., 2013, 2015a, 2015b; Cardenas et al., 2017).

In contrast to channel belts, deposits that fill and preserve the geometry of a paleo-channel (i.e., channel fills) are comparatively rare, and where they do exist are typically amalgamated within a larger channel-belt deposit (Ielpi and Ghinassi, 2014; Durkin et al., 2017 (Fig. 3.3A)). Channel fills also are commonly finer-grained overbank deposits (e.g., Bridge, 2003; Reijenstein et al., 2011; Musial et al., 2012; Bhattacharya et al., 2016), similar to the floodplain deposits that are eroded during ridge formation, and so may be less likely to be preserved as resistant ridges. While some workers on Mars have recognized, and in cases avoided analysis on, ridges with signs of lateral channel migration by bend growth or ridges with variable breadths that may indicate significant erosion (e.g., Burr et al., 2010), the assumption that ridge geometries closely approximate the original channel geometries is pervasive (Moore et al., 2003; Jerolmack et al., 2004; Fassett and Head, 2005;

Burr et al., 2010; Williams et al., 2013; Palucis et al., 2014; Kite et al., 2015b). For instance, ridges with breadth-to-bend wavelength ratios that are similar to meandering rivers on Earth is commonly used to support the hypothesis that ridge geometries closely match the original channel geometries (e.g., Burr et al., 2010; Kite et al., 2015b).

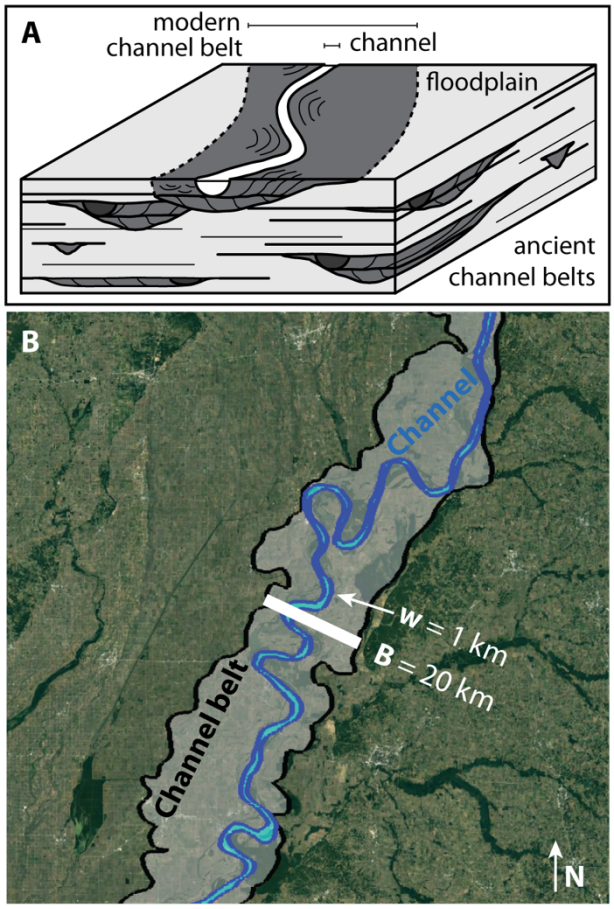

Figure 3.3--A) Stratigraphic architecture of a fluvial depositional basin including a sinuous single-thread river channel (white), floodplain deposits (light gray), multiple generations of stacked channel belts (medium gray), and rare channel fills (dark gray). Note that channel belts have widths, thicknesses, and sinuosities that can be different than the geometry of the channel. B) Example of a modern channel belt: Mississippi River below Cairo, IL. Channel belt outline is from Fernandes et al. (2016). Landsat true color image, December, 2016. Channel belt width, B, is much larger than the channel width, w.

Distinguishing between channel inversion and deposit inversion is important. Unlike the inverted channel model (Fig. 3.2A), the deposit inversion hypothesis of DiBiase et al. (2013) implies that sinuous ridges are not snapshots in time of a single geomorphic surface, but rather they are an amalgamation of fluvial deposits that represent a rich record of long-lived fluvial activity (Fig. 3.2B). The two models can also indicate opposite paleo-flow directions. For example, the modern topographic slope of branching ridge networks in Aeolis Dorsa, Mars (Fig. 3.1B) suggests a convergent drainage of river channels typical of uplands (Lefort et al., 2012), whereas analysis of the deposit stratigraphy implies a divergent, depositional channel network with the opposite flow direction (DiBiase et al., 2013; Lefort et al., 2015).

A better understanding of the processes that formed sinuous ridges can arise from focused studies on Earth where both ridge morphology and outcrop sedimentology are readily observable. Most previous studies of terrestrial sinuous ridges have focused on fluvial sedimentology, due to the excellent outcrop exposure, with little attention paid to ridge formation (e.g., Stokes, 1961; Derr, 1974; Harris, 1980; Friend et al., 1979; Friend, 1989; Maizels, 1987, 1990; Mohrig et al., 2000; Cuevas Martínez et al., 2010; Nuse, 2015). Some recent work has addressed these landforms as analogs for Mars (Pain et al., 2007; Williams et al., 2007; DiBiase et al., 2013; Zaki et al., 2018), including the role of cementation in forming the ridges (Clarke and Stoker, 2011; Williams et al., 2011). Although they did not seek to directly test the deposit and channel inversion models, Williams et al. (2009), working on ridges of the Cedar Mountain Formation in Utah, showed discrepancies between paleo-hydraulic reconstruction techniques that utilize ridge morphology versus deposit sedimentology, and cautioned against some of the common assumptions made in the channel inversion hypothesis on Mars.

Herein, we built on the analysis of Williams et al. (2007, 2009, 2011) of sinuous ridges in the Cretaceous-age Cedar Mountain Formation of southeastern Utah, and provided new observations and analyses to test the channel and deposit-inversion hypotheses. In addition, we generated a global compilation of channel-belt dimensions on Earth, which we used to develop a method for reconstructing river discharge from exhumed channel belts. After describing the terminology and study sites in Sections 3.2 and 3.3, field and remote-sensing methods are discussed in Section 3.4, and the paleo-hydraulic reconstruction method for channel belts is proposed in Section 3.5. Section 3.6 presents results for ridge and ridge-network geometries, outcrop sedimentology, and stratigraphy in Utah. Finally, we evaluate the channel and deposit-inversion hypotheses in Section 3.7, and discuss implications for reconstructing paleo-hydraulics and depositional environments from sinuous ridges on Mars.

3.2 Terminology

Terminology related to ridges, channels, and river deposits is often unclear or conflicting in previous studies. Here we use the term channel to reflect the topographic trough that is a conduit for river water flow (Fig. 3.3A). Channel fills are deposits that fill an abandoned channel following cutoff or avulsion (e.g., Bridge, 2003; Gibling, 2006; Blum et al., 2013) (Fig. 3.3A). Channel fills are important where preserved because they record the original shape of the channel; i.e., the channelfill container is the original channel (Reijenstein et al., 2011; Musial et al., 2012; Bhattacharya et al., 2016). However, the channel-filling material is typically not transported within the active channel, but rather tends to be fine-grained overbank deposits that drape channels after they are abandoned by the main flow. Overbank deposits are from unchannelized flood flows that spill out of the active channel onto the floodplain. The fill material can also be lava (e.g., Stanislaus

Table Mountain described in Burr et al., 2010) or eolian sediments, for example, that fill an abandoned channel.

Deposits from sediment transported within the active channel are referred to as channel deposits, which can be laterally extensive and thick as a result of lateral migration and aggradation of the channel (Fig. 3.3A). Channel deposits in sand-bedded rivers are often organized into channel bars and dunes, which make distinct scales of inclined stratification that relate to the depth of the channel. An amalgamation of channel deposits is referred to as a channel belt (also known as a channel-belt sand body, channel sandstone body, channel body, or channel complex in previous work; Fig. 3.3) (e.g., Gibling, 2006; DiBiase et al., 2013; Blum et al., 2013). A channel belt is often thicker and wider than the paleo-channel due to lateral channel migration, aggradation, and avulsion and reoccupation that can juxtapose and/or amalgamate multiple generations of channel deposits. Thus, channel belts can contain stratigraphic packages that record single or multiple generations of channel lateral migration (or "stories") (Mackey and Bridge, 1995). Channel belts, therefore, are distinct from channel fills in their formation process, geometry, and sedimentology. The stratigraphic architecture of fluvial depositional basins is typically dominated by stacked channel-belt sand bodies and floodplain deposits, not channel fills (Heller and Paola, 1996).

We use the term inverted channel to refer to a channel fill that stands as a topographic high (ridge) because of preferential deflation of the surrounding terrain. Hence, inverted channel by our definition implicitly assumes topographic inversion of a channel fill, and this is also how the term is often used on Mars (e.g., Burr et al., 2010). When the ridge formation process is unknown, we favor a non-interpretive landform descriptor like sinuous ridge. Ridges formed from exhumed channel belts, in contrast, are composed of channel deposits and should have geometries that are unlike the original channel due to river lateral migration and aggradation (e.g., Robinson and McCabe, 1997;

Jerolmack and Mohrig, 2007; Blum et al., 2013). Previous workers on both Earth and Mars commonly used the terms paleo-channel or inverted channel to describe ridges, but their intention to implicate channel fills versus channel belts was not always explicit (e.g., Derr, 1974; Harris, 1980; Maizels, 1987; Burr et al., 2010; Palucis et al., 2014; Kite et al., 2015a, b; Jacobsen and Burr, 2018; Fig. 3.2A). Nonetheless, many studies used ridge width or ridge curvature as direct proxies for the original channel width or channel curvature (Derr, 1974; Harris, 1980; Burr et al., 2010; DiBiase et al., 2013; Williams et al., 2013; Palucis et al., 2014; Kite et al., 2015b), and so implicitly inferred topographic inversion of a channel fill, or a channel-belt that coincidently has geometries similar to the original channel. We investigated whether ridges in Utah are exhumed channel fills (inverted channels), or exhumed channel belts instead (Fig. 3.2).

3.3 Study site and previous work

We studied fluvial sinuous ridges near the town of Green River, Utah, referred to herein as the Green River site, that are often used as terrestrial analogs to sinuous ridges on Mars (Williams et al., 2007, 2009, 2011; Burr et al., 2010; Jacobsen and Burr, 2017) (Fig. 3.4). The ridges are composed of sedimentary rocks from the early Cretaceous Ruby Ranch member of Cedar Mountain Formation in Utah, near the San Rafael Swell, a monocline, and are mostly flat lying with local stratal dips less than ~5° (Bates, 1952; Sable, 1958; Witkind, 1988; Doelling et al., 2015). The Ruby Ranch Member is characterized by drably variegated mudstones with interspersed sandstone bodies that form sinuous ridges (Kirkland et al., 1997, 1999). Accommodation space was generated in a foreland basin during thrusting associated with the eastward-migrating Sevier Orogeny (DeCelles and Currie, 1996; Currie, 2002; DeCelles and Coogan, 2006). The Sevier Mountains and Mogollon Highlands confined the Cedar Mountain Formation to the west and south. Detrital zircon provenance (Ludvigson et al., 2015) indicates sediment sources from these highlands, which is consistent with

flow directions toward the north (e.g., Harris, 1980; Nuse, 2015). The Cedar Mountain Formation was deposited over 30 M.y. (Kirkland et al., 1997), and best age constraints for the inverted-channel-rich Ruby Ranch Member bracket it with tephra to between 103.7 ± 2.6 M.a. (Ludvigson et al., 2015) and 98.2 ± 0.6 M.a. (Garrison et al., 2007) (Fig. 3.4).

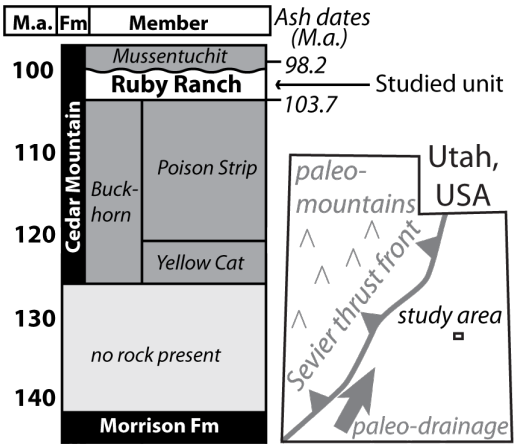

Figure 3.4–Representative stratigraphy, paleogeography, and modern geography of the field area. Left) representative stratigraphic section of Ruby Ranch member (after Kirkland et al., 1997; with revised dates from Ludvigson et al., 2015; Garrison et al., 2007). The Ruby Ranch member deposition duration is constrained by ash dates from the basal contact with the Buckhorn conglomerate (Garrison et al., 2007) and a bed within the Mussentuchit (Ludvigson et al., 2015) that unconformably overlies the Ruby Ranch Member, to within 5.5 M.y. Right) Interpreted paleogeography of the study area (after Ludvigson et al., 2015).

The ridges of the Cedar Mountain Formation have been noted since Stokes (1944), but were first studied in detail by Harris (1980) at the Green River site. He mapped bar and dune migration directions, and noted that bar migration directions were often oblique to the ridge margins, and therefore inferred these were point bars associated with river meandering. He also assumed that several ridges that align in orientation in map view are segments of a sandstone body from a single river system that has been dissected by erosion. Although Harris recognized the ridge-capping sandstones as composed of amalgamated channel deposits that have been eroded, he nonetheless used the caprock dimensions as a proxy for the paleo-channel dimensions, and calculated annual-

flood discharges of 215–600 m^3/s using an empirical relation between river discharge and channel width and depth from Schumm (1972).

Williams et al. (2009) used similar approaches at the Green River site to reconstruct discharge from empirical relations for single-thread rivers between discharge and channel width, and for meandering rivers between discharge and bend wavelength and bend radius of curvature (Schumm, 1972; Williams, 1984, 1988; Osterkamp and Hedman, 1982). However, recognizing the complicating effects of channel migration and caprock erosion, Williams et al. (2009) proposed that the third quartile of the maximum measured ridge width is a good proxy for channel width. They also compared the discharge reconstruction using ridge width to the discharge required to move sediment, a necessary lower limit, and found significant differences between the different methods. Williams et al. (2009) recognized that the ridges occur at distinct stratigraphic levels, and so the ridges must be deposits from rivers that existed at different time periods.

Given the present uncertainty as to whether channel or deposit inversion hypotheses apply, we revisited the classic Green River site to explicitly test the hypotheses and explore their implications for Mars. Our approach was to use process-based sedimentology to reconstruct the channel dimensions and paleo-hydraulics in way that was independent of ridge geometry. We then compared the results from ground-based observations (sedimentology and stratigraphic sections) to those based only on ridge geometry (knowable from remote sensing data) to evaluate the channel-inversion and deposit-inversion hypotheses.

3.4 Methods

We identified ridge segments and mapped their planform relationships using NAIP air photos (1 m resolution) and digital elevation models (DEM; 5 m resolution) acquired from the Utah Geologic Survey (Fig. 3.5A). We also surveyed each ridge with an uncrewed aerial vehicle (UAV)

and generated ortho-photos and DEMs at <20 cm per pixel using the photogrammetry software Agisoft PhotoScan. To compare the relative stratigraphic position of ridges, we needed to account for tectonic tilting associated with the San Rafael Swell. We used local measurements as reported on U.S. Geological Survey maps (Sable, 1958; Doelling et al., 2015) of bedding dips and dip directions 1° to the 000° for this area, and then subtracted this plane from the coarse DEM to create an elevation model with tectonic tilt removed (Fig. 3.5). We verified the correction by tracing in air photos the top of a prominent mudstone bed in a nearby cliff, discretizing the points in the DEM, and fitting a plane using least-squares regression to the contact elevation points, which yielded a dip of 1.4° to 014°. These corrections were similar to those reported by Williams et al. (2009) [1.5°–1.9° to the NE], who similarly used a nearby mudstone bed in the underlying Morrison Formation as a datum.

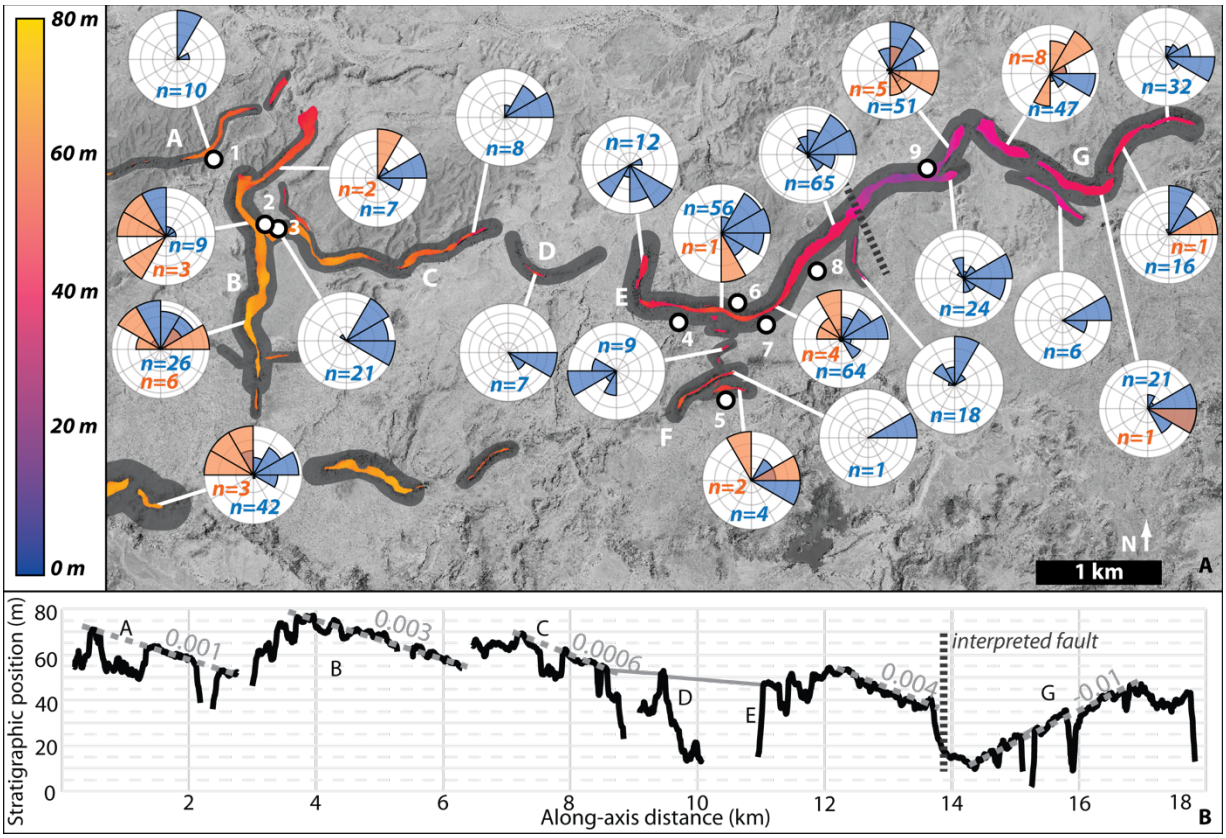

Figure 3.5–Sinuous ridges in the field area (center of map is 38.871, -110.230). A) Map showing caprocks colored by their stratigraphic position (elevation corrected for tectonic tilt; see Section 3.4) and talus-covered flanks of the ridges highlighted in gray. Ridge names are given in capital letters, stratigraphic sections (see Fig. 3.6) are given by numbers. Rose diagrams show accretion directions of dune sets (blue) and bar strata (red) binned by caprock segment. B) Caprock centerline position in stratigraphic space (elevation corrected for tectonic tilt; see Section 3.4) versus distance along a ridge centerline, with linear-least-squares-fits to caprock top surfaces (interpreted to be minimally eroded; see Section 3.7.2) given in dotted gray lines. A fault is located at the position indicated (Sable, 1958); note offset of the ridgetop. Letters correspond to ridge labels in panel A.

Similar to previous work (e.g., Harris, 1980; Williams et al., 2009), we initially treated each ridge segment as distinct, then used field observations of paleo-flow indicators and stratigraphic position to discuss which ridges represent the same stratigraphic intervals and which are distinct. Note that our names for each ridge segment differ from previous work (Harris, 1980; Williams et al., 2009) because our focus differed from theirs. We paid special attention to ridges that appear to

cross in planview, forming an ‘X’ pattern, or branch forming a ‘Y’ pattern to evaluate if they represent bifurcating paleo-channels or the intersection of channel deposits at different stratigraphic levels. Ridge centerlines were manually traced on air photos, and we discretized the centerlines into a series of nodes with a spacing approximately equivalent to the average top width of the caprock (i.e., 100 m). Subsequent measurements of breadth and relief were made at each node, and the average and 5th–95th percentile range is reported for each ridge segment (Table S1). Measurements of caprock breadth (*B*), defined as the caprock top width perpendicular to the local ridge centerline trace, were made using the ortho-rectified air photos.

Measurements of ridge shape and relief were made from the Utah Geologic Survey DEMs (5 m/pixel). Ridge relief was calculated from the DEM as the difference between the average elevation of the top of the caprock with the elevation of the inflection point in the ridge transect, where it transitions to a flat plane. Average along-axis ridge slope was measured for each ridge by taking the best-fit linear regression to the ridge-centerline elevation profile on the caprock, with the tectonic tilt removed (Fig. 3.5B), and the 5th–95th percentile confidence interval was recorded.

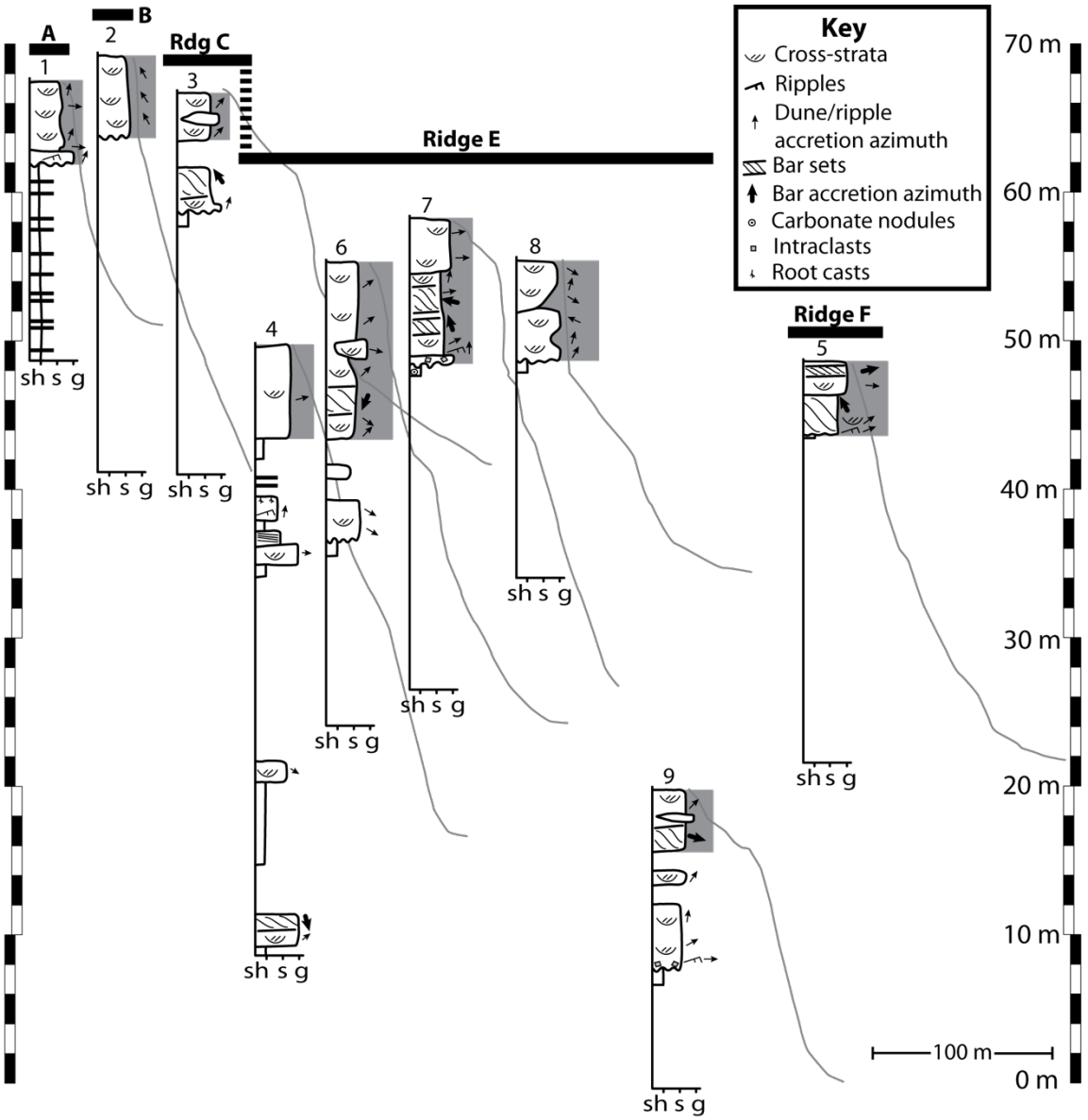

Figure 3.6–Representative stratigraphic sections placed in stratigraphic position along ridges. Bedform accretion directions noted by arrow azimuth, and median grain size given by edge of each section (sh – shale, s – medium sand sandstone, g – granule conglomerate). Positions of the stratigraphic sections are referenced to the digital elevation model with the tectonic tilt removed. Section 3.9 is offset by a fault (see Fig. 3.5), resulting in its lower position. Gray line curving off the right shoulder of the stratigraphic section represents the topographic profile from caprock down to ridge bottom, extracted from the 0.5-meter-per-pixel photogrammetric digital elevation model, and exaggerated 10x vertically to fit (see Fig. 3.15B for better detail). The caprock is highlighted with a gray box, and is often visible in the topographic profiles as a break in the slope. Most ridges are covered with talus below the caprock; covered sections are blank on the stratigraphic sections.

For each ridge, we measured vertical stratigraphic sections in the field, and noted bedding types (Fig. 3.6). Ridges are composed of a flat-topped, relatively thick, cliff-forming sandstone or conglomerate unit on top, referred to as the caprock, that is typically atop a talus-covered slope composed of mudstone and thinner sandstone bodies. Caprock thickness, T, was measured as the vertical thickness of the uppermost sandstone body in each stratigraphic section (e.g., Fig. 3.6). We traced beds laterally along a ridge to correlate stratigraphic position for measured sections on the same ridge. For sandstone and conglomerate, we documented the median grain size (D_{50}) by eye with a grain size card and cross-bedding set thicknesses with a ruler. Dip directions of ripple and dune cross-sets were measured using cross section exposures (Figs. 3.7B–D), as well as plan-view exposures of bedform troughs, such as rib-and-furrow structures (Fig. 3.7C; Stokes, 1953; Miall, 1996; Bhattacharya et al., 2016; Wu et al., 2016). Most ridge caprocks have an additional, larger (>~0.5 m) scale of cross stratification, which lacks troughs and rolls over and pinches out laterally, which we interpreted to represent bar clinoforms or channel-margin lateral accretion bedding (Fig. 3.7F; e.g., Miall, 1996; Mohrig et al., 2000; Hajek and Heller, 2012; Blum et al., 2013; Bhattacharya et al., 2016).

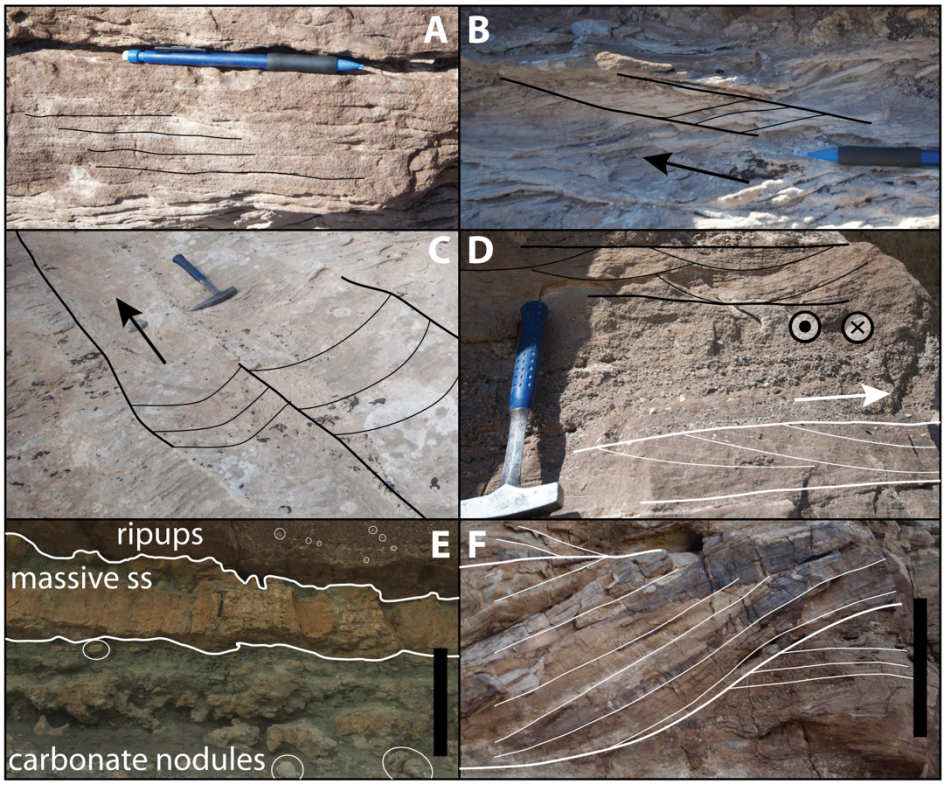

Figure 3.7–Sedimentary structures observed in the ridges: A) planar-laminated fine sandstone; B) climbing ripples, paleo-flow along arrow; C) rib-and-furrow structures seen in planview from dune trough cross stratification, with sets indicated by thin lines and bounded by thick lines, paleo-flow along arrow; D) trough cross-stratification seen in cuts both perpendicular (black lines, indicating trough cross-stratification) and parallel (white lines), with sets defined by thin lines and set boundaries indicated by thick lines; E) mud intraclasts circled within sandstone, massive sandstone, carbonate-nodule-rich mudstone; F) bar-scale accretion sets (thick lines indicate set boundaries, thin lines indicate inclined bedding) showing rollover to the top right, indicating that close to the full bar height is preserved. Pencil in A and B is approximately 0.2 m, hammer in C and D is approximately 0.3 m, scale bars in E and F are approximately 1 m.

3.5 Paleo-hydraulic reconstruction calculations

3.5.1 Inverted channels

Based on the channel topographic inversion hypothesis, the bankfull channel width, w, bankfull depth, d, and channel bed slope, S, are assumed to be accurately reflected as the ridge breadth, caprock thickness, and caprock top slope. From conservation of mass:

$$Q = Udw \,, \qquad \text{Eq. 3.1}$$

where U is the cross-section-average bankfull flow velocity and Q is the bankfull channel discharge.

We determined flow velocity from the flow resistance method of Engelund and Hansen (1967) that is based on the idea of partitioning hydraulic roughness in sand-bedded rivers between the bed sediment (skin friction) and drag from bedforms such as ripples and dunes (Einstein, 1950). Note that this relation is intended only to apply to sand-bedded rivers with dunes, such as occur in the study area; for gravel-bedded rivers, we recommend using the friction relation of Ferguson (2007). Following the method of Engelund and Hansen (1967), the skin friction component of the Shields stress, τ_{*}, was calculated from

$$\tau_{*,s} = 0.06 + 0.4\tau_*^2 \ , \qquad \text{Eq. 3.2}$$

where τ_* is the dimensionless bankfull Shields stress, and $\tau_{*,s}$ in Eq. 3.2 should not exceed τ_*. The bankfull Shields stress, under the assumption of steady and uniform flow, is

$$\tau_* = \ dS/RD_{50} \ , \qquad \text{Eq. 3.3}$$

where $R = (\rho_s - \rho_w)/\rho_w$, ρ_w is water density, ρ_s is the density of sediment, and D_{50} is the median particle diameter. The skin friction component of the Shields stress is defined as

$$\tau_{*,s} = u_{*,s}^2/RgD_{50}, \qquad \text{Eq. 3.4}$$

where g is acceleration due to gravity. The skin friction component of the shear velocity ($u_{*,s}$) is related to the flow velocity through (Engelund and Hansen, 1967)

$$U/u_{*,s} \ = \ (1/\kappa) \ ln \ [11d_s/k_s] \ , \qquad \text{Eq. 3.5}$$

where $\kappa = 0.4$ is von Karman's constant, $k_s = 2.5D_{50}$ is the grain roughness lengthscale and d_s is the skin friction component of the flow depth under steady and uniform flow ($u_{*,s} = \sqrt{gd_sS}$).

To apply the Engelund and Hansen method, we combined Eqs. 3.4 & 3.5 and rearranged to solve for flow velocity as

$$U = (1/\kappa) ln\left[11(RD_{50}/Sk_s)\tau_{*,s}\right]\sqrt{RgD50\tau_{*,s}}\,, \qquad \text{Eq. 3.6}$$

in which we set $R = 1.65$ and $g = 9.81$ m/s^2. To find the bankfull discharge under the channel inversion assumption, Eq. 3.6 is combined with Eq. 3.1; grain size, D_{50}, is constrained by field data; d, w, and S are inferred from the ridge caprock geometry as discussed in Section 3.4; and $\tau_{*,s}$ comes from Eqs. 3.2 & 3.3. We propagated uncertainty from the measured breadth along a given ridge, using the 5% and 95% bounds on the ridge breadth distribution, through the discharge calculation (Eqs. 3.1-3.6) using standard Gaussian error propagation.

Note that Eqs. 3.1-3.6 can be combined and rewritten as a simple power-law relation between discharge and channel width, which is similar to those often used on Earth (Maizels, 1987; Williams et al., 2009) and other extraterrestrial bodies (Jaumann et al., 2008; Burr et al., 2010; Matsubara et al., 2015; Irwin et al., 2015; Jacobsen and Burr, 2018),

$$Q = a\, w^b\,, \qquad \text{Eq. 3.7}$$

where $a = \sqrt{gS}C_f^{-1/2}\left(\frac{w}{d}\right)^{-3/2}$ and $C_f = gdS/U^2$, which depends on D_{50}, d, and S (Eq. 3.6). To demonstrate the comparison, we inserted values common to single-threaded sand-bedded rivers (g = 9.81 m/s^2, $S = 0.005$, $C_f = 0.02$, $w/d = 18$) and found $a = 0.02$ and $b = 2.5$, which are similar to empirical values (e.g., $a = 0.1$ and $b = 1.86$ from Eaton (2013); $a = 1.9$ and $b = 1.22$ from Osterkamp and Hedman (1982)) that are often used on extraterrestrial bodies (Jaumann et al., 2008; Burr et al., 2010; Matsubara et al., 2015; Jacobsen and Burr, 2018). Although using empirical fits to find a and b in Eq. 3.7 is simpler, we prefer using Eqs. 3.1-3.6 because they explicitly incorporate gravity and sediment and fluid properties that can vary in different environments, and allow for variable C_f due

to the presence of dunes. We therefore only use Eq. 3.7 to demonstrate the difference between these approaches.

The biggest uncertainty in applying either Eqs. 3.1-3.6 or Eq. 3.7 to sinuous ridges is determining the channel width. For example, if the ridge width reflects the channel-belt width, rather than the channel width (Figs. 3.2 & 3.3), then discharge might be overestimated.

3.5.2 Process sedimentology

To test methods that estimate river discharge relying on ridge geometry alone, we built on well-established previous work in physical sedimentology (Mohrig et al., 2000; Wilkerson and Parker, 2011; Trampush et al., 2014) to develop a paleo-hydraulic method that is independent of ridge morphology. The most straightforward paleochannel parameters that can be inferred from outcrop observations are median grainsize and channel depth, reconstructed from thicknesses of sets of cross-strata. Fluvial bars grow to a height approximately equivalent to the channel depth, and therefore the thickness of fully preserved bar clinoforms, where available, should closely approximate the channel depth (Mohrig et al., 2000; Hajek and Heller, 2012). We found that bar set thicknesses were 1–2.5 m (Fig. 3.8; Table S2), indicating that the rivers were relatively shallow. Dune-scale cross sets are more abundant, and the mean dune-set thickness within channel deposits (t_d) can be related to the original dune heights (h_d) by (Paola and Borgman, 1991; Leclair and Bridge, 2001)

$$h_d / t_d = 2.9 \text{ (bounds:2.2-3.6)}, \qquad \text{Eq. 3.8}$$

where 2.9 is the mean and the bounds represent their reported expected range. To relate channel depths (d) to dune height (h_d), Bradley and Venditti (2017) found that rivers with depths <2.5 m had a ratio of $d/h_d = 3.5$. Because our observations of bar set thicknesses were < 2.5 m and because bars are thought to be a more reliable indicator of flow depth than dunes (Mohrig et al., 2000; Hajek and Heller, 2012), we used their shallow river relation

$d / h_d = 3.5$ (bounds:2.1-9.9), Eq. 3.9

where 3.5 is the mean value and the bounds represent the 5%–95% range of their data. If we were to use instead the general relation of Bradley and Venditti (2017) for all rivers, this would shift our estimated mean flow depths for the Green River site up by a factor of ~2, which is relatively small compared to the uncertainty in other parameters and within the bounds evaluated for Eq. 3.9. We made multiple measurements of dune cross-set thicknesses in the caprock of each ridge (Table S2; Section 3.4), and used the mean values to calculate paleo-channel depths from Eqs. 3.8 and 3.9. We estimated the 5% and 95% uncertainty bounds on the paleo-channel depth using reported bounds on Eqs. 3.8 and 3.9 and standard Gaussian error propagation.

To reconstruct channel width independent of the ridge width, we assumed a single-thread channel based on our field observations at the Green River site (Section 3.6), and used the median ratio of width to depth from the Trampush et al. (2014) global compilation of bankfull channel geometry:

$w/d = 18$. Eq. 3.10

Braided rivers can have much wider channels, which, for those cases, would make Eq. 3.10 a conservative lower bound. To reconstruct bed slope, S, we used a dimensionless empirical relation between bankfull Shields stress and particle Reynolds number $Re_p = \sqrt{RgD_{50}}D_{50}/\nu$ after the methodology of Paola and Mohrig (1996), Wilkerson andParker (2011) and Lynds et al. (2014),

$\tau_* = 17Re_p^{-1/2}$, Eq. 3.11

based again on the global compilation of single thread rivers from Trampush et al. (2014), where $\nu = 10^{-6}$ m^2/s is the kinematic viscosity of water. Eq. 3.11 can be combined with Eq. 3.3 and rearranged to solve for channel slope with known values of R, g, D_{50}, and d. For D_{50}, we used the average of many median grain size measurements from each ridge caprock. Finally, we used these estimates of

channel depth, slope, and width and Eqs. 3.1-3.6 to calculate paleo-river discharge. The uncertainty in channel width, slope, and discharge from the sedimentology-based reconstructions was assessed by propagating the uncertainty in paleo-channel depth (from Eqs. 3.8-3.9) through the calculations (Eqs. 3.1-3.6, 3.10-3.11) using Gaussian uncertainty propagation.

The equations in the sedimentology approach (Eqs. 3.8-3.10) were derived using physics-based, dimensionless parameters that explicitly incorporate g and R, and are known to control sediment transport physics in rivers (Garcia, 2006; Parker et al., 2007; Wilkerson and Parker, 2011). For example, Eq. 3.11 is the dimensionless version of the relations for bankfull Shields stress given by Trampush et al. (2014) that explicitly includes gravity, fluid, and sediment properties. Moreover, the empirical fits are based on a large data compilation of terrestrial river channels (Trampush et al., 2014), which spans a wide range of climates and environments and is commonly used to benchmark theory in fluvial geomorphology. While these equations have been little tested outside of Earth-like conditions, the approach to characterize fluvial systems through non-dimensionalization has been shown to be robust in physical experiments and models across a wide range of fluid and sediment properties (e.g., Southard and Boguchwal, 1990; Parker et al., 2007; Lamb et al., 2012a; Grotzinger et al., 2013). Dimensional empiricisms such as Eq. 3.7, on the other hand, may be problematic for application to Mars because they do not explicitly incorporate fully the dynamic scales.

3.6 Results

The Green River site contains several ridges, and we focused our observations on seven of the more prominent examples (Ridges A-G; Figs. 3.5 & 3.6), including the 4-kilometer-long ridge E, which is the longest continuous ridge in the study area. Results herein include observations of ridge morphology, ridge caprock dimensions, ridge caprock sedimentology, ridge stratigraphy, and junctions between branching ridges to evaluate the channel and deposit-inversion hypotheses.

Ridge geometries, sedimentological observations, and paleo-hydrologic calculations are summarized in Fig. 3.8, which shows the averages and 5th–95th percentile range of values for each parameter (Tables S1 & S2). The tops of the ridges are at a similar relative elevation, once corrected for tectonic tilt; most are within ~15 m of each other across the 30 km^2 study area (Fig. 3.5). Mean ridge relief ranges from 14–27 m (Fig. 3.8B), though it is often asymmetric between the two ridge sides. In particular, the relief of the north slopes for the east-west-running ridges (A, C-G) is on average 21 m, whereas the south sides are on average 16 m. This asymmetry in relief is coincident with the tectonic tilt of bedding and the overall slope of the modern topography, both of which dip toward north.

Ridge caprocks are cliff-forming sandstones (Fig. 3.6) with mean breadths varying between 22 and 54 m between ridges, although locally breadth can reach up to 130 m (Fig. 3.8D) and in some locations the caprock is absent due to erosion (ridges A, C, D, E, G in Fig. 3.5). Caprocks range in mean thickness from 4 to 7 m (Fig. 3.8B). Elevation of the caprock top surface varies along a ridge by up to 5 m at a 20-meter lengthscale. Along-axis ridge-top slopes are around 0.003 m/m (Fig. 3.8F) with tectonic tilt removed, oriented toward north or east, although different segments within a ridge can dip opposite to each other (Fig. 3.5B).

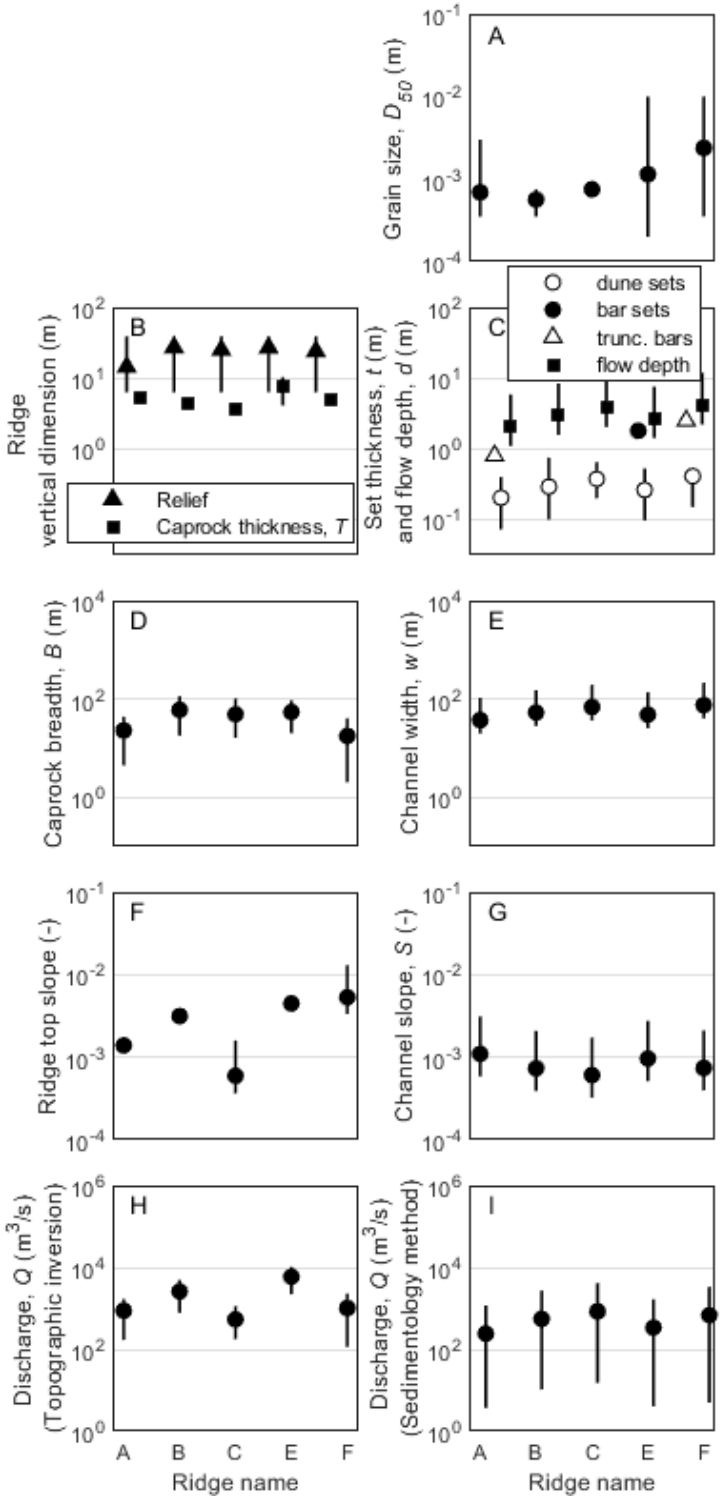

Figure 3.8–Ridge parameters and paleo-hydraulic reconstructions. Symbols represent mean values (geometric mean for grain size) and lines span 5th-95th percentile of the distribution. Left column: Distribution of parameters for ridge morphology (panels B, D, F) and the associated water discharge reconstruction (H) assuming topographic inversion (see Section 3.5.1). Uncertainty on relief (panel B) and breadth (D) are the 5th-95th percentile of the data distribution; uncertainty on

slope (F) is the 5-95% confidence interval of a least-squares linear regression; uncertainty on discharge reconstruction (H) using Gaussian uncertainty propagation from caprock breadth. Right column: measured caprock median grain sizes (A), measured dune- and bar-set thicknesses, and reconstructed flow depths from dune cross sets (C), and reconstructed bankfull paleo-channel width (E), channel-bed slope (G) and water discharge (I) using the sedimentology reconstruction method (Section 3.5.2). Uncertainty on grain size (panel A) is the 5th-95th percentile range of the measured median grain sizes. Uncertainty on depth (C) is combined from uncertainty in the expected range of the ratio of dune height to dune set thickness (Eq. 3.8; Leclair and Bridge, 2001), and 90% range of the ratio of dune height to channel depth for small channels (Eq. 3.9; Bradley and Venditti, 2017). Uncertainty in width (E), slope (G), and discharge (I) are estimated from Gaussian uncertainty propagation of the 5% and 95% bounds on reconstructed paleo-channel depth.

Fig. 3.6 shows vertical stratigraphic sections and topographic profiles at representative locations along the ridges A-C, E, and F. Caprocks are composed of amalgamated beds of sandstone, pebble conglomerate with clasts up to 3 cm, and occasional mudstone lenses (Fig. 3.9) that together have a median grainsize of medium to coarse sand (Fig. 3.8A). Sandstone beds are composed of medium to coarse sand and contain abundant sets of dune trough cross-stratification that range in thickness between 0.07 and 0.8 m, with averages for each ridge between 0.2 and 0.4 m (Fig. 3.8C). Along ridge tops, dune trough stratification is visible in planview as rib-and-furrow structures (Fig. 3.7C), indicating paleo-flow directions generally along ridge axes, which is consistent with the crosssectional-view cross-strata dip directions (rose diagrams in Fig. 3.5A). We identified 15 examples of truncated bar-scale inclined stratification (e.g., Figs. 3.7F, 3.9A, 3.9B, 3.8C), which ranged from 0.5 to 2.5 m, and two examples of fully preserved bar sets 1.8 m thick (Figs. 3.6, 3.8C). Most caprocks are composed of multiple sets of bar-scale inclined strata (multiple stories) that have migration directions oblique to dune migration directions (Figs. 3.5A, 3.6, 3.9A, 3.9B).

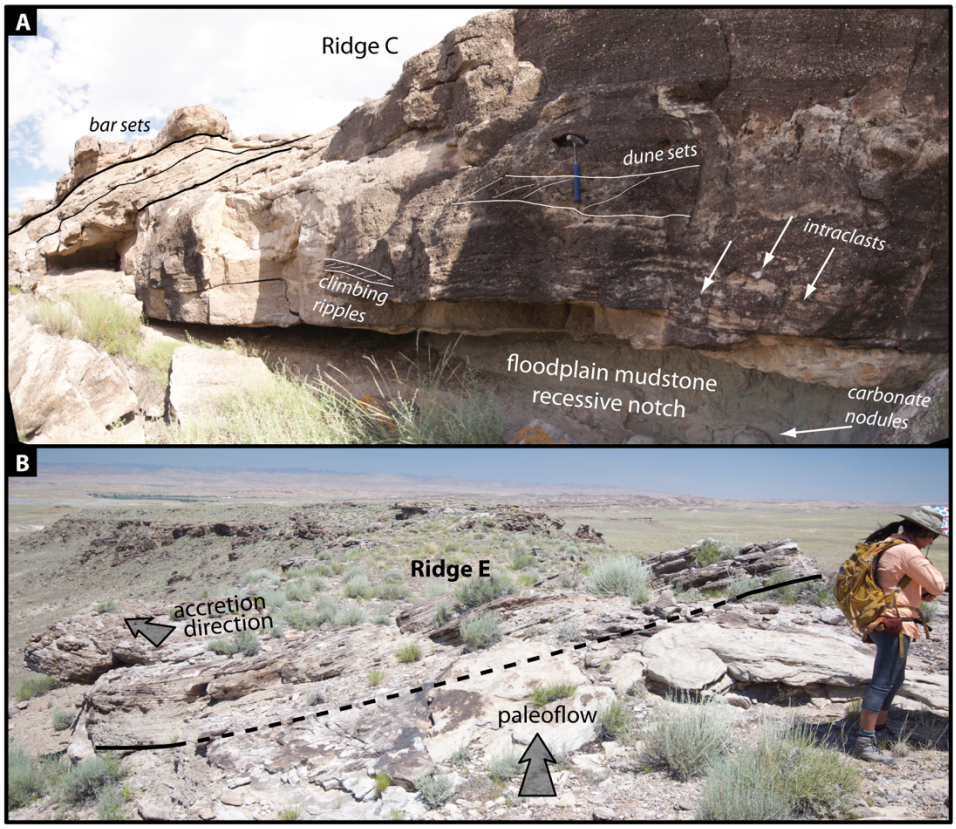

Figure 3.9–Ridge caprocks and their sedimentary structures. A) Caprock of ridge C exhibiting bar-scale inclined strata, dune cross sets, climbing ripples, and mud intraclasts in the sandstone/conglomerate caprock, which overhangs an erosional niche of mudstone exhibiting carbonate nodules. Note that the bar strata indicate an accretion direction oblique to the caprock axis and almost perpendicular to the paleo-flow direction indicated by dune sets. Hammer in foreground for scale, approximately 0.3 m. Photo location indicated in Fig. 3.10C. B) Caprock of ridge E, showing bar strata indicating accretion nearly perpendicular to the flow direction inferred from dune migration. We interpret the strata as representing a bank-attached laterally accreting channel margin. The associated channel fill is not preserved and must have been adjacent to the modern ridge caprock (e.g., Fig. 3.2B). Photo location indicated in Fig. 3.11A.

The caprock sandstones and conglomerates unconformably overlie mudstones, and often have centimeter to decimeter-scale mud rip-up clasts and coarse (2 cm) pebble lags present in the lower caprock strata (Figs. 3.6 & 3.9A). Below the caprock, ridge flanks are largely covered with talus, and limited exposures reveal abundant mudstone with occasional thin (<0.2 m) interbedded sandstone bodies that extend for at least tens of meters laterally (Figs. 3.6 & 3.10A). The mudstones

are purple to white, friable, and contain abundant decimeter-scale nodules (Fig. 3.9A). Thin sandstones are composed of fine to medium sand, and are planar laminated or contain centimeter-scale current-ripple cross stratification that indicate paleo-flow directions away from the ridge axes (Fig. 3.6). Root casts, mud cracks, and burrows are present in some of the thin sandstone sheets. At one location with better exposure (Ridge E, stratigraphic section 4; Fig. 3.6), three thicker (1–2 m) sandstone bodies are present in the lower parts of the ridge, with dune and bar-scale inclined strata of medium-to-coarse sandstone, which is similar to that in the caprock. Paleo-current indicators for these lower sandstone bodies are toward 090 (Fig. 3.6), which is similar to the caprock paleo-current indicators from dune cross strata and consistent with the caprock axis orientation.

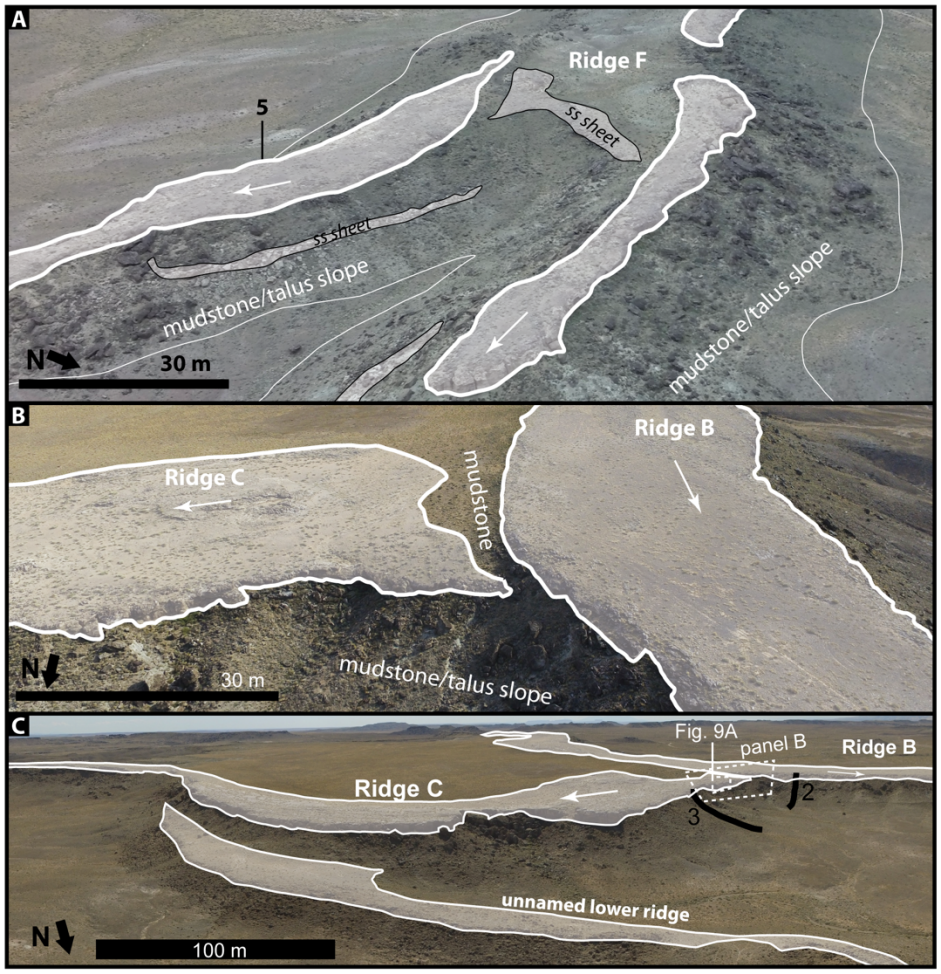

Figure 3.10–UAV panoramas of three ridge junctions. In all panels, sandstone bodies are shaded in white, caprock-forming sandstone bodies are outlined in a thick white line, non-caprock-forming sandstone bodies are outlined in a thinner black line, paleo-flow directions of the caprocks are given by arrows. A) Oblique UAV view looking southwest at the Y-junction in ridge F. The caprocks of the two branches are at indistinguishable stratigraphic positions and the caprock is eroded away at the ridge junction so it is unclear if the junction represents bifurcating sandstone bodies or a once-continuous sandstone body that has been dissected into a Y shape. Thin sandstone sheets outcrop below the caprock and do not form ridges. Stratigraphic section 5 labeled. B) Oblique UAV view looking south at the Y-junction between ridges B and C. The base of the caprock of ridge B is separated from the top of the caprock of ridge C by two meters of mudstone and the ridges contain paleo-flow indictors nearly perpendicular to each other. C) Oblique, southwest-looking UAV panorama view of ridge C and its intersections with an unnamed lower ridge and ridge B. The unnamed lower ridge is separated from the caprock of ridge C by about 10 m of mudstone. Stratigraphic sections 2 and 3, and locations of Figs. 3.9A and 3.10B are indicated.

We analyzed three ridge junctions with detailed field observations and the high-resolution stratigraphic model to determine if they represent a bifurcation or avulsion in a coeval channel network, or a crossing of sandstone bodies that are stratigraphically distinct (Fig. 3.10). At the junction between ridges B and C, the caprock of ridge C intersects below the caprock of ridge B at a distinct stratigraphic level, as noted in Williams et al. (2009). The two caprocks have nearly perpendicular paleo-flow indicators and are separated vertically by 2 m of mudstone at the junction, indicating that the sandstone bodies are not coeval (Fig. 3.10B). Similar relationships are apparent at the junction between ridge C and an unnamed ridge to its north, with the unnamed ridge occurring approximately 10 m lower in stratigraphic section (Fig. 3.10C). Other ridge junctions are not as clear; ridge F splits with both branches at similar stratigraphic levels (within the 5 m of vertical variability seen in individual caprocks), and appears to represent a "Y" junction, with branches opening in the downstream direction (Fig. 3.10A). Cover and erosion across the center of the junction obscures the ridge relationships, but the similarity between the two ridges in stratigraphic level, grain sizes and sedimentary structures, and the acute angle between paleo-current indicators, suggests that the Y-junction could represent branching of coeval river deposits.

Fig. 3.8 shows results from the paleo-hydraulic reconstruction techniques based on the sedimentology (inputs of dune-set thickness and grain size, using Eqs. 3.1-3.6, 3.8-3.11) as compared to the ridge parameters and reconstructions assuming channel inversion (inputs of mean ridge thickness, mean ridge breadth, and ridge best-fit slope, using Eqs. 3.1-3.6). Based on the dune cross strata, the computed paleochannel depths were within 2.1–4.2 m, which were generally consistent with, but in cases larger than, the thicknesses of fully preserved bar clinoforms (1.8–2.5 m) where they occurred (Fig. 3.8C). Using the sedimentology method and the dune-derived depths, paleo-channel widths were 37–75 m (Fig. 3.8E) and bed slopes ranged from 0.0006 to 0.001 (Fig. 3.8G).

These paleo-channel dimensions are smaller than the caprock dimensions, which had maximum thicknesses of 4–10 m (Fig. 3.8B) and maximum breadths of 45–130 m (Fig. 3.8D). The caprock top slopes are up to a factor of 4 times greater than the estimated paleo-channel-bed slope (Fig. 3.8F), and in cases indicate flow opposite in direction to the paleo-currents inferred from dune migration direction (e.g., Ridge G, Fig. 3.5). Discharge estimated using mean values in the channel inversion interpretation (Q = 500–6000 m^3/s) (Fig. 3.8H) overestimates discharge reconstructed by sedimentology (Q = 240–850 m^3/s) (Fig. 3.8I) by a factor of 1–20. These discharge reconstruction techniques, their uncertainties, and application to Mars are discussed in more detail in the next section.

3.7 Discussion

3.7.1 Depositional environment of ridge-forming strata

The ridge caprocks at the Green River site are composed of fluvial channel-belt deposits. Based on the thicknesses of bar and abundant dune stratification, the paleo-river channels had depths of a few meters with beds composed of sand and occasional gravel. Due to common three-dimensional exposures, we were able to identify bar-scale clinoforms with accretion directions oblique-to-perpendicular to the paleoflow directions (Figs. 3.5A, 3.9A, 3.9B), interpreted from the orientation of dune trough-cross-strata and rib-and-furrow structures (Fig. 3.7), suggesting that the bars were laterally accreting and downstream migrating (e.g., Miall, 1994; Ielpi and Ghinassi, 2015; Wang and Bhattacharya, 2018; Nuse, 2015). We did not find evidence for laterally extensive, fining-upward accretion sets typically associated with point bars or channel cutoffs typical of fully meandering rivers (Miall, 1996). We also did not observe evidence for mid-channel bars typical of braided rivers (Best et al., 2003; Bridge and Lunt, 2006). Instead, we interpret the bar strata as downstream-migrating bank-attached free bars and channel-margin lateral accretion deposits within

a low-sinuosity, single-thread, laterally migrating channel, rather than point bars within a meandering river (e.g., Okolo, 1983; Olsen, 1988; Bridge et al., 1986). The spread of dune migration directions was also low (Fig. 3.5A) and consistent with flow patterns within low-sinuosity channels rather than high-sinuosity meanders (Bridge, 2003).

Most of the strata underlying ridge caprocks is interpreted as floodplain deposits, similar to previous work (Williams et al., 2009; Nuse, 2015), and root casts, carbonate nodules, burrows and well-developed soils suggest that the land surface was frequently subaerially exposed. Garrison et al. (2007) found two laterally extensive calcareous paleosol beds elsewhere in the Ruby Ranch Member that each are interpreted to represent tens of thousands of years of soil development. Interspersed thin, rippled sandstone sheets (e.g., Fig. 3.10A) likely represent channel-proximal overbank deposits, such as crevasse splays (e.g., Mohrig et al., 2000).

The ridge-capping sandstone bodies are 1.5 times thicker (range: 1–5) than the inferred channel depths (Fig. 3.8) and are composed of amalgamated bar and dune strata indicating that the fluvial deposits are eroded remnants of channel belts that record the migration and aggradation of a river channel across its floodplain. Paleo-flow indicators within the caprock sandstones approximately match the orientation of the ridge axes, suggesting that the ridges align roughly with the channel-belt orientations (Fig. 3.5A). Sandstone body thickness, T, a few times greater than paleo-channel depths, d, is typical of channel-belt deposits in general (Mohrig et al., 2000; Jobe et al., 2016) and arises because of the general tendency for rivers to avulse and abandon the channel belt after a critical amount of aggradation, which scales with the channel depth (Bryant et al., 1995; Mohrig et al., 2000; Slingerland and Smith, 2004; Jerolmack and Swenson, 2007; Hajek and Wolinsky, 2012; Ganti et al., 2014a, 2014b). Our finding of $T > d$ is strong evidence that the caprocks are remnants of channel belts, with aggrading and laterally migrating channels, consistent with the

deposit-inversion hypothesis. Evidence for deposits that record lateral channel migration, typical of channel belts, comes from bar-scale inclined strata that dip oblique to the paleo-flow direction, inferred from dune strata, indicating channel-margin migration (Fig. 3.5). Channel-margin lateral accretion sets can extend across the entire breadth of a ridge (Fig. 3.9A, B), indicating that the channel deposits were more extensive prior to exhumation, and that the channel at the leading edge of the channel margin bar would have been located laterally beyond the current extent of the ridge caprock (Fig. 3.2B). The exposed bar and dune strata along the caprock sides (Figs. 3.7, 3.9) and the absence of a lateral contact between channel-margin deposits and floodplain facies further emphasizes that the caprock is an eroded channel-belt deposit and not a channel fill. We did not identify channel-fill deposits, such as finer grained lenticular bodies that would indicate decreasing flow energy in a progressively abandoned channel (e.g., Bridge, 2003; Blum et al., 2013); instead, bedform sizes and grain sizes were similar throughout the thickness of the caprocks (Fig. 3.6), consistent with aggradation within a channel belt.

The ridges also are not casts of river channels, but instead contain a thick sequence of fluvial channel-belt and overbank deposits (Fig. 3.6). Ridge relief far exceeds the inferred channel depth (Fig. 3.8B, C), and instead is likely set during exhumation by the relative erodibility of the caprock relative to neighboring floodplain mudstones. The strata in the ridges represent net deposition over significant time, rather than preservation of a geomorphic surface. One can estimate the minimum time represented as tens of thousands of years based on the presence of paleosols (Garrison et al., 2007), and a maximum duration of several millions of years based on ages of volcanic ash within the Ruby Ranch stratigraphy (Ludvigson et al., 2015; Garrison et al., 2007; Fig. 3.4). Some of the ridge caprocks intersect at distinct stratigraphic levels with perpendicular paleo-flow directions (Fig. 3.10B, C), and thus indicate exhumation of a depositional basin with multiple generations of stacked

channel belts and floodplain deposits, rather than an inverted geomorphic surface. Ridge E shows two examples where sandstone bodies underlying the caprock are laterally continuous along the ridge (Fig. 3.11A, B; stratigraphic section 4 in Fig. 3.6) and have paleo-current directions similar to the caprock, suggesting similar channel-belt orientations at different time periods. Similar observations of channel-belt stacking on Mars have been taken as evidence that ridges are deposits within a broader incised valley that has guided channel-belt orientations (Cardenas et al., 2017). However, other ridge strata in Utah contain sandstone bodies below the caprock with paleo-currents oriented oblique-to-perpendicular to the caprock paleo-currents (Fig. 3.11A; stratigraphic section 6, Fig. 3.6), which does not fit with an incised valley model for this location. Moreover, not all sandstone bodies form ridges, and in most cases the underlying sandstone bodies are only preserved beneath ridge-forming caprocks (Figs. 3.10A, 3.11A, 3.11B), suggesting that the exhumation process has led to preferential preservation of underlying sandstone bodies that align with ridge-forming caprocks.

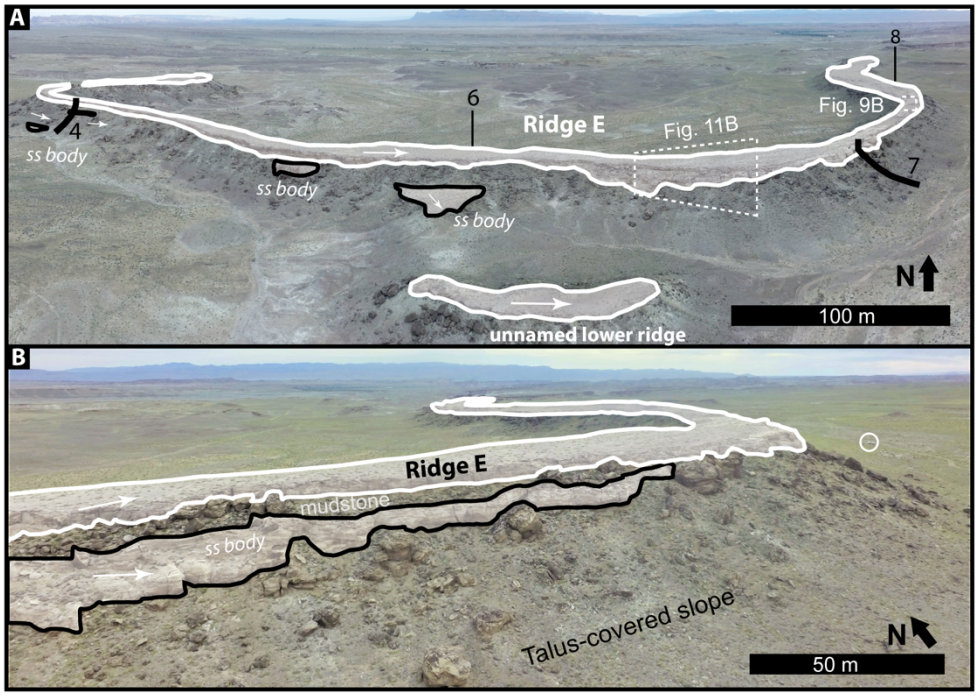

Figure 3.11–UAV panoramas of ridge caprocks that have underlying non-ridge-forming channel bodies. In all panels, sandstone bodies are shaded in white, caprock-forming sandstone bodies are outlined in a white line, non-caprock-forming sandstone bodies are outlined in a black line, paleo-flow directions of the caprocks are given by arrows. A) Oblique UAV panorama looking north at ridge E. Ridge E contains several lower sandstone bodies that do not form ridges. Sandstone bodies associated with stratigraphic section 4 have paleo-flow indicators with similar directions to those in the caprock, while sandstone bodies associated with stratigraphic section 6 have inferred paleo-flow directions nearly perpendicular to those in the caprock (Fig. 3.6). Another stratigraphically lower ridge occurs adjacent to ridge E and has inferred paleo-flow directions equivalent to those in ridge E. Locations of stratigraphic sections 4, 6-8 and Figs. 3.9B and 3.11B indicated. B) Oblique UAV photo looking northeast at ridge E. A lower sandstone body, separated from the caprock by mudstone, parallels the caprock for part of its extent and contains paleo-flow indicators aligned near those of the caprock.

The visual alignment of ridges C, D, E, and G led previous workers to hypothesize that they were once connected, forming a sandstone body at least 10 km in length (Harris, 1980; Williams et al., 2009). We found that paleo-flow directions are consistently to the east along these ridges, and caprock thicknesses, widths, stratigraphic position, and sedimentology are as consistent between these ridge caprocks as they are within a single ridge (Figs. 3.5, 3.6). Therefore, we concur that the caprocks of E-W trending ridges C, D, E, and G are part of a single sandstone channel belt that has

been dissected by erosion (Fig. 3.12A). We additionally find that this channel belt is at the same stratigraphic level as the caprocks of Ridge F and other ridges to the southwest. N-S trending ridges A and B sit at a higher stratigraphic level than ridge C-D-E-G, which is confirmed by intervening floodplain facies between the caprocks of ridges B and C (Fig. 3.10B). There are several smaller, stratigraphically lower ridges with paleo-currents that differ significantly from the upper ridge caprocks, suggesting that channel-belt orientations were different in the lower part of the ridge-forming stratigraphy (Figs. 3.5A, 3.10, 3.11, 3.12A).

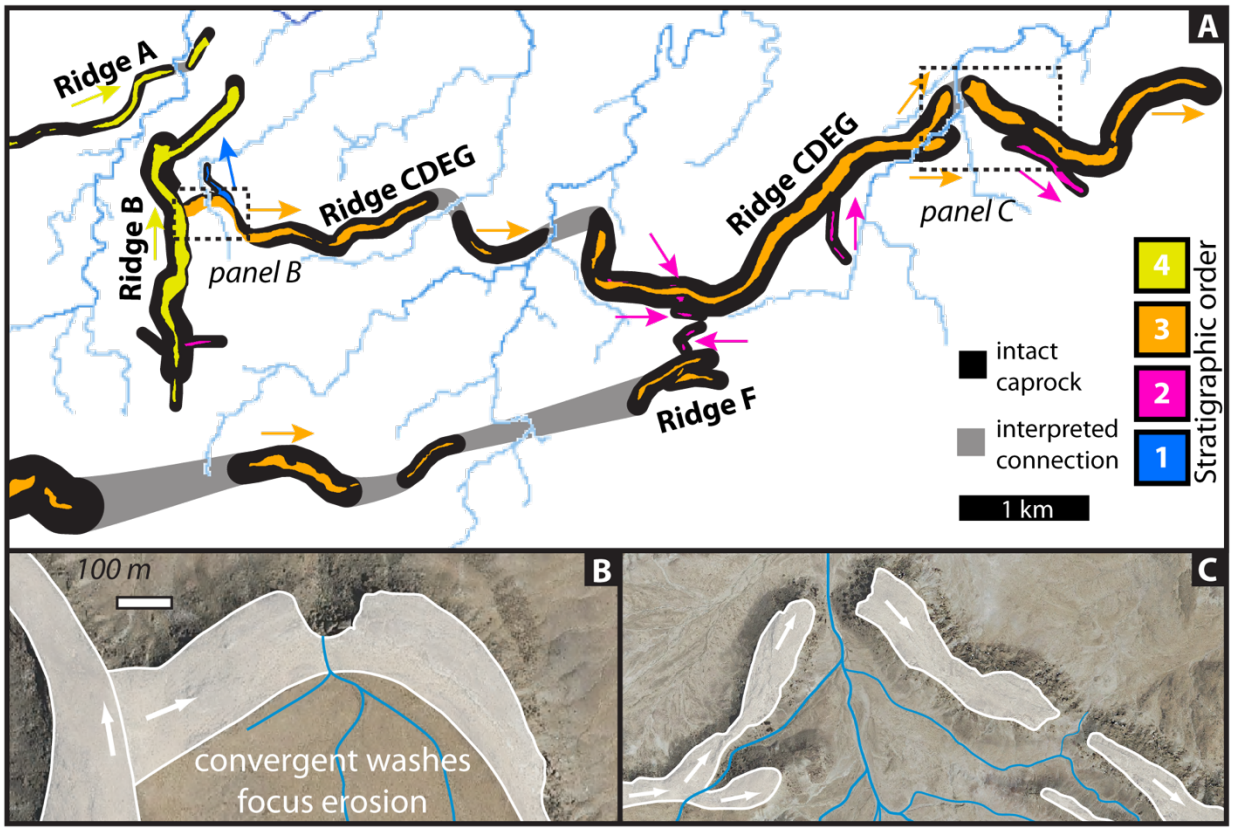

Figure 3.12–Interpreted ridge segment connections and erosion by modern washes. Locations of panels B and C are shown in panel A. A) Interpretation of ridge connections, relative stratigraphic positions, paleo-flow directions, and networks of modern washes calculated from DEMs (blue lines). Ridges C, D, E, and G are inferred to be remnants of a larger channel-belt sandstone body. Ridge B, which appears to be at a similar stratigraphic level as Ridge A, superposes Ridge C (Fig. 3.10B). Modern washes preferentially bisect the ridges where they are convex in the direction of down tectonic dip. B) Modern wash partially eroding through a caprock by accumulating flows

from a plateau on the up-dip side and focusing them across a single area that currently stands as a waterfall. C) Fully developed ridge bisection.

Although most ridge junctions represent caprocks intersecting at different stratigraphic levels, in some cases caprocks do appear to bifurcate (Fig. 3.10A). These examples may represent deposits from a coeval network of channel belts, which either bifurcate or are abandoned through avulsions. However, due to the eroded state of the ridges, it is also possible that some of the caprock bifurcations at the same stratigraphic level result from erosion of a notch during exhumation that has split a single sandstone body that was once more laterally extensive, or from two crossing caprocks that are amalgamated at the junction with poor preservation of the junction stratigraphy. For these cases, remote sensing was not enough to distinguish different stratigraphic levels, and even detailed field analyses could not verify the origin of the ridge bifurcation.

3.7.2 Ridge exhumation and degradation

The variability in caprock thicknesses and breadths along a given ridge is due in part to erosion. Abundant talus blocks of caprock material, up to 5 m in diameter (Fig. 3.13), indicate that caprock sides are actively backwasting, and differences in extent of backwasting can lead to large variations in caprock breadth over short distances (Fig. 3.13A) even to the point where a mudstone ridge is only partially covered by caprock (Fig. 3.13B). Often there is a recessive notch, decimeters in height, that undercuts the mudstone directly below the caprock, creating overhangs ~1 m in scale (Figs. 3.9A, 3.13C). Talus production through caprock undermining likely armors the underlying mudstone and may set the pace of lateral escarpment retreat (Ward et al., 2011).

Caprock thicknesses are also variable along a ridge (Figs. 3.6, 3.8B), and field observations show that the ridge surface cuts across different stratigraphic levels indicating some top-down

erosion (Figs. 3.5B, 3.13B), similar to observations on Mars (DiBiase et al., 2013). We infer that variability in ridge-top profiles is due to erosion, in addition to uncertainty in correcting for tectonic tilt and local deformation, resulting in ridge-top slopes that locally change dip directions and can be opposite of the paleo-flow direction inferred from bedforms (Fig. 3.5B).

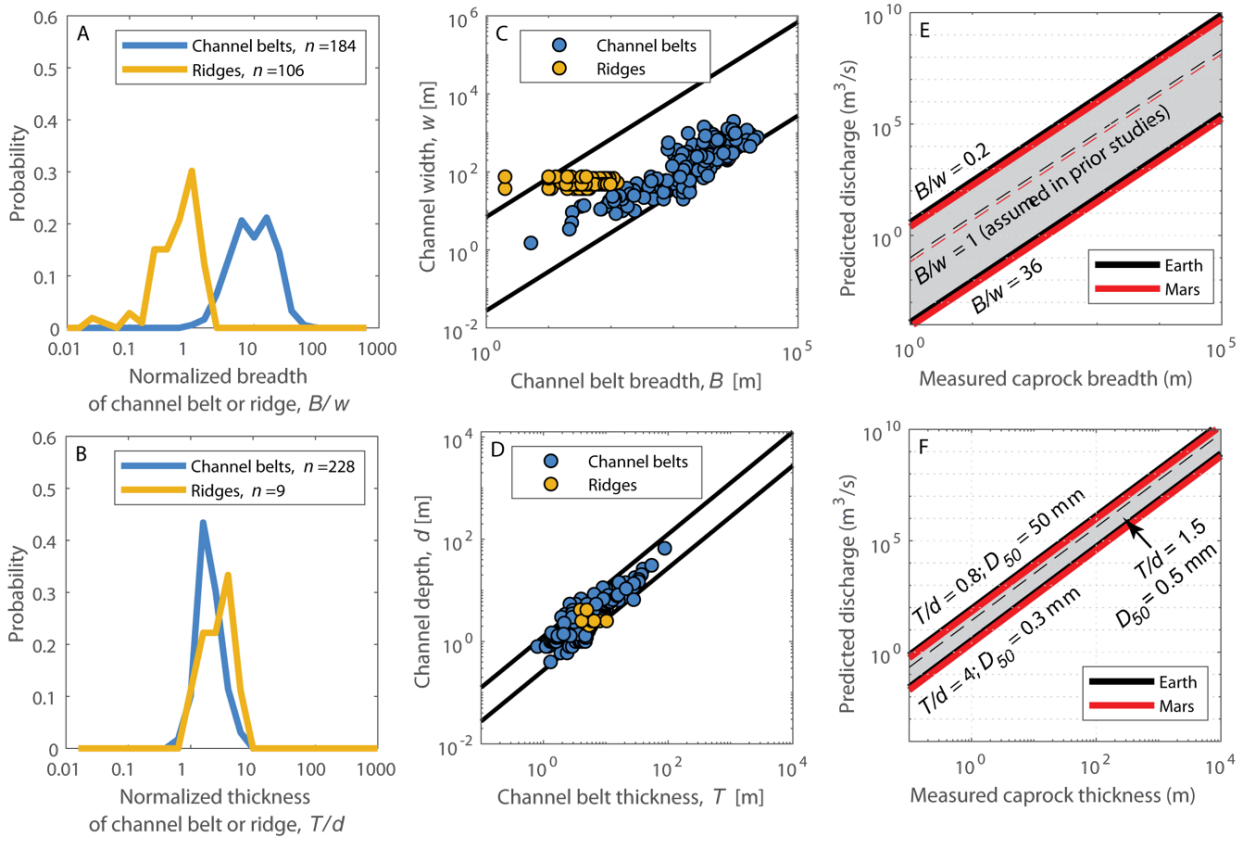

Figure 3.13–Ridge, channel belt, and paleo-channel parameters based on a compilation of uneroded channel belt deposits on Earth and eroded ridges at the Green River site. A) Probability density of uneroded channel-belt sandstone widths and, B) thicknesses, normalized by independently inferred paleo-channel widths and depths taken from a number of data compilations (Mohrig et al., 2000; Foreman et al., 2012; Zaleha, 2013; Jobe et al., 2016; Milliken et al., 2018). Also shown are all the measurements of ridge caprock breadth (spaced every 100 m along) and thickness (measured at each stratigraphic section) from the six studied Green River ridges, normalized by estimated average paleo-channel widths and depths using the sedimentology reconstruction method for each ridge. C and D) Data from panels A and B showing correlation between ridge or channel-belt breadth and channel width, and ridge or channel-belt thickness and channel depth. The lines represent the 5th and 95th percentile of the distribution ($B/w = 0.2 – 36$ and $T/d = 0.8$ - 4). E) Discharge reconstruction using Eq. 3.7 with $a = 0.1$ and $b = 1.866$ (Eaton, 2013), a relation commonly applied to ridges on Mars assuming channel inversion. The shaded grey zone, spanning a factor of over 30,000, represents the potential uncertainty associated estimating discharge from measurements of ridge width alone using Eq. 3.7 because of the unknown size of

the channel belt, relative to the original channel, and the unknown degree of lateral erosion during exhumation (i.e., $B/w = 0.2 – 36$). Dashed line is B/w ratio of unity, which is a typical assumption in previous work. F) Our preferred method to reconstruct river discharge using caprock thickness as a proxy for channel depth (Eq. 3.12). The dashed line gives the best-estimate values, using $T/d = 1.5$ and $D_{50} = 0.5$ mm as described in Section 3.7.4. The grey region, spanning a factor of 30, represents the uncertainty in converting caprock thickness to channel depth based on data in panels B and D, and the uncertainty in grain size by assuming representative sand and gravel end members. Red lines in panels E and F show the same discharge calculations made for Martian conditions (using a prefactor = $1.257^{-1.866}$ in Eq. 3.7 in panel E (Burr et al., 2010); parameters $g = 3.71$ m/s^2, $\varrho_s = 3.0$ g/cm^3 used in panel F).

Deposit inversion in Green River appears to occur because of the resistance of thick sandstone bodies to erosion, as compared to thinner sandstone bodies and mudstone. Bimodality in grain size of this type is typical of lowland fluvial systems where floodplain facies are dominated by fine-grained overbank deposits and channel-belt deposits are sandy (e.g., Heller and Paola, 1996). In the case of the Green River site, the mudstone is friable, whereas sandstones are better cemented and form vertical cliffs. However, not all sandstone bodies form ridges (e.g., Fig. 3.11). Our qualitative observations suggest no significant difference in grain size or hardness between ridge-forming and non-ridge-forming sandstone bodies. Instead, ridge-forming caprocks tend to be the thickest sandstone bodies in the field area, often exceeding 3 m, whereas non-ridge-forming sandstone bodies are typically thinner. Thicker caprocks may be needed to generate sufficient talus to armor the slope and slow its erosion (Ward et al., 2011).

The gaps between the E-W trending ridges C, D, E, G, which we infer to once have been a connected sandstone body, align with modern washes (Fig. 3.12A). These washes drain to the north, perpendicular to the trend of the ridges, until they encounter a ridge, at which point they turn to run alongside the ridge until a gap allows flow to the north again. Because tectonic tilt of the bedding is to the north, the southern parts of the caprock would have been exhumed first, thus guiding the washes to the gap locations and producing focused fluvial incision during subsequent ridge

excavation. This hypothesis explains why the gaps between ridges occur on what would have been curved ridge segments that are convex to the north; these segments would have been the last to be exhumed and water would have been funneled across them. Ridge C shows an example of a north-convex point being incised by a modern wash (Fig. 3.12B), and the gap between ridges E and G exemplifies that process when complete (Fig. 3.12C).

3.7.3 Evaluating paleo-hydraulic reconstructions for exhumed channel belts

The ridges at the Green River site contain a thick sequence of fluvial floodplain and channel-belt deposits that record a rich history of fluvial activity over millions of years. Channel fills are rare, and instead the sandstone bodies record the extent of channel lateral migration and aggradation, consistent with deposit inversion. The ridge-forming caprocks tend to represent thicker, amalgamated channel-belt sandstones, and erosion during exhumation has removed much of the neighboring floodplain material and thinner channel-belt sandstones, except where they are shielded below more resistant caprocks, making the ridge network an incomplete representation of the original stratigraphic architecture of the depositional basin. Moreover, the ridge-forming channel-belt sandstones are heavily degraded, largely by lateral backwasting, making the original channel-belt extents unknown. Because channel fills are typically fine grained (e.g., Bridge, 2003; Reijenstein et al., 2011; Musial et al., 2012), it is likely that any channel fills that existed were eroded along with the fine-grained floodplain material. Sandstone bodies have been dissected by erosion, and ridge junctions often form because of caprocks intersecting at distinct stratigraphic levels, and thus they do not represent an exhumed river network. Together, these observations at Green River are consistent with the deposit inversion model proposed by DiBiase et al. (2013) and demonstrate the uncertainty in applying paleo-hydraulic techniques that assume channel inversion.

Using the sedimentology reconstruction as a baseline, we find that caprock average thickness, breadth, and along-axis slope tend to exceed the inferred paleo-channel depth, width, and bed slope, and so using those ridge parameters directly in Eqs. 3.1-3.6 under the channel-inversion hypothesis overestimates the paleo-discharge by a factor of 1–20 (Figs. 3.8H, 3.8I). If ridge breadth and thickness values larger than the average were used instead in an attempt to account for ridge erosion (e.g., Williams et al., 2009 used third quartile), the paleo-discharge could be overestimated by a factor up to 50. Likewise, caprock breadths are vanishingly small in other places due to erosion (Figs. 3.8D, 3.13), making inferring channel width from ridge width ambiguous. Using ridge slope as an estimate for channel slope was found to have the largest contribution to the overestimation of discharge, and in cases the ridge top slopes, even after being corrected for tectonic tilting, indicate opposite paleo-current directions (Fig. 3.5B). Opposition of ridge-top and paleo-channel slopes has also been observed on Mars (DiBiase et al., 2013; Lefort et al., 2015).

In comparison to previous work at the Green River site, Williams et al. (2009) used empirical relations for river discharge that rely on measurements of river width alone, similar to Eq. 3.7, assuming that channel width is represented by the third quartile of the maximum measured ridge breadth, and found Q = 370 and 350 m^3/s for our Ridges B and E (their D and B, using Osterkamp and Hedman (1982)). Although their estimate of discharge based on ridge width is similar to ours based on sedimentology (Q = 550 and 340 m^3/s median values for our Ridges B and E), we caution that the correlation between ridge width and paleo-channel width is unlikely to be generally applicable to ridges on Mars. If the ridges are exhumed channel belts as they are in Green River, not inverted channel fills, then the caprock breadth reflects the extent of river lateral migration within a larger channel belt, modified by erosion, rather than the channel width. We are not aware of a reason why eroded channel belt widths should correlate with channel widths. The end member scenario of

very narrow channel belts, referred to as ribbon sandstone bodies (e.g., Friend et al., 1979), might produce sand bodies with breadths that are similar in scale to the channel width. Ribbon sandstones could potentially explain the consistency between ridge-based and sedimentology-based discharge reconstructions at the Green River site, but this idea is difficult to evaluate given the eroded state of the ridges. Nonetheless, more generally, it is well documented that channel-belt widths, for a given channel size, can vary by several orders of magnitude (e.g., Robinson and McCabe, 1997; Jerolmack and Mohrig, 2007; Jobe et al., 2016; Fernandes et al., 2016).

To expand our analysis to channel belts outside of the Green River site, Fig. 3.14A shows a large compilation of data from uneroded terrestrial channel belts across a wide range of environments (Mohrig et al., 2000; Foreman et al., 2012; Zaleha, 2013; Jobe et al., 2016; Milliken et al., 2018). This compilation indicates that the ratio of channel-belt width to channel width can vary from $2 < B/w < 36$ where these bounds represent the 5th to 95th percentile of the distribution, due to varying extents of lateral channel migration. For the Green River site, the ratio of average ridge caprock breadth to estimated channel width is far smaller and varies from $0.2 < B/w < 2$ (5th–95th percentile) (Fig. 3.14A), consistent with narrowing of the channel-belt sandstones during ridge exhumation. To estimate the general uncertainty in inferring channel width from ridge width alone, we used the lower bound of ridge widths from Green River as a highly eroded endmember, and the upper bound from the data compilation as an uneroded endmember with extensive lateral migration. This analysis yields a potential uncertainty in the ratio of B/w spanning over two orders of magnitude ($0.2 < B/w < 36$) (Fig. 3.14A) due to the unknown amounts of lateral migration and erosion. As an example, work by Fernandes et al. (2016) shows that the modern channel belt on the Mississippi River is far wider than the modern channel by a factor of ~20 (Fig. 3.3B). Martin et al. (2018) found a similar

result in a high-resolution seismic study of ancient channel belts of the Mungaroo Formation, Australia.

Williams et al. (2009) also evaluated relations based on the radius of curvature and wavelength of isolated bends at the Green River site, and extracted these values from the ridge geometry, which yielded discharges of 300 m^3/s and 500 m^3/s for our ridges B and E. Their result is consistent with ours, but again it is unclear if ridge bend wavelength serves as an indicator of channel geometry in general. If ridges are exhumed channel belts, then ridge curvature should reflect the channel-belt curvature, modified by erosion, rather than the channel pattern. Fig. 3.3B illustrates an example where the Mississippi river has far greater sinuosity with smaller bend wavelengths as compared to the channel belt. Similar examples also exist in seismic records of ancient channel belts (Martin et al., 2018). We are not aware of studies on the controls on channel-belt curvature. Consistency between the width-to-bend wavelength ratio for ridges as compared to meandering channels is often used to support the inverted channel hypothesis (Burr et al., 2010; Kite et al., 2015b); however, similar ratios might also exist for channel belts because both their widths and bend wavelengths are larger. Channel curvature might be inferred more directly from sets of curvilinear features in planview that appear similar to scroll bars on meandering rivers (Moore et al., 2003; Burr et al., 2009; Jacobsen and Burr, 2018), but likely represent intersection between dipping lateral accretion strata and the land surface on Mars (e.g., Jerolmack et al., 2004; Goudge et al., 2018). These features could record the channel margin geometry, but they are not apparent at the Green River site. Importantly, bend curvature correlations with discharge have been evaluated on Earth only for meandering rivers with active bend growth and cutoffs (Williams, 1988); thus, their applicability is unclear for the Green River ridges and most ridges on Mars, which have low sinuosity and lack evidence for point bars or cutoffs that would indicate meandering (see Moore et al., 2003;

Kite et al., 2015b for notable exceptions). Although ribbon sandstones might have breadths similar to the paleo-channel widths, these sandstone bodies are characterized by a lack of lateral migration (Friend et al., 1979), and thus are atypical of actively meandering rivers where the discharge-bend curvature relations apply.

3.7.4 Paleo-hydraulic reconstruction of ridges on Mars

Detailed sedimentological observations of dune and bar strata is not possible for the vast majority of ridges on Mars, where only orbital data is available. Instead, we propose that the most reliable indicator of paleo-channel depth that can be measured from orbital data is caprock thickness. Unlike ridge width that can potentially vary by orders of magnitude for a given channel width (Fig. 3.14A), channel-belt thickness tends to have a relatively tight linear correlation with channel depth. Based on our large compilation of channel-belt deposits on Earth and observations for Utah ridges, the median channel-belt thicknesses and ridge caprock thicknesses, relative to channel depths, is T/d = 1.5, with a 5th–95th percentile range of T/d = 0.8–4 (Fig. 3.14B). Our observations of caprock thicknesses at Green River alone support a similar ratio (Fig. 3.14B), suggesting that top-down erosion of caprocks at Green River is small compared to backwasting that narrows ridge breadth (Fig. 3.14A). The correlation between channel-belt thickness and channel depth is tied to the mechanics of river avulsion, the process by which rivers abruptly shift course and abandon a former channel belt. Analysis of terrestrial channel-belt sandstones, theory, and laboratory experiments indicate that avulsions tend to occur once the aggradation thickness is a small multiple of the channel depth (Bryant et al., 1995; Mohrig et al., 2000; Slingerland and Smith, 2004; Jerolmack and Swenson, 2007; Hajek and Wolinsky, 2012; Ganti et al., 2014a, 2014b). Caprock thickness, thus, represents a potentially robust metric to infer channel depth within a factor of ~2 (Fig. 3.14B).

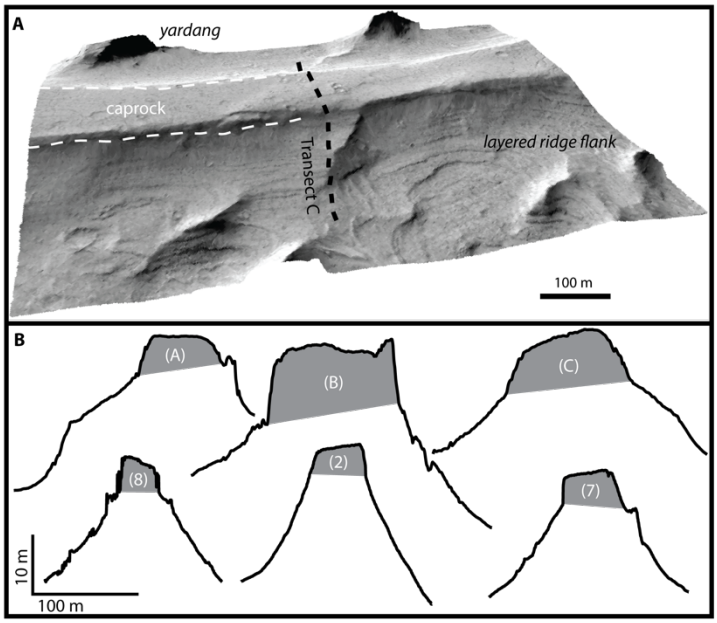

Figure 3.14–A) Zoomed-in perspective view of a ridge in Aeolis Dorsa, Mars shown in Fig. 3.1B without vertical exaggeration (Coordinates: -6.142, 151.450). Image shows the cliff-forming caprock that casts a shadow, likely indicating an overhang, with layered rock visible below, indicating that the ridge caprock has been eroded. The caprock annotation is purposefully absent on the right side for visibility. HiRISE DEM with draped imagery using images PSP_002279_1735 and PSP_002002_1735. Courtesy Jay Dickson. B) Cross sections of ridges on Mars (top row: letters A-C with corresponding locations indicated on Figure 1B, and transect C is also shown above on Fig. 3.15A) and in our Utah field site (bottom row; numbers 2, 7, and 8 correspond to stratigraphic section numbers (Fig. 3.6)) where profiles were taken. Photogrammetric DEMs from UAV photos. Scale is identical between ridges; vertical exaggeration ~5x. Ridge profiles are truncated at the base of the talus slope. The gray shaded area denotes the inferred caprock thicknesses using both the imagery (e.g., shadows) and the topography (cliff) as indicators of a break in slope at the base of the cliff-forming caprock.

Applying the method on Mars requires analysis of high-resolution imagery and digital terrain models (e.g., HiRISE) to identify caprocks, measure their thicknesses, and evaluate their preservation and possible burial from talus. We suggest utilizing the common morphologic expression of sinuous ridges with cliff-forming caprocks underlain by recessive mudstones that form sloping hillsides (Fig. 3.15). Fig. 3.15B shows example topographic profiles from ridges in Utah and from a ridge on Mars (also shown in Fig. 3.1B) where cliff-forming caprocks are present and measurable. For the cases in Utah, the thicknesses of the cliff-forming units inferred from the

topography correspond with our field measurements of caprock thicknesses (Fig. 3.6). In addition to using topography, Mars imagery can also reveal shadows from overhangs and a lack of talus cover to support a caprock interpretation (Fig. 3.15A). Given the resolution of available datasets on Mars (e.g., HiRISE stereo DEMs are reported to have <0.5 m vertical precision (Kirk et al., 2008)), caprocks at least a few meters thick should be targeted. For example, DiBiase et al. (2013) used HiRISE stereo DEMs to identify and measure the thickness of a channel-belt caprock in the Aeolis Dorsa region, Mars, and used the thickness data to calculate channel depth and river discharge, similar to our recommended approach.

Grain size is another obstacle in applying our sedimentology-based reconstruction method to Mars; however, the method is relatively insensitive to grain size (Parker et al., 2007). For example, assuming medium sand ($D_{50} = 0.3$ mm) versus medium gravel ($D_{50} = 50$ mm) introduces an uncertainty in the reconstruction of water discharge of a factor of about three. For river deltas, an additional constraint based on delta lobe size, which relates to backwater hydrodynamics, also can be used to constrain channel-bed slope or grain size (DiBiase et al., 2013).

For analysis of exhumed channel belts on Mars using available remote sensing data, we recommend the following steps: 1) Measure caprock thickness. High-quality caprock measurements will occur where talus does not obscure the caprock and a clear cliff scarp is visible (e.g., Fig. 3.15). 2) Infer paleo-channel depth using the measured caprock thickness and $T/d = 1.5$, with a 5th–95th percentile range of $T/d = 0.8$–4 (Fig. 3.14B) Make a grain size estimate. If no constraints are available, we recommend using medium-to-coarse sand ($D_{50} = 0.5$ mm), which is typical for ridges in Utah and rivers with muddy floodplains that are likely to make ridges during exhumation. Bounds for medium sand and medium gravel (0.3–50 mm) can be used for conditions typical of lowland depositional rivers on Earth (e.g., Lamb and Venditti, 2016), which introduces an additional factor

of ~3 uncertainty on Q. 4) Eqs. 3.1-3.6, 3.10, and 3.11 then can be combined to calculate a bankfull river discharge:

$$Q = 74.2 C_f^{-1/2} (Rg)^{3/8} \nu^{1/4} D_{50}^{1/8} d^2, \qquad \text{Eq. 3.12}$$

where $C_f = u_*^2/U^2, u_*^2 = gdS$ for steady and uniform flow, and U can be computed from Eqs. 3.2-3.6 following the method of Engelund and Hansen (1967).

Fig. 3.14E and F show the sensitivity of the discharge reconstructions with inputs that rely on remote sensing alone for the inverted-channel method that utilizes ridge width (Eq. 3.7, with coefficient and exponent from Eaton (2013)) and our proposed method for deposit inversion of exhumed channel belts that utilizes caprock thickness (Eq. 3.12). The largest uncertainty for the inverted channel method that utilizes ridge width alone (Eq. 3.7) is the unknown ratio between ridge breadth to channel width, which can vary from $0.2<B/w<36$ (5th–95th percentile) for single-threaded channels due to unknown channel belt extents and ridge erosion, leading to potential uncertainty of over four orders of magnitude in discharge (Fig. 3.14E). Note that Fig. 3.14E does not account for the additional uncertainty in the assumed constants *a* and *b* in Eq. 3.7, which likely vary for rivers of different depth, slopes, and bed sediment sizes, in addition to gravity (Section 3.5.1). For deposit inversion (Eq. 3.12), the largest uncertainty is due to the unknown ratio between channel-belt thickness and channel depth (T/d=0.8–4), and secondarily grain size (using $0.3<D_{50}<50$ mm), which yields an uncertainty of about a factor of 27 in discharge using Gaussian error propagation (Fig. 3.14F). The uncertainty associated with accurately measuring the caprock breadth or thickness on Mars is not accounted for here. The deposit inversion method has far less uncertainty due to the tight correlation between channel depth and caprock thickness, as expected due to river avulsion mechanics during channel-belt formation (Bryant et al., 1995; Mohrig et al., 2000; Slingerland and Smith, 2004). Martian gravity and basaltic-sediment density also can be explicitly incorporated in

the deposit-inversion reconstruction, which shifts the discharges to slightly smaller values (Fig. 3.14E, F).

As an example application on Mars, we used data from DiBiase et al. (2013) because it is one of the rare studies that report caprock thickness. DiBiase et al. (2013) measured caprock thickness of ~10 m and a caprock width of ~600 m for what they infer to be a trunk channel complex (i.e., channel belt) that transitions into a series of bifurcating delta lobes in the Aeolis Dorsa region, Mars. Using their measurements and assuming a single-thread channel, we estimated a paleo-channel depth of 6.7 m (range: 3–13 m), width of 120 m (range: 49–230 m), and corresponding bankfull discharge of 2300 m^3/s (range: 370–8800 m^3/s) using $T/d = 1.5$ (range: 0.8–4), $D_{50} = 0.5$ mm, and Eqs. 3.10 and 3.12. In contrast, if the entire ridge breadth is taken to be a proxy for channel width, then the inferred channel width is 600 m and the discharge is 10,000 m^3/s using Eq. 3.7 with the Eaton (2013) parameters, approximately 5-fold larger than the best-estimate value using the caprock thickness approach, and similar to the peak annual flood on the Mississippi River (Lamb et al., 2012b). Complicating the interpretation of ridge breadth, the caprock from the DiBiase et al. (2013) study area also contains a number of smaller superposed ridges that have breadths ~50 m (see their Fig. 3.5), which yielded a discharge estimate using Eq. 3.7 of 97 m^3/s, a factor of 100 smaller than using the entire caprock breadth. Based on typical stratigraphic architecture of fluvial deposits (e.g., Heller and Paola, 1996; Blum et al., 2013) and the unlikely preservation of channel fills during exhumation, we suspect that the smaller ridges are still unlikely to be channel fills, but might reflect smaller amalgamated channel belts with lesser extents of river lateral migration (e.g., ribbon sandstones; Friend et al., 1979), similar to the interpretation of DiBiase et al. (2013). Regardless of the specific interpretation, this example illustrates the ambiguity of inferring channel widths and

channel-belt extents from measurements of eroded caprock breadths, and how that ambiguity can result in significant uncertainty in water discharge estimates.

3.7.5 Implications for Mars

The inverted channel hypothesis proposes that ridges accurately reflect the geometry of river channels, preserved as a geomorphic surface in inverted relief. Instead, our observations in Utah are consistent with deposit inversion in which river lateral migration and aggradation led to the formation of channel belts that were likely wider and thicker than the original channel, but then were modified by scarp retreat during exhumation. Channel fills that preserve the original channel geometry, in contrast, are not preserved. Our global compilation of terrestrial channel belts supports the view that channel belts are often significantly wider than the original channels. Perhaps more importantly, deposit inversion indicates that substantial time is recorded in the ridge caprock and underlying strata, including multiple generations of rivers occupying a single channel belt, and multiple generations of channel belts building thick ridge-bearing strata. Reinterpreting sinuous ridges as exhumed channel belts, therefore, implies likely smaller river discharges and far greater durations of fluvial activity on Mars, potentially by millions of years.

The work of Harris (1980) at the Green River site is often used to justify the likely nature of ridges on Mars as composed of channel fills, but his terminology is different than what is commonly used today in sedimentology (which we presented in Section 3.2). We believe that this difference in terminology has led to misunderstanding of his results. In particular, Harris termed the ridges synonymously as channels, paleochannels, and channel fills by definition, but then went on to define channels (or channel fills) as a body of clastic material, regardless of size and shape, generally sandstone and/or fine conglomerate, originally deposited by rapidly flowing water in an ancient stream course, which has internal structures indicating the direction of sediment transport. This

description is equivalent to our definition of a channel-belt sandstone body, not a paleo-channel fill as we use the term. Harris divided the channel-belt deposits (his “channels fills”) into what he termed point-bar and channel-fill deposits, a classification scheme that continued with Williams et al. (2007, 2009) and has been applied to ridges on Mars (Burr et al., 2010; Williams et al., 2013; Kite et al., 2015a; Jacobsen and Burr, 2017). However, Harris goes on to define point bars as lateral accretion sets, and we now recognize that downstream-migrating bars and channel migration can create lateral accretion sets in the absence of active meandering and point bars (e.g., Okolo, 1983; Olsen, 1988; Bridge et al., 1986). More importantly, Harris's description of what he calls channel fills is consistent with our definition of channel deposits that make up the channel belt. In other words, they are the trough-cross-stratified sandstone facies and lateral accretion sets that result from aggradation and lateral migration of the active river channel, rather than finer grained overbank deposits that fill and preserve the geometry of abandoned channels. Several studies cite Harris (1980) to support the idea that ridges on Mars, especially in their straight segments, are composed of channel fills that closely preserve the original channel shape (e.g., Williams et al., 2007; Williams et al., 2009; Burr et al., 2010), citing, for example, Gibling (2006) to define channel fills (e.g., Jacobsen and Burr, 2017). While Gibling's definition of channel fills is similar to ours: “the filling of a channel without change in its perimeter (banks and basal surface), for example the fill of an abandoned channel,” this is inconsistent with how Harris uses the term. The differing terminology aside, Harris's description of the caprocks is similar to ours: they are composed of bar and dune strata that record the aggradation and lateral migration of the active channel to form a channel belt, rather than a channel-geometry-preserving fill.

On Mars, the topographic inversion hypothesis is often implicitly assumed in order to link ridge segments together to form a river network. However, in the Cedar Mountain Formation, ridge

junctions typically represent caprock sandstone bodies that intersect at distinct stratigraphic levels, and therefore were not coeval. Channel-belt thicknesses are commonly a small fraction of the total ridge relief; therefore, detecting decimeter stratigraphic offsets between adjoining ridge caprocks that we observed in Utah would be difficult by remote sensing alone. Nonetheless, larger stratigraphic offsets and caprocks crossing at distinct stratigraphic intervals are apparent on Mars (Burr et al., 2010; DiBiase et al., 2013; Kite et al., 2015a; Goudge et al., 2018) (Fig. 3.1B). Moreover, DiBiase et al. (2013) inferred paleo-flow directions, based on the dip of bedding, to be opposite to the orientation inferred from ridge-top slopes, and attributed this to differential erosion, similar to our observations in Utah. Although multiple episodes of channel erosion and rapid volcanic infill have also been proposed as an explanation for stratigraphically distinct ridges (e.g., Burr et al., 2009), channel-belt stacking is the primary characteristic of the architecture of fluvial sedimentary basins (Gibling, 2006; Heller and Paola, 1996), and cross-cutting ridges would be a necessary consequence of preferential erosion of floodplain deposits during exhumation. On Mars, ridges with stacked patterns are apparent for some ridges at Aeolis Dorsa (Fig. 3.1; DiBiase et al., 2013), Arabia Terra (Davis et al., 2016), Hypanis Vallis (Fawdon et al., 2018), Gale Crater, near Juventae Chasma, Eberswalde, Hypanis Vallis, and in fans on crater walls like those in Harris and Saheki Craters.

In contrast to Utah where runoff and river erosion is important in exhuming the ridges, eolian erosion appears to be the dominant exhumation process on Mars (e.g., Zimbelman and Griffin, 2010). Whereas fluvial erosion is focused in steep areas which accumulate the largest amount of water, eolian erosion may be more uniform or have a directionality associated with the dominant winds. Therefore, eolian erosion may help to explain longer ridges, more uniform ridge widths, and the preservation of more complex ridge crossing patterns observed on Mars (Burr et al., 2009; Burr et al., 2010) (e.g., Fig. 3.1). Uniform ridge geometries on Mars has been interpreted to indicate

minimal caprock erosion (Burr et al., 2010; Williams et al., 2013; Kite et al., 2015b), but it might instead indicate a uniformity in the erosion process due to the wind. Cliff-forming caprocks are also targeted on Mars as indicators of a preserved paleo-channel width (e.g., Burr et al., 2010) because Harris noted that exhumed channel fills (his definition) have steep caprock sides. However, our results suggest that the cliff-forming caprocks instead are due to significant erosional backwasting of a once larger channel-belt sandstone body (Fig. 3.13). Like Utah, Mars ridges also show exposed strata along cliff-forming caprocks and ridges (e.g., Weitz et al., 2008; Wiseman et al., 2008; DiBiase et al., 2013), suggesting that significant lateral erosion has occurred, further complicating the interpretation of ridge breadth.

A final implication for Mars is that deposit inversion requires a prolonged surface environment that supported fluvial activity and rivers aggrading, in cases >300 m of strata (Kite et al., 2013), followed by a transition to regional erosion and exhumation. On Earth, deposits of this size form over geologic time (Sadler, 1981) and embedded crater counts of the 300 m of strata in Aeolis Dorsa suggest it formed over at least millions of years (Kite et al., 2013). Other fluvial sinuous ridges across Mars are interpreted to represent fluvial systems ranging in age from mid-Noachian (Davis et al., 2016) to early- and mid-Hesperian (Weitz et al., 2010; Kite et al., 2013), which overlaps with the latest interpretations of fluvial activity indicated by valley networks (Ramirez and Craddock, 2018). Valley networks have been the basis of interpreting fluvial activity on Mars, including location and timing (Hynek et al., 2010) and total volume of water flow (Luo et al., 2017), but debate remains on whether flows occurred sporadically as the result of rare events like impacts (Segura et al., 2002) or were due to a persistent hydrological cycle (Ramirez and Craddock, 2018). Valley networks are erosional fluvial landforms, and erosional systems in general are poor recorders of environmental history over deep time. In contrast, sinuous ridges on Mars may be composed of

strata from depositional rivers, which can record a rich history of surface environments over millions of years. Moreover, the recognition of ridges as fluvial deposits will expand geographic coverage of geologic indicators of fluvial activity on the Martian surface, which are needed to test global climate models, such as the numerous ridges observed in Arabia Terra (Davis et al., 2016) that appear inconsistent with the "Icy Highlands" hypothesis (Wordsworth et al., 2013). The transition from Noachian and Hesperian depositional fluvial systems to surface deflation by the wind, as indicated by sinuous ridges, likely coincides with the aridification of Mars (Ramirez and Craddock, 2018), which is also interpreted based on myriad other evidence, including sedimentology (Banham et al., 2018), mineral abundance in global stratigraphy (Ehlmann et al., 2011), and valley network abundance (Di Achille and Hynek, 2010).

3.8 Conclusions

Sinuous ridges in the Cedar Mountain Formation near Green River, Utah, extend for hundreds of meters, are up to 130 m wide, and stand up to 40 m above the surrounding plain. Ridge caprocks are composed of 3–10 meter-thick sandstone bodies, with dune and bar inclined strata, which we interpret as channel belts that record the lateral migration and aggradation of single-threaded, sand-bedded rivers with 2.1–4.2 m channel depths, rather than channel fills. Some ridges are bisected into segments by washes that preferentially erode portions that are convex in the direction of tectonic dip, and caprocks also degrade laterally by scarp retreat. Due to the combination of amalgamation, erosion, and tectonic modification, ridge dimensions do not record paleo-channel dimensions and ridge top slope is altered to the point that some ridges dip opposite to the inferred paleo-flow direction. From our observations in Utah and a global compilation of terrestrial channel belts, caprock breadth is found to be a potentially unreliable indicator of paleo-channel width because caprocks are eroded remnants of channel-belt sandstone bodies that were once much wider than the

paleo-channel, with ridge-to-channel width ratios that could range between 0.2 and 36. In contrast, caprock thickness is more tightly constrained to 0.8–4 times the paleo-channel depth due to the mechanics of river avulsion and channel-belt abandonment, and erosion dominated by scarp retreat. Ridge intersections in planview typically result from crossing of unrelated sandstone bodies at different stratigraphic levels, rather than a bifurcating channel network.

For sinuous ridges formed by exhumation of fluvial channel belts, like in the Cedar Mountain Formation, we developed a method for reconstructing the original channel dimensions and discharge using remote sensing alone for applicability on Mars. The reconstruction is based on measuring the caprock thickness, and using this value to constrain channel depth. Based on our observations in Utah and a compilation of terrestrial channel belts, we caution against using ridge width and curvature as proxies for channel width and curvature; since the ridges are eroded remnants of channel belts, they can have geometries much different than the original channels. An example from Aeolis Dorsa, Mars, shows that mistaking ridge width for channel width could result in significant error in estimated river discharge. More importantly, the ridges on Mars are unlikely to be a snapshot of a paleolandscape, but instead indicate exhumation of a fluvial depositional basin formed over geologic time periods. Such new interpretations would bolster the hypothesis of consistent long-lived fluvial systems on early Mars.

Supplementary data availability

The two supplementary tables contain raw data and can be found online at https://doi.org/10.1016/j.icarus.2019.04.019.

Acknowledgements

Field data collection was aided by the 2015 field classes of Texas A& M, University of Wyoming, and Caltech. This work was supported by NASA (grant NNX16AQ81G to Caltech and

NNX13AG83G to RMEW), Caltech's Terrestrial Hazard Observation and Reporting program, and the Donors of the American Chemical Society Petroleum Research Fund (53544DNI8 to RCE). ATH acknowledges graduate fellowship support from NASA (80NSSC17K0492) and NSF (1144469). We also thank two anonymous reviewers for their helpful comments.

3.9 Works cited

Anderson, R. and J. Bell (2010). Geologic mapping and characterization of Gale Crater and implications for its potential as a Mars Science Laboratory landing site. Mars J 5: 76–128.

Balme, M. R., P. M. Grindrod, E. Sefton-Nash, J. M. Davis, S. Gupta and P. Fawdon (2016). Aram Dorsum: A Noachian Inverted Fluvial Channel System in Arabia Terra, Mars (and Candidate ExoMars 2018 Rover Landing Site). Lunar and Planetary Science Conference.

Banham, S. G., S. Gupta, D. M. Rubin, J. A. Watkins, D. Y. Sumner, K. S. Edgett, J. P. Grotzinger, K. W. Lewis, L. A. Edgar, K. M. Stack-Morgan, R. Barnes, J. F. Bell, M. D. Day, R. C. Ewing, M. G. A. Lapotre, N. T. Stein, F. Rivera-Hernandez and A. R. Vasavada (2018). "Ancient Martian aeolian processes and palaeomorphology reconstructed from the Stimson formation on the lower slope of Aeolis Mons, Gale crater, Mars." Sedimentology **65**(4).

Bates, C. E. (1952). Photogeologic maps of the Stinking Spring Creek 13 and 14 quadrangles, Emery County, Utah. Open-File Report.

Best, J. L., P. J. Ashworth, C. S. Bristow and J. Roden (2003). "Three-Dimensional Sedimentary Architecture of a Large, Mid-Channel Sand Braid Bar, Jamuna River, Bangladesh." Journal of Sedimentary Research **73**(4): 516-530.

Bhattacharya, J. P., P. Copeland, T. F. Lawton and J. Holbrook (2016). "Estimation of source area, river paleo-discharge, paleoslope, and sediment budgets of linked deep-time depositional systems and implications for hydrocarbon potential." Earth-Science Reviews **153**: 77-110.

Blum, M., J. Martin, K. Milliken and M. Garvin (2013). "Paleovalley systems: Insights from Quaternary analogs and experiments." Earth-Science Reviews **116**(0): 128-169.

Bradley, R. W. and J. G. Venditti (2017). "Reevaluating dune scaling relations." Earth-Science Reviews **165**: 356-376.

Bridge, J. (2003). Rivers and Floodplains. Malden, Mass, Blackwell Publishing.

Bridge, J., N. Smith, F. Trent, S. Gabel and P. Bernstein (1986). "Sedimentology and morphology of a low-sinuosity river: Calamus River, Nebraska Sand Hills." Sedimentology **33**(6): 851-870.

Bridge, J. S. and I. A. Lunt (2006). Depositional models of braided rivers. Braided rivers: Process, deposits, ecology and management. Oxford, Blackwell Publishing. **36:** 11-50.

Bryant, M., P. Falk and C. Paola (1995). "Experimental study of avulsion frequency and rate of deposition." Geology **23**(4): 365.

Burr, D. M., M.-T. Enga, R. M. E. Williams, J. R. Zimbelman, A. D. Howard and T. A. Brennand (2009). "Pervasive aqueous paleoflow features in the Aeolis/Zephyria Plana region, Mars." Icarus **200**(1): 52-76.

Burr, D. M., R. M. E. Williams, K. D. Wendell, M. Chojnacki and J. P. Emery (2010). "Inverted fluvial features in the Aeolis/Zephyria Plana region, Mars: Formation mechanism and initial paleodischarge estimates." Journal of Geophysical Research: Planets **115**(E07011).

Cardenas, B. T., D. Mohrig and T. A. Goudge (2018). "Fluvial stratigraphy of valley fills at Aeolis Dorsa, Mars: Evidence for base-level fluctuations controlled by a downstream water body." GSA Bulletin **130**(3-4): 484-498.

Clarke, J. D. A. and C. R. Stoker (2011). "Concretions in exhumed and inverted channels near Hanksville Utah: implications for Mars." International Journal of Astrobiology **10**(3): 161-175.

Cuevas Martínez, J. L., L. Cabrera Pérez, A. Marcuello, P. A. U. Arbués Cazo, M. Marzo Carpio and F. Bellmunt (2010). "Exhumed channel sandstone networks within fluvial fan deposits from the Oligo-Miocene Caspe Formation, South-east Ebro Basin (North-east Spain)." Sedimentology **57**(1): 162-189.

Currie, B. S. (2002). "Structural Configuration of the Early Cretaceous Cordilleran Foreland-Basin System and Sevier Thrust Belt, Utah and Colorado." The Journal of Geology **110**(6): 697-718.

Davis, J. M., M. Balme, P. M. Grindrod, R. M. E. Williams and S. Gupta (2016). "Extensive Noachian fluvial systems in Arabia Terra: Implications for early Martian climate." Geology **44**(10): 847-850.

DeCelles, P. G. and J. C. Coogan (2006). "Regional structure and kinematic history of the Sevier fold-and-thrust belt, central Utah." Geological Society of America Bulletin **118**(7-8): 841-864.

DeCelles, P. G. and B. S. Currie (1996). "Long-term sediment accumulation in the Middle Jurassic–early Eocene Cordilleran retroarc foreland-basin system." Geology **24**(7): 591-594.

Derr, M. E. (1974). Sedimentary structure and depositional environment of paleochannels in the Jurassic Morrison Formation near Green River, Utah, Brigham Young University, Dept. of Geology. **21:** 3-39.

Di Achille, G. and B. M. Hynek (2010). "Ancient ocean on Mars supported by global distribution of deltas and valleys." Nature Geoscience **3**(7): 459-463.

DiBiase, R. A., A. B. Limaye, J. S. Scheingross, W. W. Fischer and M. P. Lamb (2013). "Deltaic deposits at Aeolis Dorsa: Sedimentary evidence for a standing body of water on the northern plains of Mars." Journal of Geophysical Research: Planets **118**(6): 1285-1302.

Doelling, H. H., P. A. Kuehne, G. C. Willis and J. B. Ehler (2015). Geologic Map of the San Rafael Desert 30'x60' Quadrangle, Emery and Grand Counties, Utah. UT, Utah Geological Survey.

Durkin, P. R., R. L. Boyd, S. M. Hubbard, A. W. Shultz and M. D. Blum (2017). "Three-Dimensional Reconstruction of Meander-Belt Evolution, Cretaceous McMurray Formation, Alberta Foreland Basin, Canada." Journal of Sedimentary Research **87**(10): 1075-1099.

Eaton, B. (2013). "Hydraulic geometry: empirical investigations and theoretical approaches." Treatise on geomorphology, fluvial geomorphology **9**: 313-329.

Ehlmann, B. L., J. F. Mustard, S. L. Murchie, J.-P. Bibring, A. Meunier, A. A. Fraeman and Y. Langevin (2011). "Subsurface water and clay mineral formation during the early history of Mars." Nature **479**(7371): 53-60.

Einstein, H. A. (1950). The bed-load function for sediment transportation in open channel flows, United States Department of Agriculture. **1026**.

Engelund, F. and E. Hansen (1967). A monograph on sediment transport in alluvial streams, Tekniskforlag Skelbrekgade 4, Copenhagen V, Denmark.

Fassett, C. I. and J. W. Head (2005). "Fluvial sedimentary deposits on Mars: Ancient deltas in a crater lake in the Nili Fossae region." Geophysical Research Letters **32**(14).

Fawdon, P., S. Gupta, J. M. Davis, N. H. Warner, J. B. Adler, M. R. Balme, J. F. Bell, P. M. Grindrod and E. Sefton-Nash (2018). "The Hypanis Valles delta: The last highstand of a sea on early Mars?" Earth and Planetary Science Letters **500**: 225-241.

Ferguson, R. (2007). "Flow resistance equations for gravel-and boulder-bed streams." Water Resources Research **43**(5).

Fernandes, A. M., T. E. Tornqvist, K. M. Straub and D. Mohrig (2016). "Connecting the backwater hydraulics of coastal rivers to fluvio-deltaic sedimentology and stratigraphy." Geology **44**(12): 979-982.

Foreman, B. Z., P. L. Heller and M. T. Clementz (2012). "Fluvial response to abrupt global warming at the Palaeocene/Eocene boundary." Nature **491**(7422): 92-95.

Friend, P. F. (1989). "Space and time analysis of river systems, illustrated by Miocene systems of the northern Ebro Basin in Aragon, Spain." Revista de la Sociedad Geológica de España **2**: 55-64.

Friend, P. F., M. J. Slater and R. C. Williams (1979). "Vertical and lateral building of river sandstone bodies, Ebro Basin, Spain." Journal of the Geological Society **136**(1): 39-46.

Ganti, V., Z. Chu, M. P. Lamb, J. A. Nittrouer and G. Parker (2014). "Testing morphodynamic controls on the location and frequency of river avulsions on fans versus deltas: Huanghe (Yellow River), China." Geophysical Research Letters **41**(22): 7882-7890.

Ganti, V., M. P. Lamb and B. McElroy (2014). "Quantitative bounds on morphodynamics and implications for reading the sedimentary record." Nature Communications **5**: 3298.

Garcia, M. H. (2006). ASCE Manual of Practice 110—Sedimentation Engineering: Processes, Measurements, Modeling and Practice. World Environmental and Water Resource Congress 2006: Examining the Confluence of Environmental and Water Concerns.

Garrison, J. R., D. Brinkman, D. J. Nichols, P. Layer, D. Burge and D. Thayn (2007). "A multidisciplinary study of the Lower Cretaceous Cedar Mountain Formation, Mussentuchit Wash, Utah: a determination of the paleoenvironment and paleoecology of the Eolambia caroljonesa dinosaur quarry." Cretaceous Research **28**(3): 461-494.

Gibling, M. R. (2006). "Width and thickness of fluvial channel bodies and valley fills in the geological record: A literature compilation and classification." Journal of Sedimentary Research **76**(5): 731-770.

Goudge, T. A., D. Mohrig, B. T. Cardenas, C. M. Hughes and C. I. Fassett (2018). "Stratigraphy and paleohydrology of delta channel deposits, Jezero crater, Mars." Icarus **301**: 58-75.

Grant, J. A. and S. A. Wilson (2012). "A possible synoptic source of water for alluvial fan formation in southern Margaritifer Terra, Mars." Planetary and Space Science **72**(1): 44-52.

Grotzinger, J., A. Hayes, M. Lamb and S. McLennan (2013). "Sedimentary processes on Earth, Mars, Titan, and Venus." Comparative Climatology of Terrestrial Planets **1**: 439-472.

Hajek, E. A. and P. L. Heller (2012). "Flow-Depth Scaling In Alluvial Architecture and Nonmarine Sequence Stratigraphy: Example from the Castlegate Sandstone, Central Utah, U.S.A." Journal of Sedimentary Research **82**(2): 121-130.

Hajek, E. A. and M. A. Wolinsky (2012). "Simplified process modeling of river avulsion and alluvial architecture: Connecting models and field data." Sedimentary Geology **257-260**: 1-30.

Harris, D. R. (1980). Exhumed paleochannels in the Lower Cretaceous Cedar Mountain Formation near Green River, Utah, Brigham Young University. **27:** 51-66.

Heller, P. L. and C. Paola (1996). "Downstream changes in alluvial architecture: an exploration of controls on channel-stacking patterns." Journal of Sedimentary Research **66**(2).

Hynek, B. M., M. Beach and M. R. Hoke (2010). "Updated global map of Martian valley networks and implications for climate and hydrologic processes." Journal of Geophysical Research: Planets **115**(E9).

Ielpi, A. and M. Ghinassi (2014). "Planform architecture, stratigraphic signature and morphodynamics of an exhumed Jurassic meander plain (Scalby Formation, Yorkshire, UK)." Sedimentology **61**(7): 1923-1960.

Ielpi, A. and M. Ghinassi (2015). "Planview style and palaeodrainage of Torridonian channel belts: Applecross Formation, Stoer Peninsula, Scotland." Sedimentary Geology **325**: 1-16.

Irwin, R. P., K. W. Lewis, A. D. Howard and J. A. Grant (2015). "Paleohydrology of Eberswalde crater, Mars." Geomorphology **240**: 83-101.

Jacobsen, R. E. and D. M. Burr (2017). "Dichotomies in the fluvial and alluvial fan deposits of the Aeolis Dorsa, Mars: Implications for weathered sediment and paleoclimate." Geosphere **13**(6): 2154-2168.

Jacobsen, R. E. and D. M. Burr (2018). "Errors in Martian paleodischarges skew interpretations of hydrologic history: Case study of the Aeolis Dorsa, Mars, with insights from the Quinn River, NV." Icarus **302**: 407-417.

Jaumann, R., R. H. Brown, K. Stephan, J. W. Barnes, L. A. Soderblom, C. Sotin, S. Le Mouélic, R. N. Clark, J. Soderblom, B. J. Buratti, R. Wagner, T. B. McCord, S. Rodriguez, K. H. Baines, D. P. Cruikshank, P. D. Nicholson, C. A. Griffith, M. Langhans and R. D. Lorenz (2008). "Fluvial erosion and post-erosional processes on Titan." Icarus **197**(2): 526-538.

Jerolmack, D. J. and D. Mohrig (2007). "Conditions for branching in depositional rivers." Geology **35**(5): 463-466.

Jerolmack, D. J., D. Mohrig, M. T. Zuber and S. Byrne (2004). "A minimum time for the formation of Holden Northeast fan, Mars." Geophysical Research Letters **31**(21).

Jerolmack, D. J. and J. B. Swenson (2007). "Scaling relationships and evolution of distributary networks on wave-influenced deltas." Geophysical Research Letters **34**(23).

Jobe, Z. R., N. C. Howes and N. C. Auchter (2016). "Comparing submarine and fluvial channel kinematics: Implications for stratigraphic architecture." Geology **44**(11): 931-934.

Kargel, J. S. and R. G. Strom (1992). "Ancient glaciation on Mars." Geology **20**(1): 3-7.

Kirk, R., E. Howington-Kraus, M. Rosiek, J. Anderson, B. Archinal, K. Becker, D. Cook, D. Galuszka, P. Geissler and T. Hare (2008). "Ultrahigh resolution topographic mapping of Mars with MRO HiRISE stereo images: Meter-scale slopes of candidate Phoenix landing sites." Journal of Geophysical Research: Planets **113**(E3).

Kirkland, J. I., B. Britt, D. L. Burge, K. Carpenter, R. Cifelli, F. DeCourten, J. Eaton, S. Hasiotis and T. Lawton (1997). "Lower to middle Cretaceous dinosaur faunas of the central

Colorado Plateau: a key to understanding 35 million years of tectonics, sedimentology, evolution, and biogeography." Brigham Young University Geology Studies **42**: 69-104.

Kirkland, J. I., R. L. Cifelli, B. B. Britt, D. L. Burge, F. L. DeCourten, J. G. Eaton and J. M. Parrish (1999). "Distribution of vertebrate faunas in the Cedar Mountain Formation, east-central Utah." Vertebrate Paleontology in Utah: Utah Geological Survey Miscellaneous Publication **1**: 201-217.

Kite, E. S., A. D. Howard, A. Lucas and K. W. Lewis (2015a). "Resolving the era of river-forming climates on Mars using stratigraphic logs of river-deposit dimensions." Earth and Planetary Science Letters **420**: 55-65.

Kite, E. S., A. D. Howard, A. S. Lucas, J. C. Armstrong, O. Aharonson and M. P. Lamb (2015b). "Stratigraphy of Aeolis Dorsa, Mars: Stratigraphic context of the great river deposits." Icarus **253**(0): 223-242.

Kite, E. S., A. Lucas and C. I. Fassett (2013). "Pacing early Mars river activity: Embedded craters in the Aeolis Dorsa region imply river activity spanned ≳(1–20)Myr." Icarus **225**(1): 850-855.

Lamb, M. P., J. P. Grotzinger, J. B. Southard and N. J. Tosca (2012). "Were aqueous ripples on Mars formed by flowing brines." Sedimentary Geology of Mars **102**: 139-150.

Lamb, M. P., J. A. Nittrouer, D. Mohrig and J. Shaw (2012). "Backwater and river plume controls on scour upstream of river mouths: Implications for fluvio-deltaic morphodynamics." Journal of Geophysical Research: Earth Surface **117**(F1).

Lamb, M. P. and J. G. Venditti (2016). "The grain size gap and abrupt gravel-sand transitions in rivers due to suspension fallout." Geophysical Research Letters **43**(8): 3777-3785.

Le Deit, L., E. Hauber, F. Fueten, M. Pondrelli, A. P. Rossi and R. Jaumann (2013). "Sequence of infilling events in Gale Crater, Mars: Results from morphology, stratigraphy, and mineralogy." Journal of Geophysical Research: Planets **118**(12): 2439-2473.

Leclair, S. F. and J. S. Bridge (2001). "Quantitative interpretation of sedimentary structures formed by river dunes." Journal of Sedimentary Research **71**(5): 713-716.

Lefort, A., D. M. Burr, R. A. Beyer and A. D. Howard (2012). "Inverted fluvial features in the Aeolis-Zephyria Plana, western Medusae Fossae Formation, Mars: Evidence for post-formation modification." Journal of Geophysical Research: Planets **117**(E3).

Lefort, A., D. M. Burr, F. Nimmo and R. E. Jacobsen (2015). "Channel slope reversal near the Martian dichotomy boundary: Testing tectonic hypotheses." Geomorphology **240**: 121-136.

Loizeau, D., N. Mangold, F. Poulet, J. P. Bibring, J. Bishop, J. Michalski and C. Quantin (2015). "History of the clay-rich unit at Mawrth Vallis, Mars: High-resolution mapping of a candidate landing site." Journal of Geophysical Research: Planets **120**(11): 1820-1846.

Ludvigson, G. A., R. M. Joeckel, L. R. Murphy, D. F. Stockli, L. A. González, C. A. Suarez, J. I. Kirkland and A. Al-Suwaidi (2015). "The emerging terrestrial record of Aptian-Albian global change." Cretaceous Research **56**: 1-24.

Luo, W., X. Cang and A. D. Howard (2017). "New Martian valley network volume estimate consistent with ancient ocean and warm and wet climate." Nature Communications **8**: 15766.

Lynds, R. M., D. Mohrig, E. A. Hajek and P. L. Heller (2014). "Paleoslope reconstruction in sandy suspended-load-dominant rivers." Journal of Sedimentary Research **84**(10): 825-836.

Mackey, S. D. and J. S. Bridge (1995). "Three-dimensional model of alluvial stratigraphy: theory and application." Journal of Sedimentary Research **65**(1).

Maizels, J. K. (1987). "Plio-Pleistocene raised channel systems of the western Sharqiya (Wahiba), Oman." Geological Society, London, Special Publications **35**(1): 31-50.

Maizels, J. K. (1990). "Raised channel systems as indicators of palaeohydrologic change: a case study from Oman." Palaeogeography, Palaeoclimatology, Palaeoecology **76**(3–4): 241-277.

Malin, M. C. and K. S. Edgett (2003). "Evidence for persistent flow and aqueous sedimentation on early Mars." Science **302**(5652): 1931-1934.

Martin, J., A. M. Fernandes, J. Pickering, N. Howes, S. Mann and K. McNeil (2018). "The Stratigraphically Preserved Signature of Persistent Backwater Dynamics in a Large Paleodelta System: The Mungaroo Formation, North West Shelf, Australia." Journal of Sedimentary Research **88**(7): 850-872.

Matsubara, Y., A. D. Howard, D. M. Burr, R. M. E. Williams, W. E. Dietrich and J. M. Moore (2015). "River meandering on Earth and Mars: A comparative study of Aeolis Dorsa meanders, Mars and possible terrestrial analogs of the Usuktuk River, AK, and the Quinn River, NV." Geomorphology **240**: 102-120.

Miall, A. D. (1994). "Reconstructing fluvial macroform architecture from two-dimensional outcrops: examples from the Castlegate Sandstone, Book Cliffs, Utah." Journal of Sedimentary Research **64**(2).

Miall, A. D. (1996). The geology of fluvial deposits, Springer.

Milliken, K. T., M. D. Blum, J. W. Snedden and W. E. Galloway (2018). "Application of fluvial scaling relationships to reconstruct drainage-basin evolution and sediment routing for the Cretaceous and Paleocene of the Gulf of Mexico." Geosphere **14**(2): 749-767.

Mohrig, D., P. L. Heller, C. Paola and W. J. Lyons (2000). "Interpreting avulsion process from ancient alluvial sequences: Guadalope-Matarranya system (northern Spain) and Wasatch Formation (western Colorado)." Geological Society of America Bulletin **112**(12): 1787-1803.

Moore, J. M., A. D. Howard, W. E. Dietrich and P. M. Schenk (2003). "Martian layered fluvial deposits: Implications for Noachian climate scenarios." Geophysical Research Letters **30**(24).

Musial, G., J.-Y. Reynaud, M. K. Gingras, H. Féniès, R. Labourdette and O. Parize (2012). "Subsurface and outcrop characterization of large tidally influenced point bars of the Cretaceous McMurray Formation (Alberta, Canada)." Sedimentary Geology **279**: 156-172.

Nuse, B. R. (2015). Flow processes and sedimentation in a low-sinuosity high net-sand content fluvial channel belt: 3D outcrop study of the Cedar Mountain Formation, Utah MS Thesis, Colorado School of Mines. Arthur Lakes Library.

Okolo, S. A. (1983). Fluvial distributary channels in the Fletcher Bank Grit (Namurian R2b), at Ramsbottom, Lancashire, England. Modern and ancient fluvial systems, International Association of Sedimentologists Special Publication 6. **6:** 421-433.

Olsen, H. (1988). "The architecture of a sandy braided-meandering river system: an example from the lower triassic Soiling Formation (M. Buntsandstein) in W-Germany." Geologische Rundschau **77**(3): 797-814.

Osterkamp, W. R. and E. R. Hedman (1982). Perennial-streamflow characteristics related to channel geometry and sediment in Missouri River basin.

Pain, C., J. Clarke and M. Thomas (2007). "Inversion of relief on Mars." Icarus **190**(2): 478-491.
Pain, C. F. and C. D. Ollier (1995). "Inversion of relief — a component of landscape evolution." Geomorphology **12**(2): 151-165.
Palucis, M. C., W. E. Dietrich, A. G. Hayes, R. M. E. Williams, S. Gupta, N. Mangold, H. Newsom, C. Hardgrove, F. Calef and D. Y. Sumner (2014). "The origin and evolution of the Peace Vallis fan system that drains to the Curiosity landing area, Gale Crater, Mars." Journal of Geophysical Research: Planets **119**(4): 705-728.
Paola, C. and L. Borgman (1991). "Reconstructing random topography from preserved stratification." Sedimentology **38**(4): 553-565.
Paola, C. and D. Mohrig (1996). "Palaeohydraulics revisited: palaeoslope estimation in coarse-grained braided rivers." Basin Research **8**(3): 243-254.
Parker, G., P. R. Wilcock, C. Paola, W. E. Dietrich and J. Pitlick (2007). "Physical basis for quasi-universal relations describing bankfull hydraulic geometry of single-thread gravel bed rivers." Journal of Geophysical Research: Earth Surface **112**(F4).
Ramirez, R. M. and R. A. Craddock (2018). "The geological and climatological case for a warmer and wetter early Mars." Nature Geoscience **11**(4): 230-237.
Reijenstein, H. M., H. W. Posamentier and J. P. Bhattacharya (2011). "Seismic geomorphology and high-resolution seismic stratigraphy of inner-shelf fluvial, estuarine, deltaic, and marine sequences, Gulf of Thailand." AAPG Bulletin **95**(11): 1959-1990.
Robinson, J. W. and P. J. McCabe (1997). "Sandstone-body and shale-body dimensions in a braided fluvial system: Salt Wash Sandstone Member (Morrison Formation), Garfield County, Utah." AAPG bulletin **81**(8): 1267-1291.
Sable, V. H. (1958). Photogeologic Map of the Tidwell-2 Quadrangle, Emergy and Grand Counties, Utah. Miscellaneous Geologic Investigations, USGS**:** Map I-162.
Sadler, P. M. (1981). "Sediment accumulation rates and the completeness of stratigraphic sections." The Journal of Geology: 569-584.
Schumm, S. A. (1972). "Fluvial paleochannels." Special Publication - Society of Economic Paleontologists and Mineralogists.
Segura, T. L., O. B. Toon, A. Colaprete and K. Zahnle (2002). "Environmental effects of large impacts on Mars." Science **298**(5600): 1977-1980.
Slingerland, R. and N. D. Smith (2004). "River avulsions and their deposits." Annual Review of Earth Planetary Sciences **32**: 257-285.
Southard, J. B. and L. A. Boguchwal (1990). "Bed configurations in steady unidirectional water flows; Part 3, Effects of temperature and gravity." Journal of Sedimentary Research **60**(5): 680-686.
Stokes, W. L. (1944). "Morrison Formation and related deposits in and adjacent to the Colorado Plateau." Geological Society of America Bulletin **55**(8): 951-992.
Stokes, W. L. (1953). Primary sedimentary trend indicators as applied to ore finding in the Carrizo Mountains, Arizona and New Mexico; Part 1, Technical report for April 1, 1952 to March 31, 1953. United States, [U. S. Atomic Energy Commission] : Washington, DC, United States.
Stokes, W. L. (1961). Fluvial and eolian sandstone bodies in Colorado Plateau. SP 22: Geometry of Sandstone Bodies, American Association of Petroleum Geologists. **A055:** 151-178.
Trampush, S. M., S. Huzurbazar and B. J. McElroy (2014). "Empirical assessment of theory for bankfull characteristics of alluvial channels." Water Resources Research **50**(12): 9211-9220.

Wang, J. and J. P. Bhattacharya (2018). "Plan-view Paleochannel Reconstruction of Amalgamated Meander Belts, Cretaceous Ferron Sandstone, Notom Delta, South-central Utah, Usa." Journal of Sedimentary Research **88**(1): 58-74.

Ward, D. J., M. M. Berlin and R. S. Anderson (2011). "Sediment dynamics below retreating cliffs." Earth Surface Processes and Landforms **36**(8): 1023-1043.

Weitz, C. M., R. Milliken, J. A. Grant, A. S. McEwen, R. M. E. Williams and J. L. Bishop (2008). "Light-toned strata and inverted channels adjacent to Juventae and Ganges chasmata, Mars." Geophysical Research Letters **35**(19).

Weitz, C. M., R. E. Milliken, J. A. Grant, A. S. McEwen, R. M. E. Williams, J. L. Bishop and B. J. Thomson (2010). "Mars Reconnaissance Orbiter observations of light-toned layered deposits and associated fluvial landforms on the plateaus adjacent to Valles Marineris." Icarus **205**(1): 73-102.

Wilkerson, G. V. and G. Parker (2011). "Physical basis for quasi-universal relationships describing bankfull hydraulic geometry of sand-bed rivers." Journal of Hydraulic Engineering **137**(7): 739-753.

Williams, G. P. (1984). Paleohydrologic equations for rivers. Developments and Applications of Geomorphology, Springer**:** 343-367.

Williams, G. P. (1988). Paleofluvial estimates from dimensions of former channels and meanders. Flood Geomorphology. V. R. Baker, R. C. Kochel and P. C. Patton. New York, John Wiley & Sons**:** 321-334.

Williams, R. M. E. (2007). Global spatial distribution of raised curvilinear features on Mars. Lunar and Planetary Science Conference.

Williams, R. M. E., T. C. Chidsey Jr and D. E. Eby (2007). "Exhumed paleochannels in central Utah—Analogs for raised curvilinear features on Mars." Central Utah: Diverse Geology of a Dynamic Landscape: 221-235.

Williams, R. M. E., R. P. Irwin, D. M. Burr, T. Harrison and P. McClelland (2013). "Variability in martian sinuous ridge form: Case study of Aeolis Serpens in the Aeolis Dorsa, Mars, and insight from the Miracкina paleoriver, South Australia." Icarus **225**(1): 308-324.

Williams, R. M. E., R. P. Irwin and J. R. Zimbelman (2009). "Evaluation of paleohydrologic models for terrestrial inverted channels: Implications for application to martian sinuous ridges." Geomorphology **107**(3-4): 300-315.

Williams, R. M. E., R. P. Irwin, J. R. Zimbelman, T. C. Chidsey and D. E. Eby (2011). "Field guide to exhumed paleochannels near Green River, Utah: Terrestrial analogs for sinuous ridges on Mars." Geological Society of America Special Papers **483**: 483-505.

Williams, R. M. E. and C. M. Weitz (2014). "Reconstructing the aqueous history within the southwestern Melas basin, Mars: Clues from stratigraphic and morphometric analyses of fans." Icarus **242**: 19-37.

Wiseman, S. M., R. E. Arvidson, J. C. Andrews-Hanna, R. N. Clark, N. L. Lanza, D. Des Marais, G. A. Marzo, R. V. Morris, S. L. Murchie, H. E. Newsom, E. Z. Noe Dobrea, A. M. Ollila, F. Poulet, T. L. Roush, F. P. Seelos and G. A. Swayze (2008). "Phyllosilicate and sulfate-hematite deposits within Miyamoto crater in southern Sinus Meridiani, Mars." Geophysical Research Letters **35**(19).

Witkind, I. J. (2004). Geologic map of the Huntington 30'x60' Quadrangle, Carbon, Emery, Grand, and Uintah Counties, Utah, Utah Geological Survey.

Wordsworth, R., F. Forget, E. Millour, J. W. Head, J. B. Madeleine and B. Charnay (2013). "Global modelling of the early martian climate under a denser CO2 atmosphere: Water cycle and ice evolution." Icarus **222**(1): 1-19.

Wu, C., M. S. Ullah, J. Lu and J. P. Bhattacharya (2016). "Formation of point bars through rising and falling flood stages: Evidence from bar morphology, sediment transport and bed shear stress." Sedimentology **63**(6).

Zaki, A. S., C. F. Pain, K. S. Edgett and R. Giegengack (2018). "Inverted stream channels in the Western Desert of Egypt: Synergistic remote, field observations and laboratory analysis on Earth with applications to Mars." Icarus **309**: 105-124.

Zaleha, M. J. (2013). "Paleochannel hydraulics, geometries, and associated alluvial architecture of Early Cretaceous rivers, Sevier Foreland Basin, Wyoming, USA." Cretaceous Research **45**: 321-341.

Zimbelman, J. R. and L. J. Griffin (2010). "HiRISE images of yardangs and sinuous ridges in the lower member of the Medusae Fossae Formation, Mars." Icarus **205**(1): 198-210.

Chapter 4

4 FLUVIAL SINUOUS RIDGES OF THE MORRISON FORMATION, USA: MEANDERING, SCARP RETREAT, AND IMPLICATIONS FOR MARS

Hayden, A. T., & Lamb, M. P. In press at JGR: Planets.

Key Points:

1. Sinuous ridges in the Morrison Formation were formed by exhumation of channel belts.
2. Scarp retreat heavily modified channel-belt width but not thickness; a new erosion model relates width and relief to uneroded dimensions.
3. Multiple proxies for paleo-discharge on Mars yield consistent estimates.

Abstract

Sinuous ridges have been interpreted as evidence for ancient rivers on Mars, but relating ridge geometry to paleo-hydraulics remains uncertain. Three analog ridge systems from the Morrison Formation, Utah, are composed of sandstone caprocks, up to 50 m wide and 8 m thick, atop mudstone flanks. Ridge caprocks have narrowed significantly compared to sandstone bodies preserved in outcrop, consistent with a new ridge-erosion model that can be used to estimate original sandstone-body extent. Ridge networks represent caprocks intersecting at distinct stratigraphic levels, rather than a preserved channel network. Caprocks are interpreted as amalgamated channel belts, rather than inverted channels, with dune and bar cross stratification that was used to reconstruct paleo-channel dimensions. Curvilinear features on ridge tops are outcropping lateral accretion sets (LAS) from point bars and indicate meandering. We found that caprock thickness scales with paleo-channel depth, and LAS curvature scales with paleo-channel width. Application of these relations to a ridge in Aeolis Dorsa, Mars, yielded consistent water

discharge estimates (310-1800 m^3/s). In contrast, using ridge width or ridge radius of curvature as paleo-channel proxies overestimated discharge by a factor of 30-500 compared to the sedimentology-based reconstructions. In addition, the ridge-erosion model suggests that scarp retreat may be less efficient on Mars, resulting in taller and wider ridges, with more intact caprocks. Altogether, our results support the hypothesis that ridges are exhumed channel belts and floodplain deposits implying long-lived fluvial activity recorded within a depositional basin.

Plain Language Summary

Ridges across Mars have sinuous shapes that resemble rivers, but they are topographic highs (hills) rather than troughs. These landforms potentially hold valuable clues about ancient rivers that once flowed on Mars, but to decipher these clues, we must understand how the ridges formed. We studied ridges in Utah that resemble the martian ridges, and may have formed in a similar way. We found that the Utah ridges are composed of sandstone caprocks that overlie mudstone, and are from a thick sequence of sedimentary rocks from the Jurassic period. The sandstones were deposited by rivers as a channel belt, and the mudstones represent the neighboring river floodplains. These rocks were subsequently uplifted, and ridges formed as the weaker mudstones eroded faster than the sandstones. We found that both the thickness of the sandstones and curvature of bar-accretion surfaces within can be used to estimate ancient river water discharge. We also found that the sandstones have been narrowed by erosion, and we developed a scarp-erosion model describing this process. We applied the methods tested in Utah to ridges on Mars, and found consistent agreement. Our results suggest that the ridges on Mars are exhumed and eroded deposits from ancient river-channel belts.

4.1 Introduction

The surface of Mars has topographic ridges in places (e.g., Fig. 4.1) that have a planform shape similar to rivers and have been used to constrain hydrology through time (e.g., Burr et al., 2009; 2010; Jacobsen and Burr, 2018; Kite et al., 2013; 2019; Palucis et al., 2014). Ridges can form in a variety of ways, but ridges with an inferred fluvial origin (fluvial ridges) have been used to characterize the history of water on Mars because they are common (e.g., Burr et al., 2009; Davis et al., 2016; 2019), observed planetwide, and visible from orbit (Fig. 4.1). Because of their association with liquid water, fluvial ridges are important for exploration, including at landing sites for rovers like Mars 2020 (Jezero Crater; Goudge et al., 2018) and ExoMars (Balme et al., 2020). Ridges on Mars also have been used to argue for unexpectedly wide rivers (Kite et al., 2019), large seas or oceans (Cardenas et al., 2018; DiBiase et al., 2013; Hughes et al., 2019), significant durations of fluvial activity (Kite et al., 2013), and other indicators of a likely warm and wet early climate (e.g., Davis et al., 2016).

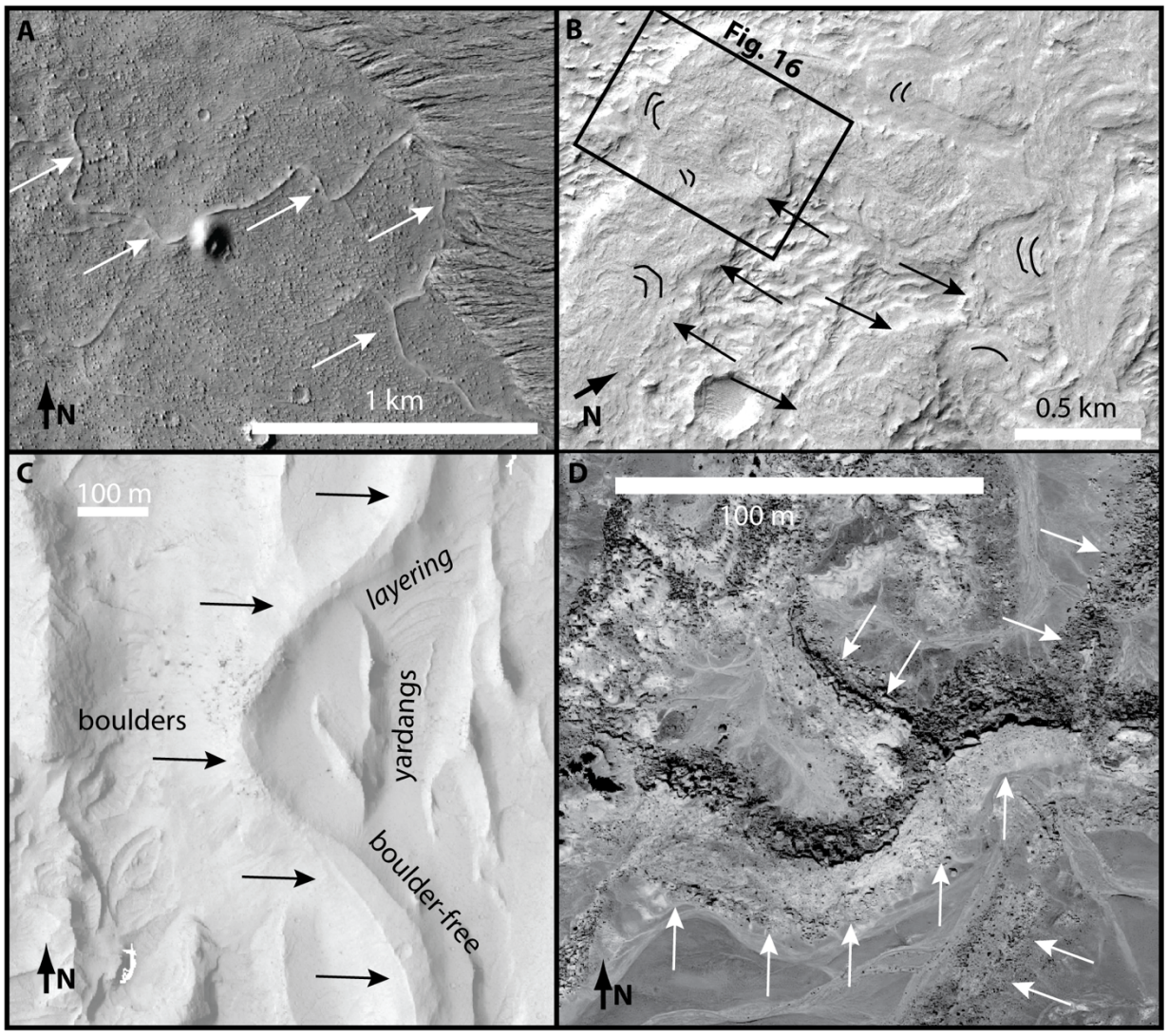

Figure 4.1-- Examples of fluvial ridges from Mars and Earth. Arrows point to ridges; each arrow orientation follows a single ridge. a. Long ridges being exhumed from cliffs (3.23 S, 152.29 E; Aeolis Dorsa, Mars; CTX image P22_009478_1768_XN_03S207W; credit: NASA/JPL/Malin Space Science Systems). b. Sinuous ridge on Mars, showing lateral accretion sets (indicated by black arcs). (5.96 S, 153.43 E; Aeolis Dorsa; HiRISE image ESP_02085_1740). c. Variable boulder cover and caprock widths on a ridge in Aeolis Dorsa (6.111 S, 151.430 E; HiRISE PSP_002279_1735). d. Stacked sinuous ridges being exhumed from a cliff in our Ferron Creek North site in Utah (39.136, -110.925; image from National Agriculture Image Program).

Fluvial ridges form when a body of rock that has a planview shape similar to a river is exhumed by differential erosion of the surrounding material (Pain and Ollier, 1995; Pain et al., 2007). Two main hypotheses exist for forming that body of rock. If the indurated material, whether of fluvial

or non-fluvial origin, fills a river channel and forms a cast, then the subsequent ridge can preserve the paleo-channel and channel-network geometry at a snapshot in time (e.g., Stanislaus Table Mountain, CA; Burr et al., 2009). This process is termed topographic inversion because what was in negative relief now stands in positive relief, and the resulting ridges are called inverted channels (Fig. 4.2A). Here we use the term channel to reflect the topographic trough that is a conduit for river water flow, whereas the channel-filling material—lava, in the case of Stanislaus Table Mountain—is a channel fill because it preserves the shape of the channel. Channel fills are not common in fluvial deposits, but they can occur, for example, when a meander bend cuts off and the resulting abandoned channel loop (or oxbow lake) fills with overbank mud without significant modification to the channel geometry (e.g., Blum et al., 2013; Bridge, 2003; Gibling, 2006). Fluvial channel fills are important where preserved because they record the original channel shape and can be used to estimate paleo-discharge (Bhattacharya et al., 2016; Musial et al., 2012; Reijenstein et al., 2011). Hence, the inverted channel interpretation implies topographic inversion of a channel fill (e.g., Burr et al., 2010). However, muddy channel fills are often easily eroded, and thus have not been observed to form ridges on Earth during exhumation; lava channel fills, on the other hand, can produce ridges.

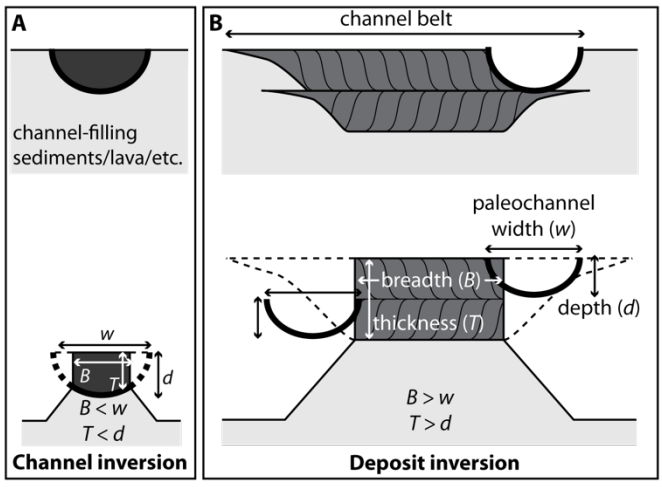

Figure 4.2--Schematic hypotheses for the formation of fluvial sinuous ridges, and deposit stratigraphy, after Hayden et al. (2019). a. Schematic of the topographic inversion hypothesis: a channel (black semi-circle) has been filled with a resistant material (dark gray) and is subsequently

exhumed to form a ridge with caprock dimensions (breadth, B, and thickness, T) that are slightly smaller than the original channel dimensions (width, w, depth, d) due to erosion. b. Schematic of the deposit inversion hypothesis: a channel (black semi-circle) aggrades and migrates across the floodplain (light gray), building a channel-belt sandstone body (medium gray) that is larger than the original channel. During exhumation, erosion modifies the channel-belt sandstone primarily by lateral backwasting reducing the ridge width.

The alternate hypothesis suggests that the indurated ridge-forming material is a channel-belt deposit, and when exhumed, the process is referred to as deposit inversion rather than topographic inversion (DiBiase et al., 2013; Hayden et al., 2019; Fig. 4.2B). River channels build deposits of coarse-grained (sandy) sediment that are far more extensive laterally and vertically than the river channel as a result of channel lateral migration and aggradation within an otherwise muddy floodplain (e.g., Gibling, 2006; Jerolmack and Mohrig, 2007; Mohrig et al., 2000). Channel deposits are accreted at the margins of an active channel as it shifts laterally and aggrades vertically, and thus are distinctly different than fluvial channel fills. We refer to the body of amalgamated channel deposits as a channel belt (also known as a channel-belt sand body, channel sandstone body, channel body, or channel complex; Blum et al., 2013; DiBiase et al., 2013; Gibling, 2006). Channel belts by our definition can contain stratigraphic packages that record single or multiple generations of channel lateral migration and vertical accretion (i.e., multiple stories) (Mackey and Bridge, 1995). Stacked sandstone channel belts within a muddy floodplain facies represent the dominant stratigraphic architecture of fluvial deposits (Hajek and Wolinsky, 2012; Heller et al., 2015).

Discerning between a topographically inverted channel and an exhumed channel belt is important for a number of reasons. First, the different formation mechanisms imply different durations of fluvial activity recorded in the ridge: inverted channels imply a relict geomorphic surface that was preserved at an instant in time, whereas exhumed channel belts imply partial deflation of a depositional basin that may have been constructed over thousands to millions of years.

Second, the interpretation defines the relationship between the geometry of the ridges and the paleo-channels, which is needed to constrain ancient surface hydrology. As an example, Lefort et al. (2012) interpreted a branching network of ridges as a topographically inverted tributary network based on observations of increasing elevation with increasing distance from the branch point. However, DiBiase et al. (2013) and Lefort et al. (2015) interpreted the same landform to have paleo-flow in the opposite direction based on the observations that branching was likely from distributary channel belts, and that modern topographic slope was likely modified by subsequent erosion or crustal deformation. The interpretations also change the appropriate methodology for quantification of river discharge from ridge observations. For example, Hayden et al. (2019) demonstrated over two orders of magnitude of uncertainty in relating ridge width to paleo-channel width due to lateral accretion and amalgamation of channel deposits during channel-belt formation and scarp retreat during ridge exhumation. This uncertainty is amplified in calculations relying on channel width; for example, discharge is commonly calculated using a relation that depends approximately on channel width squared (e.g., Eaton, 2013; Williams, 1986; 1988).

In addition to ridge width, another property of ridges used to reconstruct paleo-channels is ridge curvature and wavelength because curvature in meandering rivers scales with river width and discharge (e.g., Dury, 1976; Williams, 1986; 1988). Under the inverted channel hypothesis, ridge centerline curvature has been used as a proxy for channel curvature. It has been argued that ridge curvature is less affected by erosion than ridge width (Burr et al., 2010; Kite et al., 2015). However, it is uncertain whether this method applies when the ridges are actually exhumed channel belts because it is unlikely that channel-belt curvature mirrors paleo-channel curvature. Curvature-based reconstructions have also been applied to subparallel, concentric, curvilinear features on the surface of ridges on Mars that are observed in orbital images (e.g., Cardenas et al., 2018; Goudge et al.,

2018; Malin and Edgett, 2003; Fig. 4.1B). The curves are reminiscent of scroll bars, or abandoned river levees, associated with meandering rivers on Earth. If they are preserved levees, they could be useful because levees bound channels (Ferguson & Brierley, 1999; Leopold et al., 1964). However, levees are unlikely to be preserved both during amalgamation of channel deposits (Mason and Mohrig, 2019) and during exhumation and erosion to form a ridge. Instead, the curvilinear features may be erosional landforms; that is, exposed traces of channel-margin lateral accretion sets (LAS) as they intersect the deflating land surface. Both scroll bars and lateral accretion sets are indicative of a laterally migrating river channel (Fig. 4.3); however, their curvature has been observed to differ by up to a factor of 20, with scroll bar curvature being less representative of channel geometry (Mason and Mohrig, 2019). There has yet to be an analysis of similar curvilinear features of ridges on Earth to help constrain their origin.

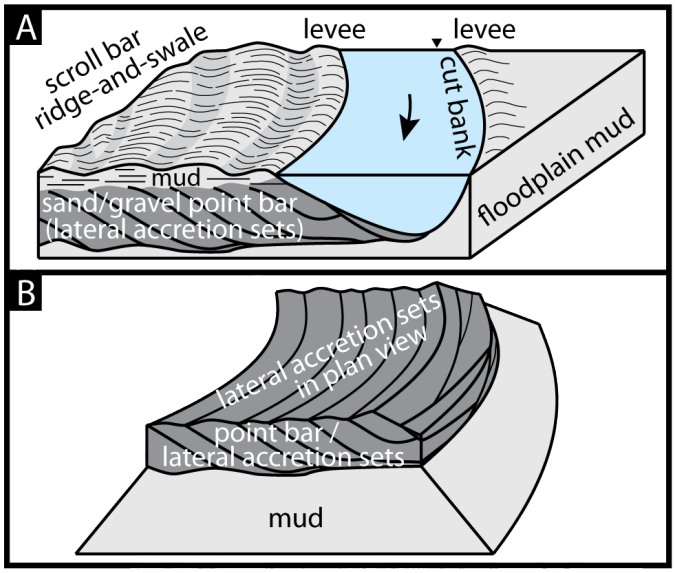

Figure 4.3-- Comparison of modern scroll bars (panel A) and exhumed point bars (panel B). a. A channel migrating laterally generates ridge-and-swale topography at its surface from secondary flow circulating muddy overbank deposits. In the subsurface, the migrating channel creates lateral accretion sets that are typically coarse-grained (sand and/or gravel; darkest gray), sometimes separated by muddy deposits (lightest gray). Panel modified after Shiers et al. (2018). b. Exhumed point bar (i.e., panel A after the mudstone, including scroll bar, has been eroded away). Fine-grained deposits often erode more quickly than coarse-grained deposits, which results in the sand body standing in positive relief while the mud of the scroll bar and fluvial channel fill are eroded.

At the finer scale, the muddy laminations between lateral accretion sets also erode, causing a topography reminiscent of the ridges and swales of a scroll bar, though it arises from a different set of processes.

Another uncertainty in interpreting fluvial ridges is the extent to which they are eroded. Erosional modification of ridge geometry has long been noted (Derr, 1974). Ridges on Mars have abundant yardangs and gaps between ridge segments (Burr et al., 2009; 2010). Williams et al. (2009) and Hayden et al. (2019) observed that variability in breadth of ridges in the Cedar Mountain Formation is likely due to erosion. Williams et al. (2009) proposed that using the upper-third-quartile of ridge breadth might compensate for erosion. Hayden et al. (2019) found that ridge caprock breadths were between 0.2-2 times the width of the paleo-channels as reconstructed from sedimentological observations. However, neither study documented the outcrops of uneroded sandstone bodies that are needed to directly constrain the amount or mechanism of narrowing during ridge formation.

To address uncertainties in formation of fluvial sinuous ridges and paleo-hydraulic reconstructions, here we report new observations of fluvial sinuous ridges from the Jurassic Morrison Formation in eastern Utah. We selected sites that showed visible examples of ridges protruding from cliff outcrops, enabling quantification of ridge erosion, and ridges with LAS traces visible from orbital images, enabling an assessment of LAS and ridge curvature as proxies for channel curvature. Terrestrial analogs have been important to the study of fluvial ridges because detailed in situ analyses cannot readily be performed for ridges on Mars. In particular, detailed sedimentological analysis of ridge deposits on Earth has allowed for the assessment of channel inversion versus deposit inversion, and provided a baseline to test paleo-hydraulic reconstruction methods (Hayden et al., 2019; Williams et al., 2009). After describing the study sites in Section 4.2, we discuss our field methods

in Section 4.3, and paleo-hydraulic reconstruction methods in Section 4.4. Section 4.5 presents the field observations, which we use in Section 4.6 to develop and test a scarp-retreat erosion model for ridge narrowing that can be used to reconstruct original channel-belt widths. We also compare the paleo-hydraulic reconstruction methods in Section 4.6, and apply those methods to an example ridge in the Aeolis Dorsa region of Mars.

4.2 Study Site and Background

We studied terrestrial-analog fluvial ridges in the Morrison Formation, southwest Utah. We focused our work on three main sites: the Ferron Creek North (FCN) site in the Brushy Basin Member of the Morrison Formation, and Ferron Creek South (FCS) and Wild Horse Mesa (WHM) sites in the Salt Wash Member of the Morrison Formation (Fig. 4.4). Sites were selected from outcrops of the Morrison Formation around the San Rafael Swell for the prominent ridges with neighboring cliff outcrop exposures (FCN and WHM) or lateral accretion sets (FCS), as observed in aerial images. Most previous work on ridge formation in the area took place nearer to the Green River site in the Cedar Mountain Formation (Cardenas et al., 2020; Hayden et al., 2019; Williams et al., 2007, 2009, 2011). The Cedar Mountain Formation sits directly above the Morrison Formation (Kirkland et al., 1999).

Ridges in the Morrison Formation were first studied by Derr (1974), who used the three-dimensional exposures to study the fluvial structures, interpreting dune trough-cross-strata and point bar strata as deposits from meandering rivers. Derr neglected amalgamation and erosion and, rather than a channel-belt model, assumed that the ridge sandstone caprocks directly represent the paleo-channel width, depth, and wavelength, and used empirical relations from Schumm (1972) to estimate paleo-discharge of 100-1000 m3/s. Williams et al. (2007) and Clarke and Stoker (2011) identified ridges in different parts of the Brushy Basin Member as analogs for ridges on Mars. Williams et al. (2007) observed that ridges in the Morrison Formation comprised point-bar, channel, and overbank

deposits, and noted similarities to fluvial strata and stacked ridges observed on Mars. Clark and Stoker (2011) interpreted an anastomosing river morphology based on ridges to the east of our Wild Horse Mesa site.

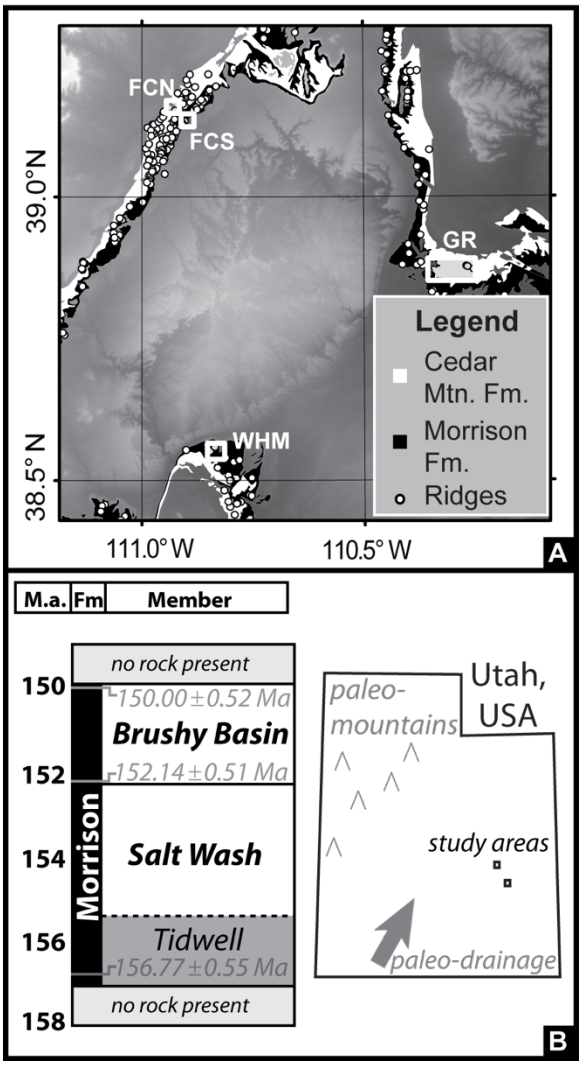

Figure 4.4-- Field area. a. San Rafael Swell, Utah, USA, topography shown in grayscale. The Morrison and Cedar Mountain Formations outcrop around the San Rafael Swell. There are many sinuous ridges throughout the formations; we focus on three sites in this paper (FCN, FCS, WHM). The remaining site (GR) is the Green River site studied by Williams et al. (2007; 2009; 2011), Hayden et al. (2019), and Cardenas et al. (2020). b. Representative stratigraphic section of upper Morrison Formation (dates from Trujillo and Kowallis, 2015) and interpreted paleogeography of the study areas.

The Morrison Formation contains fluvial sedimentary rocks spread across the interior United States, covering Montana, Wyoming, Utah, Colorado, New Mexico, and Arizona, broadly reflecting sediment deposition from the Cordilleran deformation belt (Christiansen et al., 2015; Stokes, 1944; 1961; Fig. 4.4). It contains vertically and laterally amalgamated (i.e., multi-story) fluvial sandstones with nonmarine mudstones and siltstones (Tyler and Ethridge, 1983). Fluvial morphology in some cases has been interpreted as braided based on width-thickness ratios of sandstone bodies, grain size, interpreted sinuosity, interpreted paleoenvironment, and an apparent lack of lateral accretion sets (Chesley and Leier, 2018; Kjemperud et al., 2008; Peterson, 1984; Robinson and McCabe, 1997). However, other workers identified lateral accretion sets and interpreted a meandering planform (Derr et al., 1974; Hartley et al., 2015; Heller et al., 2015).

The Brushy Basin Member is the topmost member of the Morrison Formation in our field area. A nearby stratigraphic section at Little Cedar Mountain indicates 100 m total thickness. Deposition occurred between 152.14-150.00 Ma based on recalibrated ash dates (Trujillo and Kowallis, 2015). Ashes taken from the Brushy Basin Member at other locations have dates ranging from 149.7 to 151.23 Ma (Trujillo and Kowallis, 2015). This member contains paleosols indicating a semi-arid to wet climate (Demko et al., 2004), and ichnofossils indicating that the climate was wetter up section (Hasiotis, 2004). Fluvial morphology of the Brushy Basin has a variety of interpretations (Demko et al., 2004; Galli, 2014; Yingling and Heller, 1992), but most recently Heller et al. (2015) interpreted high channel sinuosities and a meandering river pattern.

The Salt Wash Member underlies the Brushy Basin Member and was formed during a subset of the time between 157-152 Ma (Trujillo and Kowalis, 2015). It represents a fluvial megafan that prograded from the syntaxis of the Mogollon Highlands and the Sevier mountain front (Owen et al., 2015a; Turner and Peterson, 2004; Tyler and Ethridge, 1983). The channel belts are more densely

stacked in the Salt Wash Member than in the Brushy Basin Member, forming larger and more amalgamated sandstone bodies (Heller et al., 2015). Robinson and McCabe (1997) found ratios of sandstone body width, B0, to thickness, T0, ranging from 10 to 70. Owen et al. (2015b) quantified proximal-to-distal trends and found total thickness of the Salt Wash Member decreases from 174 to 40 m, and average channel belt thickness decreases from 15 to 3.8 m. As with the Brushy Basin Member, the Salt Wash Member was interpreted as a braided system (Kjemperud et al., 2008; Peterson, 1984; Robinson and McCabe, 1997), but more recently has been argued to be a meandering system due to the presence of LAS observed from orbital images (Hartley et al., 2015). Chesley and Leier (2018) interpreted small sandstone bodies as crevasse-splay deposits, medium sandstone bodies with LAS as deposits from laterally migrating sand-bedded-river deposits, and large sandstone bodies as amalgamated braided-river deposits on the basis of having amalgamated downstream-accreting bar strata. They also noted that vertically juxtaposed sandstone bodies can have paleo-flow indicators that differ by more than 90o.

4.3 Field methods

We used air photos and digital elevation models (DEMs) to study ridge morphology. Aerial photographs came from the National Agricultural Image Program 2016 dataset at 1 m/px and from our own quadcopter surveys. We used quadcopter images to generate orthorectified images with AgiSoft Metashape at 10 cm/px. Digital elevation models (DEMs) at 50 cm/px were acquired by airborne lidar for the Ferron Creek sites. For the Wild Horse Mesa site, we used a 5 m/px DEM from the Utah Automated Geographic Reference Center. Ridge measurements were made after removing the local tectonic dip (~4° to the WNW for the Ferron Creek sites and 5° to the SW for the Wild Horse Mesa site; Doelling et al., 2015; Witkind, 2004). Ridge centerline elevations, caprock extent, and the edge of talus slope were manually traced in the high-resolution air photos. Axes-perpendicular transects were generated along the ridge centerlines at 50-m spacing. These transects were used to

generate elevation profiles from the DEMs. For each profile, we manually defined the top and bottom of the caprock by slope-breaks bounding the most-vertical portion at the top of the ridge, and defined the base of the talus slope from the air photo (e.g., Figs. 4.5B; 4.17B). Ridge relief (*Z*) for each transect was calculated as the elevation between the base of the talus slope and the base of the caprock, caprock thickness (*T*) was measured as the elevation between the top and bottom of the caprock, and ridge flank slope (*S*) was measured as the angle above horizontal for the line connecting the bottom of the caprock and talus slope (Fig. 4.5). Relief excludes the caprock thickness so they are independent parameters. Ridge breadth (*B*) was measured as the distance along the transect between the caprock boundaries defined from the air photos. Breadth was measured once for each transect, while relief, thickness, and slope were measured once on each side. Ridge centerline radius of curvature (*C*) was taken by visually fitting a circle to the ridge centerline at each bend following the methods of Williams (1986). We measured the radius of curvature of the lateral accretion sets in planview (C_{LAS}) by visually fitting circles to the LAS traces observed in aerial images of ridge tops, taking multiple measurements for each bend segment where multiple LAS were visible.

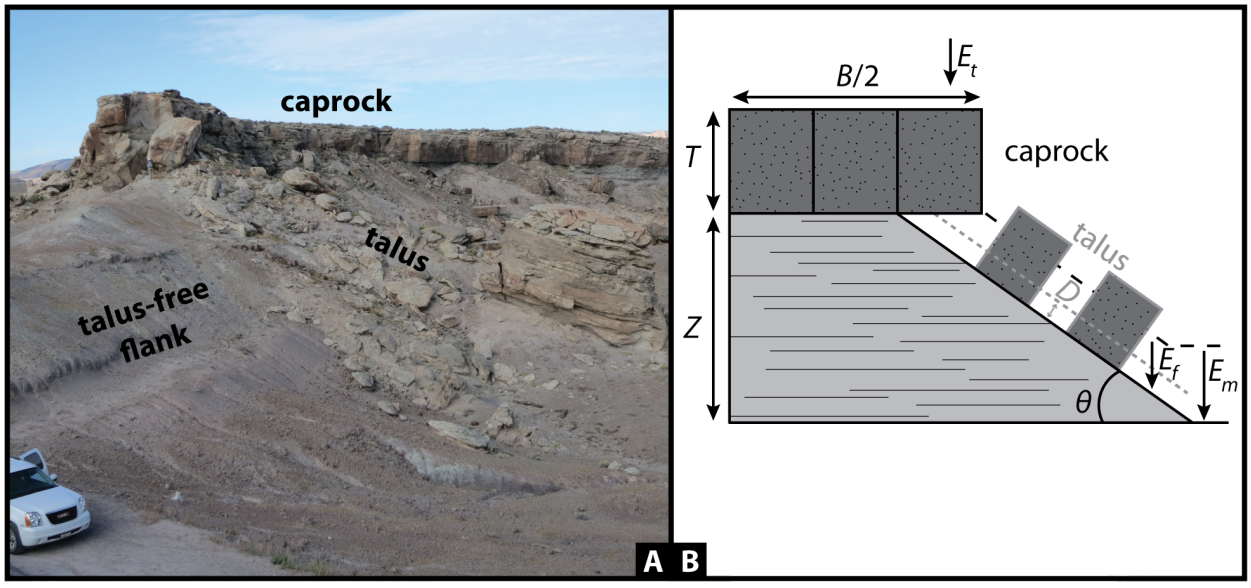

Figure 4.5-- Description of ridge geometry and measurements. **a.** Photo of a ridge in the GR field area. The talus-armored section of the ridge retains caprock while the talus-free section has no

caprock. **b.** Sketch of an idealized ridge of height (Z), caprock thickness (T), breadth (B), and flank slope (θ). In our erosion model (Section 4.6.2), the surrounding plains erode vertically at the rate E_m, the flank erodes vertically at the rate E_f, and there is an average talus thickness, D, on the flank slope.

We made sedimentological observations in the field in vertical sections up the ridges, measuring the thickness of every bed > 2 cm using a ruler, median grainsize (D50) using a sand card, and noting sedimentary structures (Fig. 4.6). For each caprock we calculated the mean grainsize, weighting measurements by the bed thickness. We measured the thickness of sets of cross stratification using a ruler and recorded their accretion direction. Channel deposits in sand-bedded rivers are often organized into channel bars, dunes, and ripples, which all make distinct scales of inclined stratification. Ripple cross-strata are the smallest scale (<2 cm in the field area; Fig. 4.6A). Dune trough cross-strata are often larger (<1 m in our field area) and form trough shapes that are viewed in outcrop as festoon or curving sets (Fig. 4.6B) or in planview as rib-and-furrow structures visible on ridge tops (Fig. 4.6C). We used ripple and dune accretion directions as paleo-current direction indicators (e.g., McLaurin and Steel, 2007; Smith, 1972). We interpreted the largest mode of cross strata as bar clinoforms (Fig. 4.6D). Complete bar strata typically have a sigmoidal shape, but bar strata in our field area are all truncated. Bars can migrate in downstream or cross-stream directions, and bar-scale cross sets indicating cross-stream accretion, e.g., due to point bar growth in a meandering river (Hartley et al., 2015), were interpreted as lateral accretion sets (LAS) (e.g., Fig. 4.3).

We also mapped channel belts exposed in cliff outcrops that were connected to ridges. For these cases, we measured the width and thickness of the channel-belt sandstone body exposed in the cliff exposure using a tape measure or laser range finder, and corrected the measurements to be

perpendicular to the paleo-flow direction for comparison to the eroded widths and thicknesses of the ridges.

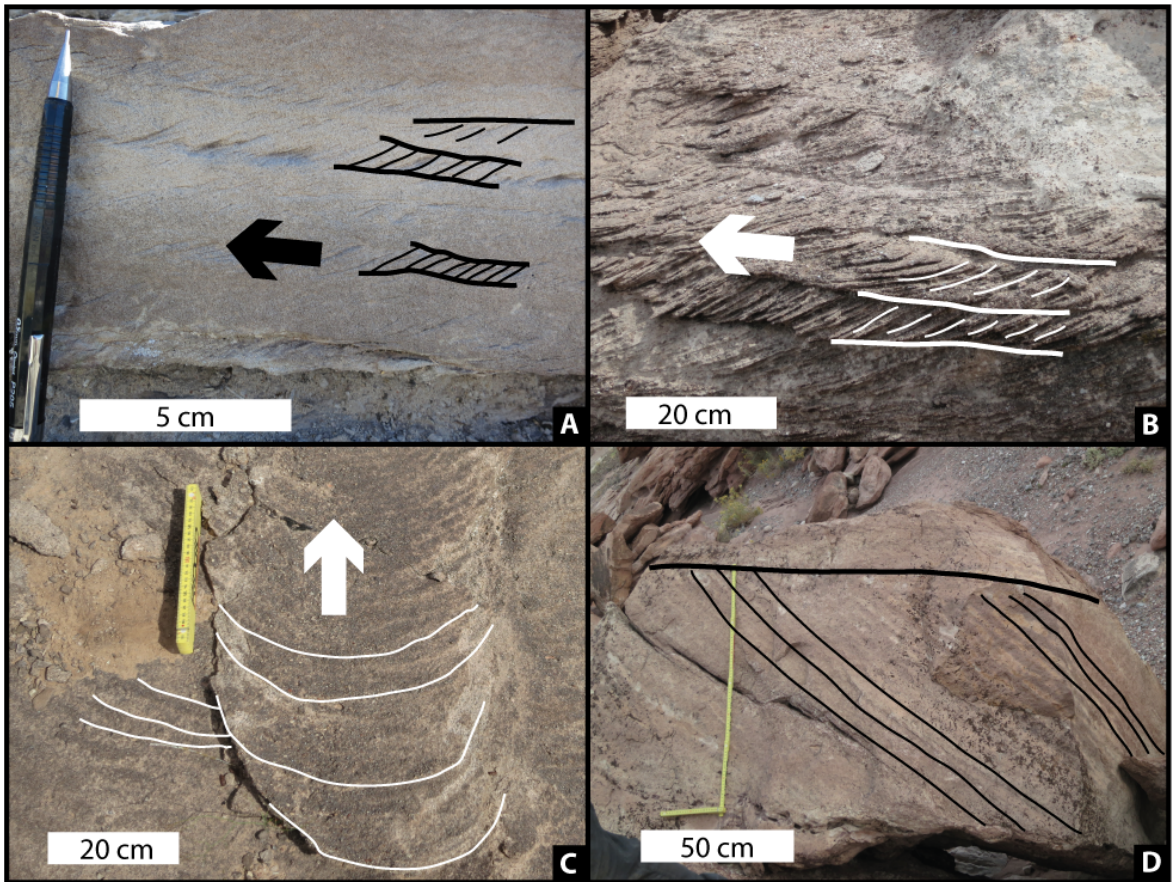

Figure 4.6-- Examples of sedimentary structures observed in the field sites, arrows indicate paleo-flow direction interpreted from accretion direction when applicable. a. Ripples in Ferron Creek North; b. Truncated dune cross-strata in Ferron Creek North. c. Rib-and-furrow structures (planview expression of dune trough cross-strata); d. Truncated bar clinoforms in Ferron Creek North.

4.4 Paleo-hydraulic methods

We used classic methods in sedimentology to reconstruct likely channel dimensions for the Morrison ridges, following Hayden et al. (2019), and we compared the results to methods based on ridge geometry. The ridge geometry methods we evaluated included relating caprock thickness to paleo-channel depth (DiBiase et al., 2013; Hayden et al., 2019), and relating ridge caprock breadth to paleo-channel width (Burr et al., 2010; Kite et al., 2015; Williams et al., 2013). We also evaluated

using the radius of curvature of the ridges and of exposed LAS surfaces, which, along with ridge wavelength, have been used extensively on Mars (Burr et al., 2010; Goudge et al., 2018; Kite et al., 2015; 2019; Moore et al., 2003; Williams et al., 2013).

4.4.1 Paleo-hydraulics from sedimentary structures

We consider the sedimentology paleo-hydraulic reconstruction to be the most accurate, because it has been well tested and used for decades (Allen, 1965; Hajek and Heller, 2012; Mohrig et al., 2000). Following Hayden et al. (2019), this method uses cross-stratification from bar clinoforms (Fig. 4.6D) or dune cross-strata (Fig. 4.6B) as indicators of bankfull channel depth. Bars are the preferred depth indicator because, where bar strata are not truncated by subsequent erosion, the bar clinoform thickness (t_b) is approximately equal to the bankfull channel depth (d) (Hajek and Heller, 2012; Mohrig et al., 2000):

$$d/t_b = 1. \quad \text{Eq. 4.1}$$

Mohrig et al. (2000) found bounds on Eq. 4.1 of 0.3-2.5 for individual measurements from the modern North Loup River, so we estimate that the uncertainty on the mean of a suite of measurements is a factor of two.

Dunes also scale with flow depth (Bradley and Venditti, 2017); however, dune cross-strata are typically truncated by erosion from later generations of dunes, leaving dune set thicknesses (t_d) that are a fraction of the original dune heights (Leclair and Bridge, 2001; Paola & Borgmann, 1991). Combining the mean relationship between dune height and channel depth for small rivers (d is 3.5 times dune height with a range of 2.1-9.9, for $d < 2.5$ m) of Bradley and Venditti (2017) with the mean relationship between truncated dune set thicknesses and original dune heights (dune heights are 2.9 times t_d with a range of 2.2-3.6) from Leclair and Bridge (2001), we found

$$d/t_d = 10.2 \text{ (bounds: } 4.7 - 18.7). \quad \text{Eq. 4.2}$$

Using the small-river data of Bradley and Venditti (2017) is consistent with flow depths we interpret from the bars in our field area.

In addition to channel depth, the other parameters needed to calculate water discharge (Q) are channel width (w) and mean flow velocity (U), following mass balance (i.e., $Q = wdU$). Single-thread rivers tend to all have similar width-depth ratios, and we used the median and 5th-95th percentile range of the Trampush et al. (2014) global compilation of bankfull geometry as:

$$w/d = 18 \text{ (bounds: 8.4 - 53).} \quad \text{Eq. 4.3}$$

Width-depth ratios for braided rivers are higher than for single-thread rivers (e.g., van den Berg, 1995), so Eq. 4.3 underestimates width for braided paleo-channels.

To get flow velocity (U), we used the flow resistance method of Engelund and Hansen (1967) that is based on partitioning hydraulic roughness in sand-bedded rivers between the bed sediment (skin friction) and drag from bedforms (Einstein, 1950):

$$U = \frac{1}{\kappa}\ln\left[11\frac{RD_{50}}{Sk_s}\tau_{*s}\right](RgD_{50}\tau_{*s})^{0.5}, \quad \text{Eq. 4.4}$$

where $\kappa = 0.41$ is von Karman's constant, R is the submerged specific density of the sediment (R = 1.65 for quartz in water), D_{50} is the median grain size, S is the bed slope, $k_s = 2.5D_{50}$ is the grain roughness lengthscale, and g is the acceleration of gravity. τ_{*s} is the skin friction component of the Shields stress calculated from $\tau_{*s} = 0.06 + 0.4\,\tau_*^2$ (Engelund and Hansen, 1967), where τ_* is the total Shields stress ($\tau_* = dS/RD_{50}$ assuming steady and uniform flow). In paleo-hydraulic applications where slope is not known *a priori*, τ_* can be calculated from the empirical Trampush et al. (2014) relationship recommended by Hayden et al. (2019):

$$\tau_* = 17\,Re_p^{-0.5}, \quad \text{Eq. 4.5}$$

where Re_p is the particle Reynolds number $Re_p = (RgD_{50})^{0.5} D_{50}/\nu$, and ν is the kinematic viscosity of water. Slope is then obtained from Eq. 4.5 and the normal-flow approximation. Combining these equations gives an expression for bankfull river discharge (Hayden et al., 2019):

$$Q = 74.2\, C_f^{-1/2} (Rg)^{3/8}\, \nu^{1/4} D_{50}^{1/8} d^2, \qquad \text{Eq. 4.6}$$

where $C_f = U_*^2/U^2$ is the friction coefficient, $U_*^2 = \tau_*/RgD_{50}$ is the shear velocity and U can be computed from Eq. 4.4 following the method of Engelund and Hansen (1967). To use Eq. 4.6, there are two inputs from field measurements: flow depth constrained from dune or bar cross strata (Eqs. 4.1 and 4.2), and median grain size.

The major source of uncertainties in applying Eq. 4.6 are in the reconstructions of paleo-channel depth (factor of 2 from Eqs. 4.1 or 4.2), channel width (factor of 2.5; Eq. 4.3), and bed shear velocity (factor of 5 uncertainty from Eq. 4.5). Combining these factors with Gaussian error propagation assuming log-normal distributions on each parameter, we estimate uncertainty on Eq. 4.6 to be a factor of 9. Despite high uncertainty, we prefer this physics-based method to prior empirical methods, such as scaling channel width to discharge (e.g., Williams, 1988), because it identifies all important variables and explicitly accounts for material properties and gravity that may be different on Mars.

4.4.2 Ridge caprock thickness as a proxy for channel depth

In addition to the sedimentology method (Section 4.4.1), we evaluated paleo-hydraulic tools to estimate channel size and discharge based on ridge properties alone, since ridge bar and dune strata cannot readily be observed on Mars from orbit. Hayden et al. (2019) proposed that caprock thickness for fluvial ridges can be used as a proxy for bankfull paleo-channel depth due to the tendency of a channel to abandon its course after aggrading by an amount that scales with channel depth (Bryant et al., 1995; Ganti et al. 2014a, b; 2016; Hajek and Wolinsky, 2012; Jerolmack and Swenson, 2007;

Mohrig et al., 2000; Slingerland and Smith, 2004). Erosion and amalgamation by subsequent re-occupations of the same channel position can modify the relation to channel depth, but Hayden et al. (2019) found tight constraints on the relationship between caprock or channel-belt thickness (T) and paleo-channel depth (d) using a compilation of channel-belts worldwide and ridges in the Cedar Mountain Formation,

$$T/d = 1.5 \text{ (5}^{\text{th}}\text{-95}^{\text{th}}\text{ percentile bounds: 0.8-4).} \quad \text{Eq. 4.7}$$

Eq. 4.7 can be used in conjunction with Eq. 4.6 to calculate discharge in the absence of constraints on dune or bar cross strata thicknesses. The bounds on Eq. 4.7 yield a similar level of uncertainty (factor of ~2) as Eqs. 4.1 and 4.2. If grainsize is also unknown, as is the case for most ridges on Mars, end-member sand- and gravel-bedded scenarios can be used. Due to the low power on D_{50} in Eq. 4.6, the discharge varies by a factor of only 1.9 across the two dominant modes in D_{50} observed on Earth: medium sand (0.3 mm) and medium gravel (50 mm) (Trampush, et al., 2014). We view all grainsizes within this range as equally likely, so we take the geometric mean of the bounds (3.9 mm) as a central estimate for Eq. 4.6. The uncertainty in using Eq. 4.6 with unknown grainsize therefore is the product of uncertainty in Eq. 4.6 and uncertainty in grainsize around the central estimate (1.4; from $\sqrt{1.9}$) — a factor of 12.

4.4.3 Radius of curvature of ridges and lateral accretion sets

Median radius of curvature (C) of multiple channel bends scales with channel width for meandering rivers (e.g., Hickin, 1978; Nanson, 1980; van de Lageweg et al., 2014). The relationship commonly used comes from Williams (1986, 1988),

$$w = 0.71\, C^{0.89}. \quad \text{Eq. 4.8}$$

Assuming channel inversion, Eq. 4.8 (or a similar one relating width and planform wavelength) has been applied to ridges on Mars when ridge centerlines are interpreted to reflect paleo-channel

channel centerlines (e.g., Burr et al., 2009; Jacobsen and Burr, 2018; Jerolmack et al., 2004; Moore et al., 2003).

For exhumed and eroded channel-belt deposits, it is unlikely that ridge centerlines track paleo-channel centerlines. Instead, the radius of curvature of lateral accretion sets, where observed, should be a better representation of the curvature of the inner bank of a channel (i.e., $C_{inner} = C_{LAS}$). To apply Eq. 4.8 to channel-margin curvature, we fitted a power law to the original Williams (1986; Table 1) data (widths: 10^0-10^3) between channel width and the radius of curvature of the inner bank. We estimated the radius of curvature of the inner bank as $C_{inner} = C - w/2$ under the assumptions that the banks are parallel to the centerline and the bend can be represented as part of a circle. The exponent was within a standard deviation of one, so we forced it to one to make the equation dimensionally correct, and found

$$w = 0.5\, C_{inner}. \qquad \text{Eq. 4.9}$$

Goudge et al. (2018) assumed the same relation in reconstructing paleo-channel width at Jezero Crater from LAS traces.

To find discharge using curvature of the ridge centerline or LAS as constraints, we used Eqs. 4.8 or 4.9 to estimate channel width, Eq. 4.3 to calculate channel depth, and then used depth to find discharge using Eq. 4.6, assuming a range in possible D_{50} as described in Section 4.4.2. We estimate uncertainty on Eqs. 4.8 or 4.9 as similar to that on Eqs. 4.1, 4.2, or 4.7 (factor of 2), so the total uncertainty in reconstructing discharge from curvature is also interpreted to be 9 or 12 for known or unknown grainsize, respectively.

4.4.4 Ridge Width

Ridge width has been used in the past to directly infer channel width (e.g., Burr et al., 2010; Kite et al., 2015). However, more recently this proxy was evaluated extensively by Hayden et al. (2019) and they showed that ridge width can deviate significantly from channel widths (by factors

>30) if ridge caprocks are channel-belt sandstones that have been built through lateral accretion and amalgamation, and later narrowed by erosion during exhumation to form a ridge. The controls on ridge width narrowing due to erosion is a topic we revisit herein in the Morrison Formation for ridges that can be traced into cliff-outcrop exposures where the uneroded channel belt can be observed (Section 4.6.2).

4.5 Results

4.5.1 Ferron Creek North

The Ferron Creek North site contains seven ridges in the Brushy Basin Member, and is notable for the five ridges (Ridges A, B, E, F, and G) that extend into cliff outcrops where the non-exhumed sandstone bodies are exposed in full cross sections (Figs. 4.7A, 4.7B). The ridges are composed of sandstone caprocks 1-6 m thick and 9-30 m wide that all overlie mudstone. The tectonic-dip-corrected digital elevation model (Fig. 4.7A) shows the caprocks are at four stratigraphic levels: Ridge A is above Ridge B, which in turn is above Ridges C and D, and Ridges C and D are above Ridges E, F, and G (Figs. 4.7B, 4.7C). Field observations at ridge crossings confirm these relationships; there are mudstones that separate the sandstone caprocks of crossing ridges indicating that the sandstone bodies are at distinct stratigraphic levels (Figs. 4.8, 4.9). Best-fit caprock slopes running along the ridges, after removing tectonic tilt, range from 10^{-5}-10^{-2} (Fig. 4.7C), and all ridges have relief 2-10 m above the surrounding terrain (Fig. 4.7D; SI Table 1). The slopes of individual flanks range 1-70°. Ridges only have a few bends, and the radius of curvature for ridge centerlines range from 40-100 m for Ridges A, B, and E (Fig. 4.7B).

Caprocks are composed of medium sandstone with cross stratification (Fig. 4.6). Dune cross strata, identified by their height and trough shape in cross section and rib-and-furrow structure in planview, ranged in height from 10-40 cm and indicated flow directions that generally paralleled the

local ridge axes (Fig. 4.7A). One structure in Ridge B was 1 m in height, had an accretion direction perpendicular to the ridge axis, and had planar cross strata, so it was interpreted as a laterally accreting bar (Fig. 4.7A). A similar structure was observed on the edge of Ridge A. Mudstones underlie all caprocks, and contain sparse, thin sandstone beds with thicknesses ranging from 1 to 50 cm (Figs. 4.8, 4.9).

Based on similar elevations (Fig. 4.7C), caprock thicknesses (Fig. 4.7D), and paleo-flow directions (Fig. 4.7A), we interpret the caprocks of Ridges C and D to be segments of the same sandstone body. Similarly, we interpret Ridges E-F-G to be segments of the same sandstone body.

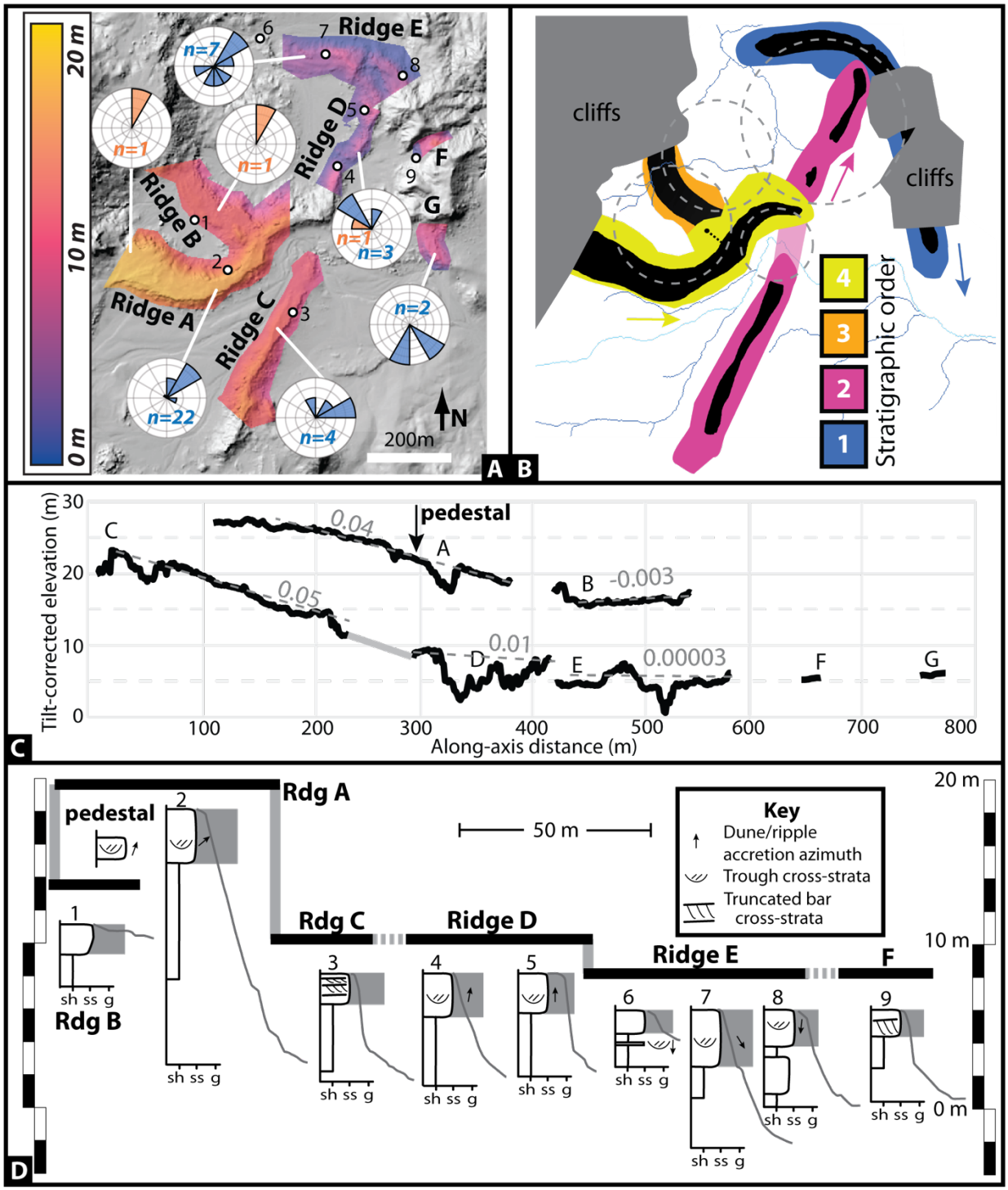

Figure 4.7-- Ferron Creek North (FCN) site. **a.** Map of field area with each ridge highlighted; colors represent height in stratigraphic models (DEM rotated to remove tectonic dip). Colored regions highlight ridge caprocks and flank slopes. Numbers are stratigraphic sections. Rose diagrams represent accretion direction of bar sets (red) and paleo-flow directions interpreted from dune trough cross-stratification (blue) within the ridge caprocks; *n* is the number of observations made along the ridge caprock. Background image is the hillshade of the lidar DEM. **b.** Interpretation of ridge

superpositions shown in panel A, with same scale. Ridge caprocks are indicated in black, ridge flanks are indicated in dark colors, semi-transparent portions indicate interpreted ridge connections. Interpreted paleo-flow direction indicated in a colored arrow next to the ridge. Modern washes given in branching blue networks. Black dot connected by a dotted line to the yellow ridge (Ridge A) is the pedestal described in the text. Gray dashed circles are the locations where radius of curvature of the centerline was measured. **c.** Elevation profiles along ridge axes corrected for tectonic tilt, with the caprock top given in black lines, interpreted connections given in gray lines. Dashed gray lines indicate best-fit topographic slope. **d.** Representative stratigraphic sections (numbers indicate location on panel A; shale, sandstone, and gravel indicated by sh, ss, g, respectively), with cross-stratification noted. Also included (thick gray, sloping lines) are the cross-sectional profiles off the side of the ridge; note that for many of them, there is a break in slope coincident with caprock though in other places the slope break is less obvious due to erosion and talus accumulation (Figs. 4.8, 4.9). Vertical exaggeration ~5x; scale bar only applies to topographic transects in this panel. Lines at the top highlight caprocks of similar stratigraphic position; black solid lines are on the same ridge, gray dotted lines indicate an interpreted tie line.

Ridge A extends from the large cliff on the northwest of the field area allowing direct observation of the equivalent material that surrounded the ridge and was removed during exhumation (Fig. 4.8). At the cliff face, the sandstone body that composes the ridge caprock is uneroded, 100 meters wide, and 4 meters thick. At the edge of the sandstone body, we observed thickening and subsequent thinning of the sandstone, which we interpret as levees, with internal S-shaped stratification that we interpret as bar clinoforms. Thin sandstone beds, or wings (Mohrig et al., 2000), thin away from the core of the body (Fig. 4.8) and interfinger into the neighboring mudstone. The wing sandstone beds contain climbing ripple strata, indicating paleo-flow away from the sandstone body. This geometry matches observations of other channel belts in which the wings formed from overbank deposition (e.g., Chesley & Leier, 2018; Mohrig et al., 2000). From the cliff exposure to the ridge terminus 170 m from the cliff, ridge breadth decreases from 100 m to 10 m, ridge relief increases from 0 to 13 m, mean ridge flank slope increases from non-existent to a final value of 29°, and caprock thickness remains approximately constant at 3-4 m (Fig. 4.8E). From comparison to the cliff outcrop exposure, most of the ridge is composed of only the center of the sandstone body; the neighboring mudstone, thinner sandstone wings, and margins of the sandstone body have been completely eroded away during ridge formation. Blocks of the sandstone body now make up talus

on the ridge flank (Fig. 4.8). Further support for the interpretation of ridge narrowing comes from a pedestal of mudstone with a 70-cm thick sandstone block at the top, located 20 m to the side of the Ridge A (Fig. 4.8B). The pedestal sandstone body is of comparable thickness, at the same stratigraphic level, and contains similar sedimentary structures and paleo-current directions as the caprock of Ridge A (Fig. 4.7). Thus, we interpret the pedestal sandstone to be a remnant of the once much wider former extent of the Ridge A caprock sandstone body (Figs. 4.8B, 4.8E).

Ridge B also emerges from the large cliff, and its other end terminates under Ridge A (Fig. 4.8). The ridge-capping sandstone body is widest at these outcrops (60 m) and narrows away from the outcrops (to 30 m). Thickness varies between 3-5 m and is uncorrelated with distance from the outcrops. Similar to Ridge A, the sandstone body at Ridge B, where fully preserved at the outcrops, has thin sandstone wings with climbing-ripple cross stratification indicating paleo-flow away from the caprock (Fig. 4.8). The wings and channel-body margins are not preserved in the middle of the ridge.

The capping sandstones for Ridges E, F, and G also are fully exposed in cliff outcrops (Fig. 4.9). In cliff exposures, we measured the width of Ridge E to be 30 meters, and observed Ridges F and G to have two sets of wings that align with two stacked sets of ~1 m thick LAS in the channel-body (Fig. 4.9B). Importantly, the escarpment erosion around Ridge F allows observations of the finite width of the caprock sandstone body, and the lateral transition to floodplain facies (Fig. 4.9B).

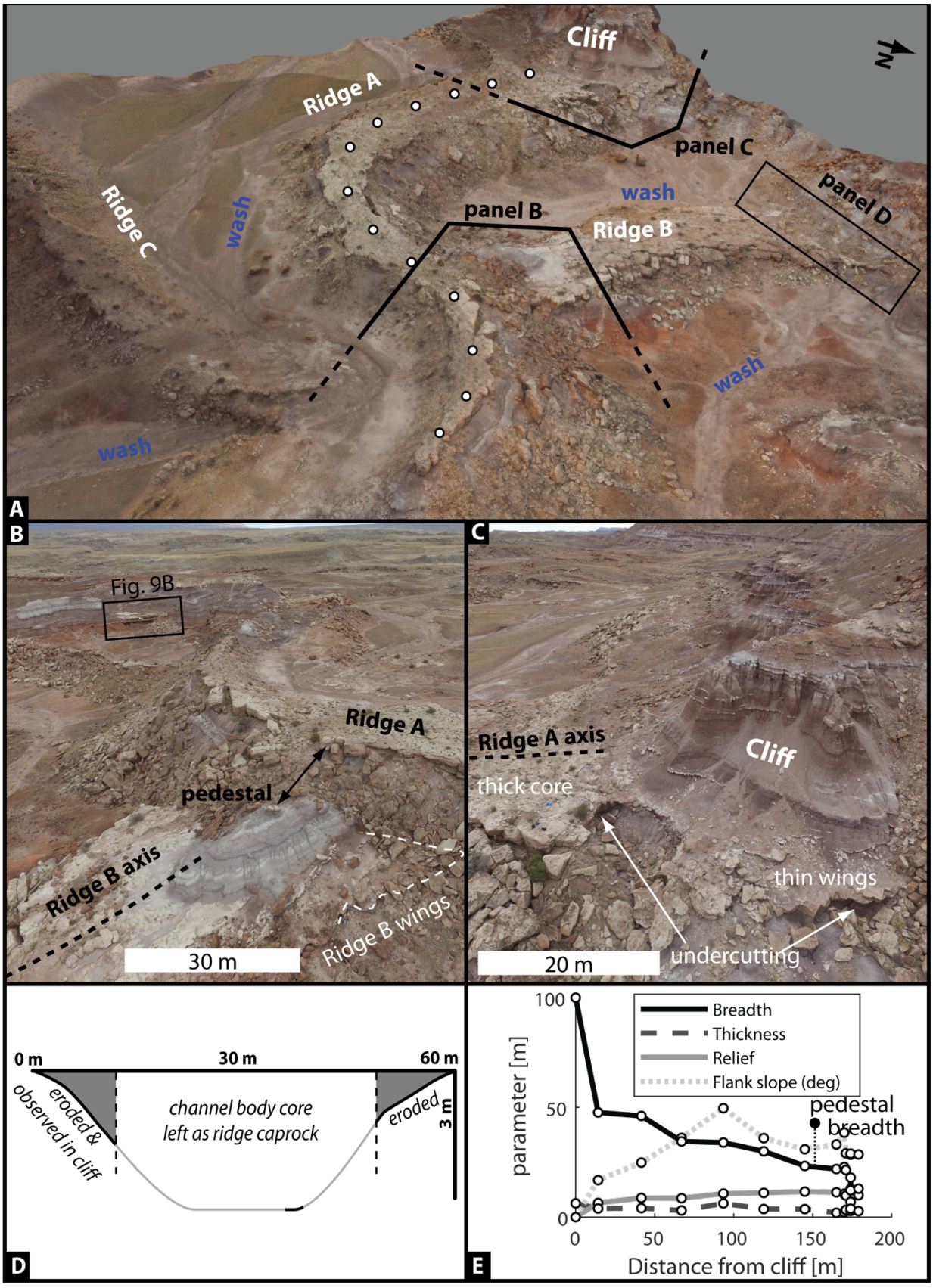
A
Cliff
Ridge A
panel C
Ridge C
wash
panel B
wash
Ridge B
panel D
wash
wash
N
B
Fig. 9B
Ridge A
pedestal
Ridge B axis
Ridge B wings
30 m
C
Ridge A axis
Cliff
thick core
thin wings
20 m
undercutting
D
0 m
30 m
60 m
eroded & observed in cliff
channel body core left as ridge caprock
eroded
3 m
E
100
50
0
parameter [m]
Breadth
Thickness
Relief
Flank slope (deg)
pedestal breadth
0
50
100
150
200
Distance from cliff [m]

Figure 4.8-- Ridge A exemplifies many of the characteristics we observe for ridges throughout the field site. **a.** Oblique view of Ferron Creek North site in 3D model created in Agisoft Metashape from quadcopter photos (view to southwest from near stratigraphic section #4 on Fig. 4.7A). Ridge A is widest near the cliff (top of the panel) and narrows further away until there is no ridge caprock left (bottom of the panel). White dots indicate data positions for panel (e). **b.** Quadcopter photo looking NE from near #1 on Fig. 4.7A, showing that Ridge A superposes Ridge B with mudstone between them and significant talus cover on the flanks. There is a remnant pedestal located 20 m to the side of Ridge A. Ridge B has wings that can be observed in the mudstone under the caprock of Ridge A. **c.** Quadcopter photo looking perpendicular to the axis of Ridge A from near #1 on Fig. 4.7A, showing thin wings on the side of the ridge that can be observed in the cliff. The thin wings are eroded along the rest of the ridge, leaving only the thicker central core. **d.** Reconstructed geometry of the uneroded caprock for Ridge B based on observations made of exposures of the wings, and within cracks in the caprock that allow us to sample the caprock thickness (black line in lower right corner). Black outlines are observed thicknesses, gray outlines are inferred. **e.** Geometry of FCN Ridge A as a function of distance from the cliff exposure where it is uneroded. The pedestal is the caprock remnant to the north of Ridge A (panel B), and the breadth indicated by that point on the figure indicates the width of Ridge A if it extended to the pedestal.

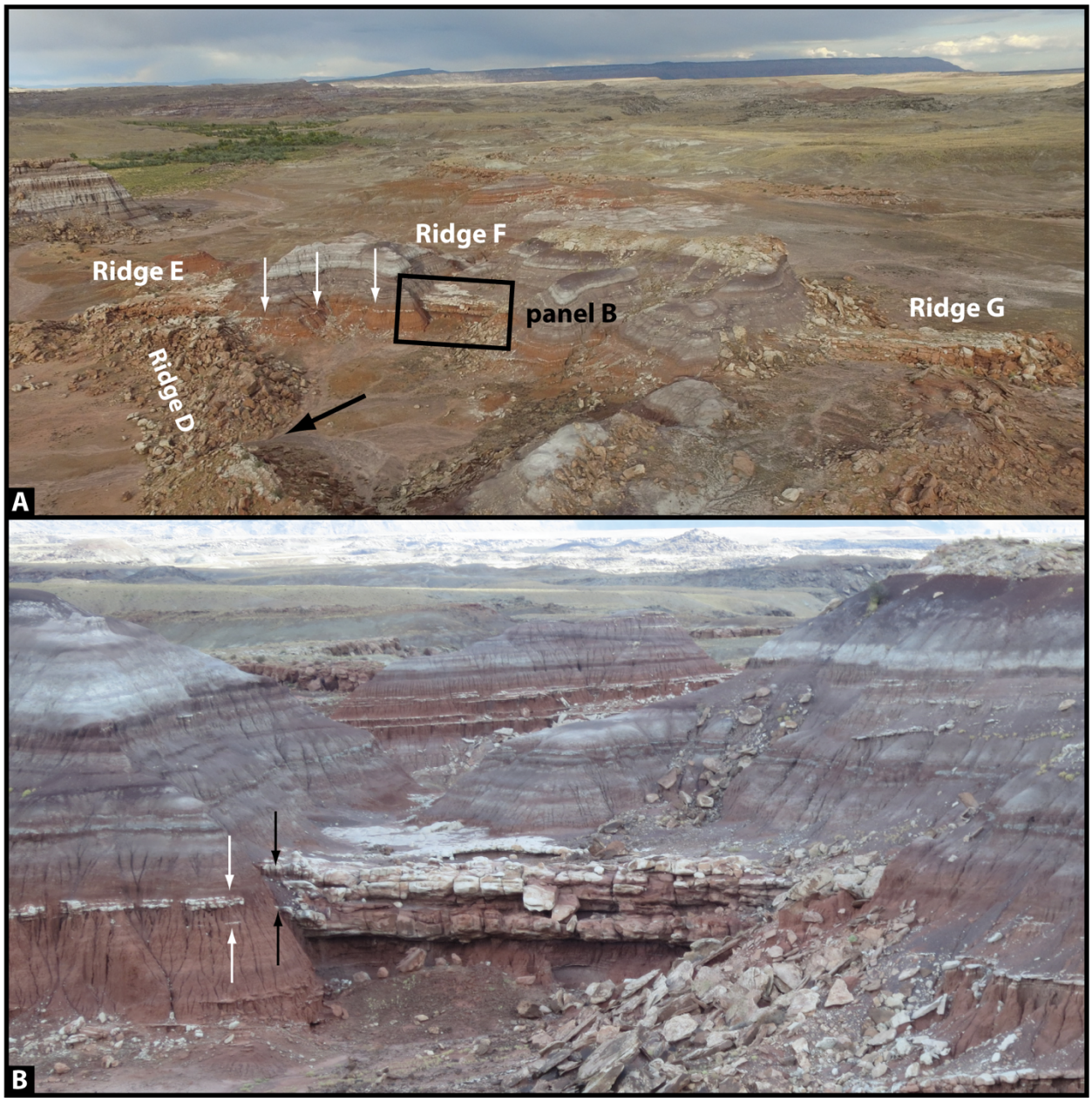

Figure 4.9-- Quadcopter photos of Ferron Creek North looking northeast to Ridges D-G. **a.** Ridges E, F, G all emerge from a series of cliffs, indicating they are exhumed from the mudstone and likely represent a single continuous channel body. The mudstone cliffs with only minimal sandstone visible demonstrate that the channel body is laterally narrow. White arrows trace the upper white sandstone layer shown in panel B. Black arrow indicates where Ridge D is segmented by a wash, with the caprock remnants collapsed into the wash. **b.** Looking east at Ridge F, emerging from two cliffs. Paleo-flow in the channel body is to the right on the image. Note that the channel body, while eroded and undercut in the image center, likely did not extend much farther towards the foreground because the caprock thins significantly from the black arrows to the thin "wing" sandstone sheets given by white arrows over < 10 m lateral distance.

Other indicators of erosion include recessive erosional niches in the mudstone underlying ridge caprocks (Figs. 4.8, 4.9), and abundant talus on flank slopes made up of blocks of caprock sandstone (Figs. 4.8, 4.9). Caprock tops exhibit rib-and-furrow structures and caprock sides exhibit cross-strata, indicating that erosion has removed some material vertically and laterally. Caprock sandstone bodies are > 1.5 meters thick (Fig. 4.7D), suggesting thinner sandstone bodies are more rapidly eroded during exhumation. Finally, we note the presence of numerous washes that tend to flow alongside the ridges. In some cases, washes cross ridges and erode them: Ridge D has been segmented by a wash (note the missing caprock in Figs. 4.7B, 4.9A), and Ridges B and C have washes crossing them (Fig. 4.7B).

4.5.2 Ferron Creek South

The Ferron Creek South site contains three ridge segments in the Salt Wash Member, and is notable for lateral accretion sets (LAS) visible in planview (Ridge B; Figs. 4.10, 4.11). Two shorter ridges (A & C) cross over a longer one (B), and the tilt-corrected elevation model shows that Ridges A & C are at a similar stratigraphic position, about 3 meters higher than Ridge B (Figs. 4.10A, 4.10B). Field observation indicates mudstone between the caprocks of Ridge B and the overriding Ridges A and C (Fig. 4.11D). Based on similar elevations (Fig. 4.10C), caprock thickness (Fig. 4.10D), and paleo-flow directions (Fig. 4.10A), we infer that Ridges A and C are part of the same sandstone body (Fig. 4.10B).

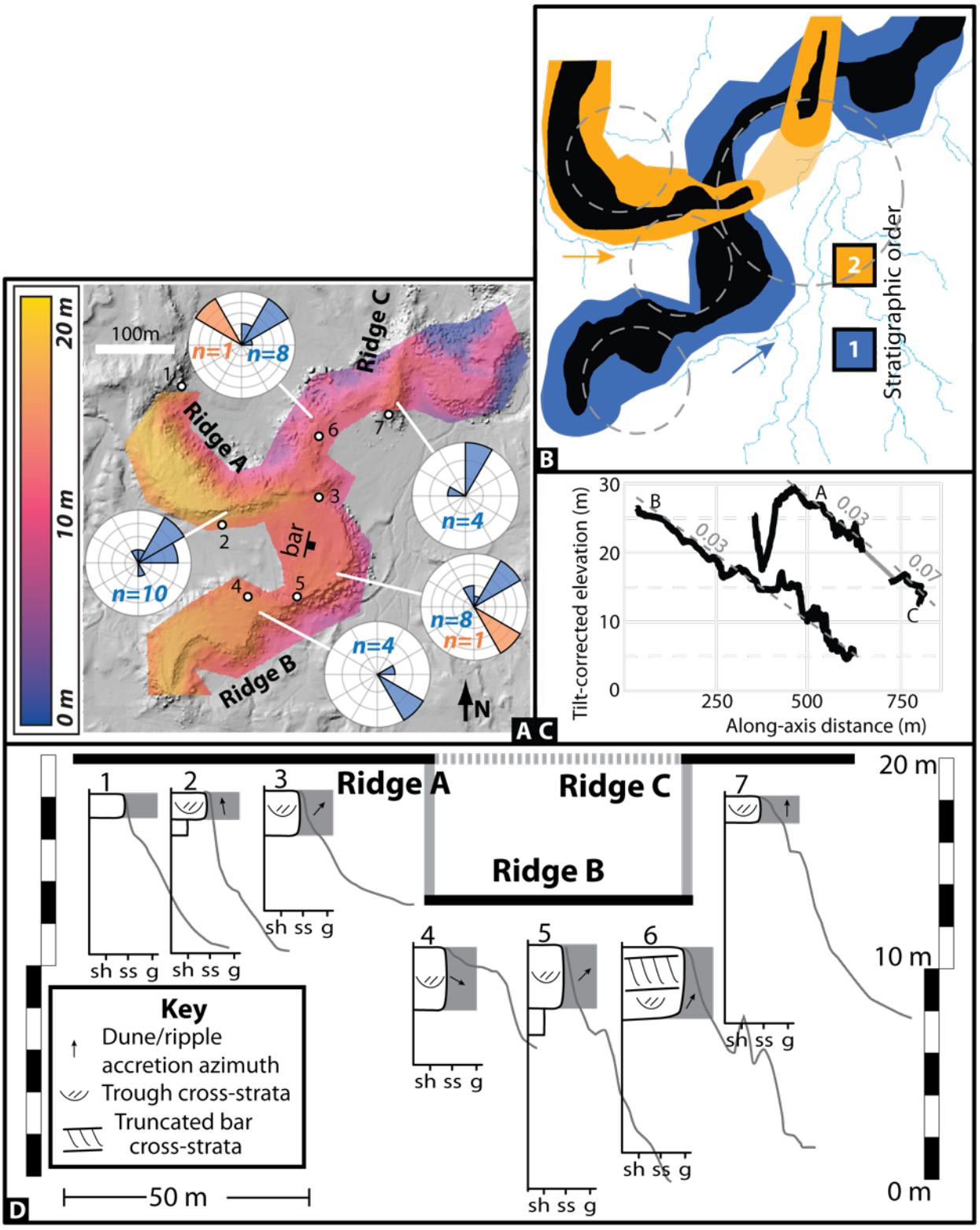

Figure 4.10-- Ferron Creek South site. **a.** Lidar digital elevation map: colors represent height in the stratigraphic model (DEM rotated to remove tectonic dip) and colored regions include the ridge caprock and the flank slopes. Numbers are stratigraphic sections (shown in panel D). Rose

diagrams represent accretion direction of bar sets (red) and dune trough cross-stratification (blue). **b.** Interpretation of stratigraphic positions of ridges, shown at same scale as panel (a). Ridge caprocks are indicated in black, ridge flanks are indicated in dark colors. Interpretations of ridge connections in transparent colors. Interpreted paleo-flow indicated in a colored arrow next to the ridge it represents. Modern washes are given in branching blue networks. Gray dashed circles are the locations where radius of curvature of the centerline was measured. **c.** Ridge elevation profiles taken from the dip-corrected DEM along each ridge top centerline (black lines). Gray line indicates inferred connection between Ridges A and C. Dashed gray line indicates best-fit line used to calculate ridgetop slope. **d.** Representative stratigraphic sections (numbers indicate location on panel A; shale, sandstone, and gravel indicated by sh, ss, g, respectively), with cross-stratification noted. Thick gray, sloping lines are the elevation profiles off the side of the ridge. Vertical exaggeration ~5x; scale bar only applies to topographic profiles (gray lines) in this panel. Bold black horizontal lines show interpreted stratigraphic position and gray dotted lines represented interpreted tie lines between ridges.

Best-fit caprock slopes range 0.03-0.08 after removing tectonic tilt, relief ranges from 4-14 m, and caprock thickness varies from 1.5-8.4 m (Fig. 4.10C, 10D; SI Table 1). Caprock breadth varies from 10-70 m, with variation dominated by a periodic widening at portions that exhibit lateral accretion sets with narrowing between those locations (Figs. 4.10A, 4.10B). Radius of curvature of ridge centerlines varies from 90-170 m at different bends. For Ridge FCS-B, the LAS traces have radii of curvature from 65-140 m so are slightly smaller than the curvatures of the caprock centerline (individual ridge bends have radii of curvature between 120-500 meters).

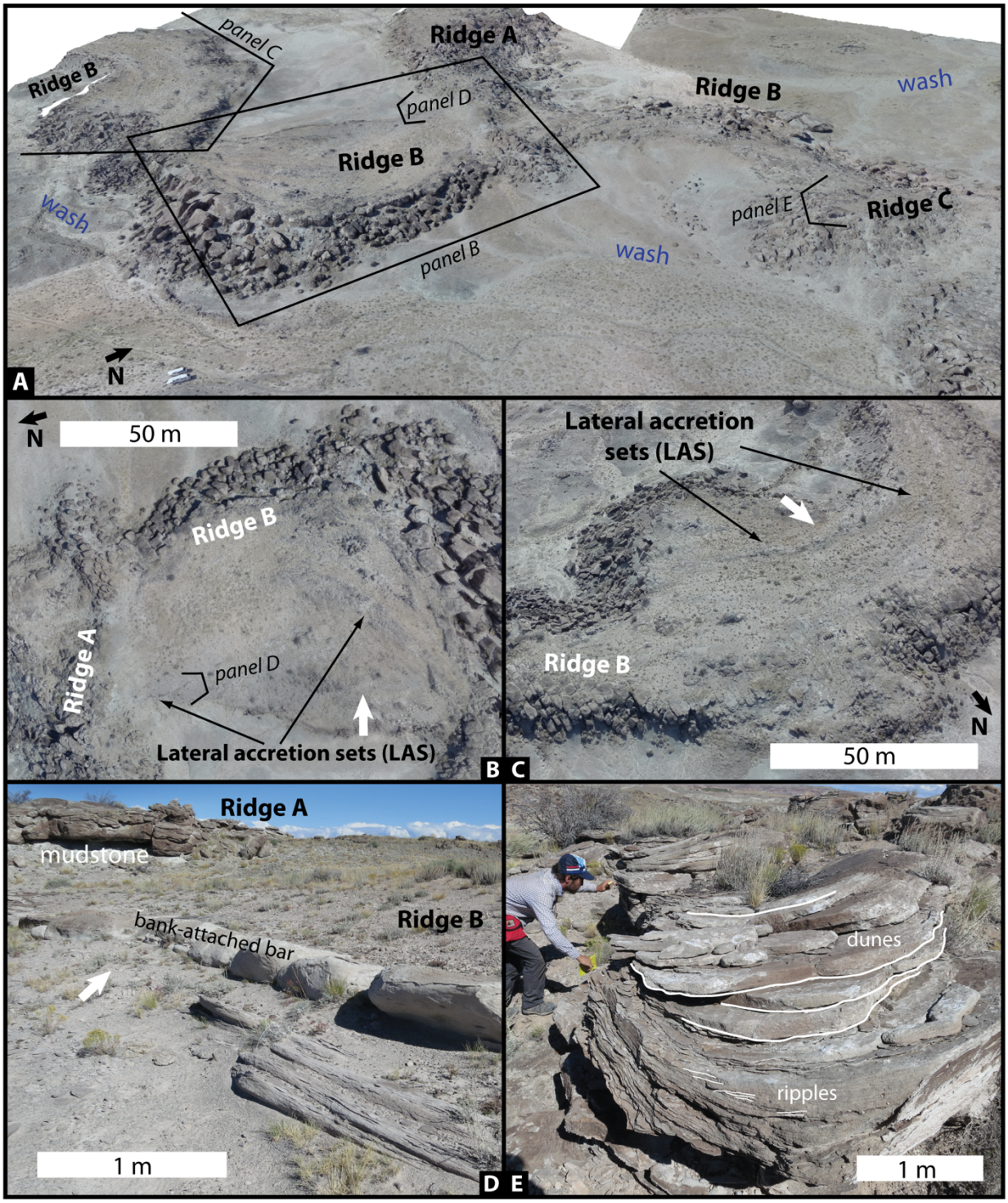

Figure 4.11-- Field photos of Ferron Creek South site. **a.** 3D model of the field site made in Agisoft Metashape from quadcopter photos. View is to the southwest, field vehicles in the lower left for scale. All ridges have talus-covered flanks. Ridge B contains lateral accretion sets, interpreted as a point bar. Locations of other panels are shown. **b**. 3D model zoomed in on Ridge B, showing a closer view on some of the curving lateral accretion sets, with an accretion direction indicated by the white arrow. Location of panel D is shown. **c**. Oblique quadcopter view of another portion

Ridge B, showing lateral accretion sets with an accretion direction indicated by the white arrow. **d.** Image on the top of Ridge B, showing eroded, outcropping, planar beds that make the LAS traces observed from areal imagery. LAS accretion directions (white arrow) are perpendicular to the paleo-flow direction inferred from superimposed dune-scale trough cross strata (Fig. 4.10A), consistent with point-bar strata. Ridges A and B are separated by mudstone (upper left of the left panel). **e.** Dune sets with internal ripples on Ridge B; view towards the northeast.

The caprocks are made up of medium sandstone, with some gravel up to 1 cm diameter observed in Ridge B. Several types of inclined stratification were observed (Figs. 4.6C, 4.10D, 4.11). Dune trough cross-sets were observed to be 10-40 centimeters in height, and in some cases contained ripple cross-strata (Fig. 4.11E; SI Table 2). The dune sets had accretion directions indicating paleo-flows in similar directions to the ridge axes (Fig. 4.10A). Unlike Ferron Creek North, channel-belt wings were not observed at Ferron Creek South, nor were cliff exposures available to verify original sandstone body thicknesses. Instead, this site showed abundant large (>1 m thick), planar sets of inclined strata that extended laterally for tens of meters, with accretion directions approximately perpendicular to inferred paleo-flow direction from dune cross strata (Figs. 4.10A, 4.11D). We interpreted the larger, planar sets as resulting from bank-attached laterally accreting point bars (i.e., LAS). Field observations show that the semi-concentric curved lines visible from orbital images are traces of LAS beds as they intersect the eroding land surface (Figs. 4.11A, 4.11B, 4.11C). The inclined beds are up to 20 cm in thickness, and tend to erode along bedding planes, such that individual beds make small ridges that protrude from the ridge top. LAS traces had radii of curvature varying from 70-140 m, slightly smaller than the ridge centerlines (SI Table 3).

Like the Ferron Creek North site, here there is abundant evidence for ridge erosion due to scarp retreat. Mudstone flanks are covered in large (up to 12 m diameter) talus blocks, with the largest and most abundant blocks on the highest relief flanks (e.g., near the bank-attached bar on

Ridge B; Fig. 4.11). Evidence of vertical degradation comes from the exposed lateral accretion sets and other exposed strata on ridge tops (Fig. 4.11).

4.5.3 Wild Horse Mesa

The Wild Horse Mesa site contains three ridges in the Salt Wash Member, and is notable for two lower ridges visibly outcropping from under a higher ridge (Figs. 4.12, 4.13). Using the tilt-corrected digital elevation model, we observed that the ridges span 50 meters of stratigraphy and the upper ridge (Ridge A) caprock is 15 meters higher than the lower ridge caprocks (Ridges B and C), which are at approximately the same stratigraphic level (Fig. 4.12). Tectonic-corrected slopes for the ridge tops range from 0.02-0.05, and relief ranges between 4-32 meters (Fig. 4.12). Caprock thickness varies from 2-9 m (Fig. 4.12D), and bend radius of curvature of the ridge centerline varies from 280-340 m (Fig. 4.12B, SI Table 3). Breadth varies from 10-74 m (Figs. 4.12A, 4.12B; SI Table 1), with the narrowest portions of each ridge being at the ridge ends (e.g., south end of Ridge B; Fig. 4.12B) or at a crossing of a modern wash (e.g., west end of Ridge C; Fig. 4.12B).

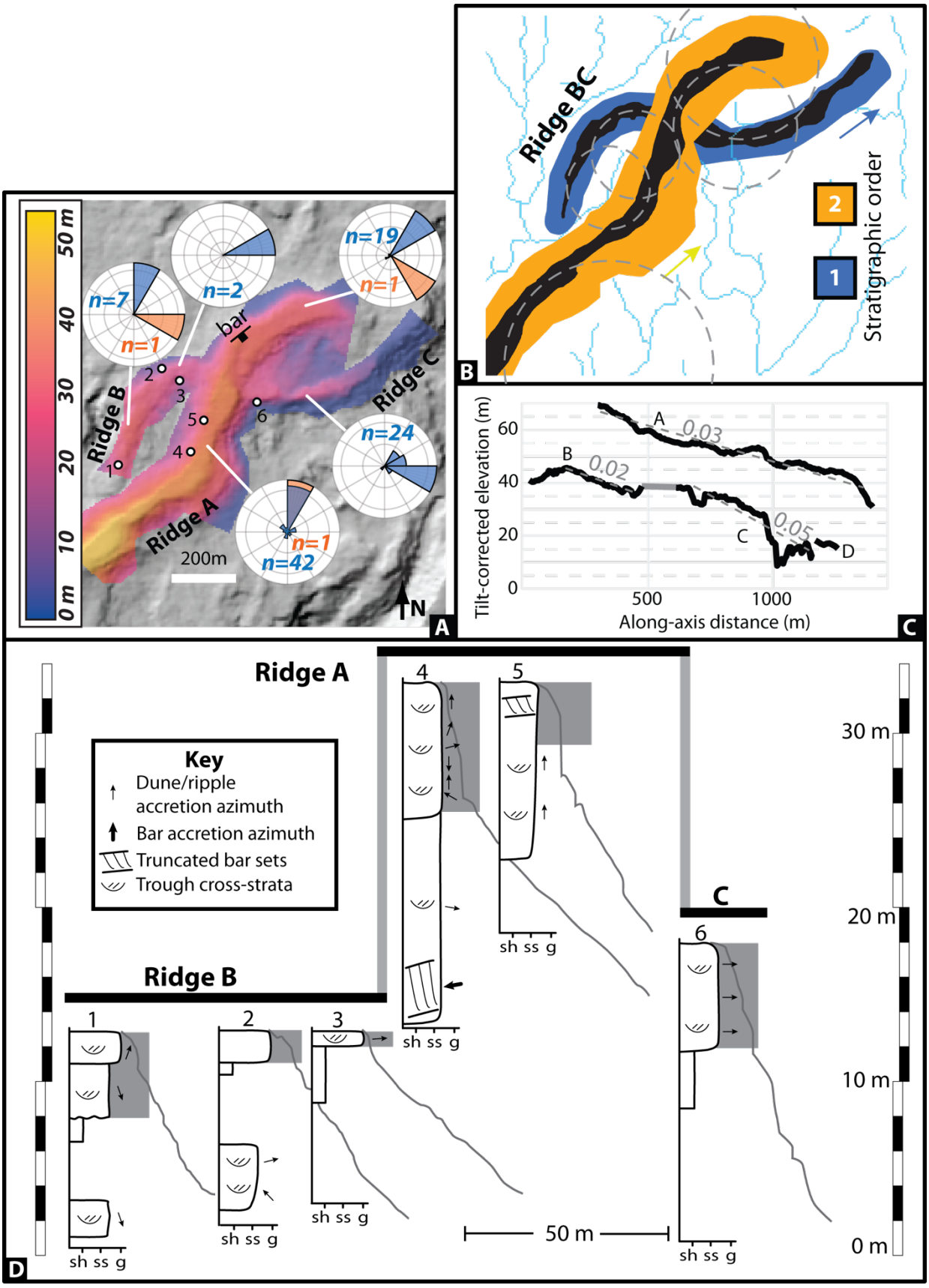
A
50 m
40
30
20
10
0 m
n=7
n=1
n=2
n=19
n=1
bar
Ridge B
Ridge C
Ridge A
n=24
n=1
n=42
200m
N
1
2
3
4
5
6
B
Ridge BC
Stratigraphic order
2
1
C
Tilt-corrected elevation (m)
60
40
20
0
A
B
C
D
0.03
0.02
0.05
500
1000
Along-axis distance (m)
D
Ridge A
Key
Dune/ripple accretion azimuth
Bar accretion azimuth
Truncated bar sets
Trough cross-strata
Ridge B
sh ss g
50 m
30 m
20 m
10 m
0 m

Figure 4.12-- Wild Horse Mesa site. **a.** Colors represent height of the ridges and their flanks in stratigraphic the model (DEM rotated to remove tectonic dip). Numbers are stratigraphic sections (shown in panel D). Rose diagrams represent accretion direction of bar clinoforms (red) and dune trough cross-stratification (blue). Location marked 'bar' is shown in Fig. 4.13. **b.** Interpretation of stratigraphic positions of ridges, shown at same scale as panel (a). Ridge caprocks are indicated in black, ridge slopes and ridges lacking caprock are indicated in dark colors, interpreted paleo-flow direction indicated in a colored arrow next to the ridge, and modern washes given in branching blue networks. Gray dashed circles are the locations where radius of curvature of the centerline was measured. **c.** Ridge elevation profiles taken from the stratigraphic model along each ridge centerline (black lines). Gray lines indicate inferred connection between Ridges B and C. Dashed gray line is a best-fit line used to calculate ridge top slope. **d.** Representative stratigraphic sections (numbers correspond to locations on panel A; shale, sandstone, and gravel indicated by sh, ss, g, respectively), with cross-stratification noted. Cross-sectional profiles off the side of the ridge given in gray sloping lines. Vertical exaggeration ~5x; scale bar only applies to topographic profiles (gray lines) in this panel. Bold black horizontal lines show interpreted stratigraphic position and gray dotted lines represented interpreted tie lines between ridges.

Caprocks are dominantly composed of medium sandstone with some gravels up to 1 cm in diameter. Caprocks also contain abundant inclined stratification of a variety of types. Dune cross-strata have thicknesses 8-41 cm and indicate paleo-flow generally aligning with ridge axes (Fig. 4.12A). Truncated bar clinoforms are up to 2 m tall, which is smaller than the caprock thickness, suggesting the caprock of Ridge A contains multiple generations of amalgamated deposits. We also observed a laterally extensive set of inclined strata perpendicular to paleo-flow (Fig. 4.13A) that we interpreted as laterally accreting bank-attached bar strata; though, unlike Ferron Creek South, here the LAS was not apparent in air photos (e.g., Fig. 4.13B). Based on alignment, proximity (Figs. 4.12A, 4.12B), similar elevations (Fig. 4.12C), and caprock thicknesses (Fig. 4.12D), we interpret the caprocks of Ridges B and C to be segments of the same sandstone body running continuously underneath Ridge A. Mudstone was observed to separate the caprocks at the crossing locating (Fig. 4.13B).

Ridge flanks are armored with caprock talus blocks that are up to 10 m in diameter, indicating extensive lateral erosion of the caprock (Fig. 4.13B). Washes follow the topographic slope to the

south, and divert around ridges. One wash crosses Ridge C near its intersection with Ridge A, and has visibly narrowed the caprock (Fig. 4.12B). A similar notching is seen in Ridge B near its intersection with Ridge A (Fig. 4.13B), but that ridge is taller and so the current washes flow around the outside.

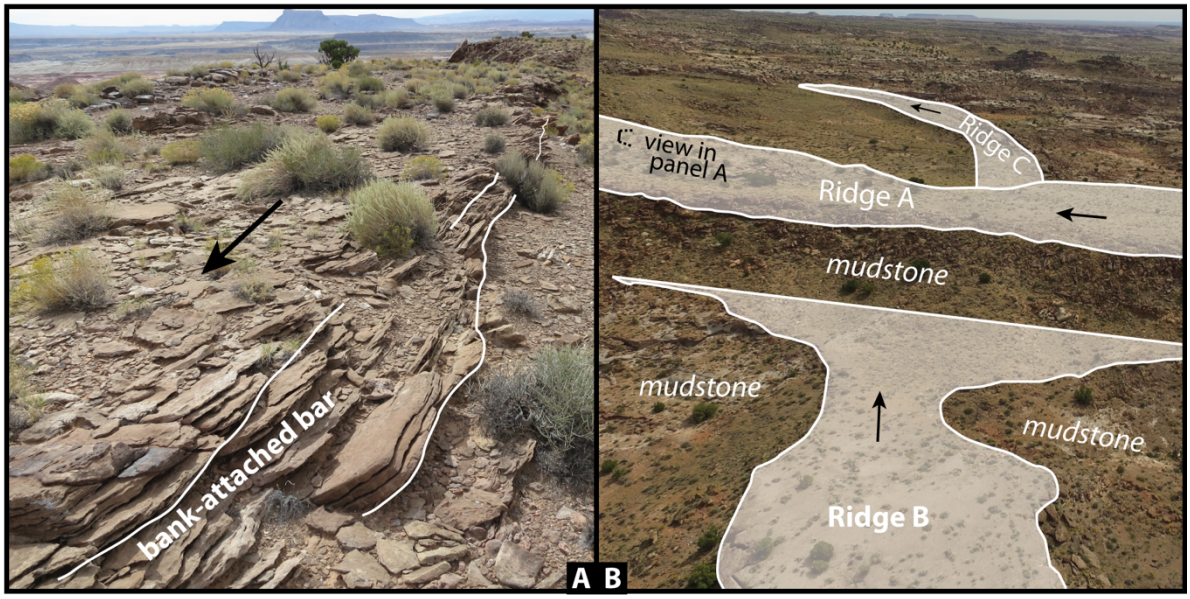

Figure 4.13-- Wild Horse Mesa site. **a.** Bank-attached bar strata on top of Ridge A, interpreted from laterally extensive, planar beds with an accretion direction to the southeast (see strike and dip symbol on Ridge A on Fig. 4.12A), perpendicular to the interpreted paleo-flow direction and the ridge axis. **b.** Quadcopter image looking east over the ridge intersection. Mudstone occurs below Ridge B and between the caprocks of Ridges A and B.

4.5.4 Summary of data and paleo-hydraulics from all sites

Fig. 4.14 summarizes medians and 5-95 percentiles for ridge dimensions, sedimentological observations, and resultant paleo-hydraulic reconstructions for the Morrison Formation ridges we studied at Ferron Creek North (FCN), Ferron Creek South (FCS), and Wild Horse Mesa (WHM). All data are also given in Supplemental Tables 1-3. Grain size of the caprocks (16 observations at FCN, 20 at FCS, and 44 at WHM) varies across the sites with mean D_{50} values for each ridge ranging

from fine sandstone to fine gravel, and grain size of non-caprock material ranged from mud to fine sandstone. Set thicknesses and organization indicate caprocks comprise between 1-3 generations of amalgamated deposits and, using Eqs. 4.1 and 4.2, are indicative of paleo-flow depths ranging 2.8-5.8 m based on truncated-bar strata (5 observations at FCN, 2 at FCS, and 4 at WHM) and dune strata (13 observations at FCN, 18 at FCS, and 40 at WHM). Using the methods from Section 4.4.1 for the sedimentological reconstruction, paleo-channel median widths were 50-104 meters and median slopes were 0.0003-0.001. Based on observations of lateral accretion sets, channel-body wings, and the abundance of mudstone, we interpreted that the paleo-channels were single-thread, which is consistent with prior work on the Morrison Formation (Derr, 1974; Heller et al., 2015).

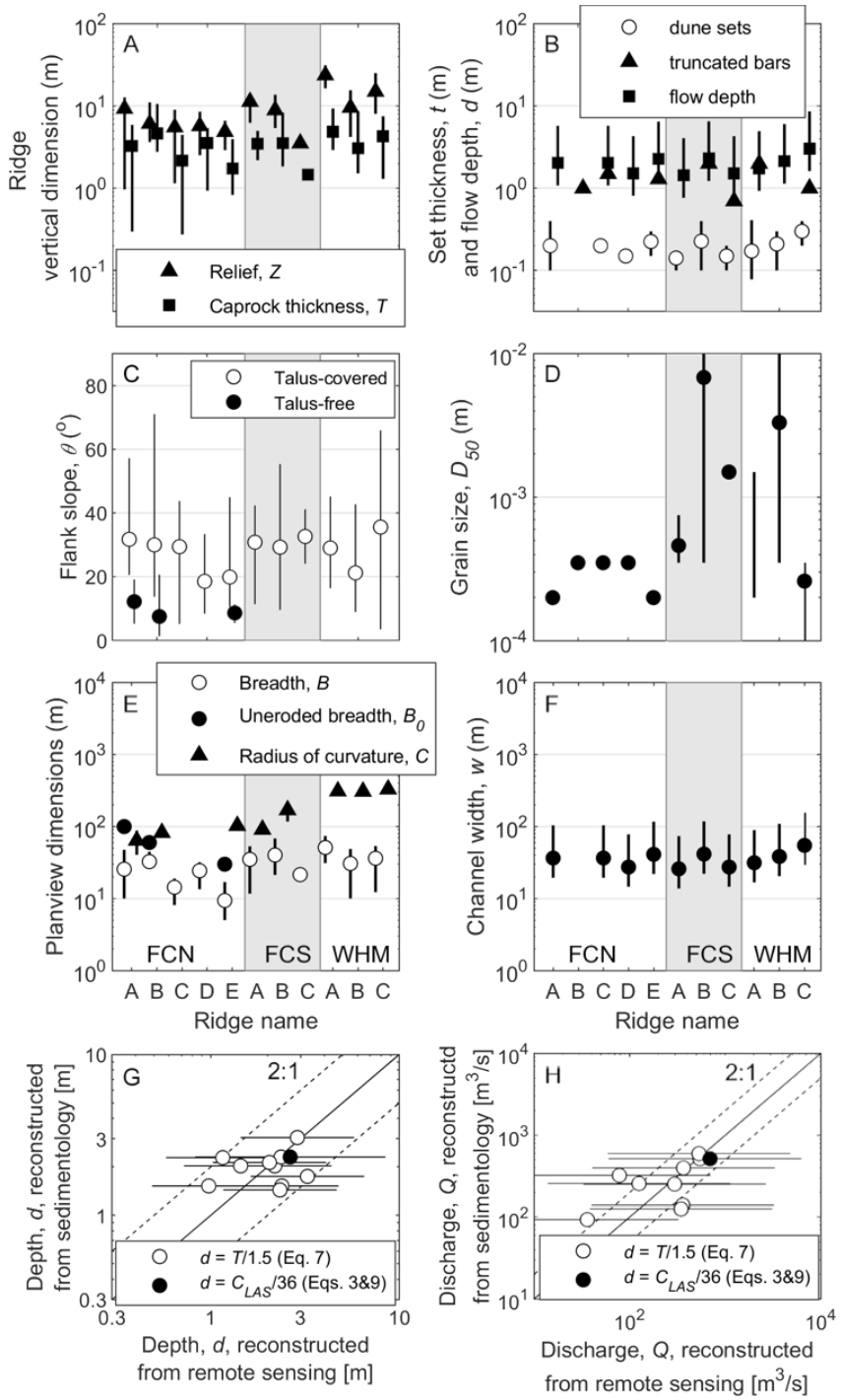

Figure 4.14-- Ridge parameters, and paleo-channel parameters and paleo-hydraulic reconstructions for the Ferron Creek North (FCN), Ferron Creek South (FCS), and Wild Horse Mesa (WHM) sites. Each point represents the median measurement for a ridge and the bar represents the 5th-95th percentile range of our observations when applicable. Ridge letters given at bottom of panels E & F apply to panels A-F, shaded regions divide different field areas. **A.** Ridge relief and caprock thickness. **B.** Thickness of cross stratification interpreted as truncated dunes and truncated bars. These are used to reconstruct flow depth with Eq. 4.1, which yields minimum values equal to the truncated bar thickness (triangles), or Eq. 4.2 (squares). Uncertainty on flow

depth is from the bounds on Eq. 4.2. **C.** Distribution of flank slopes on both sides of each ridge, grouped by flanks with visually very little to no talus cover (n = 12) and those with some or significant cover (n = 94). **D.** Grain sizes measured in stratigraphic sections within each caprock. Dots are mean values weighted by bed thickness and bars span 5-95 percentile of measurements. Each caprock at Ferron Creek North had constant D_{50}. **E.** Ridge breadth, uneroded breadth (measured where observed in cliff outcrops), and radius of curvature of the ridge centerline. **F.** Paleo-channel width reconstruction (Eq. 4.3). **G &H.** Paleo-hydraulic reconstructions of bankfull channel depth (panel g) and bankfull water discharge (panel h) from sedimentology (Section 4.4.1) and from ridge observations that can be made from remote sensing; white dots are using caprock thickness as a proxy for channel depth (Eq. 4.7) and black dots use the curvature of lateral accretion sets as a proxy for channel width (LAS; Eq. 4.9); depth is then calculated from Eq. 4.3. Paleo-channel depth from the three reconstruction methods agree within a factor of two, which is the same as the estimated uncertainty in the methods (Eqs. 4.1, 4.2, 4.7, and 4.9).

Caprock thickness and breadth, and flank relief and slope were all measured in ridge-perpendicular elevation transects, of which we have 38 at FCN, 24 at FCS, and 38 at WHM. In comparison to paleo-channel dimensions reconstructed from sedimentology, caprock thicknesses are more similar to inferred channel depths than ridge reliefs are. Median relief for each ridge ranges 4-27 m, median caprock thickness ranges 1.5-4.9 m, and median ridge breadth ranges 10-50 m. In cliff exposures where caprock-forming sandstones are uneroded, breadths reach up to 100 meters. The measured widths and thicknesses of these uneroded bodies are consistent with values of other uneroded sandstone bodies in the Morrison Formation, which range from 30-150 m breadth and 3.8-15 m thickness (Chesley and Leier, 2018; Owen et al., 2015b; Stokes, 1961). Median radius of curvature of ridge centerlines ranges 70-120 m (4 observations at FCN and at WHM, and 5 observations at FCS), and the range of 6 lateral accretion sets observed at FCS is 70-140 m. Ridge along-axis slopes are steeper than channel bed slopes inferred from sedimentology by a factor of 10-100. Flank slopes of the studied ridges range 1-70°, with median values for each ridge between 20-30°. Ridge flanks without talus cover fall on the low end of that range, and ridges with more talus cover have steeper slopes.

Paleo-hydraulic reconstructions of depth and discharge are comparable (Figs. 4.14G, 4.14H) between the methods that rely on sedimentary structures (Section 4.4.1) and methods based on caprock thickness and LAS curvature, which can be measured using remote sensing (Sections 4.4.2 and 4.4.3). A similarity between reconstructions from sedimentology and caprock thickness was also found by Hayden et al. (2019) for nearby ridges in the Cedar Mountain Formation.

4.6 Discussion

4.6.1 *Sinuous ridges in the Morrison are exhumed channel belts*

Similar to the interpretations of the sinuous ridges in the Cedar Mountain Formation by Hayden et al. (2019) and Cardenas et al. (2020), we interpret the ridges at all three of our field sites to be exhumed channel belts rather than topographically inverted channel fills (i.e., inverted channels) based on the following observations. First, lateral accretion sets within sandstone bodies indicate lateral channel migration across a floodplain (e.g., Ridges FCS-B, WHM-A; Figs. 4.11, 4.13A), and caprock architecture indicates channel aggradation (e.g., Ridge FCN-F; Fig. 4.9) and/or avulsion and reoccupation, rather than filling of an abandoned channel. Caprocks are composed of amalgamated fluvial strata, including ripples, dunes, and bars, which indicates long-lived flows and reworking, and sand grain size and interpreted flow depths are consistent through each caprock section (Fig. 4.7D, 10D, 12D). In contrast, fluvial channel fills would be expected to be fine-grained (e.g., a filled oxbow lake) and have decreasing flow depth indicators up section, as an abandoned channel pathway fills in with overbank material (Bhattacharya et al., 2016; Musial et al., 2012; Reijenstein et al., 2011). Overbank sandstone wings are interpreted as channel-levee deposits, that downlap onto the floodplain (Allen et al., 1983; Friend et al., 1979; Mohrig et al., 2000) (FCN Ridges A, B, F; Figs. 4.8, 4.9). These are the classic components of channel-belt deposits (e.g., Allen et al., 1983; Friend et al., 1979; Kjemperud et al., 2008; Mohrig et al., 2000).

Second, the uneroded sandstone bodies exposed at cliff outcrops are thicker and wider than the reconstructed paleo-channel dimensions, as expected for a channel belt. Importantly, the Morrison Formation provides important insights into the sizes of the ridge-capping sandstone bodies before they were exhumed to form ridges. Uneroded ridges have breadths up to 100 meters (Figs. 4.8, 4.14), while paleo-channel widths were reconstructed to be less than 50 meters (Fig. 4.14), though the sizes do overlap within uncertainty. The thicker and wider sandstone bodies, as compared to the paleo-channel dimensions, support the interpretation that these are channel-belt deposits built through lateral channel migration, not channel fills. Further, our observations of dramatic narrowing of the sandstone bodies during ridge formation indicate that the similarity between ridge breadth and paleo-channel widths in some cases is because erosion has coincidently narrowed the channel-belt widths to sizes similar to paleo-channel width estimates in some places. However, in other locations erosion has been negligible (e.g., next to cliffs) or has removed the ridge caprock entirely (Fig. 4.5A), supporting the argument of Hayden et al. (2019) that ridge breadth is a highly uncertain proxy for paleo-channel width.

Third, stratigraphic superposition of multiple sandstone bodies indicates exhumation of a package of rocks formed over significant time, rather than a deflated geomorphic surface (Figs. 4.7, 4.10, 4.12). Field examination shows that caprocks are typically separated by floodplain facies like mudstone (Figs. 4.8, 4.9, 4.11, 4.13), indicating changes in channel location through time, with hiatuses that likely lasted thousands of years for mud accumulation and paleosol development (e.g., Leeder, 1975). Dated ash beds constrain deposition for the two members over the course of 2-6 M.y. (Fig. 4.4). Thus, the ridges represent exhumed, stacked channel-belt deposits that accumulated by the lateral migration and aggradation of rivers over millions of years, rather than being simple inverted fills of paleo-channels.

4.6.2 *Ridge modification by scarp retreat*

Ridges on Earth and Mars are typically observed as regional topographic highs—disconnected from outcrops where a complete section of the stratigraphy can be observed—making it difficult to constrain how much erosional modification of the ridge capping sandstone bodies occurred during ridge formation. The Ferron Creek North site, where ridges emanate from cliffs, is important because it allows for an assessment of the erosion processes and geometries through observations of the pre-eroded sandstone body geometry, which can be used to improve our understanding of ridge formation and morphology.

Observations from Ferron Creek North indicate that sandstone bodies rapidly narrow during exhumation to form a ridge (Fig. 4.8), but the caprock thickness varies little (Figs. 4.7, 4.8, 4.10, 4.12; SI Table 1). This indicates that lateral backwasting is a major form of ridge erosion, and that vertical erosion, while nonzero (e.g., there are exposed strata on ridge tops; Figs. 4.6C, 4.11, 4.13) is relatively minor. Data for Ridge FCN-A also shows that, with distance from the cliff exposure, ridge relief increases slightly and then plateaus, caprock thickness remains roughly constant, and flank slope generally increases (Fig. 4.8). Here, we seek to explain these correlations by proposing a ridge exhumation model that incorporates scarp retreat.

We hypothesize that Ridge FCN-A was progressively exposed as the overlying rocks were removed by lateral retreat of the cliff that now abuts the ridge on its west end (Fig 7A). Thus, a space-for-time substitution can be used to understand progressive formation of the ridge. That is, near the cliff, the ridge has only been recently exposed, whereas farther from the cliff, the ridge has been exposed for longer and undergone more erosion. Thus, our observations suggest that as ridges are exhumed, their breadth decreases, ridge relief and flank slope increase, and caprock thickness remains roughly constant (Fig. 4.8). We also observed that ridge flanks without talus often have more relaxed slopes than their talus-covered counterparts (Fig. 4.14C) and that ridges without

caprocks also lack talus on the flanks (Fig. 4.5A), which, together with the observed increase in slope with increasing relief, indicate that talus cover, flank steepness, and ridge growth are related. In addition, most ridges have washes at the base of their flanks that seem to be efficient at removing talus (Figs. 4.8, 4.9, 4.11).

We used these observations as motivation for a ridge erosion model building on previous work for scarp retreat (e.g., Glade et al., 2017; 2018; Ward et al., 2011). We assumed a strongly indurated caprock with thickness (T) and breadth (B), above a weakly indurated ridge flank with relief (Z) and slope (θ) (Fig. 4.5B). The flank erodes downward, undercutting the caprock; as the caprock is undercut, the overhang collapses and delivers the caprock material to the flank as talus.

We assumed that relief (Z) increases linearly in time (t) at the rate of vertical erosion of the ridge toe (E_m),

$$dZ/dt = E_m. \qquad \text{Eq. 4.10}$$

By geometry, breadth (B) decreases as the caprock is undercut at the rate of vertical lowering of the flank projected under the ridge (Fig. 4.5B):

$$\frac{dB}{dt} = -\frac{2FE_m}{\tan\theta}, \qquad \text{Eq. 4.11}$$

where the factor of two accounts for two flanks of the ridge, and F is the rate of vertical lowering of the ridge flank, E_f, relative to the flank toe, E_m (i.e., $F = E_f/E_m$; Fig. 4.5B). If $F = 1$, then the toe of the flank is laterally fixed by geometry, and all of the ridge relief generation by Eq. 4.10 results in caprock undercutting. This could be the case if there is a stream at the base of the ridge that fixes the location of the flank toe. Alternatively, if $F = 0$, then the ridge flank does not erode, and the ridge flank extends at constant slope to accommodate any relief generation, rather than undercutting the caprock. This could be the case if the ridge flank is armored in resistant talus.

Change in caprock thickness (T) occurs at the rate of vertical caprock sandstone erosion (E_s)

$$\frac{dT}{dt} = E_s. \qquad \text{Eq. 4.12}$$

By conservation of mass, talus per unit ridge length is generated by caprock undercutting at the rate $T\mathrm{d}B/\mathrm{d}t$. Talus falls on the flank slopes, where some fraction (f) stays; the remainder exits the system by rolling into the wash at the end of the slope or is eroded *in situ*. We track the amount of talus as a mean thickness of cover (D) by averaging the total volume of talus produced ($f\,T\,\mathrm{d}B/\mathrm{d}t$) over the entire length of both flanks ($2Z/\sin\theta$) minus the vertical erosion rate of the talus (E_t):

$$\frac{dD}{dt} = f\,T\left(\frac{dB}{dt}\right)/\left(\frac{2Z}{\sin\theta}\right) - E_t. \qquad \text{Eq. 4.13}$$

Rather than modeling any specific erosion process (e.g., gullying, soil creep; Glade et al., 2017; 2018; Ward et al., 2011), based on our field observations we made the assumption that flank slope is a linear function of the fraction of the flank that is covered in talus rather than mudstone (e.g., talus cover varies and flank slope increases with increasing erosion; Figs. 4.5, 4.8E, 4.14C). The fraction of talus cover, described as the ratio of average talus thickness, D, to a reference value for 100% cover, D_0, defines whether the flank slope reaches a steepness like a weak mudstone ($S_m = \tan\theta_m$) or like a stronger sandstone ($S_s = \tan\theta_s$)

$$\tan\theta = S_s/\left(\frac{S_s}{S_m} + \frac{D}{D_0}\left(1 - \frac{S_s}{S_m}\right)\right). \qquad \text{Eq. 4.14}$$

To solve Eqs. 4.10-4.14, we first non-dimensionalized the equations by dividing all lengths by initial caprock thickness, T_0. Because we do not know the rates of ridge formation for our field sites, we eliminated time through substitution of variables and solved the equations as a function of ridge relief using Eq. 4.10. We imposed a toppling instability for $B{:}T < 1$, after which the caprock is completely eroded. S_m was set from the minimum slopes observed in the field data to be $\theta_m = 6°$, and S_s was set from the maximum slopes observed in the field data to be $\theta_s = 50°$ (Fig. 4.14C). The ridge flanks were assumed to erode at the same rate as the flank toe (i.e., $F = 1$) because we observed

washes at the toe of most ridges that would pin the toe lateral position (e.g., Figs. 4.7, 4.10, 4.12) and the plain and the flanks are made of the same mudstone material (e.g., Figs. 4.8, 4.9, 4.11). Initial conditions for the model are $B = B_0$ and $T = T_0$, $\theta = \theta_m$, and $Z = T_0 \tan(\theta_m)$. Based on our field observations of negligible change in caprock thickness along a ridge (e.g., Fig. 4.8), we also made the simplifying assumption that $E_s = 0$. Because talus is made of the same material as the caprock, then, likewise, $E_t = 0$. We also assumed that $D_0 = T_0$ based on our observations that median talus block diameter is comparable to median caprock thickness; that is, the flank slope will be fully covered in talus when the cover is comparable to the thickness of the blocks shed from the caprock. We estimated T_0 for each ridge as the 95th percentile of the measured caprock thickness.

Even with these assumptions, the model is underdetermined because we do not know f and B_0. Here we took advantage of the construct of the equations in which the flank slope in nondimensional space depends only on f and Z/T_0, whereas B depends additionally on B/T_0. First, we used an iterative procedure to calculate f, trying values between 0-1, and selecting the value that minimized the sum of the square differences for the model predictions of θ given Z/T_0 (i.e., model versus data in Figs. 4.15A and 4.15B). Only Ridges FCN-A and FCN-B had enough data points to constrain f; we found $f = 0.3, 0.2$. For ridges with too few measurements to have a good fit ($n < 4$, corresponding to ridge lengths below 200 meters) we then applied $f = 0.3$ from FCN-A to those ridges. Using the estimated f for each ridge, we then found the best fitting B_0 value by minimizing the sum of square differences for the model predictions of B/T_0 from Z/T_0 (i.e., model versus data in Figs. 4.15D, 4.15E, 4.15F).

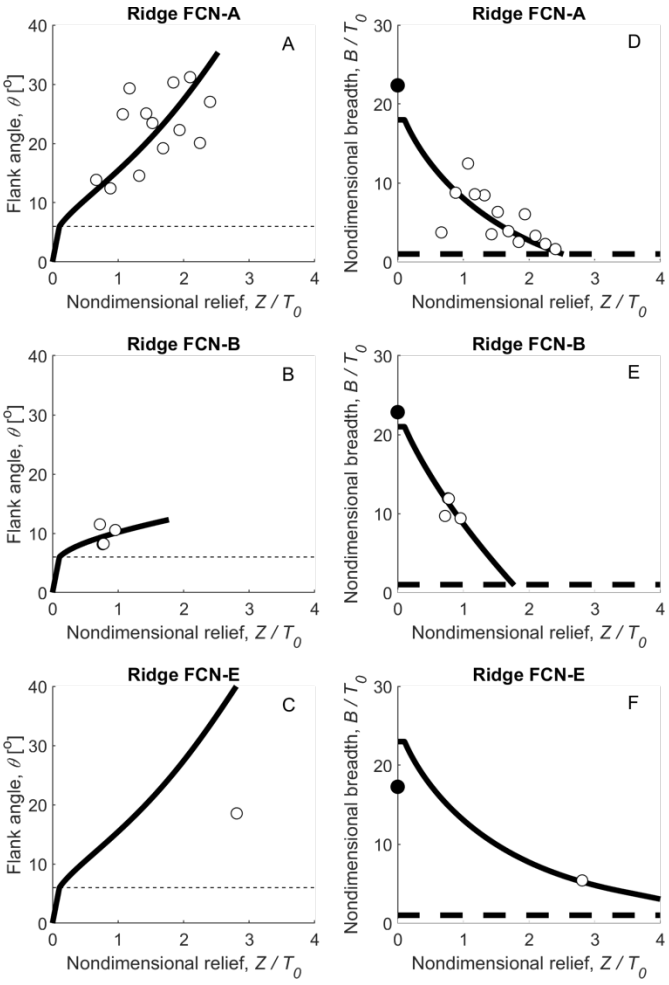

Figure 4.15-- Ridge data and erosion model for FCN Ridges A, B, and E used to find the best fit values for f, the fraction of talus produced that accumulates on the flank, and B_0, the uneroded caprock breadth. White dots are ridge data, black dots (panels D-F) are measurements of the uneroded sandstone body in cliff outcrop, and the solid lines are the model best fit (Eqs. 4.10-4.14). The thin dashed line in panels A-C is the minimum flank slope, S_m. The thick dashed line (panels D-F) is the toppling threshold of $B/T_0 = 1$. Non-dimensional relief is the ridge relief (Z) relative to the uneroded caprock thickness (T_0), and the non-dimensional breadth is the ridge breadth (B) relative to T_0. Due to the lack of data for Ridge FCN-E, we used $f = 0.3$, which is the best fit value from FCN-A.

The model is influenced more heavily by some parameters than others. The f parameter is sensitive to the mudstone slope (S_m; dashed line Figs. 4.15A, 4.15B, 4.15C) and initial caprock thickness (T_0), and relatively insensitive to sandstone slope. The breadth trajectory (Figs. 4.15A, 4.15B, 4.15C) has a concavity that increases with the fitted value of f and decreases with higher

estimated F. Breadth is measured in high-resolution air photos and therefore has accuracy to better than 1 meter, while caprock thickness and flank relief and slope are measured from elevation transects we estimate uncertainty to be within 20%.

As relief grows in the model, the caprock breadth narrows due to undercutting, and the flank slopes increase due to talus armoring (Fig. 4.15). The model and data both show a slower rate of ridge narrowing with increasing relief because, by geometry, the steeper flank slope that develops due to talus armoring results in less undercutting (and therefore less ridge narrowing) per unit of flank-slope downcutting. The data also support the assumed minimum ratio of $B/T = 1$ due to toppling by gravity—the model predicts a maximum ridge relief before toppling of $Z/T_0 = 2.3$ for Ridge FCN-A, which matches the maximum ridge relief achieved, while Ridge FCN-B does not reach its maximum value, which is consistent with its lack of segmentation (Figs. 4.15D, 4.15E). The model predicts a reconstructed initial sandstone body width of $B_0 = 85$ m ($B_0/T_0 = 18$) for Ridge FCN-A, which is similar to (15% smaller than) the measured values of $B_0 = 100$ m at the cliff exposure (and 22% smaller than the observed $B_0/T_0 = 23$). For the other two ridges with less data due to their shorter length, we reconstruct $B_0 = 90$ and 40, which are 50% and 40% larger than the B_0 values measured at the cliff exposure; likewise, $B_0/T_0 = 21$ and 23, which are 14% smaller and 35% higher than the measured values. For other ridges, the calculated initial breadths ($B_0 = 40$-160 m) are similar to those measured for non-ridge forming, uneroded sandstone bodies observed elsewhere in the Morrison Formation (30-150 m; Chesley and Leier, 2018; Owen et al., 2015b; Stokes, 1961). This analysis suggests that the ridges analyzed have degraded breadths by 40-140 meters (50-90%). Reconstructed values of B_0/T_0 for the pre-erosion channel bodies span 9-25, which is consistent with the smaller reported aspect ratios of channel-belt sandstone bodies from Robinson and McCabe (1997). In summary, our model provides a means to estimate original channel-belt widths from

observations of ridge relief and caprock thickness, and supports the idea that ridge widths can be substantially narrowed during exhumation, especially for tall ridges.

4.6.3 Paleo-hydraulics from remote sensing

On Mars, detailed observations of ridge sedimentology are not possible from orbital images, and therefore paleo-hydraulic methods that rely on ridge geometry, rather than sedimentology, are needed. It is common to use ridge width as a proxy for paleo-channel width (e.g., Burr et al., 2010; Kite et al., 2015; Williams et al., 2013). The uneroded channel-belt widths are wider than the paleo-channel widths for the Morrison ridges (B_o/w = 1.0-5.4) as expected; the ridges, however, have been subsequently narrowed (B/w = 0.1-2.4) by scarp retreat. While the effects of lateral migration and scarp erosion are mostly offsetting for the Morrison ridges, we are not aware of mechanism that would make this finding general. Instead, channel-belt widths are known in cases to be significantly wider than paleo-channel widths (e.g., up to a factor of 36; Hayden et al., 2019). In addition, erosion can be more or less extensive than we observed and is spatially variable along individual ridges (e.g., FCN Ridge A). Caprocks are completely absent in some cases (e.g., Fig. 4.5A), leaving mudstone ridges that likely formed originally with a caprock, and now are in a transient state of decay. Our scarp retreat model can be used to estimate the original channel-belt width, but the conversion between channel-belt width and channel width still carries an uncertainty of several orders of magnitude (Hayden et al., 2019).

Instead of caprock breadth, Hayden et al. (2019) advocated for use of caprock thickness as a proxy for channel depth. We find that the ratio of caprock thickness to channel depth for the Morrison ridges is T/d = 0.5-1.9, similar to the finding of Hayden et al. (2019) of T/d = 1.5 based on the ridges of the Cedar Mountain Formation and a large compilation of non-ridge forming channel-belt sandstones. Unlike caprock breadth, we expect caprock thickness to scale with channel geometry because rivers tend to be unstable and avulse, abandoning the channel-belt, after the channel

aggrades by about 0.5 - 3 channel depths (Bryant et al., 1995; Ganti et al., 2014a, 2014b; 2016; Hajek and Wolinsky, 2012; Jerolmack and Swenson, 2007; Mohrig et al., 2000; Slingerland and Smith, 2004). The avulsion process, therefore, sets a relatively consistent relation between channel-belt thickness achieved just prior to avulsion and the channel depth. Furthermore, because vertical caprock erosion is small compared to lateral scarp retreat, the ridge caprock thickness can be used as a reliable proxy for the original channel-belt thickness (i.e., $T/T_0 \sim 1$).

In addition to caprock thickness and breadth, Ridge FCS-B shows curvilinear features in planview, and similar features have been interpreted as scroll bars in the Morrison Formation (e.g., Hartley et al., 2015) and on Mars (e.g., Burr et al., 2009; 2010; Jerolmack et al., 2004). Scroll bars are a series of constructional river levees deposited on the inner bank of meandering river levees (Fig. 4.3). They are perched atop the point bar and often represent only a small fraction of the sedimentary material (e.g., Mason and Mohrig, 2019). In the Morrison Formation, we observed levee deposits in the form of climbing ripples and the sandstone wings at the margins of channel-belts (Figs. 4.8, 4.9), but these were not preserved as topographic highs during ridge formation and were not associated with the curving lines visible in planview on the ridge tops. Instead, our observations show that the curvilinear features are outcropping beds from lateral accretion sets that are topographic highs due to differential erosion on the deflated ridge top (Fig. 4.11). That is, they are erosional features that expose point-bar cross beds that built the channel margin, rather than constructional levees from overbank deposits.

The LAS traces in planview should be tightly correlated to channel geometry because they record the channel margin location. In contrast, we do not expect the ridge centerline curvature to track the channel curvature because the ridge is an eroded remnant of a channel belt, rather than a channel fill. Using the radius of curvature of LAS on Ridge FCS-B and Eq. 4.9, we estimated a

paleo-channel width of 48 m, which is consistent with the sedimentology reconstruction (Fig. 4.14) and the reconstruction based on caprock thickness. These paleo-hydraulic methods are further compared below in application to Mars.

4.6.4 Application to Mars

To apply the insight gained from the Morrison Formation, we illustrate the paleo-hydraulic methods and ridge erosion model with two example ridges in the Aeolis Dorsa region of Mars. Two ridges were studied because, as the ridges of the Morrison show, it is rare for individual ridges to exhibit all attributes. For the first example, we selected a broad ridge that has subparallel semicircular features on its surface that appear similar to LAS traces from the Morrison ridges (Fig. 4.16). Many martian ridges have LAS (e.g., Burr et al., 2009; 2010; Cardenas et al., 2018; Hughes et al., 2019); we selected this site based on its large breadth and availability of HiRISE stereo-pairs for making DEMs. We focused on a segment with a clear caprock and where the ridge is not amalgamated with other ridges (see Fig. 4.1B). The LAS provide evidence that the ridge caprock for this example is a channel-belt deposit from a meandering river with bank attached bars that accreted laterally (i.e., point bars). The ridge also shows a semicircular trough that could represent a cutoff channel loop (e.g., an oxbow lake; Fig. 4.16B) that was filled with mud (e.g., Musial et al., 2012; Reijenstein et al., 2011) and later exhumed, but it also could be a remnant impact crater.

We used a HiRISE stereo-DEM to measure each side of the ridge in one transect (Fig. 4.16C), finding a caprock thickness of 7 m (cliffy portion of transect), relief of 3 m and a caprock breadth of 650 m. In a HiRISE image we measured a radius of curvature of the ridge centerline as C = 1200 m, but a range of radius of curvature for the lateral accretion sets that is far smaller: C_{LAS} = 48-100 m with a median of 55 m (Fig. 4.16B). Using our scarp retreat model and the same inputs as for our sites in Utah (S_m = 0.1, S_r = 0.8, f = 0.3), we calculated a pre-erosion breadth of B_0 = 690 m for the martian ridge, which is similar to the measured breadth of 650 m due to its low relief. The depth of the

putative cutoff channel loop is 2.8 m, and its width and inner-bank radius of curvature are 55 m and 50 m, respectively. The similarity in the trough dimensions to their respective channel dimensions supports the interpretation of a cutoff channel loop.

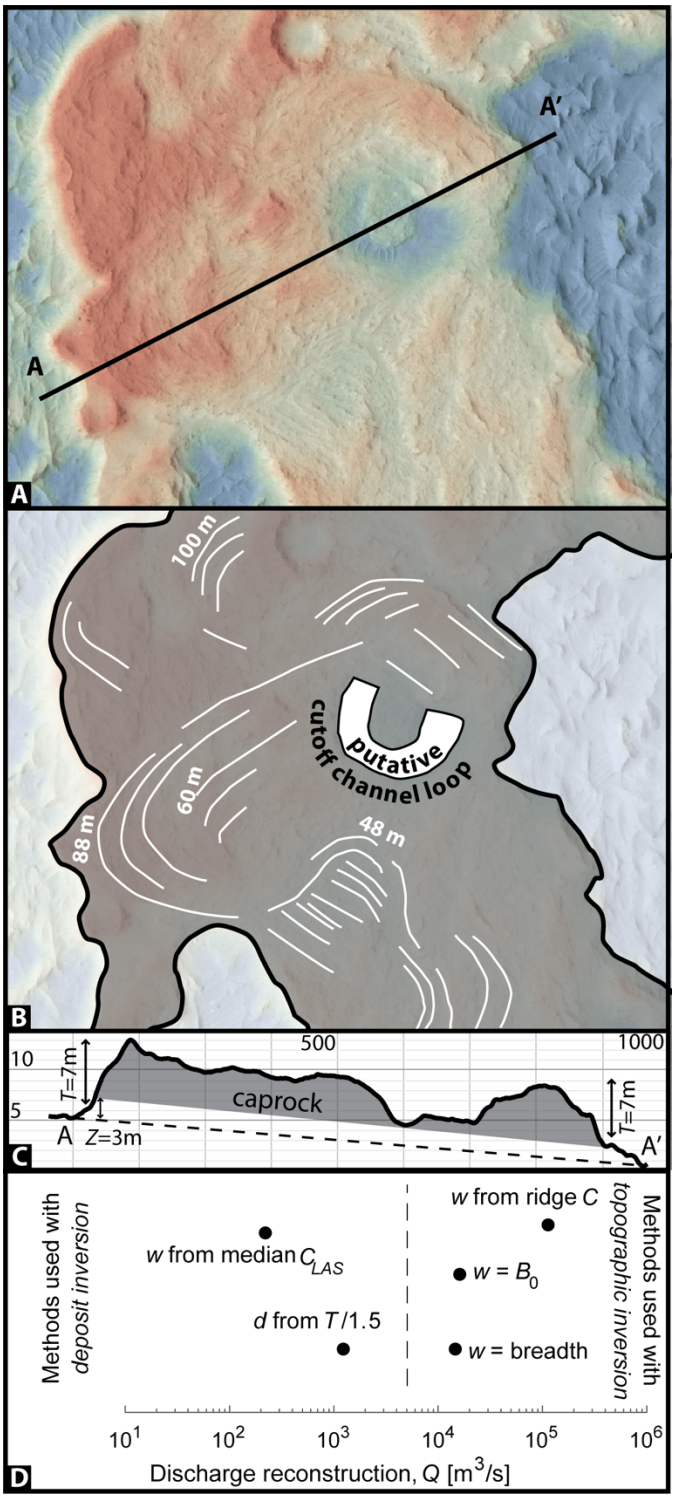

Figure 4.16-- **A)** Digital elevation model of a portion of a sinuous ridge from in Aeolis Dorsa, Mars (HiRISE image background and HiRISE stereo DEM from ESP_020805_1740 & ESP_020383_1740; 6.01 S 153.45 E). **B)** Interpretation of panel A. This ridge has interpreted lateral accretion sets (LAS; white lines) with labeled measurements of radius of curvature, and a putative cutoff channel loop. **C)** Elevation transect from panel A, showing estimated caprock

thickness of T = 7 m and estimated relief of Z = 3 m. **D)** River water discharge for the ridge, using the paleo-hydraulic methods that assume deposit inversion compared to those that assume topographic inversion (Sections 4.4.2 and 4.4.3). These include using radius of curvature of the LAS (C_{LAS}) and ridge centerline (C) as proxies for channel width (w), using ridge breadth (B) and modeled uneroded ridge breadth (B_0) as proxies for channel width, and using caprock thickness (T) as a proxy for channel depth (d).

Our preferred paleo-hydraulic methods (Section 4.4), which assume exhumation of a channel belt (i.e., deposit inversion), give water discharge values that range from 310-1800 m^3/s for an assumed D_{50} = 3.9 mm (i.e., the geometric mean of the assumed end-members: 0.3 mm and 50 mm) (Fig. 4.16). In contrast, assuming that the breadth of the ridge or the breadth of the uneroded ridge are equal to the river width gives significantly larger discharges of 154,000 and 174,000 m^3/s, respectively (Fig. 4.16). Likewise, using the ridge centerline curvature as a proxy for channel curvature yields inferred channel discharge of 51,200 m^3/s. These three calculations relying on an inverted-channel interpretation are consistent with each other within our estimated uncertainty of a factor of 9 on discharge; however, they significantly overestimate our preferred paleo-discharge values. Prior work in this region (Burr et al., 2009; 2010) avoided reconstructing discharge on features similar to this ridge ("flat" in their terminology) because they also interpreted such ridges to represent channel belts; our results therefore support their interpretation and offer a quantitative tool to calculate discharge for ridges that are exhumed channel belts.

The second example ridge from Aeolis Dorsa is one we picked because it shows narrowing along its length, and so is useful to compare to our ridge erosion model (Fig. 4.17). The first ridge was not sufficient for this example because it amalgamates with other ridges just north of the study location (Fig. 4.1B) and is unexhumed just south of the study location. Instead, we selected a variable-width ridge from a previously studied branching ridge network (Burr et al., 2010; Lefort et al., 2015; Hayden et al., 2019) that has HiRISE stereo-pairs for creating a DEM (Figs. 4.17A &

4.17B). Not all ridges have clear caprocks in topographic transects, including those in this DEM and our studied sites on Earth, so we selected this ridge mainly because the caprock could be discerned from the DEM in several places (Fig. 4.17C). We measured caprock width and thickness, and flank slope and relief along cross-ridge transects as we did for the terrestrial ridges, differentiating the caprock from the flank by slope breaks. An estimate of uneroded caprock thickness, T_0 = 25.8 m, was measured as the 95th percentile of measured caprock thicknesses along the ridge. The ridge shows an inverse correlation between caprock width and ridge relief that is concave-up like the Morrison ridges (Fig. 4.17D), suggesting narrowing as the ridge was exhumed. Using the same parameters as we used for the Morrison ridges (θ_m = 6°, θ_s = 50°, $E_s = E_t = 0$, f = 0.3, F = 1), we found the model yielded predictions of ridge narrowing greater than observed for a given change in relief (Fig. 4.17D). We tested F = 0.2 we found a better fit between the model and data, and predicted that B_0 = 130 m. This lower value of F implies that the vertical erosion rate on the ridge flank (E_f) is smaller than the vertical erosion rate at the toe of the ridge (E_m) (Fig. 4.5B). In other words, as the ridge increased in relief due to differential erosion between the ridge toe and the ridge caprock, only a fraction (20%) of that differential erosion led to caprock undercutting; the remainder of the relief was accommodated by lengthening of the ridge flank and widening of the ridge base. We found that adjusting other parameters did not produce a better fit—f modifies concavity of the breadth-erosion trajectory and different S_m reduces the fit to the flank-slope trajectory.

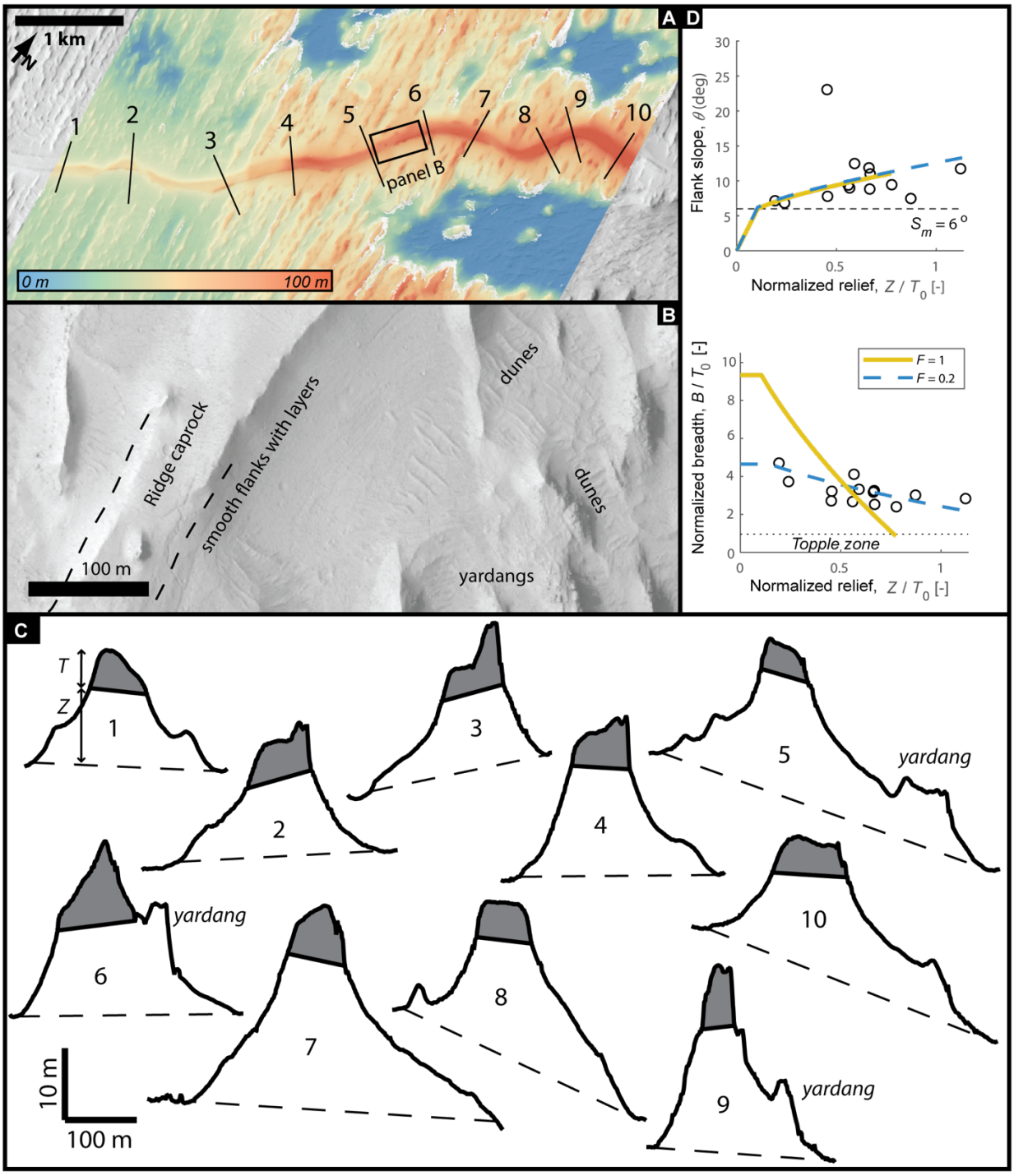

Figure 4.17-- Ridge in Aeolis Dorsa, Mars (6.24 S, 151.43 E). **a.** We measured 10 transects (black lines) along the ridge in a HiRISE stereo-pair DEM (PSS_002279_1735 & PSP_002002_1735). **b.** Zoomed-in view from panel (a) showing ridge caprock, flank slopes with layering, and eolian dunes and yardangs. **c.** Topographic profiles from HiRISE DEM shown at 10x vertical exaggeration, with locations given in panel (a). Gray shaded area is the interpreted caprock. Dashed lines connect the base of each ridge flank, as defined by a change in slope to the neighboring terrain. Some ridge flanks show yardangs in the topographic profile. **d.** Data from the

ridges (circles) and our model (colored lines) with $F = 1$ (as found for terrestrial ridges) and the best fit value $F = 0.2$, showing ridge flank slope angle (θ) as a function of nondimensional relief (Z / T_o), and nondimensional breadth (B / T_o) as a function of nondimensional relief.

There are several possible mechanisms that might explain our finding of $F < 1$ for the martian ridge. First, a talus armor could slow the erosion on the talus flank relative to the toe of the ridge; however, we found a good model fit for terrestrial ridges of $F = 1$ (Fig. 4.14) despite abundant talus (Fig. 4.1D). Moreover, at the resolution of HiRISE (<1 m per pixel), we did not observe talus on the flanks in this example (although talus is observed elsewhere in the same HiRISE image; Fig. 4.1C), and we expect it to be visible if talus size scales with T_o. Instead, the ridge flank shows horizontal lineations, which we interpret to be exposed beds of the underlying strata (Fig. 4.17B). A second possible mechanism is that eolian abrasion might be more effective on the plains surrounding the ridge as compared to on the ridge flanks, whereas the water-based erosion more common on Earth is equally effective on the flanks as on the surrounding plains. For example, saltating grains that are responsible for eolian erosion (e.g., Bagnold, 1941) might be deflected away from the flanks toward the plains. A third possible mechanism is that the ridge flank material is more resistant to erosion than the plains beyond the ridge toe. This mechanism could be possible at Aeolis Dorsa; while the ridge flank is relatively smooth and has exposed bedding, the plains appear to be composed of a different material that drapes the ridge flank and produces yardangs (Fig. 4.17B). This observation is different than the Morrison ridges where the ridge flanks and toes are composed of the same floodplain facies that erodes similarly, and where modern washes define ridge toes and likely pin them in place.

Unlike the example ridge in Fig. 4.16, this ridge (Fig. 4.17) would be classified as a “thin” ridge and an inverted channel under the criteria of Burr et al. (2009; 2010). Therefore, the ridge in

Fig. 4.17 is one in which paleo-discharge might be calculated from ridge width and wavelength directly as if the ridge were a mold of the channel dimensions. In contrast, we interpret this ridge, similar to the Morrison ridges, as a channel belt due to layering in the flanks that suggest exposed bedding planes (Fig. 4.17B) and ridge stacking observed elsewhere in the same network (Hayden et al., 2019). In this case, the values for flood discharge using measurements of width as a proxy for channel width (~150 m^3/s; Burr et al., 2010) are significantly smaller than those based on using caprock thickness as a proxy for channel depth (mean thickness 13.0 m yields Q = 4,500 m^3/s). However, because channel belts have width and thickness that relate independently to paleochannel geometry (e.g., Jerolmack and Mohrig, 2007), in other cases calculations based on caprock width can be similar to or greatly exceed calculations based on caprock thickness (e.g., Fig. 4.16).

4.6.5 *Implications for Mars*

The ridge-forming processes observed for the Morrison ridges—channel-belt construction through river migration and aggradation, then later exhumation and scarp erosion—are also observed on Mars. There are numerous examples of exposed lateral accretion sets on fluvial ridges on Mars that have been interpreted to represent channel belts of meandering rivers (Cardenas et al., 2018; Kite et al., 2015; Malin and Edgett, 2003), layered sediments that indicate vertical aggradation (DiBiase et al., 2013; Fig. 4.17B), and talus-strewn flank slopes indicating caprock erosion (e.g., Fig. 4.1C). In these cases, due to the combined effects of deposit amalgamation and scarp-retreat erosion, caprock breadth is unlikely to directly represent paleo-channel width, while caprock thickness can be related to paleo-channel depth by Eq. 4.7.

One difference between ridges on Earth and Mars is that the dominant type of erosion has likely been eolian on Mars (e.g., Zimbelman and Griffith, 2010), whereas rainfall and runoff erosion is important for the Morrison Formation. This potentially explains some differences in ridge

morphology, such as the existence of ridges extending for hundreds of kilometers on Mars (Burr et al., 2009; Williams et al., 2013), whereas terrestrial ridges are much shorter; terrestrial ridges are often segmented by fluvial washes (e.g., Figs. 4.7, 4.10, 4.12; Cardenas et al., 2020; Hayden al., 2019; Williams et al., 2009). However, scarp-retreat that causes ridge narrowing likely also occurs on Mars. For example, talus mantling the slopes of some ridges and variable caprock widths suggests erosion by scarp retreat (Fig. 4.1C). The lower value of F (flank slope erosion relative to flank toe erosion) we observed for one ridge in Aeolis Dorsa, if prevalent across Mars, indicates that ridges can grow taller and wider and have better caprock preservation than their terrestrial counterparts for a given set of channel-belt dimensions (B_0, T_0). Therefore, taller and wider ridges on Mars (e.g., Kite et al., 2019) might not necessarily indicate larger martian river channels, or even larger martian channel belts; wider ridges, instead, could simply reflect systematic differences in erosional processes between Mars and Earth. Smaller F also is consistent with longer continuous lengths of ridges on Mars (e.g., Burr et al., 2009; Williams et al., 2013) because higher relief would be needed in order for ridges to reach the toppling threshold (Fig. 4.17D). However, additional work is needed to determine if this explanation for long ridges is applicable across Mars. The toppling threshold is further useful on Mars because where caprocks are heavily degraded and discontinuous, the narrowest caprock widths may be an indicator of caprock thickness (i.e., $B \sim T$ at the threshold of toppling), and caprock thickness, in turn, scales with channel depth (Eq. 4.7).

A useful diagnostic indicator from orbital images that a ridge is an exhumed channel-belt deposit is the occurrence of lateral accretion sets, and LAS also appear to be robust paleo-hydraulic indicators. Though several instances of LAS on Mars have been studied for paleo-hydraulic reconstructions (e.g., Eberswalde and Jezero Craters; e.g., Irwin et al., 2015; Goudge et al., 2018), most occurrences of LAS likely will not be observable from orbit; this requires particular circumstances so that

differential erosion of LAS beds produces a significant texture on the ridge top at a scale that is coarser than the image resolution. Thus, the absence of such features does not imply the absence of a channel-belt deposit. For example, we made field observations of laterally aggrading bars at Wild Horse Mesa (Fig. 4.13A) and Ferron Creek North, but did not observe LAS in the 10 cm/px quadcopter photographs. In the ridges in the nearby Cedar Mountain Formation, Harris (1980) also identified 12 point bars (also documented by Cardenas et al., 2020; Hayden al., 2019; Williams et al., 2009), but the LAS from these deposits are not evident in ~20 cm/px images in Google Earth. Vertical stacking and cross-cutting of ridge-capping sandstone bodies is another indicator for exhumation of a sequence of fluvial strata, rather than a topographically inverted geomorphic surface (DiBiase et al., 2013; Hayden et al., 2019; Kite et al., 2013). Interpreting channel belts from this method likely has a lower rate of false negatives than searching for LAS, but stratigraphic offsets can be only decimeters to meters in cases (e.g., Figs. 4.7D, 4.10D, 4.12D), which also can be difficult to detect on Mars.

4.7 Conclusions

Ridges in the Morrison Formation, Utah, stand 4-24 m above the surrounding plains, and have caprocks 1.4-4.9 m thick and 10-50 m in breadth. The ridges are composed of a caprock sandstone that overlies mudstone. The sandstone bodies contain dune trough cross strata and bar-scale lateral accretion sets that indicate deposits from aggrading and laterally migrating rivers, and therefore are channel-belt deposits, rather than channel fills. Ridge caprocks occur at distinct stratigraphic levels, and reflect exhumation of a thick sequence of sedimentary strata formed over millions of years, rather than topographically inverted channels. Comparison to outcrop exposures showed that channel-belt sandstones have narrowed by 50-90% during exhumation to form a ridge, removing neighboring floodplain mudstones, overbank sandstones and levees, and major sections of

the channel belt. A new scarp-retreat model describes ridge relief growth due to differential erosion between the mudstone flanks and capping sandstone, which causes ridge narrowing by flank erosion and flank steepening in response to talus accumulation. Using the model, the original un-eroded channel-belt dimensions can be estimated from measurements of ridge relief and caprock thickness.

We estimated the paleo-channel depth and discharge based on well-tested relations that rely on observations of grain size and dune- and bar- cross-strata set thickness, and used these estimates to evaluate paleo-hydraulic reconstruction methods that can be used on Mars because they rely only on remote sensing observations. The most reliable methods were to use caprock thickness as a proxy for river depth ($T/d = 1.5$) or to use the radius of curvature of lateral accretion sets (LAS) as a proxy for river width ($w/C_{LAS} = 0.5$). LAS curvature can be measured from curvilinear features on ridge tops that result from the intersection of LAS beds, formed during meandering, with the deflating land surface. These features on Mars are often interpreted as constructional scroll bars, or levees, but are more consistent with eroded tops of LAS. Ridge widths can be larger or smaller than paleo-channel widths depending on the relative amounts of channel lateral migration during channel-belt formation and scarp retreat during ridge formation. In the Morrison Formation, these two processes largely offset to give ridge widths similar to the estimated paleo-channel widths, but we do not expect this result to be general.

The ridge-forming processes observed in the Morrison Formation are also observed on Mars, including ridges at multiple stratigraphic levels and LAS, which supports formation by exhumation of channel belts, rather than topographic inversion of channels. An example ridge in Aeolis Dorsa, Mars, contains LAS traces suggesting that it is an exhumed channel belt. Using caprock thickness and radius of curvature of LAS to reconstruct river discharge yields similar results. In contrast, using ridge width or ridge centerline curvature, under the inverted channel hypothesis, results in discharges

30-500 times larger. Another example ridge has caprock and flank dimensions that match predictions from the scarp-retreat erosion model—including decreasing ridge breadth with increasing ridge relief—but with lower relative erodibility of the ridge flank than the Morrison ridges. Thus, the generally wider, longer, and more continuous ridge segments on Mars, as compared to Earth, might imply differences in erosion processes rather than larger river channels or channel belts on Mars.

Channel belt exhumation implies that ridges represent fluvial strata deposited over geologic time rather than a preserved landscape at a snapshot in time. Thus, the potential preservation of fluvial strata in ridges makes them optimal targets for exploration with upcoming rover missions.

Acknowledgments, Samples, and Data

The authors wish to thank the members of Caltech's fall 2015 advanced field course (Joe Biasi, Austin Chadwick, Florian Hoffman, Ellen Leask, Luca Malatesta, and Marshall Trautman) for field assistance. Thanks to Jay Dickson for the HiRISE stereo DEM analyzed in Figure 17, and to NSF National Center for Airborne Laser Mapping for the lidar for the Ferron Creek sites (seed grant Project ID 2016-06). Thanks also to Tim Goudge and Becky Williams for formal reviews that helped us improve the manuscript. This work was supported by NASA (grant NNX16AQ81G to MPL and graduate fellowship support 80NSSC17K0492 to ATH). The authors have no real or perceived financial conflicts of interest.

Data availability statement

Supplemental information includes SI Table 1 (raw ridge measurements), SI Table 2 (raw sedimentology measurements), and SI Table 3 (summary measurements). The lidar DEM of the Ferron Creek field sites is on the NCALM website (http://calm.geo.berkeley.edu/ncalm/dtc.html),

the HiRISE stereo DEMs are accessible on the Geoscience node of the NASA Planetary Data System (https://pds-geosciences.wustl.edu/dataserv/default.htm),.

4.8 Works cited

Allen, P., L. Cabrera, F. Colombo and A. Matter (1983). "Variations in fluvial style on the Eocene–Oligocene alluvial fan of the Scala Dei Group, SE Ebro Basin, Spain." Journal of the Geological Society **140**(1): 133-146.

Bagnold, R. (1941). The Physics of Blown Sand and Desert Dunes. New York, William Morrow & Company.

Balme, M. R., S. Gupta, J. M. Davis, P. Fawdon, P. M. Grindrod, J. C. Bridges, E. Sefton-Nash and R. M. E. Williams (2020). "Aram Dorsum: An Extensive Mid-Noachian Age Fluvial Depositional System in Arabia Terra, Mars." Journal of Geophysical Research: Planets **125**(5): e2019JE006244.

Bhattacharya, J. P., P. Copeland, T. F. Lawton and J. Holbrook (2016). "Estimation of source area, river paleo-discharge, paleoslope, and sediment budgets of linked deep-time depositional systems and implications for hydrocarbon potential." Earth-Science Reviews **153**: 77-110.

Blum, M., J. Martin, K. Milliken and M. Garvin (2013). "Paleovalley systems: Insights from Quaternary analogs and experiments." Earth-Science Reviews **116**(0): 128-169.

Bradley, R. W. and J. G. Venditti (2017). "Reevaluating dune scaling relations." Earth-Science Reviews **165**: 356-376.

Bridge, J. (2003). Rivers and Floodplains. Malden, Mass, Blackwell Publishing.

Bryant, M., P. Falk and C. Paola (1995). "Experimental study of avulsion frequency and rate of deposition." Geology **23**(4): 365.

Burr, D. M., M.-T. Enga, R. M. E. Williams, J. R. Zimbelman, A. D. Howard and T. A. Brennand (2009). "Pervasive aqueous paleoflow features in the Aeolis/Zephyria Plana region, Mars." Icarus **200**(1): 52-76.

Burr, D. M., R. M. E. Williams, K. D. Wendell, M. Chojnacki and J. P. Emery (2010). "Inverted fluvial features in the Aeolis/Zephyria Plana region, Mars: Formation mechanism and initial paleodischarge estimates." Journal of Geophysical Research: Planets **115**(E07011).

Cardenas, B. T., D. Mohrig and T. A. Goudge (2018). "Fluvial stratigraphy of valley fills at Aeolis Dorsa, Mars: Evidence for base-level fluctuations controlled by a downstream water body." GSA Bulletin **130**(3-4): 484-498.

Cardenas, B. T., D. Mohrig, T. A. Goudge, C. M. Hughes, J. S. Levy, T. E. Swanson, J. Mason and F. Zhao (2019). "Anatomy of Exhumed River-channel Belts: Bedform- to Belt-scale Kinematics of the Cretaceous Cedar Mountain Formation, Utah, USA." EarthArXiv.

Chesley, J. T. and A. L. Leier (2018). "Sandstone-Body Variability in the Medial–Distal Part of an Ancient Distributive Fluvial System, Salt Wash Member of the Morrison Formation, Utah, USA." Journal of Sedimentary Research **88**(5): 568-582.

Christiansen, E. H., B. J. Kowallis, M. J. Dorais, G. L. Hart, C. N. Mills, M. Pickard and E. Parks (2015). "The record of volcanism in the Brushy Basin Member of the Morrison

Formation: Implications for the Late Jurassic of western North America." Geological Society of America Special Papers **513**: SPE513-511.

Clarke, J. D. A. and C. R. Stoker (2011). "Concretions in exhumed and inverted channels near Hanksville Utah: implications for Mars." International Journal of Astrobiology **10**(3): 161-175.

Davis, J. M., M. Balme, P. M. Grindrod, R. M. E. Williams and S. Gupta (2016). "Extensive Noachian fluvial systems in Arabia Terra: Implications for early Martian climate." Geology **44**(10): 847-850.

Davis, J. M., S. Gupta, M. Balme, P. M. Grindrod, P. Fawdon, Z. I. Dickeson and R. M. E. Williams (2019). "A Diverse Array of Fluvial Depositional Systems in Arabia Terra: Evidence for mid-Noachian to Early Hesperian Rivers on Mars." Journal of Geophysical Research: Planets **124**(7): 1913-1934.

Demko, T. M., B. S. Currie and K. A. Nicoll (2004). "Regional paleoclimatic and stratigraphic implications of paleosols and fluvial/overbank architecture in the Morrison Formation (Upper Jurassic), Western Interior, USA." Sedimentary Geology **167**(3): 115-135.

Derr, M. E. (1974). Sedimentary structure and depositional environment of paleochannels in the Jurassic Morrison Formation near Green River, Utah, Brigham Young University, Dept. of Geology. **21:** 3-39.

DiBiase, R. A., A. B. Limaye, J. S. Scheingross, W. W. Fischer and M. P. Lamb (2013). "Deltaic deposits at Aeolis Dorsa: Sedimentary evidence for a standing body of water on the northern plains of Mars." Journal of Geophysical Research: Planets **118**(6): 1285-1302.

Doelling, H. H., P. A. Kuehne, G. C. Willis and J. B. Ehler (2015). Geologic Map of the San Rafael Desert 30'x60' Quadrangle, Emery and Grand Counties, Utah. UT, Utah Geological Survey.

Dury, G. H. (1976). "Discharge prediction, present and former, from channel dimensions." Journal of Hydrology **30**(3): 219-245.

Eaton, B. (2013). "Hydraulic geometry: empirical investigations and theoretical approaches." Treatise on geomorphology, fluvial geomorphology **9**: 313-329.

Einstein, H. A. (1950). The bed-load function for sediment transportation in open channel flows, United States Department of Agriculture. **1026**.

Engelund, F. and E. Hansen (1967). A monograph on sediment transport in alluvial streams, Tekniskforlag Skelbrekgade 4, Copenhagen V, Denmark.

Ferguson, R. J. and G. J. Brierley (1999). "Levee morphology and sedimentology along the lower Tuross River, south-eastern Australia." Sedimentology **46**(4): 627-648.

Friend, P. F., M. J. Slater and R. C. Williams (1979). "Vertical and lateral building of river sandstone bodies, Ebro Basin, Spain." Journal of the Geological Society **136**(1): 39-46.

Galli, K. G. (2014). "Fluvial architecture element analysis of the Brushy basin Member, Morrison Formation, Western Colorado, USA." Volumina Jurassica **12**(2): 69-106.

Ganti, V., A. J. Chadwick, H. J. Hassenruck-Gudipati and M. P. Lamb (2016). "Avulsion cycles and their stratigraphic signature on an experimental backwater-controlled delta." Journal of Geophysical Research: Earth Surface **121**(9): 1651-1675.

Ganti, V., Z. Chu, M. P. Lamb, J. A. Nittrouer and G. Parker (2014). "Testing morphodynamic controls on the location and frequency of river avulsions on fans versus deltas: Huanghe (Yellow River), China." Geophysical Research Letters **41**(22): 7882-7890.

Ganti, V., M. P. Lamb and B. McElroy (2014). "Quantitative bounds on morphodynamics and implications for reading the sedimentary record." Nature Communications **5**: 3298.

Gibling, M. R. (2006). "Width and thickness of fluvial channel bodies and valley fills in the geological record: A literature compilation and classification." Journal of Sedimentary Research **76**(5): 731-770.

Glade, R. C. and R. S. Anderson (2018). "Quasi-steady evolution of hillslopes in layered landscapes: An analytic approach." Journal of Geophysical Research: Earth Surface **123**(1): 26-45.

Glade, R. C., R. S. Anderson and G. E. Tucker (2017). "Block-controlled hillslope form and persistence of topography in rocky landscapes." Geology **45**(4): 311-314.

Goudge, T. A., D. Mohrig, B. T. Cardenas, C. M. Hughes and C. I. Fassett (2018). "Stratigraphy and paleohydrology of delta channel deposits, Jezero crater, Mars." Icarus **301**: 58-75.

Hajek, E. A. and P. L. Heller (2012). "Flow-Depth Scaling In Alluvial Architecture and Nonmarine Sequence Stratigraphy: Example from the Castlegate Sandstone, Central Utah, U.S.A." Journal of Sedimentary Research **82**(2): 121-130.

Hajek, E. A. and M. A. Wolinsky (2012). "Simplified process modeling of river avulsion and alluvial architecture: Connecting models and field data." Sedimentary Geology **257-260**: 1-30.

Harris, D. R. (1980). Exhumed paleochannels in the Lower Cretaceous Cedar Mountain Formation near Green River, Utah, Brigham Young University. **27:** 51-66.

Hartley, A. J., A. Owen, A. Swan, G. S. Weissmann, B. I. Holzweber, J. Howell, G. Nichols and L. Scuderi (2015). "Recognition and importance of amalgamated sandy meander belts in the continental rock record." Geology **43**(8): 679-682.

Hasiotis, S. T. (2004). "Reconnaissance of Upper Jurassic Morrison Formation ichnofossils, Rocky Mountain Region, USA: paleoenvironmental, stratigraphic, and paleoclimatic significance of terrestrial and freshwater ichnocoenoses." Sedimentary Geology **167**(3-4): 177-268.

Hayden, A. T., M. P. Lamb, W. W. Fischer, R. C. Ewing, B. McElroy and R. M. E. Williams (2019). "Formation of sinuous ridges by inversion of river-channel belts in Utah, USA, with implications for Mars." Icarus **332**: 92-110.

Heller, P. L., D. Ratigan, S. Trampush, A. Noda, B. McElroy, J. Drever and S. Huzurbazar (2015). "Origins of Bimodal Stratigraphy In Fluvial Deposits: An Example From the Morrison Formation (Upper Jurassic), Western USA." Journal of Sedimentary Research **85**(12): 1466-1477.

Hickin, E. J. (1978). "Mean flow structure in meanders of the Squamish River, British Columbia." Canadian Journal of Earth Sciences **15**(11): 1833-1849.

Hughes, C. M., B. T. Cardenas, T. A. Goudge and D. Mohrig (2019). "Deltaic deposits indicative of a paleo-coastline at Aeolis Dorsa, Mars." Icarus **317**: 442-453.

Jacobsen, R. E. and D. M. Burr (2018). "Errors in Martian paleodischarges skew interpretations of hydrologic history: Case study of the Aeolis Dorsa, Mars, with insights from the Quinn River, NV." Icarus **302**: 407-417.

Jerolmack, D. J. and D. Mohrig (2007). "Conditions for branching in depositional rivers." Geology **35**(5): 463-466.

Jerolmack, D. J., D. Mohrig, M. T. Zuber and S. Byrne (2004). "A minimum time for the formation of Holden Northeast fan, Mars." Geophysical Research Letters **31**(21).

Jerolmack, D. J. and J. B. Swenson (2007). "Scaling relationships and evolution of distributary networks on wave-influenced deltas." Geophysical Research Letters **34**(23).

Kirkland, J. I., R. L. Cifelli, B. B. Britt, D. L. Burge, F. L. DeCourten, J. G. Eaton and J. M. Parrish (1999). "Distribution of vertebrate faunas in the Cedar Mountain Formation, east-central Utah." Vertebrate Paleontology in Utah: Utah Geological Survey Miscellaneous Publication **1**: 201-217.

Kite, E. S., A. D. Howard, A. Lucas and K. W. Lewis (2015a). "Resolving the era of river-forming climates on Mars using stratigraphic logs of river-deposit dimensions." Earth and Planetary Science Letters **420**: 55-65.

Kite, E. S., A. D. Howard, A. S. Lucas, J. C. Armstrong, O. Aharonson and M. P. Lamb (2015b). "Stratigraphy of Aeolis Dorsa, Mars: Stratigraphic context of the great river deposits." Icarus **253**(0): 223-242.

Kite, E. S., A. Lucas and C. I. Fassett (2013). "Pacing early Mars river activity: Embedded craters in the Aeolis Dorsa region imply river activity spanned ≳(1–20)Myr." Icarus **225**(1): 850-855.

Kite, E. S., D. P. Mayer, S. A. Wilson, J. M. Davis, A. S. Lucas and G. S. de Quay (2019). "Persistence of intense, climate-driven runoff late in Mars history." Science Advances **5**(3): eaav7710.

Kjemperud, A. V., E. R. Schomacker and T. A. Cross (2008). "Architecture and stratigraphy of alluvial deposits, Morrison formation (Upper Jurassic), Utah." AAPG bulletin **92**(8): 1055-1076.

Leclair, S. F. and J. S. Bridge (2001). "Quantitative interpretation of sedimentary structures formed by river dunes." Journal of Sedimentary Research **71**(5): 713-716.

Leeder, M. (1975). "Pedogenic carbonates and flood sediment accretion rates: a quantitative model for alluvial arid-zone lithofacies." Geological Magazine **112**(3): 257-270.

Lefort, A., D. M. Burr, R. A. Beyer and A. D. Howard (2012). "Inverted fluvial features in the Aeolis-Zephyria Plana, western Medusae Fossae Formation, Mars: Evidence for post-formation modification." Journal of Geophysical Research: Planets **117**(E3).

Lefort, A., D. M. Burr, F. Nimmo and R. E. Jacobsen (2015). "Channel slope reversal near the Martian dichotomy boundary: Testing tectonic hypotheses." Geomorphology **240**: 121-136.

Leopold, L. B., M. G. Wolman and J. P. Miller (1964). Fluvial processes in geomorphology, Courier Corporation.

Mackey, S. D. and J. S. Bridge (1995). "Three-dimensional model of alluvial stratigraphy: theory and application." Journal of Sedimentary Research **65**(1).

Malin, M. C. and K. S. Edgett (2003). "Evidence for persistent flow and aqueous sedimentation on early Mars." Science **302**(5652): 1931-1934.

Mason, J. and D. Mohrig (2019). "Scroll bars are inner bank levees along meandering river bends." Earth Surface Processes and Landforms **44**: 2649-2659.

McLaurin, B. T. and R. J. Steel (2007). "Architecture and origin of an amalgamated fluvial sheet sand, lower Castlegate Formation, Book Cliffs, Utah." Sedimentary Geology **197**(3): 291-311.

Mohrig, D., P. L. Heller, C. Paola and W. J. Lyons (2000). "Interpreting avulsion process from ancient alluvial sequences: Guadalope-Matarranya system (northern Spain) and Wasatch Formation (western Colorado)." Geological Society of America Bulletin **112**(12): 1787-1803.

Moore, J. M., A. D. Howard, W. E. Dietrich and P. M. Schenk (2003). "Martian layered fluvial deposits: Implications for Noachian climate scenarios." Geophysical Research Letters **30**(24).

Musial, G., J.-Y. Reynaud, M. K. Gingras, H. Féniès, R. Labourdette and O. Parize (2012). "Subsurface and outcrop characterization of large tidally influenced point bars of the Cretaceous McMurray Formation (Alberta, Canada)." Sedimentary Geology **279**: 156-172.

Nanson, G. C. (1980). "Point bar and floodplain formation of the meandering Beatton River, northeastern British Columbia, Canada." Sedimentology **27**(1): 3-29.

Owen, A., P. E. Jupp, G. J. Nichols, A. J. Hartley, G. S. Weissmann and D. Sadykova (2015a). "Statistical estimation of the position of an apex: application to the geological record." Journal of Sedimentary Research **85**(2): 142-152.

Owen, A., G. J. Nichols, A. J. Hartley, G. S. Weissmann and L. A. Scuderi (2015b). "Quantification of a Distributive Fluvial System: The Salt Wash DFS of the Morrison Formation, SW U.S.A." Journal of Sedimentary Research **85**(5): 544-561.

Pain, C., J. Clarke and M. Thomas (2007). "Inversion of relief on Mars." Icarus **190**(2): 478-491.

Pain, C. F. and C. D. Ollier (1995). "Inversion of relief — a component of landscape evolution." Geomorphology **12**(2): 151-165.

Palucis, M. C., W. E. Dietrich, A. G. Hayes, R. M. E. Williams, S. Gupta, N. Mangold, H. Newsom, C. Hardgrove, F. Calef and D. Y. Sumner (2014). "The origin and evolution of the Peace Vallis fan system that drains to the Curiosity landing area, Gale Crater, Mars." Journal of Geophysical Research: Planets **119**(4): 705-728.

Paola, C. and L. Borgman (1991). "Reconstructing random topography from preserved stratification." Sedimentology **38**(4): 553-565.

Peterson, F. (1984). "Fluvial sedimentation on a quivering craton: influence of slight crustal movements on fluvial processes, Upper Jurassic Morrison Formation, western Colorado Plateau." Sedimentary Geology **38**(1-4): 21-49.

Reijenstein, H. M., H. W. Posamentier and J. P. Bhattacharya (2011). "Seismic geomorphology and high-resolution seismic stratigraphy of inner-shelf fluvial, estuarine, deltaic, and marine sequences, Gulf of Thailand." AAPG Bulletin **95**(11): 1959-1990.

Robinson, J. W. and P. J. McCabe (1997). "Sandstone-body and shale-body dimensions in a braided fluvial system: Salt Wash Sandstone Member (Morrison Formation), Garfield County, Utah." AAPG bulletin **81**(8): 1267-1291.

Schumm, S. A. (1972). "Fluvial paleochannels." Special Publication - Society of Economic Paleontologists and Mineralogists.

Shiers, M. N., N. P. Mountney, D. M. Hodgson and L. Colombera (2018). Controls on the depositional architecture of fluvial point-bar elements in a coastal-plain succession. Fluvial Meanders and Their Sedimentary Products in the Rock Record. A. Ielpi, M. Ghinassi, R. H. Rainbird and D. Ventra, Special Publication International Association of Sedimentologists. **48:** 15-46.

Slingerland, R. and N. D. Smith (2004). "River avulsions and their deposits." Annual Review of Earth Planetary Sciences **32**: 257-285.

Smith, N. D. (1972). "Some sedimentological aspects of planar cross-stratification in a sandy braided river." Journal of Sedimentary Research **42**(3): 624-634.

Stokes, W. L. (1944). "Morrison Formation and related deposits in and adjacent to the Colorado Plateau." Geological Society of America Bulletin **55**(8): 951-992.

Stokes, W. L. (1961). Fluvial and eolian sandstone bodies in Colorado Plateau. SP 22: Geometry of Sandstone Bodies, American Association of Petroleum Geologists. **A055:** 151-178.

Trampush, S. M., S. Huzurbazar and B. J. McElroy (2014). "Empirical assessment of theory for bankfull characteristics of alluvial channels." Water Resources Research **50**(12): 9211-9220.

Trujillo, K. C. and B. J. Kowallis (2015). "Recalibrated legacy 40Ar/39Ar ages for the Upper Jurassic Morrison Formation, Western Interior, USA." Geology of the Intermountain West **2**(1): 1-8.

Turner, C. E. and F. Peterson (2004). "Reconstruction of the Upper Jurassic Morrison Formation extinct ecosystem—a synthesis." Sedimentary Geology **167**(3-4): 309-355.

Tyler, N. and F. G. Ethridge (1983). Fluvial Architecture of Jurassic Uranium-Bearing Sandstones, Colorado Plateau, Western United States. Modern and Ancient Fluvial Systems. J. D. Collinson and J. Lewin, Wiley Online Library.

van de Lageweg, W. I., W. M. van Dijk, A. W. Baar, J. Rutten and M. G. Kleinhans (2014). "Bank pull or bar push: What drives scroll-bar formation in meandering rivers?" Geology **42**(4): 319-322.

Van den Berg, J. H. (1995). "Prediction of alluvial channel pattern of perennial rivers." Geomorphology **12**(4): 259-279.

Ward, D. J., M. M. Berlin and R. S. Anderson (2011). "Sediment dynamics below retreating cliffs." Earth Surface Processes and Landforms **36**(8): 1023-1043.

Williams, G. P. (1986). "River meanders and channel size." Journal of Hydrology **88**(1-2): 147-164.

Williams, G. P. (1988). Paleofluvial estimates from dimensions of former channels and meanders. Flood Geomorphology. V. R. Baker, R. C. Kochel and P. C. Patton. New York, John Wiley & Sons**:** 321-334.

Williams, R. M. E., T. C. Chidsey Jr and D. E. Eby (2007). "Exhumed paleochannels in central Utah—Analogs for raised curvilinear features on Mars." Central Utah: Diverse Geology of a Dynamic Landscape: 221-235.

Williams, R. M. E., R. P. Irwin, D. M. Burr, T. Harrison and P. McClelland (2013). "Variability in martian sinuous ridge form: Case study of Aeolis Serpens in the Aeolis Dorsa, Mars, and insight from the Miracкina paleoriver, South Australia." Icarus **225**(1): 308-324.

Williams, R. M. E., R. P. Irwin and J. R. Zimbelman (2009). "Evaluation of paleohydrologic models for terrestrial inverted channels: Implications for application to martian sinuous ridges." Geomorphology **107**(3-4): 300-315.

Williams, R. M. E., R. P. Irwin, J. R. Zimbelman, T. C. Chidsey and D. E. Eby (2011). "Field guide to exhumed paleochannels near Green River, Utah: Terrestrial analogs for sinuous ridges on Mars." Geological Society of America Special Papers **483**: 483-505.

Witkind, I. J. (2004). Geologic map of the Huntington 30'x60' Quadrangle, Carbon, Emery, Grand, and Uintah Counties, Utah, Utah Geological Survey.

Yingling, V. L. and P. Heller (1992). "Timing and record of foreland sedimentation during the initiation of the Sevier orogenic belt in central Utah." Basin Research **4**(3-4): 279-290.

Zimbelman, J. R. and L. J. Griffin (2010). "HiRISE images of yardangs and sinuous ridges in the lower member of the Medusae Fossae Formation, Mars." Icarus **205**(1): 198-210.

Chapter 5

5 CONSTRAINING THE TIMESPAN OF FLUVIAL ACTIVITY FROM THE INTERMITTENCY OF SEDIMENT TRANSPORT ON EARTH AND MARS: EBRO BASIN, SPAIN

Hayden, A.T., Lamb, M.P., McElroy, B.J., Myrow, P., Mohrig, D.C., Williams, R.M.E., Cuevas Martinez, J.L., Cardenas, B.T., Findlay, C.P., Ewing, R.C.
In preparation for submission to JGR: Earth Surface

Key Points

- Rivers transport sediment intermittently, and a factor is needed to estimate timespan of fluvial activity from deposit volume and bankfull river characteristics.
- Using field observations and compiled data, intermittency factors range from 0.003-0.6, independent of timescale, grainsize and climate.
- Application to Mars implies fluvial activity over thousands to millions of years

Abstract

The timespan of fluvial activity is a key gap in our understanding of ancient environments on Earth and Mars. By mass balance, timespan can be estimated for depositional rivers by dividing deposit volume by river sediment flux, the latter of which can be constrained for bankfull conditions using fluvial strata. However, rivers transport disproportionate amounts of sediment during rare bankfull floods, and an intermittency factor that accounts for the fraction of the sediment load transported during bankfull conditions is needed to properly proportion time from ancient deposits. Here we investigated fluvial fan deposits from the Miocene Caspe Formation in Spain as an analog to fans on Mars because it has exhumed channel belts that create sinuous ridges in the modern topography, similar to those observed on Mars. We used the thicknesses of dune sets, bar sets, and channel belts to reconstruct bankfull channel dimensions and sediment flux. Combined with estimated total deposit volume and previous constraints on depositional timespan (~9 Myr), we

calculated an intermittency factor of 0.002. This intermittency factor, averaged over millions of years, is surprisingly similar to values we calculated for modern rivers over the past century, and for fans and deltas spanning timescales of months to millions of years, which span 0.00082 to 1.6 with a median value of 0.10. The intermittency factor does not correlate with bed-material grainsize or climate aridity, but does correlate with sediment supply. Our calculated intermittency factors are smaller than those previously assumed for Mars, implying potentially longer depositional timespans of 10^4-10^6 years for martian fans and deltas.

5.1 Introduction

It is unclear whether early Mars had a long-lived, stable hydrological cycle or multiple intermittent, short-lived, river-forming episodes (e.g., Wordsworth et al., 2013; 2018; Ramirez and Craddock, 2018). There is clear geologic evidence for rivers and lakes across Mars during the Noachian/Early Hesperian time periods in the form of river valleys (Craddock and Howard, 2002; Hynek et al., 2010), river, fan, and deltaic deposits (Moore et al., 2003; Fassett and Head, 2005; Burr et al., 2009; 2010), lake deposits (Grotzinger et al., 2015), crater lakes with outflow channels (Goudge et al., 2012), and crater-erosion patterns (Forsberg-Tayler et al., 2004). The era of river-forming climates appears split into at least two episodes based on distinctions between old, degraded valley networks and younger, better-preserved valley networks (Baker and Partridge, 1986; Howard et al., 2005). However, climate model predictions range from long-lived greenhouse climate (e.g., Halevy et al., 2007; Ramirez et al., 2014), to transient greenhouse conditions (Segura et al., 2002; Mischna et al., 2013), to locally wet environments (Fairen, 2010; Wordsworth et al., 2013). Furthermore, river activity durations calculated from rates of valley network erosion (e.g., Orofino et al., 2018; Rosenberg et al., 2019) and fluvial fan and delta deposition (e.g., Jerolmack et al., 2004; Kleinhans, 2005; Morgan et al., 2014) have high uncertainty and are not diagnostic of one climate

model or another. A better understanding of the timespan of river activity on Mars would help constrain early Mars climate and habitability.

One possible way to constrain the timespan of fluvial activity would be to compare the volume of sediment deposited in a landform (e.g., a fan or delta) to the fluvial sediment flux. However, this comparison is hampered because we do not have a good understanding of the intermittency of sediment transporting flood events across different climates and timescales (Sadler, 1981). For example, sediment flux in modern terrestrial rivers varies over orders of magnitude from low flows to floods (Fig. 5.1) and can be zero for long durations (e.g., Phillips et al., 2013; Lajeunesse et al., 2018). Furthermore, it is unclear whether the intermittency in sediment flux observed for modern rivers over timespans of decades should be similar over the thousands to millions of years that are necessary to build large sedimentary fans and deltas.

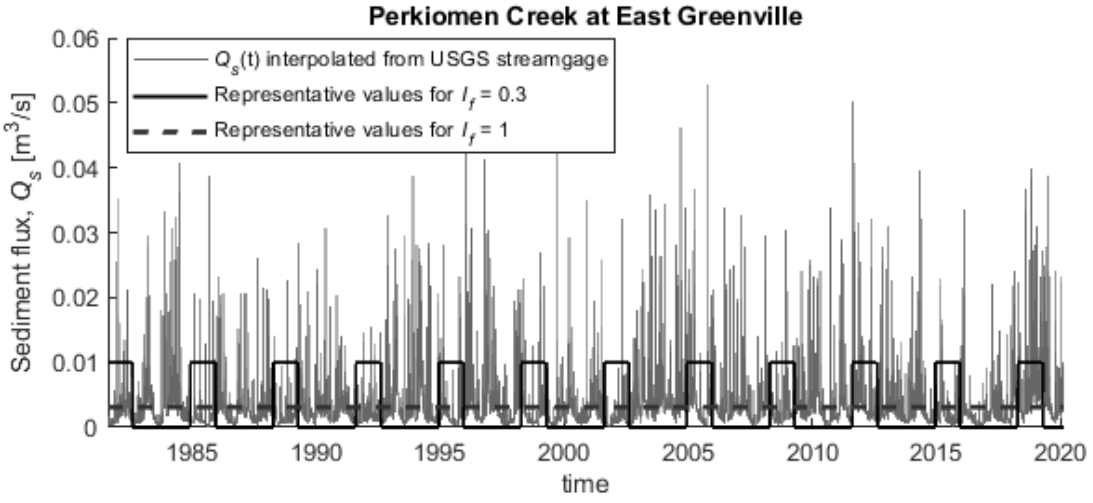

Figure 5.1–Sediment discharge (gray line) can be approximated by a single value, such as bankfull flow that occurs intermittently (black line). Knowing the volume of sediment (integral of gray curve) and bankfull sediment flux (nonzero values on black line; 0.01 m3/s) allows calculation of intermittency factor (fraction of time black line is nonzero) by adjusting intermittency factor so that the integral of the black line matches that of the gray line. We have illustrated $I_f = 0.3$ The dashed line represents the constant-flow case ($I_f = 1$).

Despite the inherent variability in fluvial sediment flux, over geomorphic timescales sediment transport is often well characterized by a reoccurring discharge event that transports the bulk of the bed-material sediment load (Wolman and Miller, 1960). This value can be calculated as the maximum of the product of the water-discharge probability distribution times the magnitude of sediment flux for those flow events, and it corresponds well to the bankfull water discharge, i.e., the discharge that fills the channel to the brim (Wolman and Miller, 1960). The bankfull discharge is the event that appears to have the largest influence on channel morphology, since it transports the most sediment and fills the channel, and therefore scales with channel width, depth, slope, and curvature. Consequently, geomorphic models often simplify the natural world by simulating only bankfull conditions (e.g., Tucker and Bras, 2000; Snyder et al., 2003). Bankfull conditions can also more readily be reconstructed from sedimentary deposits (e.g., bar strata) because some sedimentary structures scale with the size of the channel (e.g., Allen, 1965; Mohrig et al., 2000), whereas flow variability is difficult to decipher (Ganti et al., 2011).

To apply the bankfull-discharge concept to modeling the long-term evolution of alluvial rivers and fans, Paola et al. (1992) introduced the intermittency factor, I_f, which is the fraction of total time it would take to transport the sediment load if only continuous bankfull flows occurred (Fig. 5.1). That is,

$$I_f = \sum Q_s(t)/(Q_{s,bf}\sum t), \qquad \text{Eq. 5.1}$$

in which Q_s is the time-dependent sediment flux and $Q_{s,bf}$ is the sediment flux during bankfull conditions. The intermittency factor is similar in spirit to the recurrence interval of the bankfull discharge or the annual-averaged bankfull duration used by Holbrook and Wanas (2014), but is formulated based on sediment flux, not water discharge. Typically, equation (5.1) is applied only to the bed-material load, neglecting the washload (typically mud), because it is the bed-material load

(which includes both bedload and suspended bed-material) that tends to most strongly influence fluvial morphodyamics (e.g., Sinha and Parker, 1996; Church, 2006). The intermittency factor is a powerful tool for constraining the depositional timespan of sedimentary deposits because the total sediment flux into a depositional basin is the deposit volume (V), and so equation (5.1) can be rearranged to solve for the timespan of fluvial activity,

$$\sum t = V / I_f Q_{s,bf}, \qquad \text{Eq. 5.2}$$

using $\sum Q_s(t) = V$, so long as V represents the accumulated bed-material load.

Only a few measurements of intermittency factors have been reported for modern terrestrial river systems. Sklar and Dietrich (2004) estimated I_f = 0.06 for the gravel-bed Eel River using sediment volume estimated from catchment erosion rates and bankfull bed-material load estimated from magnitude frequency analysis. Wright and Parker (2005) combined USGS stream gage data, sediment-rating curves for suspended bed-material sediment flux, and bankfull survey data and found I_f = 0.26-0.35 for the sand-bedded Atchafalaya, Mississippi, and Red Rivers. Czuba and Foufoula-Georgiou (2014) used similar methods, but employed the Engelund and Hansen (1967) total-sand-load relation to calculate sediment flux, and found I_f = 0.175 for the sand-bedded Minnesota River. Naito et al. (2019) calculated I_f = 0.13 for the lower Yellow River by comparing their modeled bankfull sediment load to the measured mean bed-material load. Despite the lack of field constraints, the intermittency factor concept has been utilized extensively in landscape evolution models, often using an assumed value for I_f ranging from 0.05-1 (e.g., Sinha & Parker, 1996; Cui and Parker, 1998; Parker et al. 1998, Sun et al., 2002; Eke et al., 2014; Tucker et al., 2001; Snyder et al., 2003; Gran et al., 2013; Wickert and Schildgren, 2019; Dong et al. 2016). However, it is unknown whether the intermittency factors measured over decadal to century timescales for

modern rivers apply to longer timescales represented in depositional basins, in which changes in tectonics, climate, and autogenic dynamics may control sediment flux variability (e.g., Paola, 2013).

This intermittency-factor approach (equation (5.2)) is of particular interest in Mars science, where it has been used to estimate the timespan of ancient martian rivers from sedimentary deposits (e.g., Jerolmack et al., 2004; Kleinhans, 2005; Kleinhans et al., 2010; Morgan et al., 2014). Intermittency factors are most often assumed to be between 0.01-0.3—by analogy to bankfull recurrence intervals for water discharge and using a typical flood duration of weeks to months—or assumed to be unity, which serves as a likely upper bound (e.g., Irwin et al., 2015; Morgan et al., 2014; Williams and Weitz, 2014; Fassett & Head, 2005; Barnhart et al., 2009; Matsubara et al., 2015; Kite, 2019). Buhler et al. (2014) attempted to constrain I_f directly for a deposit on Mars (I_f = 0.00008 – 0.004) by dividing the timescale to fill a crater with sediment at the bankfull sediment flux by the formation timescale of nearby Parana Valles. Lapôtre and Ielpi (2020) compared an estimate of sediment-generation timescale to deposition timescale for a fan in Jezero crater and calculated range of I_f = 0.00005 – 0.0001. These values are smaller than those measured on Earth (I_f = 0.06 – 0.3; Wright and Parker, 2005; Czuba and Foufoula-Georgiou, 2014; Naito et al., 2019); however, they represent only a few locations, and there is significant uncertainty in the values and the assumed timespans.

Another issue in applying equation (5.2) to Mars to constrain fluvial timespan is that observations of sedimentary structures are typically needed to constrain bankfull conditions from ancient deposits, and these observations are currently limited to rovers. However, landforms visible from orbit that shows promise to constrain the bankfull geometry of ancient depositional rivers are fluvial ridges (e.g., Burr et al., 2010; Kite et al., 2015). Fluvial ridges are sinuous landforms that resemble channels in planview, but they stand in positive relief (e.g., Fig. 5.2). These landforms

likely reflect the deflation and/or exhumation of river deposits (e.g., DiBiase et al., 2013; Hayden et al., 2019), and on Mars are tied to billions of years of wind erosion. Studies of terrestrial analogs show there are two types of fluvial ridges: channel casts known as *inverted channels* or channel-belt deposits known as *exhumed channel belts* (e.g., Pain and Ollier, 1995; Pain et al., 2007; Williams et al., 2009; Burr et al., 2009; DiBiase et al., 2013; Hayden et al., 2019; Hayden and Lamb, in press). Inverted channels form when a channel is filled with an erosion-resistant material such as lava or coarse sediment, and the neighboring material is eroded away, leaving a ridge with a width that may approximate the original channel form (Burr et al., 2010), and thus allow for bankfull geometries to be measured directly from orbit. Alternatively, ridges formed as exhumed channel belts reflect the geometry of the channel-belt; the channel-belt, in turn, is the region of amalgamated, relatively coarse-grained river deposits that form from river lateral migration and aggradation (Burr et al., 2010; DiBiase et al., 2013; Hayden et al., 2019). Although channel-belts do not reflect the geometry of the river channel, the channel-belt (or fluvial ridge) thickness is a good proxy for river bankfull depth with an appropriate conversion factor of 1-3 (Hayden et al., 2019; Hayden and Lamb, in press).

In this work, we present estimates of intermittency factors for modern rivers and ancient deposits for a number of sites on Earth, and we apply the results to estimate the timespan of river activity on Mars. We present primary observations from the Miocene Guadalope-Matarranya Fan in the Caspe Formation, Spain, which is a large, ancient fluvial fan system with numerous sinuous ridges like those observed on Mars (Section 2). We conducted fieldwork in the Caspe Formation to measure sedimentary structures and ridge geometries (Section 3) to constrain the paleo-hydraulics of the system (Section 4) and estimate the intermittency factor. We also compiled published data from seven other depositional systems and used daily river data from the gaging stations for hundreds of rivers in the U.S. to calculate intermittency factors that average over timescales of 10^{2}-10^{6} years

and for sand- and gravel-bedded rivers (Section 5). Finally, we applied the new intermittency factors to previously studied alluvial deposits in the Aeolis Dorsa region of Mars to estimate the timespan of river activity there (Section 6).

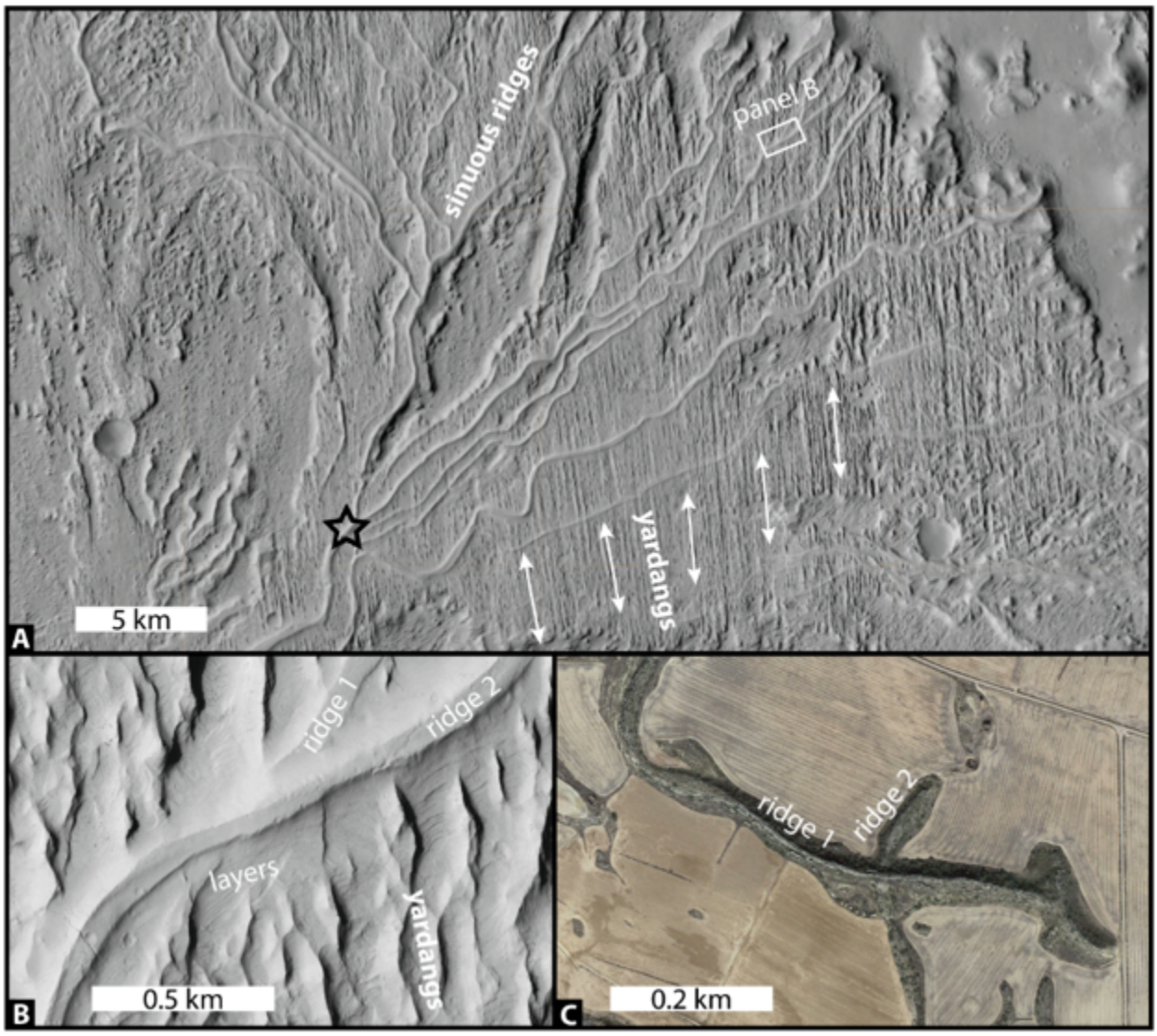

Figure 5.2–Examples of sinuous ridges from the Aeolis Dorsa region of Mars (panels A & B) and the Ebro Basin of Spain (panel C). A) Branching ridges in Aeolis Dorsa (CTX image P08_004336_1742, 151.43, -6.24) with superimposed yardangs. B) HiRISE image (PSP_002279_1735) of the same feature, zoomed in on sinuous ridges crossing with yardangs. The material under the ridge caprock shows clear layering. C) Crossing ridges at our Site 9, surrounded by farmland.

5.2 Field site

Our main terrestrial study site is the Guadalope-Matarranya fan, a large alluvial fan deposit in the Caspe Formation of the Oligocene-Miocene period in the Ebro Basin, Spain (Fig. 5.3). The site enables testing of equation (5.1) because it has abundant exposures of channel belts that can be used to reconstruct paleochannel dimensions (e.g., Cabrera, 1985; Mohrig et al., 2000; Cuevas Martinez et al., 2007; 2010), and constraints on the total timescale of sediment deposition have been measured with magnetostratigraphy (e.g., Barbera et al., 1994; 2001). The deposit furthermore represents an excellent analog for Mars because it exhibits numerous fluvial ridges (Fig. 5.2; DiBiase et al., 2013), and therefore additionally enables analysis of equation (5.1) using a remote-sensing workflow that can be used for Mars.

Modern exposure of the Guadalope-Matarranya fan covers ~3000 km^2 in the south end of the Ebro Basin (Mohrig et al., 2000; Cuevas Martinez et al., 2007; 2010). The Ebro Basin was endorheic throughout the deposition of the Guadalope-Matarranya fan, and all sediment was trapped locally. Deposition occurred in an arid to semi-arid climate (Cabrera & Saez, 1987). The Ebro River began draining the Ebro Basin through the Catalan Coastal Range sometime between 12-7.5 M.a. (Garcia-Castellanos et al., 2015), and it has now exposed at least 400 meters of stratigraphy from the Caspe Formation (Mohrig et al., 2000; Cuevas Martinez et al., 2007; 2010). The partially exposed Puig Moreno anticline runs east-west through the center of the fan, and reported tectonic dips are less than 5° away from the anticline (Fig. 5.3C).

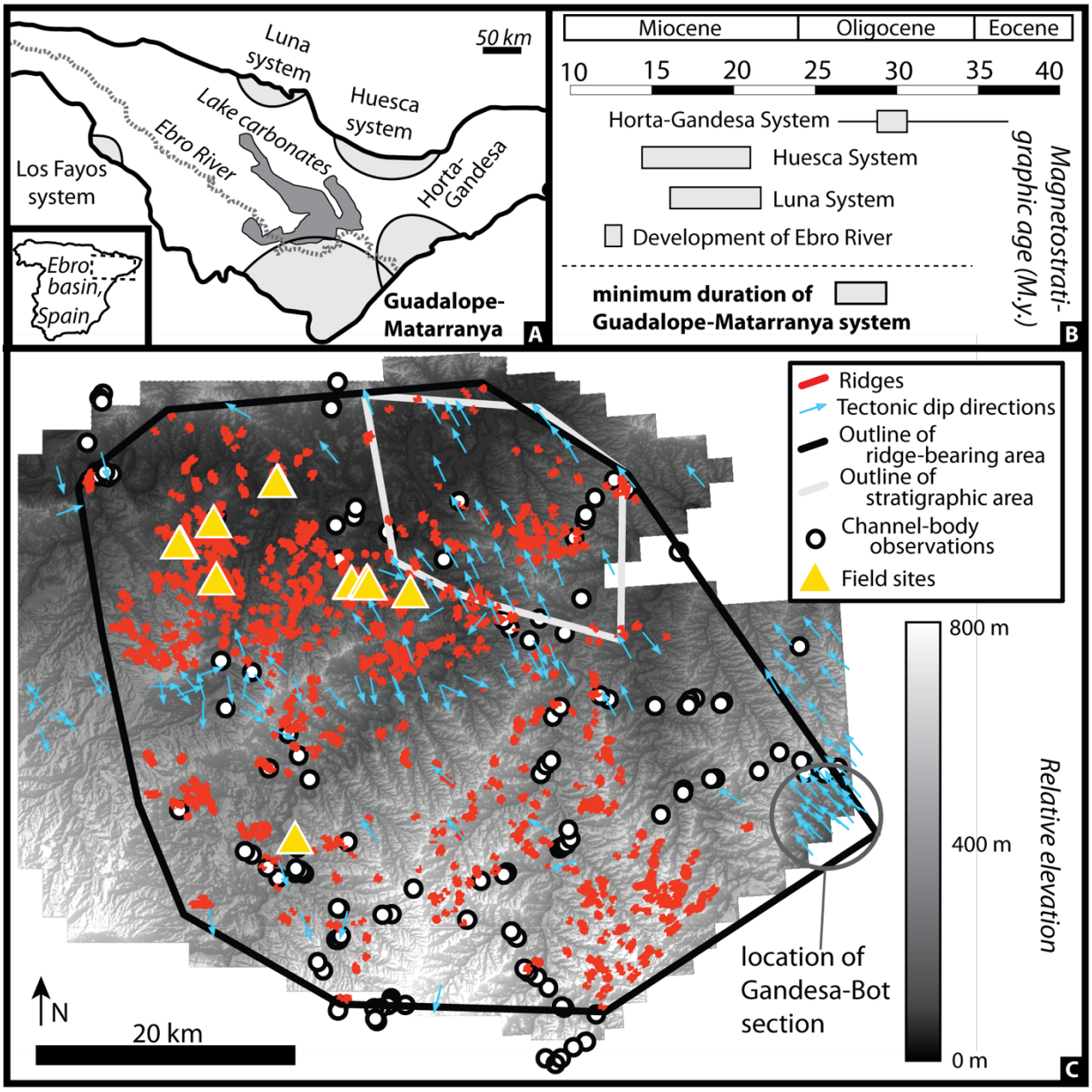

Figure 5.3–Field area. A) Overview of Guadalope-Matarranya system within the Ebro Basin, along with other Oligocene-Miocene fluvial fan systems and the modern Ebro River. B) Magnetostratigraphic data for different fan systems in the Ebro Basin. Horta-Gandesa system dates are from Jones et al., 2004; Swanson-Hysell and Barbeau, 2007; 2008; Garces et al., 2007 (box represents overlap of dates; line represents uncertainty between papers); Guadalope-Matarranya dates are from Gandesa-Bot Section as reported in Valero et al., 2014; all remaining systems are from Perez-Rivares et al., 2018. The maximum duration of the Guadalope-Matarranya fan is from the onset of the Horta-Gandesa System (36 M.a.) to the onset of the Ebro River (12 M.a.) (Jones et al., 2004, Perez-Ribarez et al., 2018), while the minimum duration is dated to be 4 M.y. from the Gandesa-Bot Section (Valero et al., 2014). C) Shaded elevation map (0.5 m/px) of area bearing ridges (red lines). Black outline is the convex hull of the Guadalope-Matarranya Fan determined from ridge-bearing locations and the Gandesa-Bot Section (Barbera et al., 2001; Jones et al., 2004;

Valero et al., 2014). White outline is the area used for the stratigraphic model, determined from the convex hull of an area of aligned tectonic dips (blue arrows). Yellow triangles are the field sites, and white dots are sedimentology measurements from uneroded channel bodies (Mohrig, unpublished).

The Guadalope-Matarranya fan deposit comprises channel-belt deposits made of sandstone and conglomerate (estimated at 2-25% of the deposit; Cuevas Martinez et al., 2010) encased in floodplain deposits comprising mudstone with sandstone sheets (Friend et al., 1979; Cabrera et al., 1985; Cuevas Martinez et al., 2010). Channel belts range from 1-15 meters thick and up to 90 meters wide, with width-to-thickness ratios averaging 6 (Cabrera et al., 1985; Cuevas Martinez et al., 2010). The most common sedimentary structures observed in the channel belts are bar sets, interpreted to represent downstream-migrating alternate bars and laterally accreting bank-attached bars (Friend et al., 1986; Mohrig et al., 2000; Cuevas Martinez et al., 2007; Gonzalez-Bonarino et al., 2010). Many channel bodies display amalgamation of distinct generations of fluvial deposits, some of which are separated by thin mudstone drapes, contain bioturbation, or coincide with erosional surfaces in the floodplain material that indicate gaps between periods of fluvial activity (Mohrig et al., 2000; Cuevas Martinez et al., 2007; 2010). Mohrig et al. (2000) found that most channel belts represent a single generation of bar lateral accretion, although 24% of channel belts showed evidence of multiple stacked accretion sets separated by low angle erosion surfaces (i.e., multiple stories).

Channel-belt paleo-hydraulic indicators vary little across the field area. Flow depths interpreted from bar set thicknesses ranged 1-3.3 meters with a mean of 1.4 meters, and remain constant in a given channel body and across the fan system (Mohrig et al., 2000). Observed changes from south to north include: single-story bodies become more common, grainsize decreases, and

paleo-current directions indicate a distributary geometry (Allen et al., 1983; Cabrera et al., 1985; 2002; Mohrig et al., 2000; Cuevas Martinez et al., 2007).

The southeastern portion of the Guadalope-Matarranya fan where the Guadalope-Matarranya fan interfingers with the Gandesa-Horta Fan has been dated with magnetostratigraphy (Gandesa/Bot sections of Barbera et al., 2001; Jones et al., 2004; Valero et al., 2014). Though the resulting dates have been the subject of debate due to conflicting stratigraphic correlations (Swanson-Hysell, 2007; 2008; Garces et al., 2008), most interpretations, including the most recent (Valero et al., 2014), show a minimum timespan of ~4 Myr, similar to the timespan reported by Mohrig et al. (2000) based on the earlier work of Barberá et al. (1994). The timespan in the Gandesa/Bot section represents a lower bound on timespan of the full Guadalope-Matarranya fan because the dated rocks represent only part of the full stratigraphic interval. For an upper-bound timespan, we use the age constraints for deposition of the entire Ebro Basin succession of 36 M.a. to 12 M.a., giving a depositional timespan of 24 Myr (Jones et al., 2004, Perez-Ribarez et al., 2018).

Sinuous ridges resembling those observed on Mars (e.g., Burr et al., 2009; Williams, 2007) are abundant across the Guadalope-Matarranya fan (Fig. 5.3; Riba et al., 1967; Friend et al., 1979; Cuevas Martinez et al., 2007). Many of the ridges were mapped in prior studies (e.g., Cuevas Martinez et al., 2007). Ridges are typically 100-1000 meters long, although many multi-kilometer ridges exist (Williams, 1975; Mohrig et al., 2000 Cuevas Martinez et al., 2010). Ridge intersections are common, and exhibit both Y- and X-shaped geometries in planview, indicating that channel belts that converge or diverge (Y shapes) or cross at different stratigraphic levels (X shapes) (Cuevas Martinez et al., 2010).

5.3 Methods

In addition to field work at the Ebro Basin to constrain the intermittency factor, we also compiled existing data from six other fluvial depositional systems, and analyzed streamgage data from 200 modern rivers. The methods for each of these three datasets are described below.

5.3.1 Field methods

The main goals of field observations in the Ebro Basin were to understand the origin of the ridges that resemble ridges on Mars, collect sedimentological data to constrain the bankfull channel characteristics and relate these to ridge properties, estimate the total volume of the fan, and calculate the intermittency factor. We visually mapped 883 ridges across the field area using a lidar digital elevation model (DEM) (0.5 m/px; downloaded from the Instituto Geographico Nacional, www.ign.es/) that we processed to highlight the steep slopes of ridge caprocks (Fig. 5.3C). Likely biases in the dataset include undersampling of short ridges within high-ridge-density areas. We then extracted 2388 elevation transects, spaced 50 meters apart, perpendicular to the manually traced centerlines of 237 ridges selected randomly across the field area. We used the transects to characterize caprock width, thickness, and relief, by manually identifying the caprock edges (as the base of an uppermost cliffy unit) and the bottom of the talus-covered flanks (Hayden et al., 2019). Measurements were corrected for the reported tectonic dips of 2° toward 345° (Beltran Cabrera et al., 1992; van den Hurk et al., 1992; Navarro Juli et al., 1993; Hernandez Samaniego et al., 1993; Sola et al., 1992) in a portion of the study area (Fig. 5.3) by adding a plane that has equal-magnitude dip in the opposite direction to the DEM.

Nine specific locations were selected for detailed fieldwork on the basis of ridge prominence in air photos, and observed ridge branching and crossing patterns that may help inform channel-belt bifurcations or stratigraphic stacking patterns. We created stratigraphic models for each of these sites

by rotating the digital elevation models (DEMs) to remove the published local tectonic dip (Beltran Cabrera et al., 1992; van den Hurk et al., 1992; Navarro Juli et al., 1993; Hernandez Samaniego et al., 1993; Sola et al., 1992). We also mapped the field sites with a DJI Phantom 4 quadcopter, and used the images in Agisoft Metashape to create a high-resolution DEM and orthophoto using photogrammetry to aid further analysis of stratigraphy (see Supplement).

To reconstruct bankfull channel geometries and sediment flux, we recorded sedimentary structures and median grainsize following Hayden et al. (2019). Median grainsize was identified visually with a grain-size card. Sedimentary structures of interest were cross-stratification, including ripples, dune sets and bar clinoforms. Ripples are the smallest of the structures, and have heights and wavelengths on the order of 1-5 centimeters (Allen, 1963). Ripple strata could be observed in outcrop and in a few cases on the tops of caprocks (Fig. 5.4). Dune cross beds were apparent in outcrop at decimeter-scale (Fig. 5.4; Allen 1963). We also observed dune sets along ridge tops as rib-and-furrow structures (Fig. 5.4; Stokes, 1961). Bar clinoforms (Fig. 5.4) resembled larger (meter-scale; Allen, 1963) dune cross-strata, but were interpreted as bar strata based on superimposed smaller-scale dune cross sets with differing paleo-current directions, and trains of S-shaped sets that "roll over" at the top, indicating a fully preserved bar structure (Mohrig et al., 2000; Hajek and Heller, 2012). Bar structures were also observed in plan-view on ridge tops as decameter scale linear or curvilinear features that represent the intersection of the cross beds with the deflated land surface (Fig. 5.4). Accretion directions of bar strata were compared to that for dune strata to determine if the bars were downstream- or laterally migrating (Sorby, 1859; Pettijohn, 1962).

We also included in our analysis previously unpublished data on the geometry of channel-belt sandstones bodies from a prior field excursion to the same area (Mohrig et al., 2000; Fig. 5.3).

This dataset includes 118 sandstone bodies ranging 4.6-100 meters wide, 0.4-9.7 meters thick, with breadth-thickness ratios of 1.4-10.3 and 1-3 stories observed.

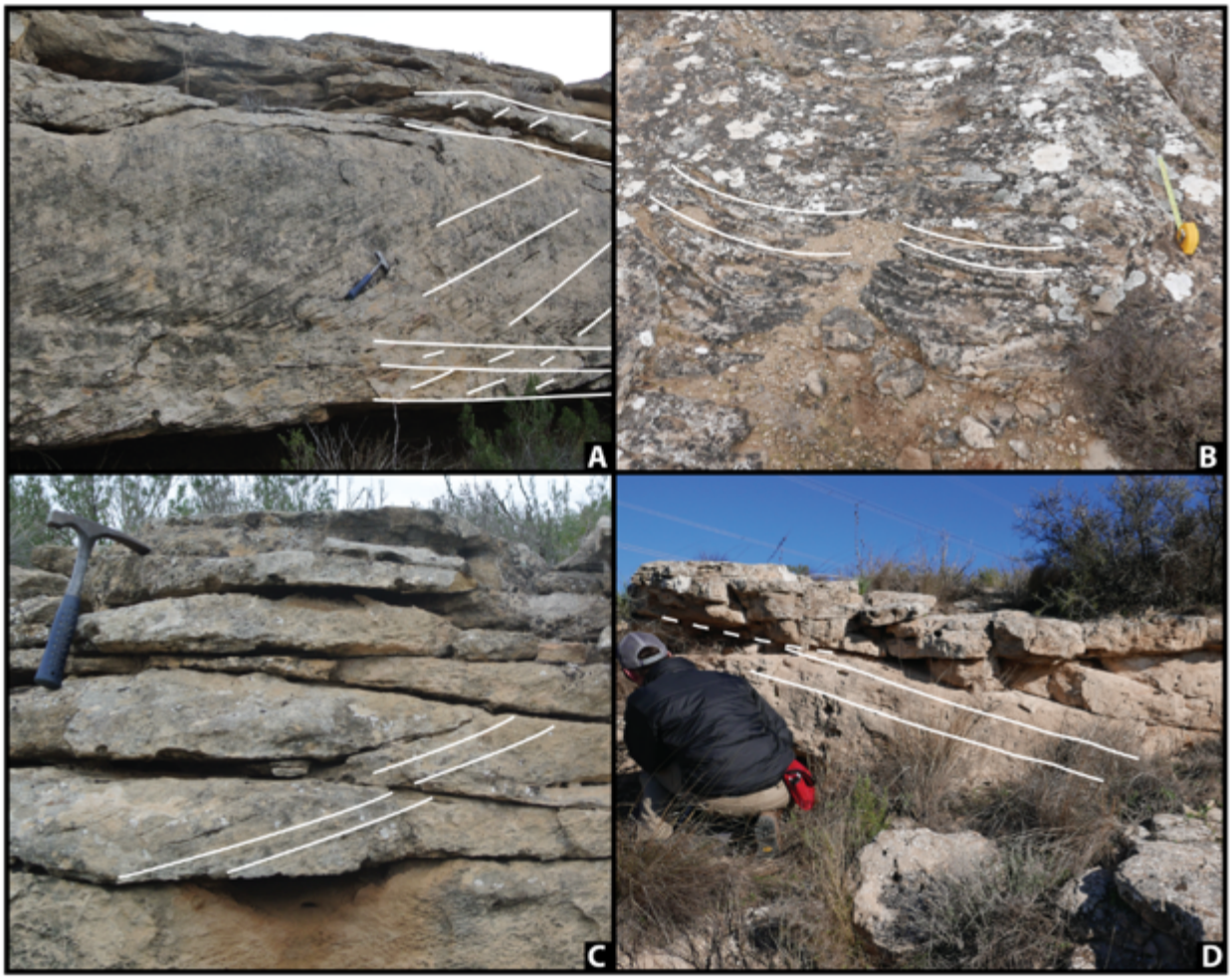

Figure 5.4–Examples of sedimentary structures. A) Stacked, truncated dune sets. B) Rib-and-furrow structures, in this case migrating along a linear bank-attached bar (see Fig. 5.6A for location). Yellow tape measure for scale. C) Climbing dunes, outlined by white lines, indicate upward aggradation as the migrate. D) Truncated bar clinoforms (white lines).

5.3.1.1 Reconstructing paleochannel geometry

We followed well-established methods in sedimentology to reconstruct paleochannel geometry from observations of fluvial deposits and ridges (e.g., Allen, 1965; Mohrig et al., 2000; Williams et al., 2009; Bhattacharya et al., 2016; Hayden et al., 2019; Hayden & Lamb, in review;

Cardenas et al., 2020). Bar clinoform thickness (h_{bar}) was assumed to approximate the flow depth at bankfull (H_{bf}) (e.g., Allen, 1965; Mohrig et al., 2000; Hajek and Heller, 2012), i.e.,

$$H_{bf} = h_{bar}. \quad \text{Eq. 5.3}$$

When only truncated bar strata were observed, then equation (5.3) yielded a minimum depth.

Dune cross-stratification can also be used to interpret flow depths, but there is higher uncertainty in this metric than in equation (5.3) because there is a distribution of dune heights present for a given flow depth (Bradley and Venditti, 2017) and a distribution of truncated dune cross set thicknesses for a given dune height (Paola and Borgmann, 1991). Combining the small-river relationship from Bradley and Venditti (2017) (we used this rather than the all-river relationship because it yields flow depths consistent with reconstructions based on bar heights) with the version of Paola and Borgmann (1991) presented by Leclair and Bridge (2001), yields

$$H_{bf}/h_{dune} = 10.2 \text{ (bounds: 6.6-35).} \quad \text{Eq. 5.4}$$

Paleohydrologic tools also have been developed for use with remote-sensing observations of fluvial ridges (Goudge et al., 2018; Hayden et al., 2019; Hayden and Lamb, in press). Hayden et al. (2019) found that thickness of a ridge caprock (T) serves as a proxy for bankfull depth

$$T / H_{bf} = 1.5 \text{ (bounds: 1-4).} \quad \text{Eq. 5.5}$$

Their compilation of the geometry of modern and ancient channel belts includes data from the Ebro Basin (Mohrig et al., 2000), as well as other sites. Equation (5.5) supports the idea that rivers tend to avulse to a new location after aggrading ~1-4 channel depth due to gravitational instability (e.g., Mohrig et al., 2000; Slingerland and Smith, 2004; Ganti et al., 2014), and that erosion during ridge formation leaves caprock thickness relatively unmodified (Hayden et al., 2019; Hayden & Lamb, in rev.).

Another tool we used to reconstruct paleochannel dimensions uses radius of curvature of lateral accretion sets (R_{LAS}), which should approximate the curvature of the channel bank (Goudge et al., 2018; Hayden and Lamb, in press), and scales with the bankfull width, W_{bf}, as:

$$W_{bf}/R_{LAS} = 2. \quad \text{Eq. 5.6}$$

We did not use ridge width or ridge curvature, because, although they have been used in cases on Mars (e.g., Burr et al., 2010; Kite et al., 2015), these have been shown to be potentially poor indicators of channel geometries for exhumed channel belts (Hayden et al., 2019; Hayden and Lamb, in press).

5.3.1.2 Calculating water discharge and sediment flux

Estimates of bankfull channel depth (H_{bf}) and median grainsize (D_{50}) were used to calculate water discharge and sediment flux (e.g., Bhattacharya et al., 2016; Hayden et al., 2019). Water discharge (Q_w) was calculated by mass balance as the product of channel cross-sectional area, A, and average flow velocity, U:

$$Q_w = AU. \quad \text{Eq. 5.7}$$

Cross-sectional area is the product of width, W, and depth, H, assuming a rectangular cross section. Bankfull channel width of single-thread rivers is linearly related with bankfull depth, so we used the median value of the bankfull ratio of width to depth from a large compilation (Trampush et al. 2014):

$$W_{bf}/H_{bf} = 18. \quad \text{Eq. 5.8}$$

Because channel deposits were mostly sand, we used the Engelund and Hansen (1967) relationship for sand-bedded rivers to calculate flow velocity:

$$U/u_{*s} = (1/\kappa)\ln[11H_S/k_s], \quad \text{Eq. 5.9}$$

where u_{*s} is the component of shear velocity due to skin friction ($u_{*s} = \sqrt{gH_sS}$, assuming normal flow), κ is von Karmán's constant ($\kappa = 0.41$), k_s is a roughness lengthscale, g is gravitational

acceleration, S is bed slope, and H_s is the component of flow depth due to skin friction (Einstein, 1950). The roughness parameter is based on the grainsize

$$k_S = n_k D_{50}, \quad \text{Eq. 5.10}$$

where n_k is found to be 2.5 for many rivers (Engelund and Hansen, 1967).

The value for H_s is related to the skin friction component of nondimensional shear stress, τ_{*s}, which is related to total nondimensional shear stress, τ_*, by an empirical relationship from Engelund and Hansen (1967):

$$\tau_{*s} = 0.06 + 0.4\tau_*^2 \ for\ \tau_{*s} \leq \tau_* ,$$

$$\tau_{*s} = \tau_* \ \text{for} \ \tau_{*s} > \tau_*. \quad \text{Eq. 5.11}$$

Parameters in equation (5.11) are $\tau_* = HS/RD_{50}$ and $\tau_{*s} = H_s S/RD_{50}$ for steady and uniform flow, and R is the submerged density of the sediment in the fluid (1.65 for quartz in water). To solve for flow velocity, we calculated H_s by combining equation (5.11) with definitions of τ_{*s} and τ_*, and then combined $H_s$with equation (5.9) and the definitions of u_{*s} and k_s. To constrain the bed slope, we used the empirical relationship of Trampush et al. (2014), who found

$$\tau_{*,bf} = 17Re_p^{-0.5}, \quad \text{Eq. 5.12}$$

where $Re_p = \sqrt{RgD_{50}}D_{50}$. Finally, to solve for flow velocity, we combined equations (5.11) and (5.12) with the definition of τ_{*s} to calculate H_s, and then combined H_s with equation (5.9) and the definitions of u_{*s} and k_s to calculate U. This resulted in an equation for bankfull water discharge that only relies on measured bankfull flow depth and grainsize, as derived originally by Hayden et al. (2019):

$$Q_{w,bf} = 74.2C_f^{-1/2}(Rg)^{3/8}\nu^{1/4}D_{50}^{1/8}H_{bf}^2. \quad \text{Eq. 5.13}$$

We estimated volumetric sediment flux of the bed-material load (Q_s; bed load plus suspended bed material) using the model from Engelund and Hansen (1967) for sand-bedded rivers because it

is simple and remains among the most accurate predictors across a broad range of flow conditions (Petkovsek, 2019). Non-dimensional flux per unit width (q_t^*) is related to the friction factor and Shields stress by

$$q_{t,sand}^* = \left(0.05/C_f\right)(\tau_*)^{5/2}, \qquad \text{Eq. 5.14}$$

where $q_t^* = Q_s/W(RgD_{50}^3)^{0.5}$. To calculate bankfull sediment flux, we combined equation (5.14) with the Engelund and Hansen (1967) relationship for C_f (i.e., $C_f^{-1/2} = (1/\kappa)\ln[11H_S/k_s]\sqrt{\tau_*/\tau_{*s}}$ by equations (5.9)-(5.11)), calculated the nondimensional shear stress, τ_*, using equation (5.12), and calculated width by applying the width-depth relation (equation (5.8)) to the depth calculated from equations (5.3) or (5.4). Note that equation (5.14) applies across all flow stages, while equations (5.8), (5.12), and (5.13) are intended only for bankfull flow. Furthermore, $Q_s = Q_{s,bf}$ when bankfull dimensions are used as inputs.

5.3.1.3 Measuring deposit volume

In addition to bankfull sediment flux, equation (5.1) requires an estimate of the total amount of transported sediment. Most sediment-flux calculations, including equation (5.14), exclude washload—generally the mud fraction in sand-bedded rivers (e.g., Einstein and Chien, 1953). Thus, for the Ebro basin, we calculated the total volume of deposited sand and gravel as

$$V = ATf(1-\lambda), \qquad \text{Eq. 5.15}$$

in which A is the area of outcrop in planview, T is the stratigraphic thickness, f is the fraction of the deposit composed of sandstone and conglomerate, and λ is porosity. This approach differs from prior applications of equation (5.1) that assumed washload was not incorporated into the deposit (e.g., Kleinhans, 2005; Kleinhans et al., 2010), but is justified for the Ebro Basin (and likely elsewhere) because fluvial strata are typically organized into coarse-grained bodies encased in fine-grained

floodplain materials. Sandstone fractions typically range 0.2 to 0.8 for terrestrial fluvial basins (Heller et al., 2015).

To measure the fan area, we used the mapped area of ridges (Fig. 5.3), focused on finding the outliers, and then calculated the area of a convex hull that encompassed both the ridge locations and previous mapped areas of the Guadalope-Matarranya Fan (Barbera et al., 2001; Valero et al., 2014), yielding 2300 km^2. To measure stratigraphic thickness, we used the portion of the mapped ridge area with greatest areal extent of consistent tectonic dips, which presented a section bounded on the bottom by the Ebro River, which overestimates the elevation of the base of the unit, and on the top by the carbonates of the Los Monegros Formation (Fig. 5.3). The minimum stratigraphic thickness is 700 m from the dip-corrected DEM as the vertical distance between the bounds. We estimated $f = 0.25$ using the upper bound on coarse-sediment fraction for the Guadalope-Matarranya fan (Cuevas Martinez et al., 2010). Porosity was taken to be $\lambda = 0.31$ by combining the fraction of modern porosity (13%) and the fraction of post-depositional matrix material (18%), both measured in a Caspe-Formation sandstone from near Alcañiz (Buj and Gisbert, 2010).

5.3.1.4 Intermittency factor and uncertainty

For the Guadalope-Matarranya fan, we calculated the intermittency factor using equation (5.1) where bankfull sediment flux was calculated from equation (5.14), the sediment volume (278 km^3 which does not include pore space) was found from equation (5.15), and the timespan of fluvial activity was assumed to be 9 Myr (i.e., the geometric mean of the bounds 4-24 Myr; Section 2).

To quantify uncertainty in our calculation of intermittency factor, we assumed that all contributing uncertainties are independent and distributed log-normally and combined them with Gaussian error propagation. The main source of uncertainty on intermittency factor is the bankfull sediment flux, which we quantified by assessing each of the terms in the calculation

($Q_{s,bf} \sim W_{bf} \tau_{*,bf}^{5/2} C_f^{-1/2}$). We constrained the uncertainty on each term as the 5-95 percentile bounds of the ratio between predicted and measured values in the Trampush et al. (2014) compilation of over 500 rivers at bankfull conditions, finding uncertainty in width (equation (5.8)), shear stress (equation (5.12)), and friction factor (equations (5.9)-(5.11)) as factors of 2.5, 5, and 2, respectively. Bankfull geometry reconstructions from equations (5.4)-(5.6) have an uncertainty of a factor of 2, which we combine into the error estimate because bankfull width scales directly with depth (equation (5.8)). Combining these factors, we estimated the uncertainty on bankfull sediment flux to be a factor of 9. Combining the uncertainties on bankfull sediment flux and on bed-material-sediment volume and duration, we estimated uncertainty on intermittency factor estimated from equation (5.1) to be a factor of 10.

5.3.2 Other depositional systems

To calculate intermittency factors for comparison to the Guadalope-Matarranya fan, we compiled data from sedimentary basins across Earth. We selected six basins that can be reasonably approximated as complete traps of bed-material load. They represent timescales of deposition of months to tens of millions of years, a range of sand bed grainsizes, and bankfull depths up to 26 m (Tables 1 and S1). For all deposits, we assumed $f = 0.25$ and $\lambda = 0.31$ based on the values we used for the Guadalope-Matarranya Fan (Cuevas Martinez et al., 2010; Buj and Gisbert, 2010), and used a factor of 10 as the uncertainty like we previously calculated for the Guadalope-Matarranya Fan (Section 3.1.4).

Devil's Gate Dam sediment catchment basin in Pasadena, California, USA, has 34 measurements of excavated volumes on month to multiyear timescales between 1919-2011 (LADPW & LACFCD, 2013) that we use for deposit volume. We also summed the excavated

volume over the entire 92 years of record as an additional data point for deposit volume (0.0092 km^3). Deposit volumes were converted to sediment volumes by multiplying by $f(1-\lambda)$. To estimate the bankfull sediment flux using equation (5.14), we used a bed slope of 0.026, which we measured in a lidar DEM (USGS, 2018) as the best-fit line to the river centerline along a 6-km reach immediately above the sediment basin, D_{50} = 1.3 mm measured 3 km downstream from the streamgage and just above the catchment basin (Psomas, 2018), H_{bf} = 0.6 m and W_{bf} = 10.1 m from (Modrick and Georgakakos, 2014), and found $Q_{s,bf} = 0.026$ m^3/s.

Wax Lake Delta, Louisiana, USA, has been growing since a drainage was cut to relieve flows from the Mississippi River. We took the 2.4-m deposit thickness (Roberts et al., 1997) to be uniform across the delta. We used annual measurements of subaerial delta area over 12 years (Roberts et al., 1997) times the thickness to find deposit volume. Median bed grainsize ranged from 0.169-0.326 mm (Shaw et al., 2013; Shaw and Mohrig, 2014), and we selected 0.2 mm as representative. Bankfull river width and mean bankfull depth (170 and 5.5 m, respectively) were measured in a surveyed cross-section of Wax Lake Outlet at Calumet (Arcement, 1988). We ignored the backwater effect and used measurements of grainsize and bankfull depth to estimate bankfull shear stress from equation (5.12). Combining width, depth, grainsize, and shear stress in equation (5.14), we calculated $Q_{s,bf} = 0.12$ m^3/s.

Numerous fluvial deposits, Paleocene to Pleistocene age, in the Gulf of Mexico have been reported and studied in detail. We focused on large, named deposits that represent distinct fluvial systems. Sediment volumes (50,000-600,000 km^3) and depositional timespan (1.8-10.6 Myr) were taken from geophysical measurements by Galloway et al. (2011). We calculated paleochannel depths (10.7-14.7 meters) by applying equation (5.5) to the median thickness of channel belts reported in a large compilation by Milliken et al. (2018), and assumed bed-material grainsize to be similar to the

modern Mississippi Delta (D_{50} = 0.3 mm; Chitale, 1970). We used the measurements of grainsize and bankfull depth to calculate the bankfull channel width by equation (5.8), bankfull shear stress from equation (5.12), and bankfull sediment flux of 5.9-8.6 m^3/s from equation (5.14).

The Mississippi River Delta has multiple depositional lobes formed at thousand-year timescales (Frazier, 1967). We used areas, approximate thickness, and depositional timespan for the five most recent lobes from Roberts (1997), and took the entire sum of the lobes formed over 14.4 k.y. as an additional data point (2,600 km^3). Bankfull flow depths for the Teche and Lafourche lobes (16 m and 27 m, respectively) were obtained by equation (5.5) from the median thickness of channel belts (Milliken et al., 2018), and the average of those values (21.6 m) was assumed for the other three lobes. Median bed-material grainsize of 0.3 mm was used based on the modern Mississippi River (Chitale, 1970). We used grainsize and bankfull depth to calculate bankfull width by equation (5.8), bankfull shear stress from equation (5.12), and bankfull sediment flux of 7.67-14.1 m^3/s from equation (5.14).

The Triassic Boreal Delta, a deposit in the modern Barents Sea, is reported to be the largest delta plain in Earth history (Klausen et al., 2019) and therefore represents the largest volume in our dataset. It is a subset of the Snadd Formation and formed during the early Carnian (Klausen et al., 2019), so we estimated that it formed in 4 Myr. It covers an area of >1.65 x 10^6 km^2 to an interpreted thickness of 0.4 km (Klausen et al., 2019), giving a deposit volume of 6.6x10^{14} m^3. Channel belts have a mean thickness of 21 m (Klausen et al., 2014), yielding paleochannel depths of 14 m by equation (5.5). Grainsize of channel bodies varies from fine to coarse sandstone (Klausen et al., 2014) so we used medium sand (0.4 mm) as our estimate. We used grainsize and bankfull depth to calculate bankfull width by equation (5.8), bankfull shear stress from equation (5.12), and bankfull sediment flux of 6.57 m^3/s from equation (5.14).

Location	Age	Deposition timespan, $\sum t$ (yr)	D_{50} (mm)	Depth, H (m)	Sediment volume [a], V_s (km^3)	Bankfull sediment flux, $Q_{s,bf}$ (m^3/s)	Intermittency factor [b], I_f (-)
Guadalope-Matarranya fan	Miocene	9 x 10^6	0.25	1.4	278	0.481 [d]	0.0020
Devils Gate Dam	Modern	0.0767-91.5 [e]	1.3 [f]	0.5 [h]	0.0000052 8-0.00158 [h]	0.0257 [d]	0.0016-0.78
Wax Lake Delta	Modern	0.955-18 [i]	0.2 [j]	5.5 [k]	0.000237-0.0406 [l]	4.65 [d]	0.0016-0.040
Gulf of Mexico fans/deltas	Pleistocene-Paleocene	1.8-10.6 x 10^6 [m]	0.3 [n]	10.7-14.7 [o]	8,690-103,000 [p]	4.78-6.93 [d]	0.0084-0.17
Mississippi River Delta	Holocene	0.452-14.4 x 10^3 [q]	0.3 [n]	16-27 [o]	68.5-450. [r]	7.67-14.1 [d]	0.059-0.44
Triassic Boreal Delta	Triassic	4 x 10^6 [s]	0.4 [t]	14 [u]	114,000 [v]	6.57 [d]	0.019

Table 5.1--Summary data for calculating deposit intermittency factors

Note: This table contains data summarized by the range for each parameter; for individual data points see supplemental Table S1.

[a]Equation (5.15), using $f = 0.25$ and $\lambda = 0.31$. [b]Equation (5.1). [d]Equation (5.14). [e]LADPW & LACFCD (2013) report volumes that replace the product of AT in equation (5.15). [f]Psomas (2018). [h]bankfull depth from Modrick and Georgekakos (2014). [i]Roberts et al. (1997). [j]Shaw et al. (2013). [k]Arcement (1980). [l]Area and thickness from Roberts et al. (1997). [m]Galloway et al. (2011). [n]Assumed to match grainsize from the modern Mississippi River (Chitale, 1970). [o]Bankfull depth from channel belt data in Milliken et al. (2018) and equation (5.5). [p]Galloway et al. (2011) report volumes that replace the product of AT in equation (5.15). [q]Bhattacharya et al. (2019). [r]Bhattacharya et al. (2019) report volumes that replace the product of AT in equation (5.15). [s]Klausen et al. (2019). [t]Klausen et al. (2014). [u]Bankfull depth from channel belt data in Klausen et al. (2014) and equation (5.5). [v]Klausen et al. (2019) report area and thickness.

5.3.3 Intermittency factors in modern rivers

We also calculated intermittency factors for 201 modern rivers to compare to our calculations from sedimentary deposits. To calculate intermittency factor for modern rivers with equation (5.1), we needed the time series of sediment flux, $Q_s(t)$, and the bankfull sediment flux, $Q_{s,bf}$. Long timeseries of sediment flux are rare, so instead we calculated sediment flux from the time series of water discharge, $Q_w(t)$, similar to previous work (Wright and Parker, 2005; Czuba and Foufoula-

Georgiou, 2014). We obtained data for 200 rivers, all of which have at least 10 years of mean daily Q_w from USGS streamgages, a rating curve (Q_w vs stage height, G), and surveyed bankfull values (Emmett, 1972; Elliott and Cartier, 1986; Foster, 2012; Trampush et al., 2014; Castro and Jackson, 2001; Andrews, 1984; Williams, 1978; Castro, pers. comm., 2020). We separately obtained data for the Onyx River, Antarctica in the form of published cross section, slope, and grain size (Shaw and Healey, 1980) and discharge timeseries (LTER et al., 2019). To convert $Q_w(t)$ to $Q_s(t)$, we combined the compiled data ($Q_w(t)$, Q_w vs G, $Q_{w,bf}$, H_{bf}, W_{bf}, S, and D_{50}) to create synthetic rating curves (Q_w vs H) to calculate the time series of depth and Shields stress ($\tau_* = HS/RD_{50}$ using the normal-flow assumption), which we then used to get time series of sediment flux.

To create a synthetic rating curve between water discharge and depth, we combined equation (5.7) with expressions for the cross-sectional area and flow velocity as functions of depth. To estimate flow velocity for sand-bedded rivers, we adjusted the coefficient n_k in equation (5.10) and combined it with equations (5.9) and (5.11) to calculate U so that equation (5.7) exactly reconstructed the surveyed value of $Q_{w,bf}$, using as inputs the surveyed values of W_{bf}, H_{bf}, S, and D_{50}. For gravel-bedded rivers, we used the flow resistance relation of Ferguson (2007)

$$U/u_* = \frac{a_1 a_2 (H/D_{84})}{\sqrt{a_1^2 + a_2^2 (H/D_{84})^{5/3}}}, \qquad \text{Eq. 5.16}$$

and adjusted the a_2 parameter for shallow flows to match the measured bankfull discharge. In Eq. (5.16), we used $a_1 = 6.5$, as recommended by Ferguson (2007), and estimated $D_{84} = 2.1D_{50}$ when only D_{50} was reported (Rickenmann and Recking, 2011).

Channel cross-sectional geometry evolved over the course of decades that the measurements were made. We estimated the cross-sectional geometry by fitting the discharge data to a channel

cross-section model from Allen et al. (2018), which relates the width and depth at any river stage (W, H) to the bankfull width (W_{bf}) and depth (H_{bf}) using a shape parameter (r).

$$H = H_{bf}\left(W/W_{bf}\right)^{r}. \quad \text{Eq. 5.17}$$

The r parameter describes the channel shape; $r = 1$ yields a triangle, and the channel becomes more rectangular with increasing r. The channel cross section area is $A = WH\left(1 - \frac{1}{r+1}\right)$ and therefore the mass-balance equation for water discharge (equation (5.7)) solved at any discharge stage becomes

$$Q_w = H^{1+\frac{1}{r}} W_{bf} H_{bf}^{-\frac{1}{r}} \left(1 - \frac{1}{r+1}\right) U. \quad \text{Eq. 5.18}$$

To solve equation (5.18) for the shape parameter, r, we used the surveyed values of H_{bf} and W_{bf} with a flow resistance relation (equations (5.9)-(5.11) or (5.18) with inputs of H, surveyed S and D_{50}, and best-fit n_k or α_1). The results were used to generate a series of synthetic rating curves for H as a function of Q_w for $1<r<10{,}000$. We then selected the r value that minimized variance in the offset, J, between our rating curve for flow depth and the USGS rating curve for stage height, defined as $J = H(Q_w) - G(Q_w)$. This fitting procedure was only applied to sub-bankfull conditions ($Q < Q_{bf}$) where flows were fully confined in the channel. Based on the calculated $H(t)$, we then calculated $\tau_*(t)$ from the normal-flow approximation and surveyed values of S and D_{50} and $R = 1.65$, calculated $W(t)$ from equation (5.17), and used equation (5.14) to calculate $Q_s(t)$ for sand-bed rivers. To estimate the sediment flux of gravel-bed rivers, instead of equation (5.14) we used the relationship of Fernandez Luque and van Beek (1976):

$$Q_{s,gravel} = 5.7W(RgD_{50}^3)^{1/2}\left(\tau_* - \tau_{*,c}\right)^{3/2}, \quad \text{Eq. 5.19}$$

where the critical Shields shear stress, $\tau_{*,c}$, was calculated from Lamb et al. (2008)

$$\tau_{*,c} = 0.25\, S^{0.15}, \quad \text{Eq. 5.20}$$

and the Shields stress was calculated assuming steady and uniform flow ($\tau_* = HS/RD_{50}$). Bankfull sediment flux was calculated from the surveyed value of $Q_{w,bf}$ using the same rating curves, and intermittency factor was calculated by combining $Q_s(t)$ and $Q_{s,bf}$ in equation (5.1).

We estimated the uncertainty in $Q_s(t)$ by comparing measured sediment fluxes from Brownlie (1981) (comprising sand- and gravel-bed rivers at different flow stages) to the values predicted from equations (5.14) and (5.16). A factor of 9 uncertainty, which is what we previously determined as uncertainty in calculating bankfull sediment flux from deposits, spans 81% of the Brownlie (1981) data, so we therefore also use a factor of 9 as the uncertainty in sediment flux, in addition to the uncertainty in I_f.

Because the channel shape parameter, r, was calibrated for sub-bankfull flows, applying it also to overbank flows makes the implicit assumption that the channel is confined in a valley or canyon with the same geometry as the channel. The other endmember geometry for overbank floods occurs for channels in an infinitely wide floodplain. In this case, the overbank flow spreads out across the floodplain so that the channel depth does not increase with increasing discharge, i.e., $Q_s(Q_w \geq Q_{w,bf}) = Q_{s,bf}$. We calculated I_f under both endmember scenarios, and found that the uncertainty due to channel shape was usually small compared to the uncertainty in sediment flux.

5.4 Results

5.4.1 Field observations

We traced ~900 ridges across the Guadalope-Matarranya fan in lidar DEMs, and recorded 2355 caprock thickness and ridge relief measurements from 235 ridges using centerline-perpendicular transects in the lidar DEM. In addition, we made detailed field observations of 28 ridges and four roadcuts at 10 sites in the north end of the area (Fig. 5.3).

As measured from the DEMs, ridges are typically 100-800 m long, and the longest is 3 km. We observed that ridges with axes parallel to the topographic strike tend to be longer than those that are parallel to the topographic dip. Sinuosity (ridge length divided by straight-line distance between endpoints) ranged from 1.0-3.0, with shorter ridges generally having a wider distribution of sinuosity values because they sample only a fraction of the ridge. The convex hull of ridge locations covered 2300 km^2 (Fig. 5.3C) and the stratigraphic thickness of the digital stratigraphic model is 0.7 km. Ridge caprocks form cliffs that are visible in the DEM, and 5-95 percentile ranges in breadth, thickness, and relief are 10-50 m, 0.5-4.4 m, and 0.3-11 m, respectively. There are no significant trends across the field area.

We show Site 4 as a typical example of ridges observed in our field sites (Fig. 5.5); the other nine sites are all similar, and comparable workups can be found in Section SI1. Site 4 has five ridges that intersect each other and stand 2-26 m above the surrounding plain (Figs. 5.5A and 5.5B). Ridges are composed of a sandstone caprock atop mudstone with thin sandstone beds (Fig. 5.5C). Caprock breadths are 6-40 m and thicknesses are 0.3-4.8 m (Fig. 5.5D). Sandstone talus blocks up to several meters in diameter line the ridge flanks and are absent in the surrounding plains. The tilt-corrected digital elevation model shows that Ridges 1 and 3 and the Plateau occur at different stratigraphic levels (Fig. 5.5B), and field observations of erosional surfaces separating caprock sandstones indicate each ridge is stratigraphically distinct (e.g., Fig. 5.6A).

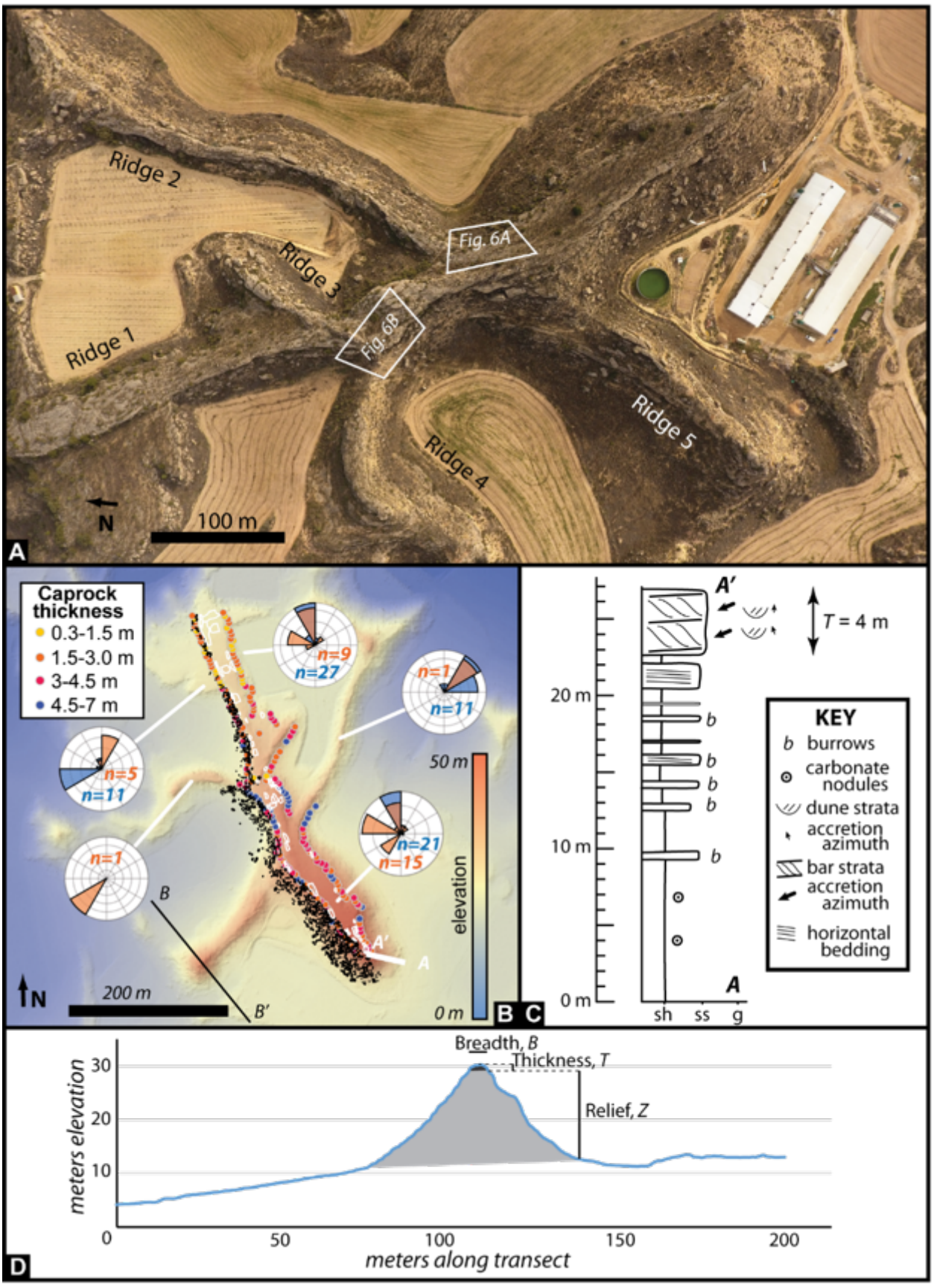
Ridge 2
Ridge 3
Ridge 1
Ridge 4
Ridge 5
Fig. 6A
Fig. 6B
N
100 m
A
Caprock thickness
0.3-1.5 m
1.5-3.0 m
3-4.5 m
4.5-7 m
n=9
n=27
n=1
n=11
n=5
n=11
n=1
n=21
n=15
B
B′
A
A′
50 m
elevation
0 m
N
200 m
B
C
A′
T = 4 m
20 m
10 m
0 m
b
A
sh
ss
g
KEY
b burrows
carbonate nodules
dune strata
accretion azimuth
bar strata
accretion azimuth
horizontal bedding
D
Breadth, B
Thickness, T
Relief, Z
meters elevation
30
20
10
0
50
100
150
200
meters along transect

Figure 5.5–Site 4. A) UAV photo showing the layout of the site and the names of the ridges used in subsequent figures. B) Elevation model of Site 4, showing measurements of accretion directions of dune sets (blue on rose diagrams) and bar clinoforms (red on rose diagrams). Thickness of caprock for Ridge 1 is shown in colored dots; the caprock is thickest where other caprocks amalgamate (e.g., intersection with ridge 2). Black outlines are talus blocks traced on the west side of the ridge. Talus dimensions are smaller than caprock width or thickness, and talus blocks are totally absent from the plains between ridges. Locations of transects in panels C and D are shown. C) Representative stratigraphic section, the tallest of all the stratigraphic sections we measured. It shows that the 4-meter-thick caprock, made of sandstone with bar and dune cross-stratification, sits atop 22 meters of mudstone with thin sandstone sheets interspersed. Structures in the thin sandstone layers include horizontal planar lamination and burrows, while the mudstone has carbonate nodules. These observations are typical of stratigraphic sections we measured across our field sites. D) Elevation transect across Ridge 5, showing a small caprock atop a large ridge. The caprock and ridge flanks are identified by slope breaks in the transect; caprock is a cliff-forming unit and the base of the flanks are where the transect significantly flattens. Note that relief excludes caprock thickness following Hayden and Lamb (in rev.).

Caprocks at Site 4 are made of fine to medium sandstone, and most contain abundant cross-strata. We observed 48 truncated sets of cross strata 0.05-0.80 m tall (means of 0.13-0.20 m for each caprock) which we interpreted as dune cross sets on the basis of their size and trough cross-bedding. We also measured 15 rib-and-furrow structures on ridge tops and found dune accretion directions are within 20° of the main ridge axis (Fig. 5.5B). We observed larger bar clinoforms that had accretion directions ranging from parallel to perpendicular to the dune accretion directions (Fig. 5.5B). In plan-view, we observed one example of a long (20+ meters) planar bar set with interbedded smaller rib-and-furrow structures, indicating superimposed dunes (Fig. 5.6A). The bar set has an accretion direction perpendicular to the paleo-flow indicated by the rib-and-furrow structures (Fig. 5.6A), indicating a bank-attached point bar.

Caprocks unconformably overlie mudstone, with some laterally extensive, vertically thin sandstone sheets interspersed (Fig. 5.5C). We examined in detail one of the ridges at Site 4 with 26 meters of mudstone exposed (Fig. 5.5C). We found 9 planar beds of fine sandstone, 0.1-1.4 meters

thick, with internal structures including burrows and planar lamination. Several layers within the mudstone contain carbonate nodules.

Site 4 has five ridge junctions, all between Ridge 1 and another ridge, which we examined in the field and the high-resolution stratigraphic model to see if they represent channel or channel-belt bifurcations or superposition of sandstone bodies at distinct stratigraphic levels. Ridge 1 occupies vertical space above the Plateau and below Ridge 3 and has distinct paleoflow directions from the other two (Fig. 5.5B), so we interpret all three as distinct. Ridge 2 is at the same vertical position as Ridge 1, but a major erosional surface separates the two (Fig. 5.6A) and their paleo-flow directions are distinct (Fig. 5.5B) so we interpret them as representing distinct stratigraphic intervals. Ridges 4 and 5 are eroded at their intersection with Ridge 1; however, there are channel bodies visible in outcrop that align with Ridges 4 and 5, so we interpret those to be the remnants. The remnants are separated from the caprock of Ridge 1 by major erosional surfaces (e.g., Fig. 5.6B), so we interpret these ridges to also be distinct. From the stratigraphic model and UAV imagery, which emulates the highest-quality remote-sensing data we would have for ridges on Mars, we were able to detect the vertical offsets between Ridges 1 and 3 and the Plateau based on cliff shadows in the imagery as well as 3D position in the DEM. In contrast, Ridges 2, 4, and 5 were at similar elevations as Ridge 1 and therefore were indistinguishable.

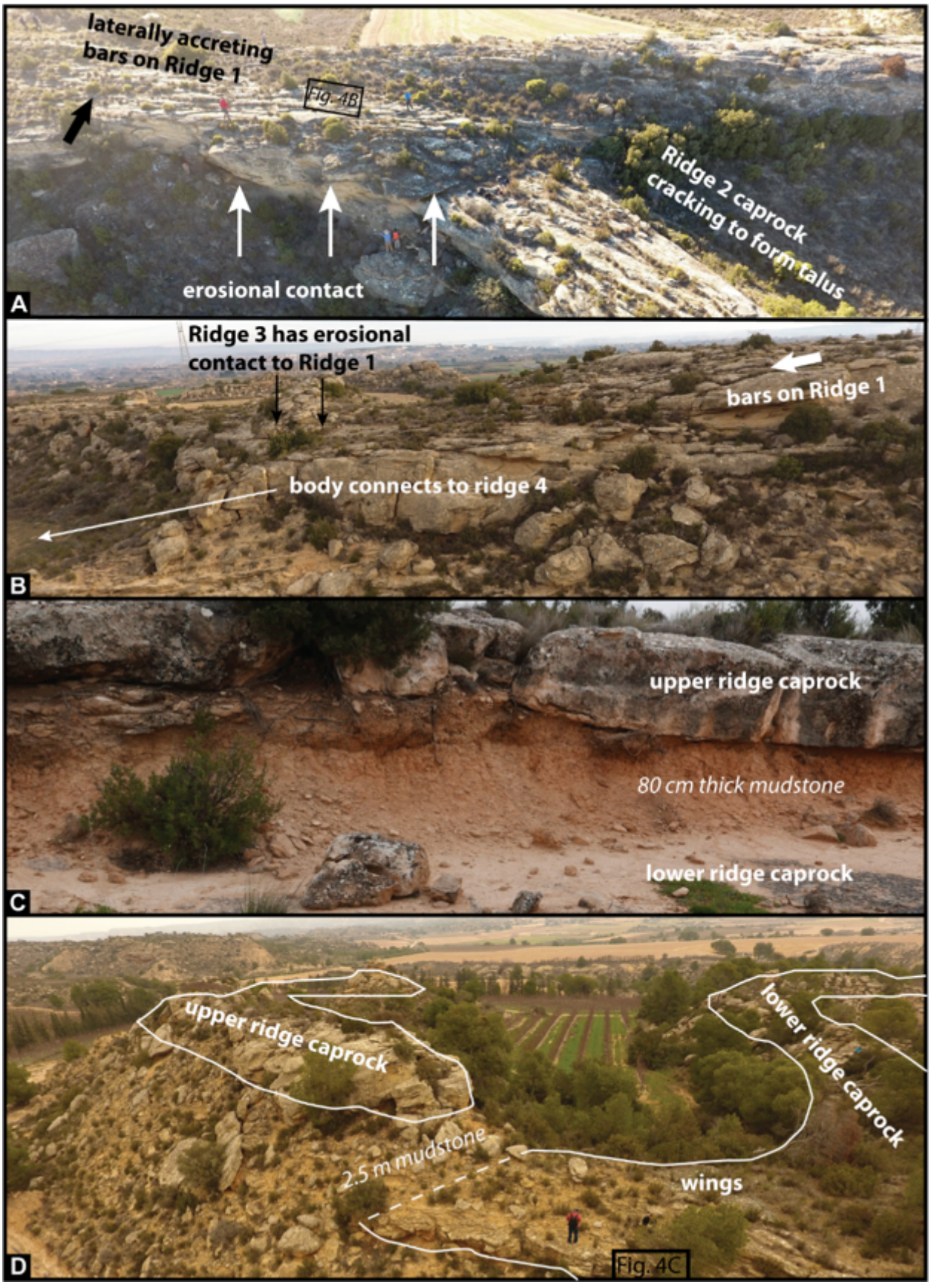
laterally accreting
bars on Ridge 1
Fig. 4B
Ridge 2 caprock
cracking to form talus
erosional contact
A
Ridge 3 has erosional
contact to Ridge 1
bars on Ridge 1
body connects to ridge 4
B
upper ridge caprock
80 cm thick mudstone
lower ridge caprock
C
upper ridge caprock
lower ridge caprock
2.5 m mudstone
wings
Fig. 4C
D

Figure 5.6 (previous page)–Different types of ridge intersections observed. A) Oblique UAV photo of the intersection of Ridges 1 and 2 at Site 4 (location shown in Fig. 5.6), with humans for scale. Though the ridges are at comparable stratigraphic levels, Ridge 1 clearly erodes into Ridge 2 (white arrows). Bars on Ridge 1 accrete (accretion direction given by black arrow) perpendicularly to the paleoflow direction interpreted from rib-and-furrow structures (Fig. 5.4B; location shown in black box). This image also shows the caprock cracking to form talus, such as the large block that people are standing on between the white arrows, which appears to have come from Ridge 2. B) Another view of Ridge 1 at Site 4 with other channel bodies amalgamated with it. Ridge 3 is clearly higher stratigraphically and shows an erosional contact with Ridge 1. Ridge 4 has no caprock at its intersection with Ridge 1, but there is a channel body amalgamated into the caprock of Ridge 1 that we interpret as previously connected to Ridge 4 on the basis of similar size and stratigraphic position. Bar structures in Ridge 1 appear to be accreting downstream (accretion direction given by thick white arrow). C) A clear example of mudstone separating ridge caprocks from Site 5 (location shown in Fig. 5.8C). D) Larger separation of caprocks by mudstone from Site 7. This site appears to have branching ridges in planview, but in the field, the caprocks of the ridges are separated by 2.5 meters of mudstone and therefore are stratigraphically distinct. The upper ridge helps preserve the wings of the lower ridge, which pinch out laterally under the upper ridge. The location of the one example of climbing dunes (Fig. 5.4C) is shown.

Figure 5.7 (next page)–Field observations of bar cross-strata. A) UAV photo of a channel belt at Site 8 that clearly incises into pre-existing floodplain deposits, including small channel conduits that could be crevasse-splays. The channel belt contains multiple levels of internal stratification that appears to be bars. B) Clear truncation by subsequent generations of bar structures as a channel belt built up at Site 4 (hammer, circled, for scale). Location shown in Fig. 5.8A. C) Bar strata at Site 10 accrete (black arrow) perpendicular to paleoflow direction (white arrow). Yellow notebook for scale.

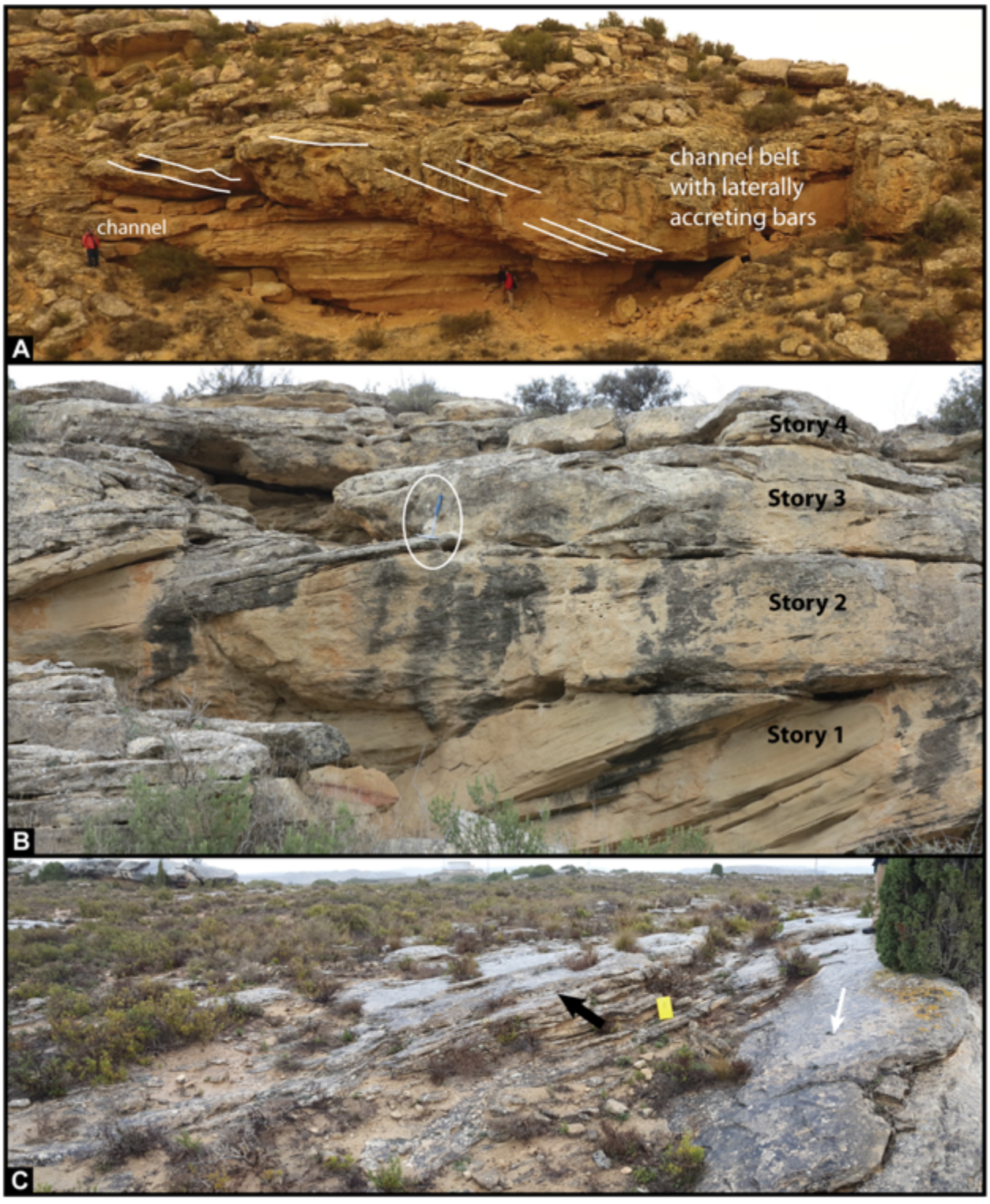
channel
channel belt
with laterally
accreting bars
A
Story 4
Story 3
Story 2
Story 1
B
C

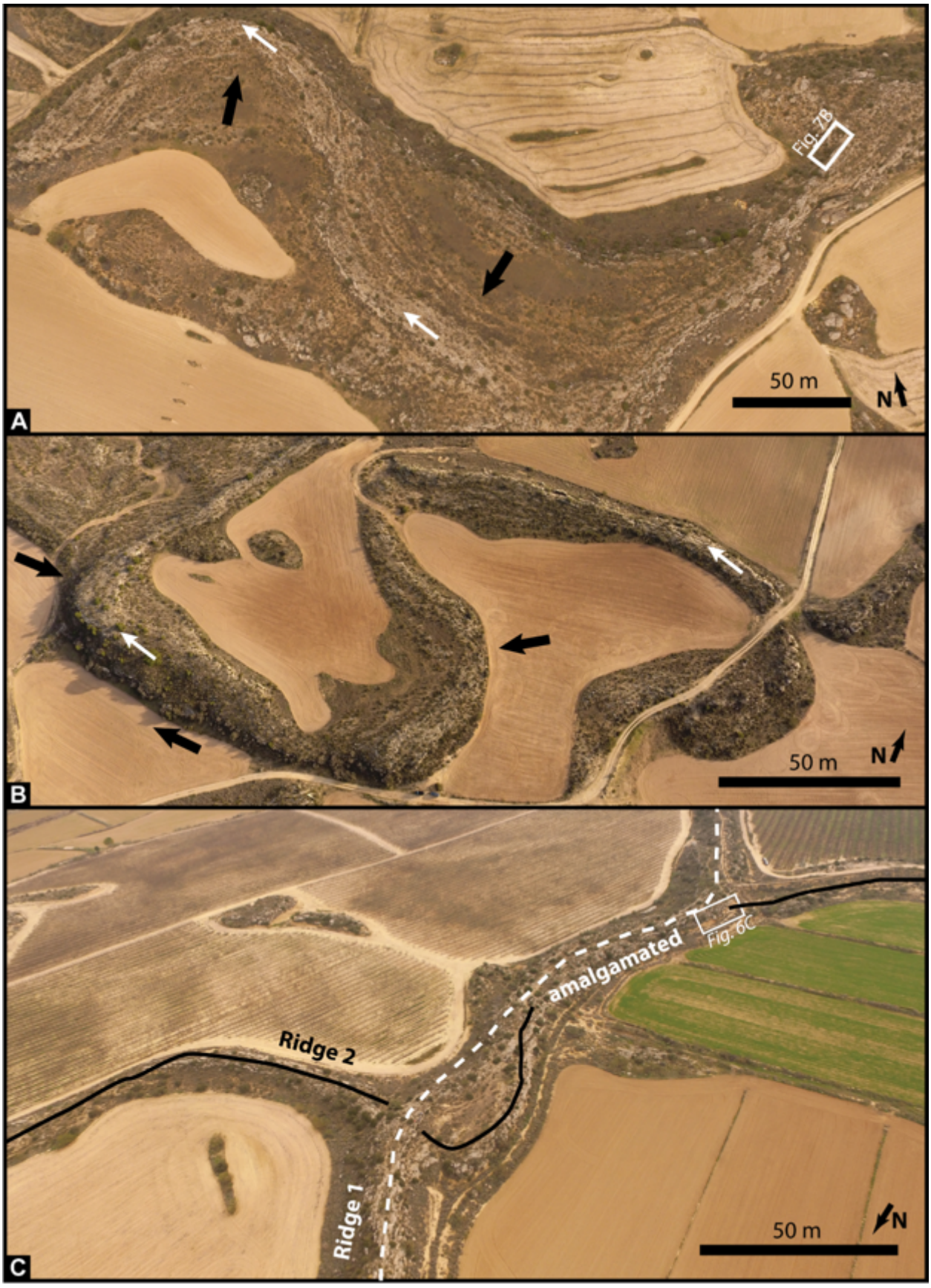
Fig. 7B
50 m
N
A
50 m
N
B
amalgamated
Fig. 6C
Ridge 2
Ridge 1
50 m
N
C

Figure 5.8–UAV images illustrating amalgamation. White arrows indicate paleoflow directions and black arrows indicate bar accretion directions. A) Site 4 exhibits exhumed point bars that accrete perpendicularly to the flow direction, towards the outside of the bend. The channel belt built vertically as it aggraded laterally so the stratigraphic position increases to the outside of each bend. Location of Fig. 5.7B shown. B) High-sinuosity ridge at Site 3 exhibits bars accreting in the direction of ridge planview concavity, indicating that the ridge is a channel belt rather than a channel cast. C) Two ridges at Site 5 that join and then separate after 100 m. This is a clear example of how smaller channel belts can amalgamate to form thicker channel belts, and also how junctions can be either tributary or distributary with respect to paleo-flow (though note that these represent channels at different timesteps, so the flow at this location did not join or bifurcate). The location of one example of mudstone separating caprocks (Fig. 5.6C) is shown.

Ridge flanks at Site 4 are covered in talus blocks made of the caprock sandstone. The dimensions of talus blocks are typically smaller than the width and thickness of the caprock (e.g., Figs. 5.5B and 5.6A), and talus cover on the flanks ranged from 0-70% by area (see west flank of Ridge 1 in Fig. 5.5B). Talus blocks are totally absent beyond the base of the ridge flanks, but farming in those areas makes it unclear whether this is due to human modification (Fig. 5.5A). We noted extensive vertical cracks in Ridge 2, which suggests that talus blocks form by splitting off from the main caprock (Figs. 5.6A; 5.15B).

The other field sites (Section SI1.1) are largely similar to Site 4. All ridges comprise a cliff-forming caprock of fine to medium sandstone atop ridge flanks of dominantly mudstone with some thin sandstone sheets. Caprocks had abundant dune cross-strata 0.03-0.70 m thick, and we observed a single set of climbing dunes at Site 8 that occur in a thinner portion of the sandstone body that extends laterally from the top of the thick core, with dune accretion directions away from the channel axis (Figs. 5.4 and 5.6D). Caprocks also had abundant truncated bar cross-strata 0.30-3.0 m thick (e.g., Figs. 5.7A and 5.7B), which have accretion directions ranging from parallel to perpendicular to the paleo-flow directions indicated by the dune cross-strata (Fig. 5.7B). Site 7 shows a point bar complex that is higher in elevation on the outside of the bend (Fig. 5.8A), indicating the river

migrated laterally as it aggraded. Site 3 has bar-accretion directions both towards and away from planview convexity of the ridge (Fig. 5.8B), indicating that modern ridge geometry can be independent of paleo-channel geometry because channels are expected to migrate in the direction of their convexity. We observed truncated bar strata stacked vertically (e.g., Figs. 5.7A and 5.7B), indicting channel-bed aggradation in addition to bar lateral accretion.

In most cases, ridge junctions represent caprocks crossing at distinct stratigraphic intervals. Stacked caprocks are typically separated by mudstone at their junctions (e.g., Figs. 5.6C and 5.6D). Other junctions show sandstone amalgamation with the upper caprock cut into the lower caprock with a clear erosional surface (Fig. 5.7). Site 6 shows additional evidence for amalgamation; two sandstone bodies separated by mudstone (Fig. 5.8C) are amalgamated together for 100 meters along the ridge length before separating again.

In addition to the ridges, we observed non-ridge forming sandstone bodies in cliff outcrop (e.g., Fig. 5.7A) and in cleanly exposed road or railroad cuts. These sandstone bodies ranged from 1.5-120 meters wide and 1.9-18.8 meters thick, with width-thickness ratios of 2-28. All have dune cross-stratification and truncated bar clinoforms. The bar clinoforms generally have aggradation directions perpendicular to the main axis of the body, indicating lateral accretion. Most channel bodies significantly thin towards their edges (e.g., Fig. 5.7A).

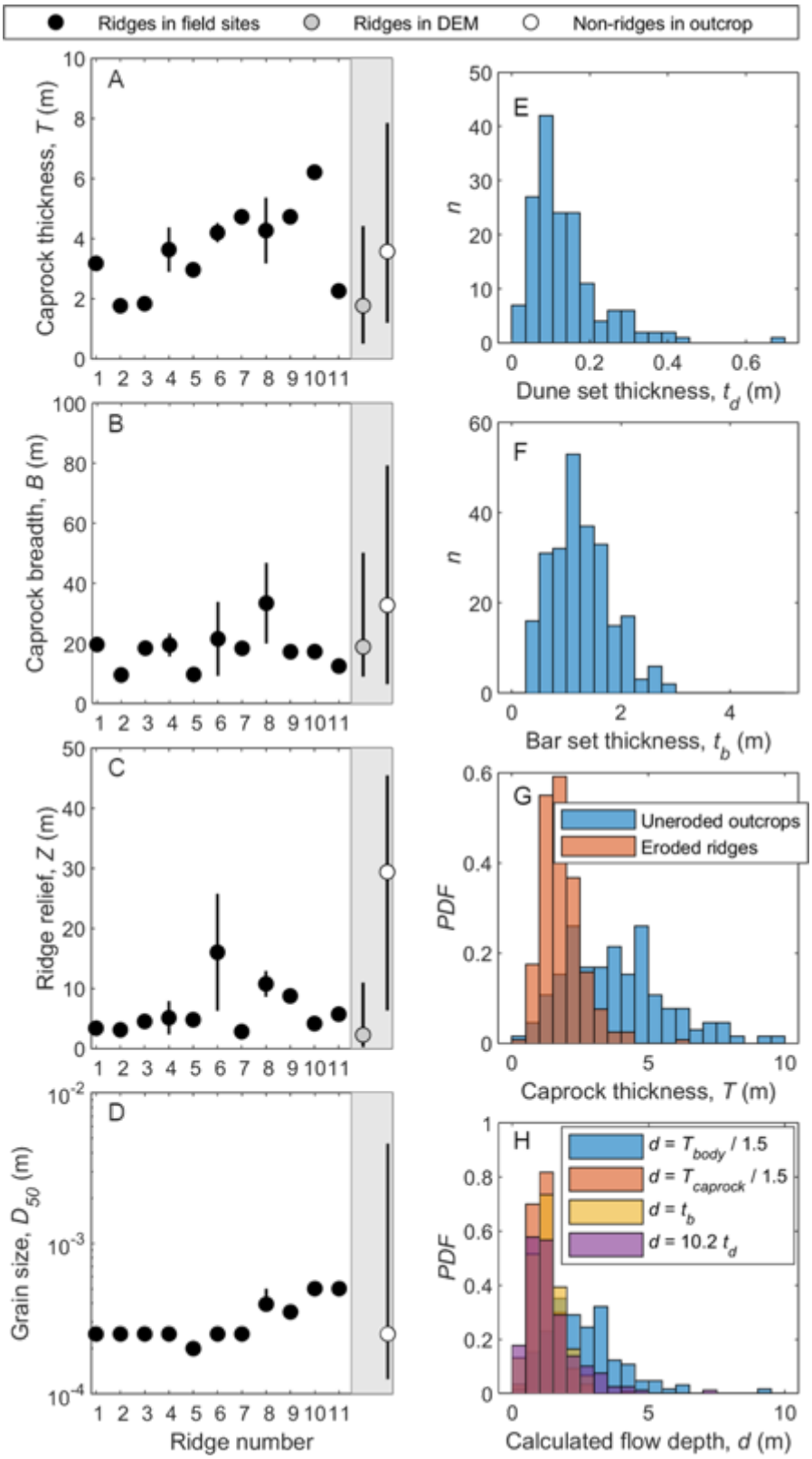

Figure 5.9–Data from the field sites studied in detail, ridges studied in the lidar DEM, and non-ridge-forming channel bodies in cliff outcrop. A-D) Measurements of caprock thickness (panel A),

caprock breadth (panel B), ridge relief (panel C), and median grain size (panel D) for each field area and of non-ridge-forming channel bodies. E-H) Observations of cross-strata and calculations of flow depth, including thickness of truncated dune sets (E), thickness of truncated bar sets (F), thickness of uneroded channel bodies in outcrop measured in the field and of eroded ridges measured in the lidar DEM (G), and calculations of flow depth from the different input parameters in panels E-G, using methods described in Section 3.1.1.

Measurements from eroded ridges and unexhumed channel bodies are summarized in Fig. 5.9, including caprock dimensions (Figs. 5.9A, 5.9B, and 5.9C), grainsize (Fig. 5.9D), and thickness of cross-strata (Figs. 5.9E and 5.9F). Caprock thickness (Fig. 5.9A) measured in the DEMs ranges from 1.9-6.1 m for our field sites and has a 5-95 percentile range of 0.6-4.3 m across the whole fan, while uneroded channel-body thickness measured in the field has a 5-95 percentile range of 1.3-7.8. Caprock breadth (Fig. 5.9B) measured in the DEMs ranges from 8.5-44 m for our field sites and has a 5-95 percentile range of 10-45 m for ridges across the whole fan, while uneroded channel-body breadths have a 5-95 percentile range of 8.1-78 meters. Caprock relief (Fig. 5.9C) measured in the DEMs ranges from 3.5-26 m for ridges at field sites and has a 5-95 percentile range of 0-10 m for all ridges, while uneroded channel-body breadth has a 5-95 percentile range of 7.8-46 meters. Grainsizes for caprocks (Fig. 5.9D) at our field sites range from fine to coarse sandstone (0.2-0.5 mm), while grainsizes at uneroded channel bodies can be much coarser (up to 20 mm) at locations closer to the fan apex (further south).

5.4.2 Paleo-hydraulics

Following prior observations of the sediments of the Guadalope-Matarranya fan (Mohrig et al., 2000) we assumed flows were consistent across the basin and combined all values of each measurement into a single reconstruction. The mean height of 242 dune cross strata is 0.14 m (Fig. 5.9E), which by equation (5.5) yielded a paleochannel depth of 1.4 m. The mean height of 13 bar clinoforms is 0.6 m (Fig. 5.9F), which by equation (5.4) yielded a paleochannel depth of 0.6. The

median thickness of 131 channel belts observed in cliff outcrop was 3.6 m and the median thickness of ridge caprocks is 1.7 m (Fig. 5.9G), which by equation (5.5) yielded paleochannel depths of 2.4 and 1.1 m, respectively. Fig. 5.9H shows the agreement in depth reconstructions where we had both sedimentology and caprock thickness reconstructions, and the histogram of values for each. All values are similar and show a unimodal distribution. The mean paleochannel depth from the four different methods is 1.4 m. Prior work reports flow depths interpreted from bar thickness ranged 1-3.3 meters with a mean of 1.4 meters that remained relatively constant vertically in a given channel body and across the fan system (Mohrig et al., 2000). On the basis of our calculations and prior work, we therefore use 1.4 m as the representative paleo-channel depth.

5.4.3 Interpretation of the ridges of the Guadalope-Matarranya Fan

We interpret the ridges in the Guadalope-Matarranya fan to be exhumed and eroded channel belts, similar to previous work in the area (Williams, 1975; Friend et al., 1979; Mohrig et al., 2000; Cuevas Martinez et al., 2007; 2010; Gonzalez Bonarino et al., 2010). We observed that ridge caprocks exhibit amalgamated strata from dunes and bars indicating channel aggradation and channel lateral migration within a channel belt. Overbank sandstone wings, one of which had climbing dunes that indicate rapid aggradation and flow direction away from channel axis (Fig. 5.4B), were interpreted as levee deposits that downlap onto the floodplain and are characteristic of channel-belt deposits (Allen et al., 1983; Friend et al., 1979; Mohrig et al., 2000). The caprocks are typically thicker than the reconstructed paleochannel depth (Fig. 5.9) and dune strata do not change up section (Cuevas Martinez et al., 2007; 2010), suggesting channel-bed aggradation. In contrast, channel fills (or topographically inverted channels) would be expected to be fine-grained and have decreasing flow depths up section, as an abandoned channel pathway fills with overbank material (Bhattacharya et al., 2016; Nichols and Fisher, 2007). Ridge junctions reflect crossings of channel-belts formed at distinct stratigraphic intervals, rather than reflecting an inverted channel network.

The reason that ridge breadths (10-50 m) are typically smaller than the reconstructed paleo-channel widths (38-105 m) is because the ridges have been eroded (Fig. 5.6). Evidence for erosion includes talus blocks and exposed strata on caprock sides indicating scarp retreat (e.g., Fig. SI6C). Bar accretion sets extend to the caprock edges indicating that the channel at the leading edge of the bar is not preserved within the caprock strata (e.g., Fig. 5.6A). Sandstone bodies preserved in cliff outcrop have wider breadths than the ridges (up to 80 m in outcrop whereas ridges tend to be less than 20 m; Fig. 5.9B), despite similar thicknesses, supporting that the caprocks have been narrowed during ridge formation.

5.5 Analysis: Intermittency factor

5.5.1 Guadalope-Matarranya fan

We used our measurements of ridge-bearing area (2300 km^2), stratigraphic thickness (0.7 km), sand fraction of $f = 0.25$, and porosity of $\lambda = 0.31$ (Buj and Gisbert, 2010) to calculate a sand and gravel volume of 278 km^3. The calculated stratigraphic thickness is 0.7 km, which slightly larger than prior estimates of 0.4 km (Cuevas Martinez et al., 2007; 2010; Barbera et al., 2001); however, both are lower bounds. The paleo-channel depth is 1.4 meters, which, combined with the median grainsize of $D_{50} = 0.25$ mm and equation (5.14), resulted in a bankfull sediment flux of $Q_{s,bf} = 0.48$ m^3/s. Combining this sediment flux estimate with the depositional timespan ($\sum t = 9$ Myr) in equation (5.1), we calculated an intermittency factor of $I_f = 0.002$ for the Guadalope-Matarranya Fan.

A low intermittency factor for the Guadalope-Matarranya Fan is supported by field observations. Cuevas Martinez et al. (2007) observed pedogenically altered mudstone laminae between some downstream-accreting bars and putative ant nests within the bars, both of which they interpreted to represent infrequent fluvial activity. Gonzalez Bonarino et al. (2010) also found bioturbation and small-scale sedimentary structures and interpreted that low or no flows existed between the main bar-forming flood events. Cuevas Martinez et al. (2010) expanded on this

argument, and described different hierarchical levels of intermittency, which they supported with evidence of Milankovitch-cycle-paced cyclicity in the lacustrine deposits of the Los Monegros Formation at the toe of the Guadalope-Matarranya fan system (Perez-Ribarez et al., 2004; Valero et al., 2014).

5.5.2 Intermittency factors in other systems

Using the methods and data described in Section 3.3, we calculated estimates for the intermittency values for modern rivers to span 0.00082-1.6 with a median of 0.10 (Fig. 5.10). Intermittency factor values for the sedimentary deposits were similar and ranged from 0.0016-0.78, with a median of 0.036 (Figs. 5.10C and 5.10D. Many of our calculated values are significantly lower than prior assumptions of I_f values—99% and 39% of our values for modern rivers are lower than the commonly used values of $I_f = 1$ and 0.05, respectively (Sinha & Parker, 1996; Cui and Parker, 1998; Parker et al. 1998, Parker 2005; Sun et al., 2002; Eke et al., 2012; Tucker and Slingerland, 1997; Snyder et al., 2000; Gran et al., 2013; Wickert and Schildgren, 2019; Dong et al. 2016). Values calculated for terrestrial rivers range 0.13-0.35 (Wright and Parker, 2005; Czuba and Foufoula-Georgiou, 2016; Naito et al., 2019), and 55% of our values for deposits are lower than that range. Values for martian rivers range $7x10^{-4}$ – $5x10^{-4}$ (Buhler et al., 2014; Lapôtre & Ielpi, 2020), and 100% of the values we found for modern rivers exceed this range (Fig. 5.10D).

To determine what sets the value of the intermittency factor within the wide range of observed values, we analyzed a number of parameters. We did not find a trend in intermittency factor with bed-material grainsize for the modern rivers (Fig. 5.10A) or deposits (Fig. 5.10C). Similarly, the intermittency factor surprisingly does not seem to change systematically with timescale. Although rivers and sedimentary deposits that represent ≤100 yrs of sediment flux have a wider range of values than sedimentary deposits formed over more than 10^6 yrs, the ranges overlap and it

is not clear if this effect is due to significantly more data for century-scale systems (n = 230 vs n = 10).

Figure 5.10 (next page)–Values for intermittency factor for modern rivers and ancient sedimentary deposits. Uncertainty bars represent a combination of uncertainty in channel geometry and in calculating discharge (see Section 3.3), and bars for prior calculations for Mars represent reported range of acceptable values. Y-axis is the intermittency factor for all panels, x-axis varies. Data for modern rivers are shown in blue on all panels; sedimentary deposits are brown. A) The 5-95 percentile interval of intermittency factor ranges between 0.0064-0.75 for silt-bed and sand-bed rivers, and decreases slightly for gravel-bed rivers to a minimum of 0.0057. Shades of blue indicate different grain sizes and are the same for the other panels and Figs. 5.11 and 5.12. Triangles are calculations from prior work (Sklar and Dietrich, 2004; Wright and Parker, 2005; Czuba and Foufoula-Georgiou, 2014; Naito et al., 2019). B) Same as panel (A), with values for the terrestrial deposits calculated in this study. Different symbols represent different systems, with only the long-term average shown for deposits with multiple timestep measurements. There is no noticeable difference between modern rivers and ancient deposits. C) Intermittency factor does not vary as a function of aridity, as measured by aridity index, which is the ratio of potential evapotranspiration to mean annual precipitation extracted from the global map of Trabucco and Zomer (2019). Onyx River in Antarctica is shown at left, represents a hyperarid climate. Circled points are ephemeral rivers, which we define as rivers with dry beds ($Q_w = 0$) at least 5% of the time. Ephemeral rivers exist in all climates, and have a median intermittency factor of 0.019, which is lower than but not beyond uncertainty from the median of 0.10 for all rivers. D) Intermittency factor as a function of measurement timescale for our modern rivers and sedimentary deposits, and for Martian deposits calculated by other studies (Buhler et al., 2014; Lapôtre and Ielpi, 2020). For modern rivers, the timescale is the duration of measurements. For modern terrestrial deposits (Wax Lake, Devil's Gate Dam) the timescale is the duration of measurements, and the longest timespan represents the total interval. For ancient terrestrial and Martian deposits, the timescale is the reported depositional duration. Shaded region represents common prior assumptions for rivers on Earth and Mars (I_f = 0.05-1). Intermittency factor is independent of measurement duration on timescales from months to millions of years, and is the same for modern rivers as ancient deposits. F) Intermittency factor appears to be related to the ratio of catchment-averaged denudation (E) to mean annual precipitation (P), times a factor of 1800 (bold dashed line). This factor is equal to (see Section 5.2.1) mean annual precipitation times catchment area (C) divided by bankfull sediment flux. An alternative formulation is the product of water-rock ratio at bankfull ($Q_{w,bf}/Q_{s,bf}$) and ratio of runoff to bankfull water discharge ($PC/Q_{w,bf}$). The medians of these values for rivers in our dataset are 12,000 and 0.15, respectively, so their product yields the 1800 we illustrate with the bold dashed line. Dotted lines illustrate a factor of 10 difference from the prediction.

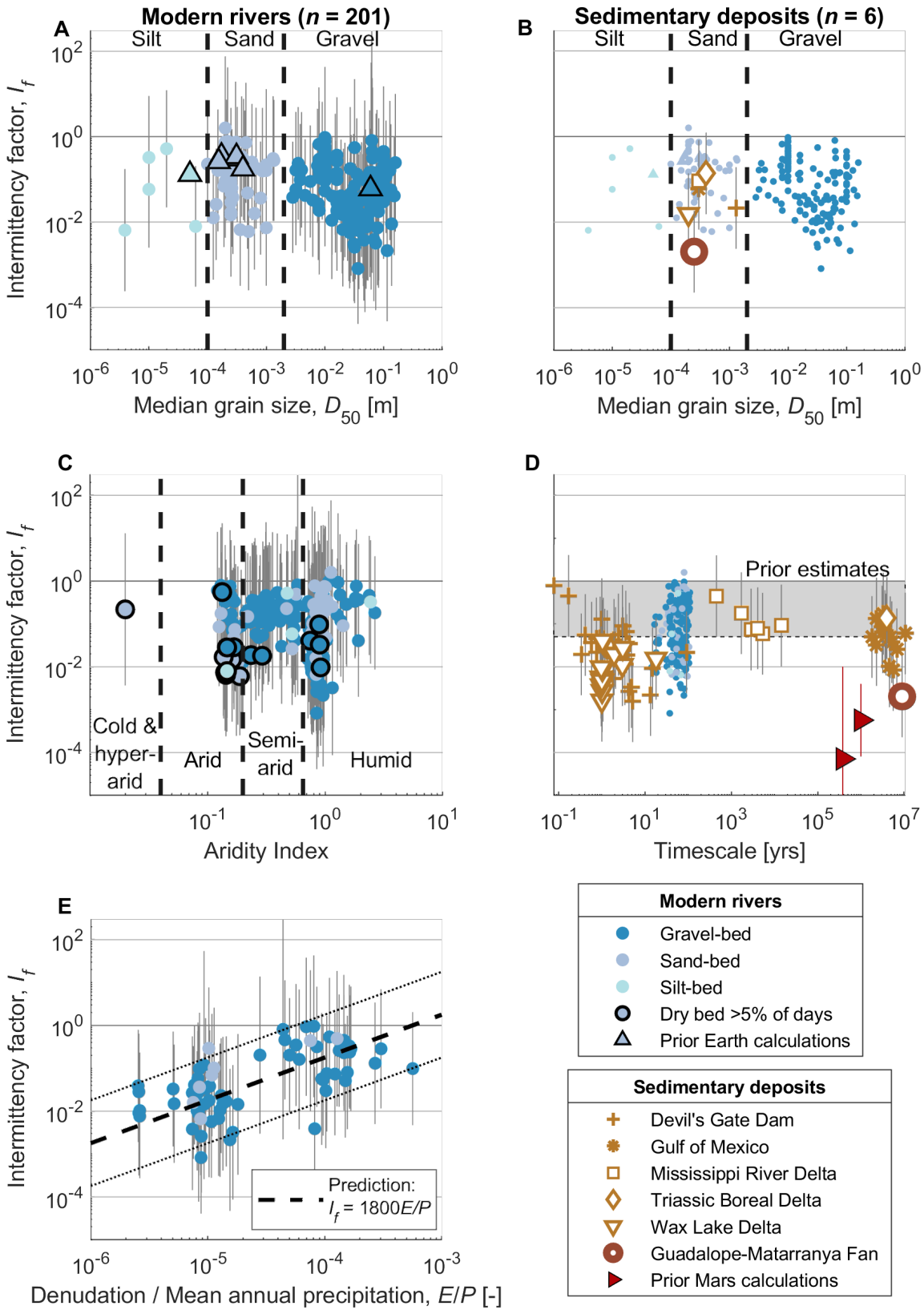
A
Modern rivers (n = 201)
Silt
Sand
Gravel
Intermittency factor, I_f
Median grain size, D_{50} [m]
B
Sedimentary deposits (n = 6)
Silt
Sand
Gravel
Median grain size, D_{50} [m]
C
Intermittency factor, I_f
Cold & hyper-arid
Arid
Semi-arid
Humid
Aridity Index
D
Prior estimates
Timescale [yrs]
E
Intermittency factor, I_f
Prediction: $I_f = 1800E/P$
Denudation / Mean annual precipitation, E/P [-]
Modern rivers
Gravel-bed
Sand-bed
Silt-bed
Dry bed >5% of days
Prior Earth calculations
Sedimentary deposits
Devil's Gate Dam
Gulf of Mexico
Mississippi River Delta
Triassic Boreal Delta
Wax Lake Delta
Guadalope-Matarranya Fan
Prior Mars calculations

It is well-established that rivers in arid climates have longer bankfull recurrence intervals than rivers in humid climates (e.g., Farquharson et al., 1992). To test whether there is a climate control on the intermittency factor, we extracted the aridity index (Trabucco and Zomer, 2019) for each stream gage location, and noted which rivers were ephemeral (which we defined as having zero flow at least 5% of the time based on the USGS streamgage data). There is not a consistent trend between the aridity index and the intermittency factor. In fact, surprisingly, even the glacier-fed Onyx River in Antarctica has a comparable intermittency factor to humid rivers in the continental United States (Fig. 5.10B). Furthermore, there are ephemeral rivers (solid-outlined points in Fig. 5.10B) in all four climate zones, and they show no variation in intermittency factor between climate zones. Of the examined climate types, rivers in semi-arid climates had higher intermittency factors (median: 0.19, range: 0.013-0.81) than humid (median: 0.041, range: 0.00082-1.6) or arid (median: 0.077, range: 0.0060-0.79) climates, but the ranges significantly overlap for all climates.

We also hypothesized that intermittency factor might relate to sediment supply. For example, rivers that are fed more sediment, relative to water, might adjust their hydraulic geometry such that they transport sediment near bankfull conditions for a larger fraction of the time, yielding a larger I_f. We estimated the long-term sediment supply from the catchment-averaged denudation rate by taking the nearest cosmogenic-derived denudation rate from the Harel et al. (2016) compilation, excluding streamgages more than 100 km from a denudation-rate measurement. We estimated the runoff from the mean annual precipitation rate, P, at each streamgage using the WorldClim 2.1 model (Fick and Hijmans, 2017). Results show that the intermittency factor follows an approximate linear scaling relation with the ratio of denudation to precipitation (E/P) (Fig. 5.10E). The regions with high E/P in our database generally have high tectonic uplift rates, such as 80-486 mm/kyr in coastal California and 40-110 in Idaho and Wyoming. Similarly, the lowest intermittency

factors occur in the rainy and tectonically stable Appalachian region, USA, where denudation rates are generally 3-20 mm/kyr (see Fig. SI9 for map).

5.6 Discussion

5.6.1 Intermittency factor and bed grainsize

It is surprising that the intermittency factor does not correlate with bed-material grainsize because sand-bedded rivers tend to transport sand for much of the time, even during low flows, whereas gravel-bedded rivers only transport gravel during bankfull floods (Trampush et al., 2014). Therefore, one might expect sand-bedded rivers to have an intermittency factor near unity, in contrast to our results. To investigate this paradox, we plotted the intermittency factor against the fraction of time where shear stress exceeded the critical value for sediment transport (calculated from equation (5.20) for gravel-bed rivers and from Parker et al. (2003) for sand-bedded (Fig. 5.11A). Most gravel-bedded rivers plot along the 1:1 line, indicating that intermittency factor in coarse-grained systems is well approximated by the fraction of time the shear stress is above critical. This makes sense because gravel-bedded rivers tend to have bankfull Shields stresses that are very near the threshold for sediment transport (Parker et al., 2007); gravel is not transported during low flows, and floods that exceed bankfull conditions may not produce bed stresses that far exceed the critical stress due to overbank flow onto the floodplain (Phillips et al., 2013). In fact, intermittency factors estimated previously from observations of the fraction of days where gravel moved (Phillips et al., 2013; Lajeunesse et al., 2018) are 0.06 and 0.01, which fall well within the range of our calculated values.

However, the sand bedded rivers do not plot on the one-to-one line and instead almost all have shear stress above critical, regardless of their intermittency factor. To help explain the sand-bed data, it is useful to reformulate equation (5.1), as

$$I_f = \left(\frac{\sum t(\tau_* > \tau_{*,c})}{\sum t}\right)\left(\frac{\overline{Q_s(\tau_* > \tau_{*,c})}}{Q_{s,bf}}\right), \qquad \text{Eq. 5.21}$$

in which $\overline{Q_s(\tau_* > \tau_{*,c})} = \frac{\sum Q_s(\tau_* > \tau_{*,c})}{\sum t(\tau_* > \tau_{*,c})}$ is the average sediment flux over the time period when sediment is in motion, i.e., $\sum t(\tau_* > \tau_{*,c})$. Equation (5.21) reveals that the intermittency factor can be thought of as the product of two terms: the fraction of time that the river exceeds the critical shear stress (time-fraction term), and the average nonzero sediment flux relative to the bankfull sediment flux (flux-ratio term). Gravel-bedded rivers tend to have flux-ratio term near unity, and therefore their intermittency factors are approximated by the fraction of time above the critical stress (Figure 11B), as explained above. In contrast, sand-bedded rivers generally have a time-fraction term near unity, such that their intermittency factors are determined by the flux-ratio term. Because sand-bed rivers move sediment almost constantly, including at low flows, the mean sediment flux is dominated by low values. Therefore, the intermittency factors for sand-bed rivers are lower than their relatively large time-fraction terms.

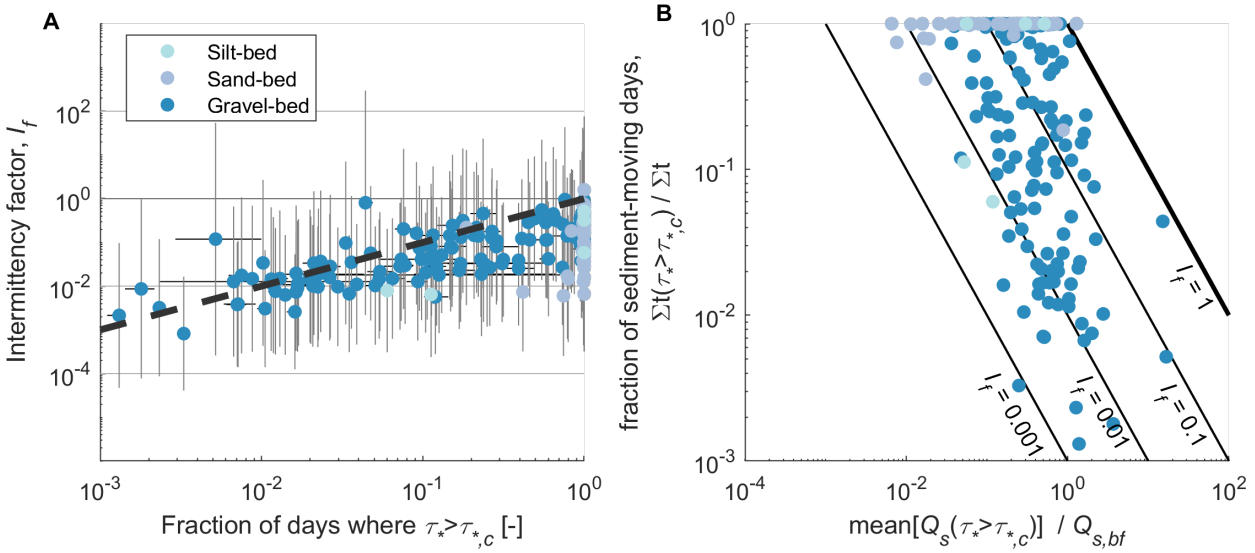

Figure 5.11–A) Intermittency factor and the fraction of days where shear stress exceeds the critical shear stress. Gravel-bed rivers show a 1:1 correlation (dashed line) between intermittency factor and fraction of time with shear stress above the critical value. Sand-bed rivers spend close to 100% of the time above critical shear stress despite having intermittency factors below 1, and therefore plot below the line to the right. B) The two terms from Eq. 21, fraction of days where sediment moves and ratio of mean sediment flux to bankfull sediment flux, plotted against each other. Because intermittency factor is the product of these two terms, lines of constant intermittency factor have a slope of -1. Colors indicate bed-material size (see Fig. 5.10A). Sand-bed rivers move

sediment at almost all flows, including low flows, so their mean sediment-moving flux is lower than bankfull sediment flux. On the other hand, gravel-bed rivers only move sediment at or above bankfull, so their mean flux is close to bankfull flux but they vary widely in the fraction of time where sediment moves.

5.6.2 Intermittency factor and timescale

We found that values for intermittency factor are similar between modern rivers and sedimentary deposits across timescales from months to millions of years (Figs. 5.10C & 5.10D). The result is surprising because additional sources of intermittency are present at large timescales, including channel meandering, sediment trapping in floodplains, and avulsions at timescales of centuries to millennia, and climate and tectonic variations over timescales of millennia to millions of years--variations like these might accumulate over longer timescales and cause lower intermittency factors at long timescales. In fact, an inverse correlation between sediment deposition rate and measurement timescale is so ubiquitous that it is named the Sadler Effect for the pioneering work on it (Sadler, 1981), and a similar inverse correlation between erosion rates and measurement timescale has also been observed (e.g., Finnegan et al., 2014).

However, recent work indicates that the Sadler Effect applies only at point-locations (e.g., individual stratigraphic sections), and that it disappears if entire deposits are included in the analysis. This occurs because mass balance requires that a deposition hiatus at one location is accompanied by active deposition at another (e.g., Sadler and Jerolmack, 2015; Paola et al., 2018). For example, the Mississippi River Delta has multiple lobes that were active at distinct times (e.g., Frazier, 1967); routing of the river through any lobe necessitates it be absent at the others, but analyzing all the lobes together shows continuous river activity. The formulation of intermittency factor in equation (5.1) shows intermittency factor equals the ratio of the mean sediment flux to the bankfull sediment flux. Because our measurements capture the entire deposit, the mean sediment flux is independent of

measurement timescale (Sadler and Jerolmack, 2015), and intermittency factor is similarly time-independent.

5.6.3 Intermittency factor, climate, and sediment supply

There is little difference between the values of intermittency factor for rivers in arid versus humid climates, though rivers in semi-arid climates lack the lowest intermittency factors found in the other climates (Fig. 5.10C). The similarity of intermittency factor across different levels of aridity is surprising because it is well-established that precipitation is more intermittent in arid climates (e.g., Farquharson et al., 1992), so it would follow logically that river intermittency mimics precipitation intermittency because water discharge is precipitation-derived. However, because of the observed climate independence and the definition of intermittency factor based on sediment flux rather than water discharge, we investigated the role of sediment supply in setting intermittency factor.

Instead of climate, we found the more important determinant for the intermittency factor is the ratio of denudation to precipitation (E/P; Fig. 5.10E). For the rivers in our study, the variability in this factor is mostly controlled by the erosion rate; mean annual precipitation spans a factor of 12 while denudation rates span a factor of 190. The finding that intermittency factor responds to sediment supply and water availability (Fig. 5.10E) supports prior observations that rivers adjust their geometry to move the available sediment and water (e.g., Parker et al., 2007; Pfeiffer et al., 2017; Phillips and Jerolmack, 2016). For instance, Pfeiffer et al. (2017) found that gravel-bed rivers with greater sediment supply also have greater bankfull Shields numbers, suggesting larger intermittency factors. We speculate that as the supply of sediment changes due to tectonics, climate, anthropogenic, or other forcings, the channel will adopt a new bankfull geometry to convey the sediment load (e.g., Wolman and Miller, 1960). Our data shows that the relation between I_f and E/P is approximately linear (Fig. 5.10E), which implies, for example, that a doubling in the sediment

supply will result in a doubling of the intermittency factor through some geometric change. We hypothesize that increasing sediment supply deepens or steepens the channel because either change results in increased bankfull shear stress, which was found to accompany increased sediment supply by Pfeiffer et al. (2017).

However, one of the main features of the intermittency factor as defined in equation (5.1) is that it depends on sediment flux at all flows, including both bankfull and non-bankfull conditions, and therefore the intermittency factor also responds to the impact of channel adjustments on sub-bankfull flows rather than only changing directly with bankfull geometry. For example, increasing bed slope will increase sediment flux at both bankfull and non-bankfull conditions and could therefore either increase or decrease intermittency factor depending on changes in non-bankfull sediment flux compared to changes in bankfull sediment flux. Similarly, bankfull depth has a complex impact on intermittency factor – bankfull depth often serves as a cutoff point above which flows become unconfined, so water discharge above bankfull has comparable sediment flux to bankfull sediment flux. Therefore, changing bankfull depth nonlinearly changes both mean sediment flux and bankfull sediment, so the resulting impact on intermittency factor is highly nonlinear.

The complexity in river response to changes in climate and tectonics, which is known to affect the preservability of climate and tectonic signals in sedimentary records (e.g., Jerolmack and Paola, 2010; Phillips and Jerolmack, 2016), is compounded by complexity of intermittency factor. Because intermittency factor appears to scale directly with the E/P ratio (Fig. 5.10E) but changes nonlinearly with channel geometry as described above, it appears that intermittency factor plays a major role in filtering how environmental signals are preserved in the sedimentary record. For example, if sediment supply doubles, some of the increase will be accommodated by increased sub-bankfull sediment flux and so the bankfull sediment flux will likely only increase a small amount.

Signal preservation is further complicated because changes are likely partitioned between channel parameters, but only bankfull depth and bed grainsize are preserved in the sedimentary record. The end result is that changes to the intermittency factor likely represent another way that rivers can adjust to a changing environment without leaving a signal.

5.6.4 Application to Mars

A main goal of this study was to determine the applicability of intermittency factors measured in modern rivers to ancient systems on Earth and Mars. We found no systematic variation over depositional timespans of months to tens of millions of years, across Earth's aridity zones, or between a variety of bed grainsizes (Fig. 5.10). While we did find that intermittency factors were larger with greater ratios of catchment-averaged erosion rate to precipitation rate (E/P), there is still significant scatter in this relation and its universality is uncertain (Fig. 5.10E). Furthermore, it is unclear whether E/P would be different on Mars. Erosion rates during the Noachian have been estimated to be 10^{-5} – 10^{-6} m/yr (Golombek et al., 2006), which are on the lower end of the cosmogenic-derived denudation rates for our catchments shown in Fig. 5.10E, indicating a possibility that I_f could be lower on Mars.

We compiled existing estimates of intermittency factor that had been used to constrain duration of fluvial activity with a mass-balance approach similar to equation (5.2) (Kleinhans, 2005; Kleinhans et al., 2010; Irwin et al., 2015; Morgan et al., 2014; Williams and Weitz, 2014; Fassett & Head, 2005; Barnhart et al., 2009; Matsubara et al., 2015; Kite, 2018; Orofino et al., 2018; Rosenberg et al., 2019). Intermittency factors in these prior studies were generally assumed to be 0.05 based on analogy to some bankfull recurrence intervals on Earth, or 1.0 based on implicitly or explicitly assuming constant bankfull flow. Our calculated intermittency factors include lower values than the most common prior estimates for Mars (Fig. 5.12A). To illustrate the differences with our values,

we applied the 5th, 50th, and 95th percentile of our intermittency factors (0.0044, 0.10, 0.58) in place of the previous assumed values, and kept the same values of volume and bankfull sediment flux from prior work (Fig. 5.12B). This resulted in significantly longer calculated depositional timespans—some values exceed 10^6 years with the 5th percentile intermittency factor. Million-year depositional timespans are consistent with other evidence, such as embedded crater counts from one site in Aeolis Dorsa (Kite et al., 2013). Given the bounds in major fluvial activity indicated by the valley networks (after the Hellas impact and before later alluvial fans, ~3.9-3.4 G.a.; Kite, 2019), this would indicate that rivers were active across a large fraction of that time.

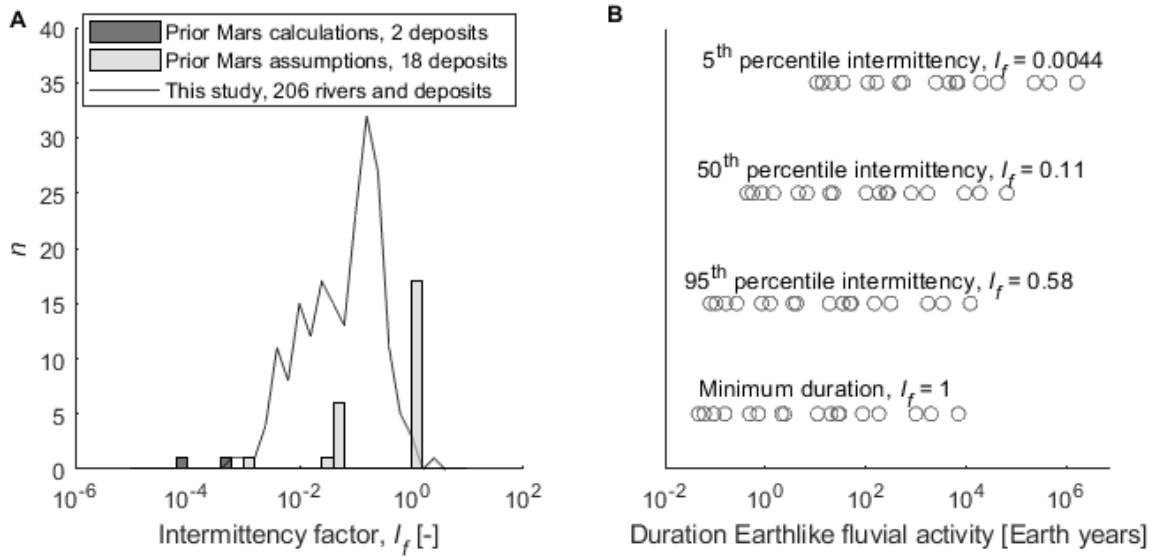

Figure 5.12-Comparison of intermittency factors (panel A) and durations of river flow (panel B) that have been estimated for Mars. A) Intermittency factors shown are assumptions based on comparison to Earth estimates (Kleinhans et al., 2010; Hauber et al., 2009; Palucis et al., 2014; Morgan et al., 2014), calculations for Mars (Buhler et al., 2014; Lapôtre and Ielpi, 2020), and calculations for Earth in this study. There are more values reported for Mars than deposits studied because many studies have examined the same deposits, and the values shown are often used as paired bounds on the guess (most often 0.05 and 1). Our calculations include lower values than most prior estimates, indicating that timescales of deposition could be consistently underestimated by orders of magnitude on Mars. Our calculated values for terrestrial systems are all higher than prior calculated values for systems on ancient Mars. B) Applying our 5th, 50th, and 95th percentile values of intermittency factor in place of prior intermittency factor extends the total duration of fluvial activity calculated from this method. The lowest values of our distribution yield the highest values of duration, and indicate that at least one river system on Mars could have flowed for millions of years with Earthlike intermittency.

In addition to the estimated values of intermittency factor, there are two calculations of intermittency factor for Mars (Buhler et al., 2014; Lapôtre and Ielpi, 2020), which are both lower ($I_f \cong 0.0001$) than our lowest calculated values (Fig. 5.12A). Their values were calculated by comparing deposit-formation timescales against total-activity timescales estimated from erosion rates, so that overestimated deposition rates or underestimated erosion rates could have resulted in I_f values that are lower than ours. Alternatively, their lower values could result from additional sources of intermittency beyond those present on Earth, such as intermittent liquid-water-supporting climates (e.g., Segura et al., 2002; Wordsworth et al., 2013), or because of lower *E*/*P* ratios on Mars.

Applying the I_f values we calculated on Earth to previously studied deposits on Mars (Fig. 5.12B) indicates that some fluvial systems could have existed for over 10^6 years on early Mars, longer than was previously assumed. Many of the landforms are intracrater deposits, indicating that local fluvial systems persisted long durations, so the identification and study of larger features would likely push the measured durations higher still. Given the even lower intermittency factors measured for martian systems (Buhler et al., 2014; Lapôtre and Ielpi, 2020), which are supported by evidence of low denudation rates (Golombek et al., 2006), the duration of fluvial activity could be even longer and potentially span over 10^7 years for many systems.

5.7 Conclusions

The Guadalope-Matarranya fan in the Ebro Basin of Spain contains many exhumed channel belts, represented as fluvial ridges, and is an excellent analog for similar features observed across Mars. Thickness of the channel bodies as well as cross-stratification from bars and dunes indicates that the deposit was created by sand-bedded rivers 1-2 meters deep, which we used to estimate a representative bankfull sediment flux of 0.48 m^3/s. Using the volume of the fan (10^{12} m^3) and the

depositional timespan (9 Myr), we estimated an intermittency factor was 0.002. Intermittency factors ranging from 0.0016-0.78 (median 0.036) were calculated for six other depositional systems by comparing published volumes and depositional timespans with reconstructions of bankfull sediment flux. The deposits we studied had volumes ranging from 10^{4}-10^{15} m^{3}, timescales of 10^{1}-10^{7} yrs, and channels 1-26 m deep. In addition, we estimated intermittency factors for 200 modern rivers to range from 0.00082-1.6 (median 0.10), which overlap with the values calculated for sedimentary deposits.

No significant differences were observed between intermittency factors for sand-bedded and gravel-bedded rivers (medians: 0.16 and 0.092). Intermittency factors for gravel-bedded rivers were found to be much less than unity because gravel-bedded rivers only transport sediment during a small fraction of time where shear stresses exceed the critical stress for transport. In contrast, sand-bedded rivers transport sediment for nearly all of the time, but their average fluxes are far less than the bankfull flux, which results in intermittency factors similar to gravel-bedded rivers. We also did not find significant differences in intermittency factor between arid and humid climates (medians: 0.077 and 0.041), or between ephemeral and non-ephemeral rivers (medians: 0.019 and 0.10). Furthermore, despite a huge range in depositional timespans from 10^{1} to 10^{6} years, intermittency factors across these timescales also were not significantly different. Time-independence of intermittency factor is likely due to its direct correlation with mean sediment flux, which has previously been shown to be time-independent when entire deposits are analyzed.

In contrast to the other parameters examined, intermittency factors are systematically larger for rivers with greater ratios of catchment-averaged erosion rate to mean annual precipitation, suggesting that rivers may adjust their geometry to achieve higher intermittency factors in catchments with greater sediment supply. The independence from time and dependence on sediment supply together indicate that intermittency factor is related to mass-balance—rivers adjust their

geometry to move the available sediment with the available water, and intermittency factor defined for sediment flux is independent of other parameters, including intermittency of precipitation.

The intermittency factors we calculated for Earth are lower values than those previously estimated on Mars. If our values apply to Mars, they suggest timespans of fluvial activity for individual systems lasting millions of years or longer. These results support the hypothesis that rivers during the late Noachian/early Hesperian lasted for geologic timescales.

5.8 Works Cited

Allen, G. H., T. M. Pavelsky, E. A. Barefoot, M. P. Lamb, D. Butman, A. Tashie and C. J. Gleason (2018). "Similarity of stream width distributions across headwater systems." Nature Communications **9**(1): 610.

Allen, J. R. (1963). "The classification of cross-stratified units. With notes on their origin." Sedimentology **2**(2): 93-114.

Allen, J. R. (1965). "A review of the origin and characteristics of recent alluvial sediments." Sedimentology **5**(2): 89-191.

Allen, P., L. Cabrera, F. Colombo and A. Matter (1983). "Variations in fluvial style on the Eocene–Oligocene alluvial fan of the Scala Dei Group, SE Ebro Basin, Spain." Journal of the Geological Society **140**(1): 133-146.

Andrews, E. D. (1984). "Bed-material entrainment and hydraulic geometry of gravel-bed rivers in Colorado." Geological Society of America Bulletin **95**(3): 371-378.

Arcement, G. J. (1988). Discharge and suspended-sediment data for the Lower Atchafalaya Bay, and Wax Lake Outlet, Louisiana, 1980-82. Open-File Report.

Baker, V. R. and J. B. Partridge (1986). "Small Martian valleys: Pristine and degraded morphology." Journal of Geophysical Research: Solid Earth **91**(B3): 3561-3572.

Barberà, X., L. Cabrera, M. Marzo, J. M. Parés and J. Agustı´ (2001). "A complete terrestrial Oligocene magnetobiostratigraphy from the Ebro Basin, Spain." Earth and Planetary Science Letters **187**(1): 1-16.

Barberà, X., J. Parés, L. Cabrera and P. Anadón (1994). "High-resolution magnetic stratigraphy across the Oligocene-Miocene boundary in an alluvial-lacustrine succession (Ebro Basin, Northeast Spain)." Physics of the earth and planetary interiors **85**(1): 181-193.

Barnhart, C. J., A. D. Howard and J. M. Moore (2009). "Long-term precipitation and late-stage valley network formation: Landform simulations of Parana Basin, Mars." Journal of Geophysical Research **114**(E1).

Bhattacharya, J. P., P. Copeland, T. F. Lawton and J. Holbrook (2016). "Estimation of source area, river paleo-discharge, paleoslope, and sediment budgets of linked deep-time depositional systems and implications for hydrocarbon potential." Earth-Science Reviews **153**: 77-110.

Bhattacharya, J. P., A. D. Miall, C. Ferron, J. Gabriel, N. Randazzo, D. Kynaston, B. R. Jicha and B. S. Singer (2019). "Time-stratigraphy in point sourced river deltas: Application to

sediment budgets, shelf construction, and paleo-storm records." Earth-Science Reviews **199**: 102985.

Bradley, R. W. and J. G. Venditti (2017). "Reevaluating dune scaling relations." Earth-Science Reviews **165**: 356-376.

Brownlie, W. R. (1981). Compilation of alluvial channel data: laboratory and field, California Institute of Technology, WM Keck Laboratory of Hydraulics and ….

Buhler, P. B., C. I. Fassett, J. W. Head and M. P. Lamb (2014). "Timescales of fluvial activity and intermittency in Milna Crater, Mars." Icarus **241**: 130-147.

Buj, O. and J. Gisbert (2010). "Influence of pore morphology on the durability of sedimentary building stones from Aragon (Spain) subjected to standard salt decay tests." Environmental Earth Sciences **61**(7): 1327-1336.

Burr, D. M., M.-T. Enga, R. M. E. Williams, J. R. Zimbelman, A. D. Howard and T. A. Brennand (2009). "Pervasive aqueous paleoflow features in the Aeolis/Zephyria Plana region, Mars." Icarus **200**(1): 52-76.

Burr, D. M., R. M. E. Williams, K. D. Wendell, M. Chojnacki and J. P. Emery (2010). "Inverted fluvial features in the Aeolis/Zephyria Plana region, Mars: Formation mechanism and initial paleodischarge estimates." Journal of Geophysical Research: Planets **115**(E07011).

Cabrera, L., M. Cabrera, R. Gorchs and F. De Las Heras (2002). "Lacustrine basin dynamics and organosulphur compound origin in a carbonate-rich lacustrine system (Late Oligocene Mequinenza Formation, SE Ebro Basin, NE Spain)." Sedimentary Geology **148**(1): 289-317.

Cabrera, L., F. Colombo and S. Robles (1985). Sedimentation and tectonics interrelationships in the Paleogene marginal alluvial systems of the SE Ebro Basin: transition from alluvial to shallow lacustrine environments, International Association of Sedimentologists, Institut d'Estudis Ilerdencs, Universitat Autònoma de Barcelona.

Cabrera, L. and A. Sáez (1987). "Coal deposition in carbonate-rich shallow lacustrine systems: the Calaf and Mequinenza sequences (Oligocene, eastern Ebro Basin, NE Spain)." Journal of the Geological Society **144**(3): 451-461.

Cardenas, B. T., D. Mohrig, T. A. Goudge, C. M. Hughes, J. S. Levy, T. Swanson, J. Mason and F. Zhao (2020). "The anatomy of exhumed river-channel belts: Bedform to belt-scale river kinematics of the Ruby Ranch Member, Cretaceous Cedar Mountain Formation, Utah, USA." Sedimentology **n/a**(n/a).

Castro, J. M. and P. L. Jackson (2001). "Bankfull Discharge Recurrence Intervals And Regional Hydraulic Geometry Relationships: Patterns In The Pacific Northwest, USA 1." JAWRA Journal of the American Water Resources Association **37**(5): 1249-1262.

Chitale, S. V. (1970). "River channel patterns." Journal of the Hydraulics Division **96**(1): 201-221.

Church, M. (2006). "Bed material transport and the morphology of alluvial river channels." Annu. Rev. Earth Planet. Sci. **34**: 325-354.

Craddock, R. A. and A. D. Howard (2002). "The case for rainfall on a warm, wet early Mars." Journal of Geophysical Research: Planets **107**(E11): 21-21-21-36.

Cuevas Martínez, J. L., P. Arbués Cazo, L. Cabrera Pérez and M. Marzo Carpio (2007). "Anatomy and architecture of ephemeral, ribbon-like channel-fill deposits of the Caspe Formation (Upper Oligocene to Lower Miocene of the Ebro Basin, Spain)." Sedimentary Processes, Environments and Basins: A Tribute to Peter Friend: 591-611.

Cuevas Martínez, J. L., L. Cabrera Pérez, A. Marcuello, P. A. U. Arbués Cazo, M. Marzo Carpio and F. Bellmunt (2010). "Exhumed channel sandstone networks within fluvial fan deposits from the Oligo-Miocene Caspe Formation, South-east Ebro Basin (North-east Spain)." Sedimentology **57**(1): 162-189.

Cui, Y. and G. Parker (1998). "The arrested gravel front: stable gravel-sand transitions in rivers Part 2: General numerical solution." Journal of Hydraulic Research **36**(2): 159-182.

Czuba, J. A. and E. Foufoula-Georgiou (2014). "A network-based framework for identifying potential synchronizations and amplifications of sediment delivery in river basins." Water Resources Research **50**(5): 3826-3851.

DiBiase, R. A., A. B. Limaye, J. S. Scheingross, W. W. Fischer and M. P. Lamb (2013). "Deltaic deposits at Aeolis Dorsa: Sedimentary evidence for a standing body of water on the northern plains of Mars." Journal of Geophysical Research: Planets **118**(6): 1285-1302.

Dong, T. Y., J. A. Nittrouer, E. Il'icheva, M. Pavlov, B. McElroy, M. J. Czapiga, H. Ma and G. Parker (2016). "Controls on gravel termination in seven distributary channels of the Selenga River Delta, Baikal Rift basin, Russia." Bulletin **128**(7-8): 1297-1312.

Einstein, H. and N. Chien (1953). "Can the rate of wash load be predicted from the bed-load function?" Eos, Transactions American Geophysical Union **34**(6): 876-882.

Einstein, H. A. (1950). The bed-load function for sediment transportation in open channel flows, United States Department of Agriculture. **1026**.

Eke, E., G. Parker and Y. Shimizu (2014). "Numerical modeling of erosional and depositional bank processes in migrating river bends with self-formed width: Morphodynamics of bar push and bank pull." Journal of Geophysical Research: Earth Surface **119**(7): 1455-1483.

Elliott, J. G. and K. D. Cartier (1986). Hydraulic geometry and streamflow of channels in the Piceance Basin, Rio Blanco and Garfield counties, Colorado, Department of the Interior, US Geological Survey.

Emmett, W. W. (1972). The hydraulic geometry of some Alaskan streams south of the Yukon River, US Dept. of the Interior, Geological Survey, Water Resources Division ….

Engelund, F. and E. Hansen (1967). A monograph on sediment transport in alluvial streams, Tekniskforlag Skelbrekgade 4, Copenhagen V, Denmark.

Fairén, A. G. (2010). "A cold and wet Mars." Icarus **208**(1): 165-175.

Farquharson, F., J. Meigh and J. Sutcliffe (1992). "Regional flood frequency analysis in arid and semi-arid areas." Journal of Hydrology **138**(3-4): 487-501.

Fassett, C. I. and J. W. Head III (2005). "Fluvial sedimentary deposits on Mars: Ancient deltas in a crater lake in the Nili Fossae region." Geophysical Research Letters **32**(14).

Ferguson, R. (2007). "Flow resistance equations for gravel-and boulder-bed streams." Water Resources Research **43**(5).

Fernandez Luque, R. and R. Van Beek (1976). "Erosion and transport of bed-load sediment." Journal of hydraulic research **14**(2): 127-144.

Fick, S. E. and R. J. Hijmans (2017). "WorldClim 2: new 1-km spatial resolution climate surfaces for global land areas." International journal of climatology **37**(12): 4302-4315.

Finnegan, N. J., R. Schumer and S. Finnegan (2014). "A signature of transience in bedrock river incision rates over timescales of 10 4–10 7 years." Nature **505**(7483): 391-394.

Forsberg-Taylor, N. K., A. D. Howard and R. A. Craddock (2004). "Crater degradation in the Martian highlands: Morphometric analysis of the Sinus Sabaeus region and simulation modeling suggest fluvial processes." Journal of Geophysical Research: Planets **109**(E5).

Foster, K. (2012). Bankfull-channel geometry and discharge curves for the Rocky Mountains Hydrologic Region in Wyoming. Scientific Investigations. U. S. G. Survey**:** 20.

Frazier, D. E. (1967). "Recent deltaic deposits of the Mississippi River: their development and chronology." Gulf Coast Association of Geological Societies Transactions **17**: 287-315.

Friend, P., J. Hirst and G. Nichols (1986). "Sandstone-body structure and river process in the Ebro Basin of Aragón, Spain." Cuadernos de Geología Ibérica **10**: 9-30.

Friend, P. F., M. J. Slater and R. C. Williams (1979). "Vertical and lateral building of river sandstone bodies, Ebro Basin, Spain." Journal of the Geological Society **136**(1): 39-46.

Galloway, W. E., T. L. Whiteaker and P. Ganey-Curry (2011). "History of Cenozoic North American drainage basin evolution, sediment yield, and accumulation in the Gulf of Mexico basin." Geosphere **7**(4): 938-973.

Ganti, V., Z. Chu, M. P. Lamb, J. A. Nittrouer and G. Parker (2014). "Testing morphodynamic controls on the location and frequency of river avulsions on fans versus deltas: Huanghe (Yellow River), China." Geophysical Research Letters **41**(22): 7882-7890.

Ganti, V., K. M. Straub, E. Foufoula-Georgiou and C. Paola (2011). "Space-time dynamics of depositional systems: Experimental evidence and theoretical modeling of heavy-tailed statistics." Journal of Geophysical Research: Earth Surface **116**(F2).

Garcés, M., L. Cabrera, E. Roca and O. Gratacós (2008). "Comment on “The diachroneity of alluvial-fan lithostratigraphy? A test case from southeastern Ebro basin magnetostratigraphy” by N. Swanson-Hysell and D. L. Barbeau, Jr." Earth and Planetary Science Letters **275**(1-2): 181-186.

Garcia-Castellanos, D. and J. C. Larrasoaña (2015). "Quantifying the post-tectonic topographic evolution of closed basins: The Ebro basin (northeast Iberia)." Geology **43**(8): 663-666.

Golombek, M. P., J. A. Grant, L. S. Crumpler, R. Greeley, R. E. Arvidson, J. F. Bell III, C. M. Weitz, R. Sullivan, P. R. Christensen and L. Soderblom (2006). "Erosion rates at the Mars Exploration Rover landing sites and long-term climate change on Mars." Journal of Geophysical Research: Planets **111**(E12).

Gonzàlez-Bonarino, G., F. Colombo and L. Abascal (2010). "Architecture of an Oligocene fluvial ribbon sandstone in the Ebro Basin, North-eastern Spain." Sedimentology **57**(3): 845-856.

Goudge, T. A., J. W. Head, J. F. Mustard and C. I. Fassett (2012). "An analysis of open-basin lake deposits on Mars: Evidence for the nature of associated lacustrine deposits and post-lacustrine modification processes." Icarus **219**(1): 211-229.

Goudge, T. A., D. Mohrig, B. T. Cardenas, C. M. Hughes and C. I. Fassett (2018). "Stratigraphy and paleohydrology of delta channel deposits, Jezero crater, Mars." Icarus **301**: 58-75.

Gran, K. B., N. Finnegan, A. L. Johnson, P. Belmont, C. Wittkop and T. Rittenour (2013). "Landscape evolution, valley excavation, and terrace development following abrupt postglacial base-level fall." GSA Bulletin **125**(11-12): 1851-1864.

Grotzinger, J., S. Gupta, M. Malin, D. Rubin, J. Schieber, K. Siebach, D. Sumner, K. Stack, A. Vasavada and R. Arvidson (2015). "Deposition, exhumation, and paleoclimate of an ancient lake deposit, Gale crater, Mars." Science **350**(6257): aac7575.

Hajek, E. A. and P. L. Heller (2012). "Flow-Depth Scaling In Alluvial Architecture and Nonmarine Sequence Stratigraphy: Example from the Castlegate Sandstone, Central Utah, U.S.A." Journal of Sedimentary Research **82**(2): 121-130.

Halevy, I., M. T. Zuber and D. P. Schrag (2007). "A sulfur dioxide climate feedback on early Mars." Science **318**(5858): 1903-1907.

Harel, M. A., S. M. Mudd and M. Attal (2016). "Global analysis of the stream power law parameters based on worldwide 10 Be denudation rates." Geomorphology **268**: 184-196.

Hauber, E., K. Gwinner, M. Kleinhans, D. Reiss, G. Di Achille, G. G. Ori, F. Scholten, L. Marinangeli, R. Jaumann and G. Neukum (2009). "Sedimentary deposits in Xanthe Terra: Implications for the ancient climate on Mars." Planetary and Space Science **57**(8-9): 944-957.

Hayden, A. T. and M. P. Lamb (in press). "Fluvial sinuous ridges of the Morrison Formation, USA: Meandering, scarp retreat, and implications for Mars." Journal of Geophysical Research: Planets.

Hayden, A. T., M. P. Lamb, W. W. Fischer, R. C. Ewing, B. McElroy and R. M. E. Williams (2019). "Formation of sinuous ridges by inversion of river-channel belts in Utah, USA, with implications for Mars." Icarus **332**: 92-110.

Heller, P. L., D. Ratigan, S. Trampush, A. Noda, B. McElroy, J. Drever and S. Huzurbazar (2015). "Origins of Bimodal Stratigraphy In Fluvial Deposits: An Example From the Morrison Formation (Upper Jurassic), Western USA." Journal of Sedimentary Research **85**(12): 1466-1477.

Hoke, M. R., B. M. Hynek and G. E. Tucker (2011). "Formation timescales of large Martian valley networks." Earth and Planetary Science Letters **312**(1-2): 1-12.

Holbrook, J. and H. Wanas (2014). "A fulcrum approach to assessing source-to-sink mass balance using channel paleohydrologic parameters derivable from common fluvial data sets with an example from the Cretaceous of Egypt." Journal of Sedimentary Research **84**(5): 349-372.

Howard, A. D., J. M. Moore and R. P. Irwin III (2005). "An intense terminal epoch of widespread fluvial activity on early Mars: 1. Valley network incision and associated deposits." Journal of Geophysical Research: Planets **110**(E12).

Hynek, B. M., M. Beach and M. R. Hoke (2010). "Updated global map of Martian valley networks and implications for climate and hydrologic processes." Journal of Geophysical Research: Planets **115**(E9).

Irwin, R. P., K. W. Lewis, A. D. Howard and J. A. Grant (2015). "Paleohydrology of Eberswalde crater, Mars." Geomorphology **240**: 83-101.

Jerolmack, D. J., D. Mohrig, M. T. Zuber and S. Byrne (2004). "A minimum time for the formation of Holden Northeast fan, Mars." Geophysical Research Letters **31**(21).

Jerolmack, D. J. and C. Paola (2010). "Shredding of environmental signals by sediment transport." Geophysical Research Letters **37**(19).

Jones, M. A., P. L. Heller, E. Roca, M. Garcés and L. Cabrera (2004). "Time lag of syntectonic sedimentation across an alluvial basin: theory and example from the Ebro Basin, Spain." Basin Research **16**(4): 489-506.

Kite, E. S. (2019). "Geologic Constraints on Early Mars Climate." Space Science Reviews **215**(1): 10.

Kite, E. S., A. D. Howard, A. Lucas and K. W. Lewis (2015a). "Resolving the era of river-forming climates on Mars using stratigraphic logs of river-deposit dimensions." Earth and Planetary Science Letters **420**: 55-65.

Kite, E. S., A. Lucas and C. I. Fassett (2013). "Pacing early Mars river activity: Embedded craters in the Aeolis Dorsa region imply river activity spanned ≳(1–20)Myr." Icarus **225**(1): 850-855.

Klausen, T. G., B. Nyberg and W. Helland-Hansen (2019). "The largest delta plain in Earth's history." Geology **47**(5): 470-474.

Klausen, T. G., A. E. Ryseth, W. Helland-Hansen, R. Gawthorpe and I. Laursen (2014). "Spatial and Temporal Changes In Geometries of Fluvial Channel Bodies From the Triassic Snadd Formation of Offshore Norway." Journal of Sedimentary Research **84**(7): 567-585.

Kleinhans, M. G. (2005). "Flow discharge and sediment transport models for estimating a minimum timescale of hydrological activity and channel and delta formation on Mars." Journal of Geophysical Research: Planets **110**(E12).

Kleinhans, M. G., H. E. van de Kasteele and E. Hauber (2010). "Palaeoflow reconstruction from fan delta morphology on Mars." Earth and Planetary Science Letters **294**(3): 378-392.

Lajeunesse, E., O. Devauchelle and F. James (2018). "Advection and dispersion of bed load tracers." Earth Surface Dynamics **6**(2): 389-399.

Lamb, M. P., W. E. Dietrich and J. G. Venditti (2008). "Is the critical Shields stress for incipient sediment motion dependent on channel-bed slope?" Journal of Geophysical Research: Earth Surface **113**(F2).

Lapôtre, M. G. A. and A. Ielpi (2020). "The Pace of Fluvial Meanders on Mars and Implications for the Western Delta Deposits of Jezero Crater." AGU Advances **1**(2): e2019AV000141.

Leclair, S. F. and J. S. Bridge (2001). "Quantitative interpretation of sedimentary structures formed by river dunes." Journal of Sedimentary Research **71**(5): 713-716.

LTER, M. D. V., M. Gooseff and D. McKnight (2019). "McMurdo Dry Valleys LTER: High frequency seasonal stream gage measurements from the Onyx River at Lower Wright in Wright Valley, Antarctica from 1972 to present."

Matsubara, Y., A. D. Howard, D. M. Burr, R. M. E. Williams, W. E. Dietrich and J. M. Moore (2015). "River meandering on Earth and Mars: A comparative study of Aeolis Dorsa meanders, Mars and possible terrestrial analogs of the Usuktuk River, AK, and the Quinn River, NV." Geomorphology **240**: 102-120.

Milliken, K. T., M. D. Blum, J. W. Snedden and W. E. Galloway (2018). "Application of fluvial scaling relationships to reconstruct drainage-basin evolution and sediment routing for the Cretaceous and Paleocene of the Gulf of Mexico." Geosphere **14**(2): 749-767.

Mischna, M. A., V. Baker, R. Milliken, M. Richardson and C. Lee (2013). "Effects of obliquity and water vapor/trace gas greenhouses in the early martian climate." Journal of Geophysical Research: Planets **118**(3): 560-576.

Modrick, T. M. and K. P. Georgakakos (2014). "Regional bankfull geometry relationships for southern California mountain streams and hydrologic applications." Geomorphology **221**: 242-260.

Mohrig, D., P. L. Heller, C. Paola and W. J. Lyons (2000). "Interpreting avulsion process from ancient alluvial sequences: Guadalope-Matarranya system (northern Spain) and Wasatch Formation (western Colorado)." Geological Society of America Bulletin **112**(12): 1787-1803.

Moore, J. M., A. D. Howard, W. E. Dietrich and P. M. Schenk (2003). "Martian layered fluvial deposits: Implications for Noachian climate scenarios." Geophysical Research Letters **30**(24).

Morgan, A. M., A. D. Howard, D. E. J. Hobley, J. M. Moore, W. E. Dietrich, R. M. E. Williams, D. M. Burr, J. A. Grant, S. A. Wilson and Y. Matsubara (2014). "Sedimentology and climatic environment of alluvial fans in the martian Saheki crater and a comparison with terrestrial fans in the Atacama Desert." Icarus **229**: 131-156.

Naito, K., H. Ma, J. A. Nittrouer, Y. Zhang, B. Wu, Y. Wang, X. Fu and G. Parker (2019). "Extended Engelund–Hansen type sediment transport relation for mixtures based on the sand-silt-bed Lower Yellow River, China." Journal of Hydraulic Research **57**(6): 770-785.

Nichols, G. J. and J. A. Fisher (2007). "Processes, facies and architecture of fluvial distributary system deposits." Sedimentary Geology **195**(1): 75-90.

Orofino, V., G. Alemanno, G. Di Achille and F. Mancarella (2018). "Estimate of the water flow duration in large Martian fluvial systems." Planetary and Space Science **163**: 83-96.

Pain, C., J. Clarke and M. Thomas (2007). "Inversion of relief on Mars." Icarus **190**(2): 478-491.

Pain, C. F. and C. D. Ollier (1995). "Inversion of relief — a component of landscape evolution." Geomorphology **12**(2): 151-165.

Palucis, M. C., W. E. Dietrich, A. G. Hayes, R. M. E. Williams, S. Gupta, N. Mangold, H. Newsom, C. Hardgrove, F. Calef and D. Y. Sumner (2014). "The origin and evolution of the Peace Vallis fan system that drains to the Curiosity landing area, Gale Crater, Mars." Journal of Geophysical Research: Planets **119**(4): 705-728.

Paola, C. (2013). "Is it possible to predict the past?" Lithosphere **5**(4): 450-451.

Paola, C. and L. Borgman (1991). "Reconstructing random topography from preserved stratification." Sedimentology **38**(4): 553-565.

Paola, C., V. Ganti, D. Mohrig, A. C. Runkel and K. M. Straub (2018). "Time Not Our Time: Physical Controls on the Preservation and Measurement of Geologic Time." Annual Review of Earth and Planetary Sciences **46**(1): 409-438.

Paola, C., P. L. Heller and C. L. Angevine (1992). "The large-scale dynamics of grain-size variation in alluvial basins, 1: Theory." Basin research **4**(2): 73-90.

Parker, G., C. Paola, K. X. Whipple and D. Mohrig (1998). "Alluvial fans formed by channelized fluvial and sheet flow. I: Theory." Journal of Hydraulic Engineering **124**(10): 985-995.

Parker, G., C. M. Toro-Escobar, M. Ramey and S. Beck (2003). "Effect of floodwater extraction on mountain stream morphology." Journal of Hydraulic Engineering **129**(11): 885-895.

Parker, G., P. R. Wilcock, C. Paola, W. E. Dietrich and J. Pitlick (2007). "Physical basis for quasi-universal relations describing bankfull hydraulic geometry of single-thread gravel bed rivers." Journal of Geophysical Research: Earth Surface **112**(F4).

Pérez-Rivarés, F. J., C. Arenas, G. Pardo and M. Garcés (2018). "Temporal aspects of genetic stratigraphic units in continental sedimentary basins: Examples from the Ebro basin, Spain." Earth-Science Reviews **178**: 136-153.

Pérez-Rivarés, J., M. G. Crespo, M. C. A. Abad and G. P. Tirapu (2004). "Magnetostratigraphy of the Miocene continental deposits of the Montes de Castejón (central Ebro basin, Spain): geochronological and paleoenvironmental implications." Geologica Acta **2**(3): 221-234.

Petkovsek, G. (2019). A review of Ackers and White sediment transport predictor. Proceedings of the Institution of Civil Engineers-Water Management, Thomas Telford Ltd.

Pettijohn, F. (1962). "Paleocurrents and paleogeography." AAPG Bulletin **46**(8): 1468-1493.

Pfeiffer, A. M., N. J. Finnegan and J. K. Willenbring (2017). "Sediment supply controls equilibrium channel geometry in gravel rivers." Proceedings of the National Academy of Sciences **114**(13): 3346-3351.

Phillips, C. B. and D. J. Jerolmack (2016). "Self-organization of river channels as a critical filter on climate signals." Science **352**(6286): 694-697.

Phillips, C. B., R. L. Martin and D. J. Jerolmack (2013). "Impulse framework for unsteady flows reveals superdiffusive bed load transport." Geophysical research letters **40**(7): 1328-1333.
Psomas (2018). Hydraulics, Sediment Transport, and Groundwater Analysis: Arroyo Seco Canyon Project Diversion, Pasadena Water & Power.
Ramirez, R. M. and R. A. Craddock (2018). "The geological and climatological case for a warmer and wetter early Mars." Nature Geoscience **11**(4): 230-237.
Ramirez, R. M., R. Kopparapu, M. E. Zugger, T. D. Robinson, R. Freedman and J. F. Kasting (2014). "Warming early Mars with CO2 and H2." Nature Geoscience **7**(1): 59-63.
Riba, O., J. Villena and J. Quirantes (1967). Nota preliminar sobre la sedimentacion en paleocanales terciarios de la zona de Caspe-Chiprana (Provincia de Zaragoza), CSIC.
Rickenmann, D. and A. Recking (2011). "Evaluation of flow resistance in gravel-bed rivers through a large field data set." Water Resources Research **47**(7).
Roberts, H., N. Walker, R. Cunningham, G. Kemp and S. Majersky (1997). "Evolution of sedimentary architecture and surface morphology: Atchafalaya and Wax Lake Deltas, Louisiana (1973-1994)."
Roberts, H. H. (1997). "Dynamic changes of the Holocene Mississippi River delta plain: the delta cycle." Journal of Coastal Research: 605-627.
Rosenberg, E. N., A. M. Palumbo, J. P. Cassanelli, J. W. Head and D. K. Weiss (2019). "The volume of water required to carve the martian valley networks: Improved constraints using updated methods." Icarus **317**: 379-387.
Sadler, P. M. (1981). "Sediment accumulation rates and the completeness of stratigraphic sections." The Journal of Geology: 569-584.
Sadler, P. M. and D. J. Jerolmack (2015). "Scaling laws for aggradation, denudation and progradation rates: the case for time-scale invariance at sediment sources and sinks." Geological Society, London, Special Publications **404**(1): 69-88.
Segura, T. L., O. B. Toon, A. Colaprete and K. Zahnle (2002). "Environmental effects of large impacts on Mars." Science **298**(5600): 1977-1980.
Shaw, J. and T. R. Healy (1980). "Morphology of the Onyx River system, McMurdo sound region, Antarctica." New Zealand journal of geology and geophysics **23**(2): 223-238.
Shaw, J. B. and D. Mohrig (2014). "The importance of erosion in distributary channel network growth, Wax Lake Delta, Louisiana, USA." Geology **42**(1): 31-34.
Shaw, J. B., D. Mohrig and S. K. Whitman (2013). "The morphology and evolution of channels on the Wax Lake Delta, Louisiana, USA." Journal of Geophysical Research: Earth Surface **118**(3): 1562-1584.
Sinha, S. K. and G. Parker (1996). "Causes of Concavity in Longitudinal Profiles of Rivers." Water Resources Research **32**(5): 1417-1428.
Sklar, L. S. and W. E. Dietrich (2004). "A mechanistic model for river incision into bedrock by saltating bed load." Water Resources Research **40**(6).
Slingerland, R. and N. D. Smith (2004). "River avulsions and their deposits." Annual Review of Earth Planetary Sciences **32**: 257-285.
Snyder, N. P., K. X. Whipple, G. E. Tucker and D. J. Merritts (2003). "Channel response to tectonic forcing: field analysis of stream morphology and hydrology in the Mendocino triple junction region, northern California." Geomorphology **53**(1-2): 97-127.
Sorby, H. C. (1859). "On the structures produced by the currents present during the deposition of stratified rocks." The geologist **2**(4): 137-147.

Stokes, W. L. (1961). Fluvial and eolian sandstone bodies in Colorado Plateau. SP 22: Geometry of Sandstone Bodies, American Association of Petroleum Geologists. **A055:** 151-178.

Sun, T., C. Paola, G. Parker and P. Meakin (2002). "Fluvial fan deltas: Linking channel processes with large-scale morphodynamics." Water Resources Research **38**(8): 26-21-26-10.

Survey, U. S. G. (2018). USGS Lidar Point Cloud CA LosAngeles 2016 L4 6413 1826c LAS 2018. U. S. G. Survey.

Swanson-Hysell, N. and D. L. Barbeau (2007). "The diachroneity of alluvial-fan lithostratigraphy? A test case from southeastern Ebro basin magnetostratigraphy." Earth and Planetary Science Letters **262**(3-4): 343-362.

Swanson-Hysell, N. and D. L. Barbeau (2008). "Reply to Garcés et al. comment on 'The diachroneity of alluvial-fan lithostratigraphy? A test case from southeastern Ebro Basin magnetostratigraphy'." Earth and Planetary Science Letters **275**(1-2): 187-192.

Trabucco, A. and R. Zomer (2019). Global Aridity Index and Potential Evapotranspiration (ET0) Climate Database. Figshare.

Trampush, S. M., S. Huzurbazar and B. J. McElroy (2014). "Empirical assessment of theory for bankfull characteristics of alluvial channels." Water Resources Research **50**(12): 9211-9220.

Tucker, G., S. Lancaster, N. Gasparini and R. Bras (2001). The channel-hillslope integrated landscape development model (CHILD). Landscape erosion and evolution modeling, Springer**:** 349-388.

Tucker, G. E. and R. L. Bras (2000). "A stochastic approach to modeling the role of rainfall variability in drainage basin evolution." Water Resources Research **36**(7): 1953-1964.

Valero, L., M. Garcés, L. Cabrera, E. Costa and A. Sáez (2014). "20 Myr of eccentricity paced lacustrine cycles in the Cenozoic Ebro Basin." Earth and Planetary Science Letters **408**: 183-193.

Wickert, A. D. and T. F. Schildgen (2019). "Long-profile evolution of transport-limited gravel-bed rivers."

Williams, G. P. (1978). "Bank-full discharge of rivers." Water Resources Research **14**(6): 1141-1154.

Williams, R. C. (1975). Fluvial Deposits of Oligo-Miocene Age in the Southern Ebro Basin, Spain, University of Cambridge.

Williams, R. M. E. (2007). Global spatial distribution of raised curvilinear features on Mars. Lunar and Planetary Science Conference.

Williams, R. M. E., R. P. Irwin and J. R. Zimbelman (2009). "Evaluation of paleohydrologic models for terrestrial inverted channels: Implications for application to martian sinuous ridges." Geomorphology **107**(3-4): 300-315.

Williams, R. M. E. and C. M. Weitz (2014). "Reconstructing the aqueous history within the southwestern Melas basin, Mars: Clues from stratigraphic and morphometric analyses of fans." Icarus **242**: 19-37.

Wolman, M. G. and J. P. Miller (1960). "Magnitude and frequency of forces in geomorphic processes." The Journal of Geology: 54-74.

Wordsworth, R., B. Ehlmann, F. Forget, R. Haberle, J. Head and L. Kerber (2018). "Healthy debate on early Mars." Nature Geoscience **11**(12): 888-888.

Wordsworth, R., F. Forget, E. Millour, J. W. Head, J. B. Madeleine and B. Charnay (2013). "Global modelling of the early martian climate under a denser CO2 atmosphere: Water cycle and ice evolution." Icarus **222**(1): 1-19.
Works, C. o. L. A. D. o. P. and T. L. A. C. F. C. District (2013). Sediment Management Strategic Plan 2012-2032.
Wright, S. and G. Parker (2005). "Modeling downstream fining in sand-bed rivers. I: Formulation." Journal of Hydraulic Research **43**(6): 613-620.

5.9 Supplement

5.9.1 Additional data from Guadalope-Matarranya Fan

This supplement expands on the results from Site 4 and on the summary from other sites as reported in the main text. All methods used are described in the Methods section of the main text. A secondary goal of this supplement is that it can be used as a field guide because all locations are easily accessible from the town of Caspe via road.

5.9.1.1 Site 1

Site 1 is notable for the numerous ridges intersecting in a pitchfork shape (Fig. 5.15). Ridge tops are at comparable elevation in the DEM, but group into three stratigraphic positions in the stratigraphic model. Field observations show that Ridge 2 superposes Ridges 1 and 3, and that there are notches eroded into ridges 2 and 5 where ridge 4 superposes them. Combining these observations, Ridge 4 superposes Ridges 2 and 5, which superpose Ridges 1, 3, and 6. Because these ridges align, we interpret them as a continuous ridge.

We also made quantitative measurements from the DEM. Best-fit slopes to the ridge centerlines are 10^{-3}, and all ridges have relief 3-16 meters above the surrounding plains. Caprock thickness varies from 2-3 meters along the ridges, and caprock breadth varies from 10-20 meters along ridge lengths.

Sedimentological investigation shows that caprocks are made of medium sandstone with some cross stratification (Fig. 5.15C). Twenty-six sets of dune cross strata ranged in height from 10-

30 centimeters and indicated flow directions within 0°-90° to the ridge axis (Fig. 5.15A). One dune set indicates paleoflow in the opposite direction from the other dune sets. We observed 19 truncated bar clinoforms with accretion directions 0°-90° to the ridge axis, and measured one to have a height of 90 cm. No planview expressions of lateral accretion sets were observed, either in remote sensing or field observation. Major erosional surfaces indicative of stories appeared absent, but bar clinoforms were generally half the caprock thickness, so it is likely that caprocks have >1 story. Amalgamation of multiple stories is further indicated by the DEM and UAV orthophotos, which show that Ridge 4 comprises a thin sinuous body atop a broad straight body (Fig. 5.15).

Mudstone dominated the ridge flanks beneath the caprocks (Fig. 5.15C). Talus blocks cover these flanks abundantly, but are absent from beyond the flanks, likely due to heavy modification for agricultural use. Talus blocks are made of sandstone and are up to 3 meters in diameter (Fig. 5.15B).

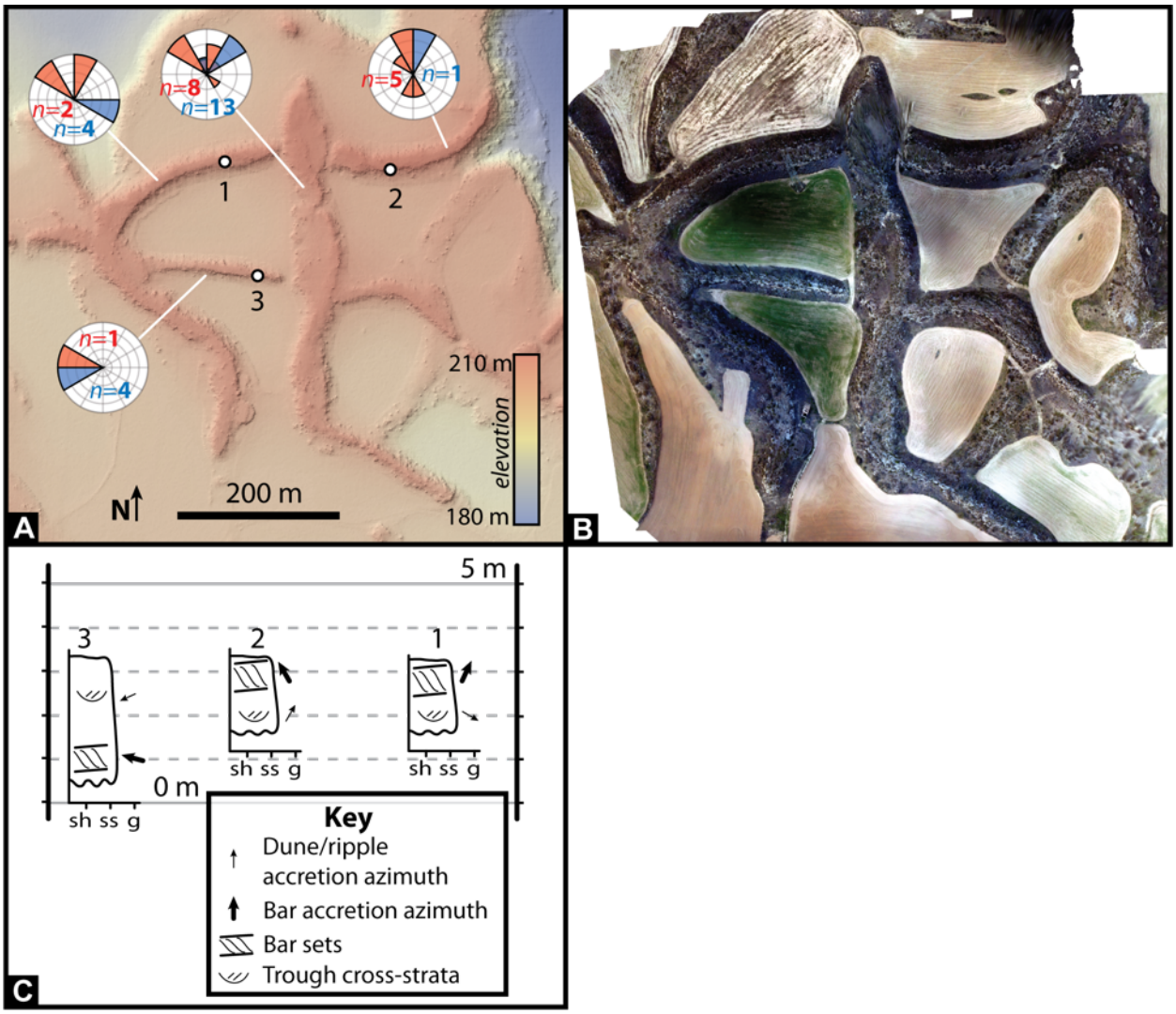

Figure 5.13--Site 1 data. A) Background is the elevation and hillshade from LiDAR DEM. Rose diagram represents paleoflow direction observations (blue) and bar accretion directions (red). White circles indicate stratigraphic sections (shown in panel C). Ridges are all at comparable stratigraphic levels, but note the notches on the ridge between stratigraphic sections 1 & 2 – this indicates ridge stacking. B) Orthophoto from 3D model from photogrammetry on UAV photos. C) Representative stratigraphic sections. All three are interpreted to be from the same ridge, so they are placed at the same stratigraphic position.

5.9.1.2 Site 2

Site 2 is notable for a ridge with high sinuosity, which is bisected by an excavated railroad track (Fig. 5.8D). The site was briefly described in Cuevas Martinez et al. (2010). We add quantitative detail to their initial observations. The ridge has relief 0.1-4.8 meters above the

surrounding plains, caprock thickness varying from 0.3-3.3 meters along ridge length, and caprock breadth varying 11-51 meters.

Sedimentological observation of the caprock revealed it to be sandstone with abundant cross-stratification from bars and dunes. Dune cross-strata indicate paleoflow directions within 30° of the ridge axis, with a small number 60° from the axis. Bar clinoforms have accretion directions between 0°-60° from the paleoflow direction indicated by dune cross strata. Some of the bar structures have accretion directions consistent with a meandering channel (i.e., accreting towards the outside of a bend, in the direction of planform convexity), while other clinoforms accreted precisely opposite that direction (Fig. 5.10D).

The caprock overlies mudstone ridge flanks. Talus blocks up to 3 meters in diameter cover the flanks, and are made of similar sandstone to the caprock. Talus was absent from the flat areas at the bases of the ridges, likely due to modification for agricultural use.

5.9.1.3 Site 3

Site 3 contains two ridges that intersect and an isolated knob (Fig. 5.16). The ridges and the knob are all at indistinguishable elevations in the DEM and stratigraphic model. Ridge 1 has a minor notch near its intersection with Ridge 2, indicating it was cut by the river that formed Ridge 1 (between sections 1 and 2, Fig. 5.16A). Best-fit slopes are ~10^{-3}, and all ridges have relief 2.3-7.9 meters above the surrounding plains. Caprock thickness varies 2.9-4.4 meters and breadth varies 9.7-23.3 meters.

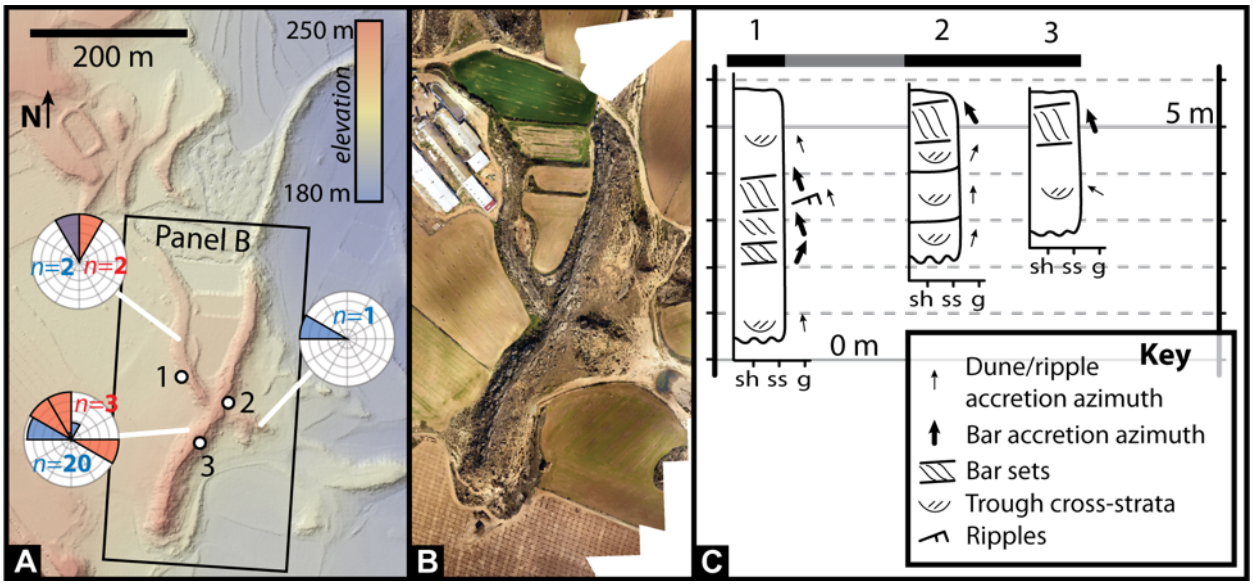

Figure 5.14--Site 3 data. A) Background is the elevation and hillshade from LiDAR DEM. Rose diagram represents paleoflow direction observations (blue) and bar accretion directions (red). White circles indicate stratigraphic sections (shown in panel C). Ridges are all at comparable stratigraphic levels. B) Orthophoto from 3D model from photogrammetry on UAV photos. C) Representative stratigraphic sections. Both ridges are interpreted as being at the same stratigraphic position (grey bar) so the tops of all three stratigraphic sections are placed at the same stratigraphic level (black bars).

Caprocks are made of medium sandstone with some cross stratification. We measured 60 dune cross strata with heights ranging from 3-31 centimeters and indicating flow directions within 30° of the ridge axis. Six bar clinoforms with heights between 0.45-1.5 meters tall had accretion directions almost all within 20° of the ridge axis. No planview expressions of lateral accretion sets were observed.

Caprocks sit atop mudstone ridge flanks covered in talus blocks. Talus blocks are up to 8 meters in diameter, and are made of sandstone that resembles the caprocks. Measurements with a Schmidt hammer indicated that the caprock is stronger than the talus blocks – it had readings with a median of 30, while the talus blocks had a median of 18. Linear talus surveys were conducted based on Wolman pebble count method, with 100 measurements taken at 5-meter intervals parallel to the ridge axis. Talus measurements were indistinguishable at 2 meters and 5 meters from the edge of the

caprock, and the blocks did not get smaller until near the base of the flanks. However, this difference could be due to human modification of the flatter areas.

5.9.1.4 Site 4

Site 4 is most notable for its complex arrangement of ridges that are arrayed like a five-pointed star (Fig. 5.5). We provide additional details here beyond those in the main text.

Three different stratigraphic levels are clearly distinct in the DEM and imagery (Fig. 5.5A, 5B), with Ridge 3 superposing Ridge 1, and Ridge 1 superposing a smaller plateau in the northwest corner. Ridges 1, 2, 4, and 5 are visually similar in the DEM, so we rely on field investigation to discern their intersections. Ridge 4 appears to connect to a channel body beneath Ridge 1 (Fig. 5.8B), and Ridge 1 appears to erode into Ridges 2 and 5 because they are at the same stratigraphic position (Fig. 5.8A). Ridges 2 and 5 are interpreted as continuous through Ridge 1 on the basis of their alignment in planview and stratigraphic position. Therefore, the order of ridges in which the parent paleochannels were active was the small plateau in the northwest, then Ridges 4 and 2/5, 1, and finally 3.

Extracting measurements from the DEM, we found that ridge relief ranges 6-26 meters, caprock thickness ranges 0.3-7 meters, and caprock breadth ranges 10-34 meters. Thickness is greatest where caprocks are amalgamated, for example where Ridge 1 intersects with Ridges 2-5 (Fig. 5.8B). Caprocks are similarly widest where they intersect (Fig. 5.8A).

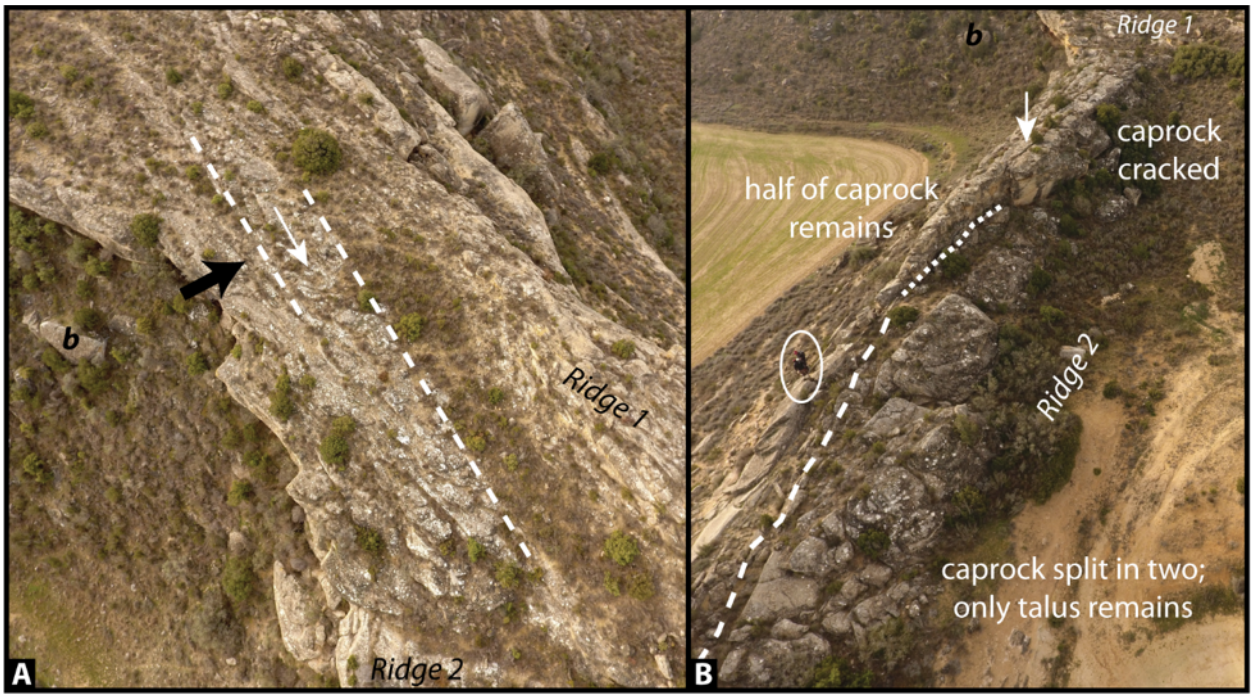

Figure 5.15—Additional images from Site 4. A) Nadir-looking view UAV of the junction between Ridges 1 and 2, showing bank-attached bars (dashed lines). View is of same location as Fig. 5.8A; lowercase "b" indicates a boulder shown in Figs. 5.8A, 5.15B. White arrow indicates paleoflow directions from rib-and-furrow structures, black arrow indicates accretion direction of bar structures. B) UAV photo looking along Ridge 2. The caprock of Ridge 2 is splitting down the middle to form talus blocks, while the portion near to Ridge 1 is more intact, it is also cracked. Person circled for scale.

Caprocks are made of medium sandstone with abundant cross-stratification. We recorded 70 dune cross-strata measurements between 16-38 centimeters tall. Accretion directions indicated paleoflow within 30° of ridge axes. We recorded 32 measurements of bar clinoforms with measured heights between 1.5-2 meters tall and accretion directions ranging 0°-100° from the paleoflow direction. Ridge 1 presented long (~50 meters) lineations parallel to the accretion direction of associated rib-and-furrow structures near the intersections with Ridges 2 & 5 (Fig. 5.17). Because of their great length, association with interpreted dune sets, and perpendicular accretion direction compared to the dunes, we interpreted these structures as lateral accretion sets from bank-attached laterally accreting bars. The lineations extend off both edges of the caprock, indicating that the

caprock used to be wider in both directions. Because lateral accretion sets often indicate the bank of the paleochannel, this furthermore indicates that the ridge caprock represents an amalgamated set of fluvial deposits rather than the paleochannel at any individual timestep.

Sandstone caprocks sit atop mudstone and fine sandstone. A long stratigraphic section (Fig. 5.8C) shows one example of the underlying material, which we found to be 60% mudstone and 40% fine sandstone. The mudstone is also observed between caprocks at all intersections between Ridge 1 and the northwest plateau. Flanks are covered in sandstone talus blocks, and the bases of the ridges are all agricultural fields in current use. On Ridge 2, the caprock has split in half down the middle into parallel sets of blocks that are similar in geometry to the largest of the talus blocks (Fig. 5.17B).

5.9.1.5 Site 5

Site 5 contains a main ridge with a pair of smaller ridge segments branching off at each end (Fig. 5.18). The segments connect with the main stem and appear to form two distinct ridges at stratigraphic levels offset from each other by 1-2 meters and amalgamated for the main central stretch. The higher ridge runs from the southeast to the northwest, and the lower ridge runs from the southwest to the northeast. The lower ridge takes sharp bends at the two ridge junctions. Field investigation of the ridge intersections clearly shows that the ridge caprocks are separated by mudstone (Fig. 5.8C). Ridge superposition at the northern intersection is confirmed by field investigation (Fig. 5.9B), though mudstone was not observed to separate the caprocks.

Both ridges have relief 0.3-4.8 meters above the surrounding plains. Caprock thickness varies from 0.2-3.2 meters and breadth varies from 12-35 meters along ridge lengths. Caprocks are made of medium sandstone with six recorded dune strata measurements and two observations of bar clinoforms. Dune sets indicate paleoflow direction within 30° of the ridge axis, and accretion

directions of the two bars are within 15° of perpendicular to the ridge axis. Ridge flanks are largely mudstone covered in talus blocks up to 3 meters in diameter that are made of medium sandstone.

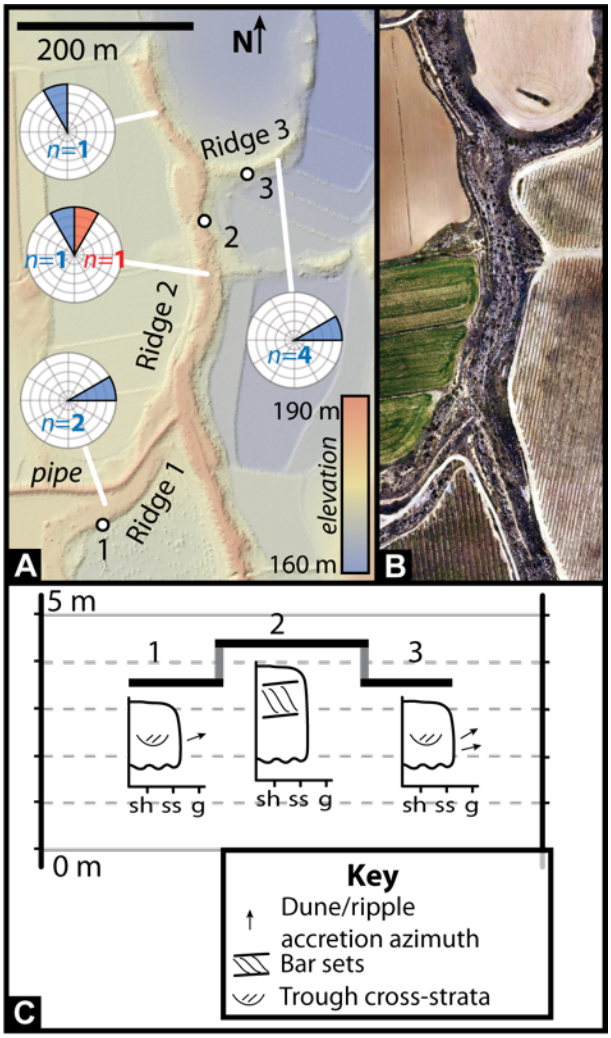

Figure 5.16--Site 5 data. A) Background is the elevation and hillshade from LiDAR DEM. Rose diagram represents paleoflow direction observations (blue) and bar accretion directions (red). White circles indicate stratigraphic sections (shown in panel C). Ridges are all at comparable stratigraphic levels, but note the notches on the ridge between stratigraphic sections 1 & 2 – this indicates ridge stacking. B) Orthophoto from 3D model from photogrammetry on UAV photos. C) Representative stratigraphic sections. Ridges 1 & 3 are interpreted to be the same channel body (see main text), so they are placed at the same stratigraphic level, offset from the top of Ridge 2 by 80 cm (black bars indicate ridge tops, gray bar indicates offset).

5.9.1.6 Site 6

Site 6 is notable for a ridge with a sequence of bends that resemble point bars going in different directions (Fig. 5.19). Ridge caprock increases in elevation towards the outside of each curve, such that the highest-elevation component of the caprock is also the highest sinuosity. Indurated sandstone bodies that are too eroded to form independent ridges occur under this main ridge at its east end, and another sandstone body superposes the main ridge at its west end. Field observation shows mudstone between the main ridge and the sandstone bodies in both locations. We fit slopes to the axis of the main ridge along its highest-elevation segment and found $6x10^{-4}$. Ridge relief is 0.7-7.9 meters above the surrounding plains. Caprock thickness varies from 0.7-5.9 meters and breadth varies from 9.9-68.5 meters.

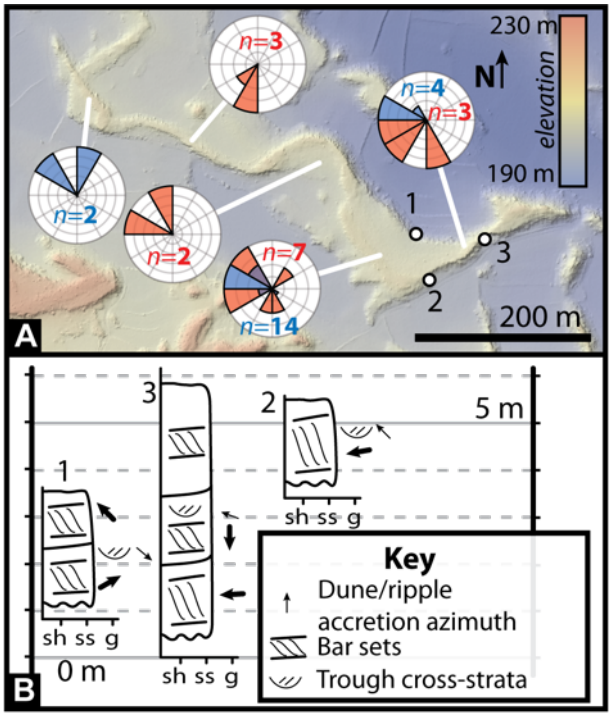

Figure 5.17--Site 6 data. A) Background is the elevation and hillshade from LiDAR DEM. Rose diagram represents paleoflow direction observations (blue) and bar accretion directions (red). White circles indicate stratigraphic sections (shown in panel C). B) Representative stratigraphic sections. All stratigraphic sections are from the same ridge, but are placed at different stratigraphic positions because it slants significantly. Fig. 5.8C corresponds to stratigraphic section 3 here.

Caprocks are made of medium sandstone and we recorded 27 measurements of dune cross-strata and 9 measurements of bar clinoforms. Dune cross strata ranged in height from 5-29 centimeters and indicated flow directions that generally paralleled the local ridge axis. One dune set indicated flow in the opposite direction. Bar clinoforms ranged from 0.6-1.5 m tall. Bar accretion directions were all within 40° of perpendicular to ridge axis and to paleoflow directions. Bars were truncated by major erosional surfaces that we interpreted as the bounding surfaces between stories. Caprocks had between one and four stories (Fig. 5.9C).

Ridge flanks were dominantly mudstone and were covered in talus blocks up to 8 meters in diameter that are made of medium sandstone.

5.9.1.7 Site 7

Site 7 contains two ridges branching in a Y shape, with the Ebro river immediately to the East (Fig. 5.20). Ridge 2 is higher and shorter than Ridge 1 in the DEM. Field observation shows that the sandstone caprocks of Ridges 1 and 2 are separated by ~2 meters of mudstone (Fig. 5.8D). Best-fit slope for Ridge 1 is $8x10^{-4}$, and both ridges have relief 8.6-12.9 meters above the surrounding plains. Caprock thickness varies from 3.2-5.4 meters, breadth varies from 17.3-46.9 meters along ridge lengths. Ridge 1 is widest at its intersection with Ridge 2.

Caprocks are made of medium sandstone, and observations of 43 dune cross sets and 9 bar clinoforms were recorded. Dune cross strata ranged in height from 5-27 centimeters and indicated flow directions that paralleled the ridge axis. One observation of climbing dunes was observed on the caprock of Ridge 1, near its intersection with Ridge 2. Bar clinoforms were 0.45-2.5 m tall, and had accretion directions within 90° of the paleoflow directions. No planview expressions of lateral accretion sets were observed, either in remote sensing or field observation.

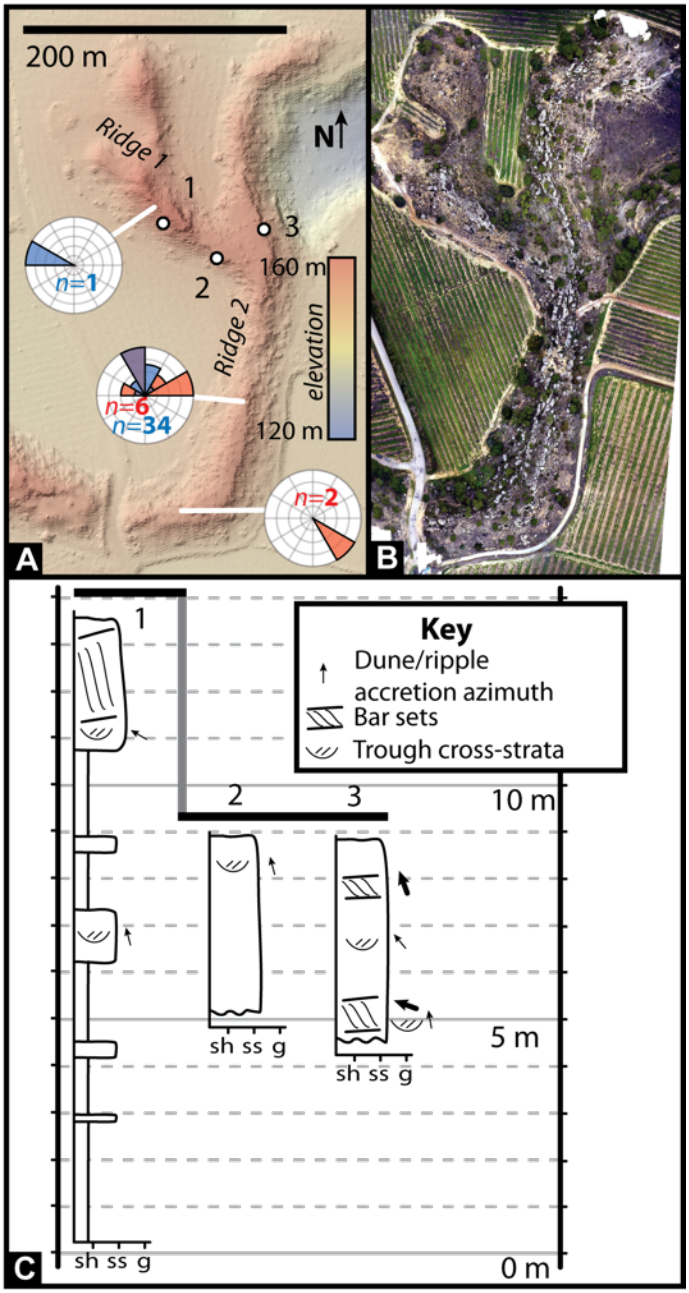

Figure 5.18--Site 7 data. A) Background is the elevation and hillshade from LiDAR DEM. Rose diagram represents paleoflow direction observations (blue) and bar accretion directions (red). White circles indicate stratigraphic sections (shown in panel C). The Ebro River is just off the edge of the image to the East, leading to the high relief in the field area. B) Orthophoto from 3D model from photogrammetry on UAV photos. C) Representative stratigraphic sections. Sections 2 & 3 are from the same ridge so the caprock tops are placed at the same stratigraphic position (black bar), and offset from the caprock top in section 1, as observed in the field (Fig. 5.7D).

Caprocks sit atop mudstone ridge flanks. Talus blocks up to 4 meters in diameter cover ridge flanks, and are made of medium sandstone. Ridge 1 is fractured along much of its length into pieces that are a similar size to the talus blocks on its sides (Fig. 5.20B).

Together, these observations indicate a clear example where branching ridges result from distinct channel bodies at distinct stratigraphic, and therefore temporal, instances. In particular, the upper ridge appears to be protecting the thinner wings of the lower ridge from erosion because their intersection is where the lower ridge is widest. Furthermore, the wings of Ridge 1 preserved in the intersection are the only location in the study where we observed climbing dunes, which form in rapid deposition rates and are therefore indicative of overbank deposits.

5.9.1.8 Site 8

Site 8 contains four parallel ridges, perched atop a sandstone mesa (Fig. 5.21). Ridge 1 is the highest stratigraphically, and the other three ridges are lower and at equivalent heights. The underlying sandstone sheet forms a cliff with 19 meters of relief above the surrounding area. Ridges have relief 0.1-1 meters above the sheet sandstone. Caprock thickness is around 1 meter and the sandstone sheet was 2 meters thick. Caprock breadth varies from 6-20 meters.

Caprocks are made of medium sandstone with some cross stratification. We observed dune cross-sets indicating paleoflows to the north on Ridge 3, and three dune cross-sets indicating paleoflow to the south on Ridge 4. One bar clinoform on each of these ridges had accretion direction perpendicular to the paleoflow direction. Bar clinoforms represented most of the caprock thickness.

A larger body outcropped in the cliff formed by the sandstone sheet, enabling detailed examination. It was 4.5 meters thick and 21 meters wide. The body was made of medium sandstone and contained many levels of truncated bar clinoforms, indicating multiple stories (Fig. 5.9A). It

truncated layers in the mudstone. We interpreted this body as a channel belt with laterally accreting bars.

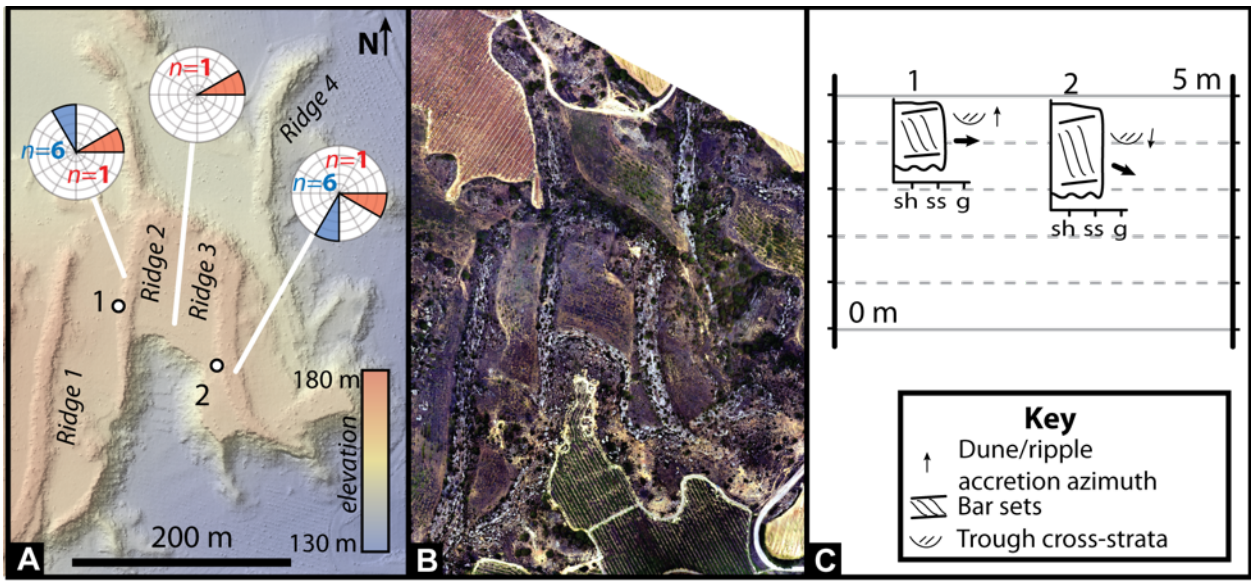

Figure 5.19--Site 8 data. A) Background is the elevation and hillshade from LiDAR DEM. Rose diagram represents paleoflow direction observations (blue) and bar accretion directions (red). White circles indicate stratigraphic sections (shown in panel C). Ridges are all at comparable stratigraphic levels, but note the notches on the ridge between stratigraphic sections 1 & 2 – this indicates ridge stacking. B) Orthophoto from 3D model from photogrammetry on UAV photos. C) Representative stratigraphic sections. The two stratigraphic sections are observed at similar stratigraphic levels and also similar elevations above the sheet sandstone (~2 meters), so their caprock tops are placed at the same stratigraphic level.

5.9.1.9 Site 9

Site 9 contains three ridges that intersect (Fig. 5.22). Ridge 1 is the highest stratigraphically, and the other two ridges are lower and at equal heights. Best-fit slope for the long ridge is $9x10^{-4}$, and ridges have relief 0.1-7.1 meters above the sheet sandstone. Caprock thickness varies from 0.4-5.2 meters and breadth varies from 8-30 meters along ridge lengths.

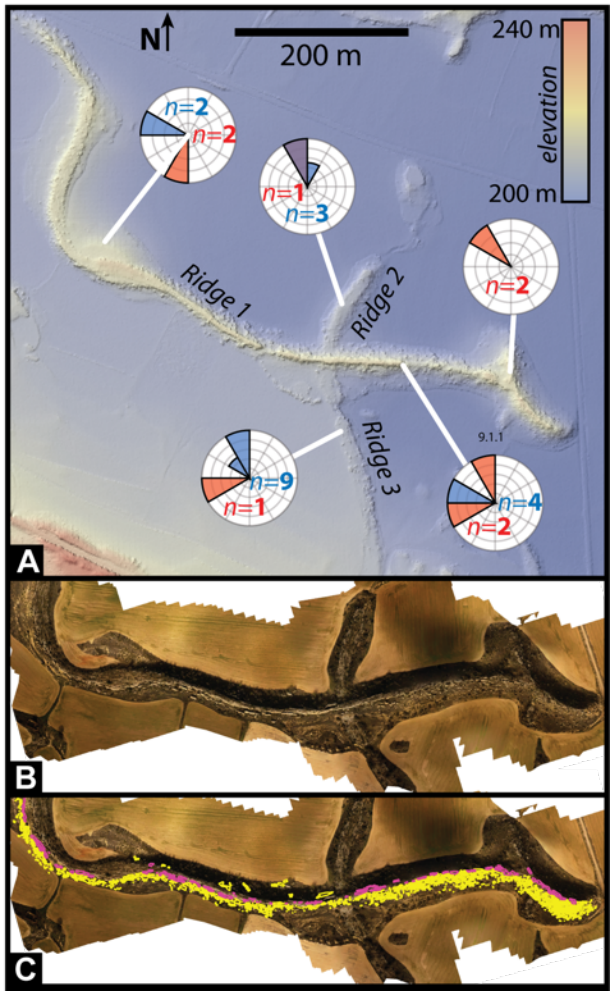

Figure 5.20--Site 9 data. A) Background is the elevation and hillshade from LiDAR DEM. Rose diagram represents paleoflow direction observations (blue) and bar accretion directions (red). White circles indicate stratigraphic sections (shown in panel C). The long ridge running east-west is at a higher stratigraphic position than the shorter ridge running north-south. B) Orthophoto from 3D model from photogrammetry on UAV photos. C) Orthophoto from 3D model from photogrammetry on UAV photos with yellow outlines tracing talus blocks on the south side of the ridge (north side is in shadow in the UAV photos, so talus there was not thoroughly documented), and pink traces outlining blocks cracking off from the caprock.

Caprocks are made of medium sandstone, and we recorded observations of 14 dune cross sets and 6 bar clinoforms. Dune cross strata ranged in height from 4-23 centimeters and indicated flow directions that paralleled the ridge axis. Bar clinoforms were 1-2.6 m tall and had accretion directions within 20° of the paleoflow directions, except for one bar on Ridge 2 that was accreting laterally. No planview expressions of lateral accretion sets were observed.

Caprocks sit atop ridge flanks made dominantly of mudstone, and mudstone separates the caprocks of Ridge 1 from the other two at their intersections. All ridges have flanks covered in talus blocks up to 14 meters in diameter (Fig. 5.22C), and the blocks are made of medium sandstone with cross-stratification similar to the caprock. Ridge 1 is fractured along much of its length into pieces that are a similar size to the talus blocks on its sides; for many of these locations, there is no longer any fully intact caprock, just the blocks.

5.9.2 Streamgage locations and aridity

Our compilation includes 200 rivers that have a USGS streamgage with 10+ years of mean daily discharge, a USGS rating curve, and surveyed bankfull geometry (at minimum bankfull width, depth, and discharge, and also slope and median grain size). We chose rivers by querying the online USGS databases of discharge and rating curves for each river where we have surveyed values (729). Most surveyed rivers had discharge timeseries available, but few had rating curves. We emailed the state USGS branches to get additional rating curves, but many of the studied rivers did not have that data available. Aridity index is extracted from Trabucco and Zomer (2019) based on latitude and longitude of USGS streamgage. Fig. SI11 shows locations on the map of aridity index.

For the Onyx River (Wright Valley, Antarctica), we used published cross sections, slope, and grain size to reconstruct bankfull discharge ("berm" in survey #2, Shaw and Healey, 1980) near to the LTER streamgage (Onyx Lower Wright Valley; McMurdo Dry Valleys LTER et al., 2019). Because the cross section is published, we selected r = 10,000 to replicate the cross section, and thereby skipped the iteration step used for the USGS rivers. This discharge is reported every 15 minutes, so to make it similar to the USGS mean daily values, we also took the mean daily values.

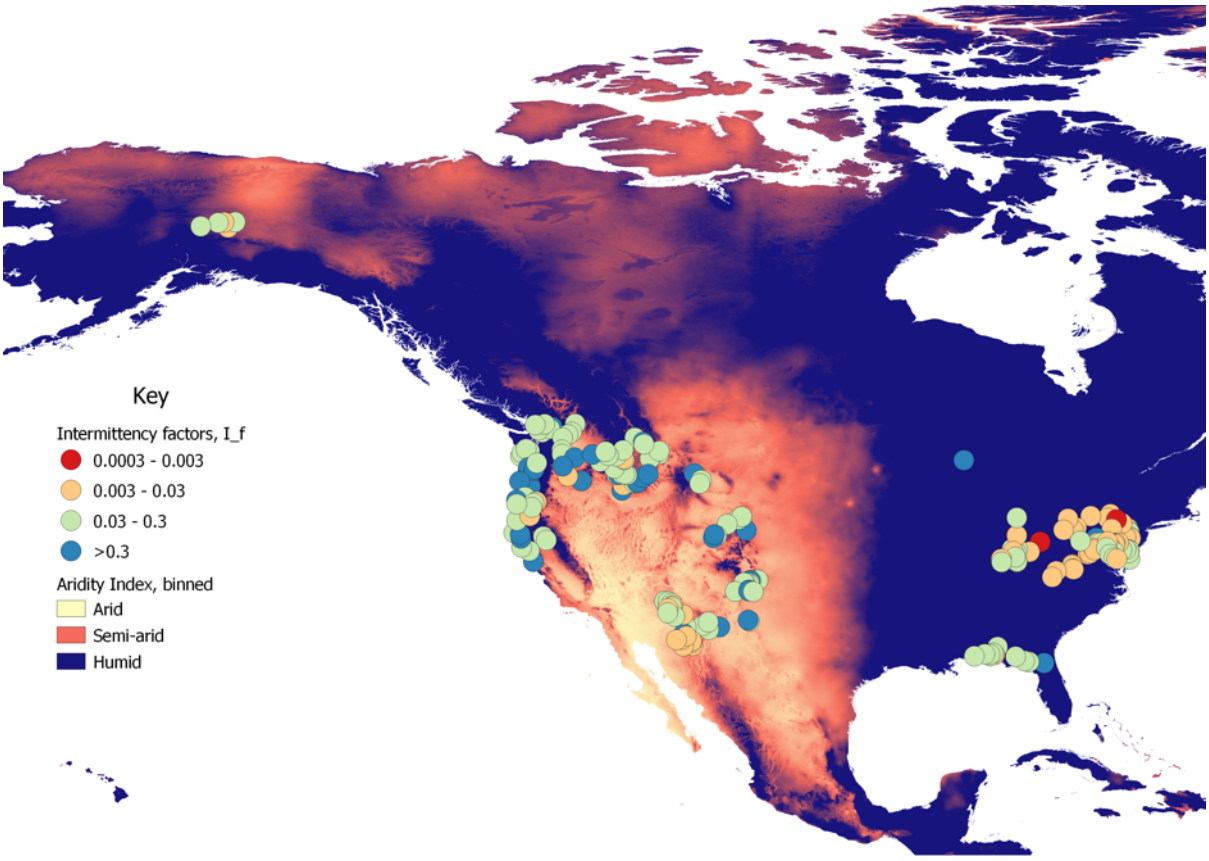

Figure 5.21– Locations of streamgages calculated in this study along with their values. Background map is Aridity Index of Trabucco and Zomer (2019), colored by those matching value ranges for arid, semi-arid, and humid. Not pictured: Onyx River, Wright Valley, Antarctica. The lowest intermittency factors in the study are in the Appalachian region.

1

Data Name	Date	Duration (yr)	D50 (mm)	Slope [a], S (-)	Bankfull sediment flux, $Q_{s,bf}$ (m3/s)	Sediment volume [b], V_s (km3)	Intermittency factor [c], I_f (-)	Aridity Index [d]	Source of paleochannel depth
Devils Gate [e]	01-Sep-1934	14.9	4	0.00704	0.0201	206000	0.0218	0.228	Survey
Devils Gate [e]	01-Jun-1935	0.748	4	0.00704	0.0201	51400	0.109	0.228	Survey
Devils Gate [e]	01-Jun-1938	3	4	0.00704	0.0201	406000	0.214	0.228	Survey
Devils Gate [e]	01-Jan-1942	3.59	4	0.00704	0.0201	357000	0.157	0.228	Survey
Devils Gate [e]	01-Dec-1943	1.92	4	0.00704	0.0201	122000	0.101	0.228	Survey
Devils Gate [e]	01-Oct-1948	4.84	4	0.00704	0.0201	24500	0.00799	0.228	Survey
Devils Gate [e]	01-Jul-1952	3.75	4	0.00704	0.0201	105000	0.0443	0.228	Survey
Devils Gate [e]	01-Sep-1955	3.17	4	0.00704	0.0201			0.228	Survey
Devils Gate [e]	01-Dec-1959	4.25	4	0.00704	0.0201	17100	0.00637	0.228	Survey
Devils Gate [e]	01-May-1962	2.42	4	0.00704	0.0201	206000	0.134	0.228	Survey
Devils Gate [e]	01-Sep-1966	4.34	4	0.00704	0.0201	225000	0.082	0.228	Survey
Devils Gate [e]	01-Feb-1969	2.42	4	0.00704	0.0201	203000	0.133	0.228	Survey
Devils Gate [e]	01-Mar-1969	0.0767	4	0.00704	0.0201	90500	1.87	0.228	Survey
Devils Gate [e]	01-Nov-1969	0.671	4	0.00704	0.0201			0.228	Survey
Devils Gate [e]	01-Dec-1971	2.08	4	0.00704	0.0201	85600	0.065	0.228	Survey
Devils Gate [e]	01-Oct-1973	1.84	4	0.00704	0.0201	14700	0.0126	0.228	Survey
Devils Gate [e]	01-Mar-1977	3.42	4	0.00704	0.0201	58700	0.0272	0.228	Survey
Devils Gate [e]	01-Mar-1978	1	4	0.00704	0.0201	75800	0.12	0.228	Survey
Devils Gate [e]	01-Jul-1978	0.334	4	0.00704	0.0201	9790	0.0463	0.228	Survey
Devils Gate [e]	01-Dec-1978	0.419	4	0.00704	0.0201			0.228	Survey
Devils Gate [e]	01-Feb-1979	0.17	4	0.00704	0.0201	115000	1.07	0.228	Survey
Devils Gate [e]	01-Mar-1980	1.08	4	0.00704	0.0201	73400	0.107	0.228	Survey
Devils Gate [e]	01-Jul-1981	1.33	4	0.00704	0.0201	46500	0.0551	0.228	Survey
Devils Gate [e]	01-Sep-1982	1.17	4	0.00704	0.0201	44000	0.0595	0.228	Survey
Devils Gate [e]	01-Apr-1983	0.581	4	0.00704	0.0201	31800	0.0866	0.228	Survey

Devils Gate	01-Jun-1988	5.17	4	0.00704	0.0201	12200	0.00374	0.228	Survey
Devils Gate	01-Feb-1992	3.67	4	0.00704	0.0201			0.228	Survey
Devils Gate	01-Jul-1992	0.414	4	0.00704	0.0201	34300	0.131	0.228	Survey
Devils Gate	01-Apr-1993	0.751	4	0.00704	0.0201	24500	0.0515	0.228	Survey
Devils Gate	01-Nov-1995	2.59	4	0.00704	0.0201			0.228	Survey
Devils Gate	01-Apr-2009	13.4	4	0.00704	0.0201	44000	0.00519	0.228	Survey
Devils Gate	01-Apr-2010	1	4	0.00704	0.0201	193000	0.306	0.228	Survey
Devils Gate	01-Mar-2011	0.915	4	0.00704	0.0201	66100	0.114	0.228	Survey
Devils Gate TOTAL	1919-2011	91.5	4	0.00704	0.0201	2940000	0.0509	0.228	Survey
Wax Lake	1973	1	0.25	0.0001	0.117	440000	0.119	1.03	Survey
Wax Lake	1974	1.02	0.25	0.0001	0.117	747000	0.199	1.03	Survey
Wax Lake	1975	0.97	0.25	0.0001	0.117	967000	0.27	1.03	Survey
Wax Lake	1976	0.955	0.25	0.0001	0.117	1450000	0.411	1.03	Survey
Wax Lake	1977	1.06	0.25	0.0001	0.117	1360000	0.348	1.03	Survey
Wax Lake	1978	1	0.25	0.0001	0.117	1280000	0.347	1.03	Survey
Wax Lake	1979	1.03	0.25	0.0001	0.117	2460000	0.645	1.03	Survey
Wax Lake	1980	0.969	0.25	0.0001	0.117	2550000	0.712	1.03	Survey
Wax Lake	1983	2.99	0.25	0.0001	0.117	8910000	0.806	1.03	Survey
Wax Lake	1984	1.05	0.25	0.0001	0.117	10900000	2.81	1.03	Survey
Wax Lake	1986	1.92	0.25	0.0001	0.117	10200000	1.44	1.03	Survey
Wax Lake	1987	1.03	0.25	0.0001	0.117	11300000	2.97	1.03	Survey
Wax Lake	1990	3.05	0.25	0.0001	0.117	22800000	2.02	1.03	Survey
Wax Lake TOTAL	1973-1990	18	0.25	0.0001	0.117	75300000	1.13	1.03	Survey
Gulf of Mexico fans/deltas	Pleistocene	2300000	0.3	0.000145	5.85	1.05E+14	0.248	0.728	Eq. 4
Gulf of Mexico fans/deltas	Pliocene	3800000	0.3	0.000145	5.85	7.33E+13	0.105	0.728	Eq. 4

Gulf of Mexico fans/deltas [g]	Upper Miocene	4800000	0.3	0.000145	5.85	8.01E+13	0.0905	0.728	Eq. 4
Gulf of Mexico fans/deltas [g]	Middle Miocene	3100000	0.3	0.000145	5.85	9.14E+13	0.16	0.728	Eq. 4
Gulf of Mexico fans/deltas [g]	Lower Miocene 2	3200000	0.3	0.000145	5.85	6.99E+13	0.118	0.728	Eq. 4
Gulf of Mexico fans/deltas [g]	Lower Miocene 1	5200000	0.3	0.000145	5.85	6.66E+13	0.0695	0.728	Eq. 4
Gulf of Mexico fans/deltas [g]	Oligocene	10600000	0.3	0.000162	5.13	1.91E+14	0.111	0.728	Eq. 4
Gulf of Mexico fans/deltas [g]	Upper Eocene Jackson	2300000	0.3	0.000145	5.85	2.53E+13	0.0597	0.728	Eq. 4
Gulf of Mexico fans/deltas [g]	Upper Eocene Yegua	1800000	0.3	0.000126	6.93	3.61E+13	0.0916	0.728	Eq. 4
Gulf of Mexico fans/deltas [g]	Middle Eocene Sparta	4600000	0.3	0.000145	5.85	1.61E+13	0.019	0.728	Eq. 4
Gulf of Mexico fans/deltas [g]	Middle Eocene Queen City	5600000	0.3	0.000126	6.93	1.9E+13	0.0156	0.728	Eq. 4
Gulf of Mexico fans/deltas [g]	Lower Eocene Upper Wilcox	6800000	0.3	0.000153	5.49	5.56E+13	0.0472	0.728	Eq. 4
Gulf of Mexico fans/deltas [g]	Upper Paleocene Middle Wilcox	3600000	0.3	0.000145	5.85	8.38E+13	0.126	0.728	Eq. 4
Gulf of Mexico fans/deltas [g]	Upper Paleocene Lower Wilcox	3300000	0.3	0.000173	4.78	1.59E+14	0.32	0.728	Eq. 4
Mississippi River Delta [h]	Maringouin Lobe	1700	0.3	0.0000852	10.9	1.92E+11	0.33	0.986	Eq. 4
Mississippi River Delta [h]	Teche Lobe	2860	0.3	0.0000682	14.1	1.74E+11	0.137	0.986	Eq. 4
Mississippi River Delta [h]	St. Bernard Lobe	5290	0.3	0.0000852	10.9	1.98E+11	0.109	0.986	Eq. 4
Mississippi River Delta [h]	Lafourche Lobe	4080	0.3	0.000115	7.67	1.45E+11	0.147	0.986	Eq. 4
Mississippi River Delta [h]	Plaquemines Lobe	452	0.3	0.0000852	10.9	1.27E+11	0.821	0.986	Eq. 4
Mississippi River Delta [h]	8400-0 k.a.	14400	0.3	0.0000852	10.9	8.36E+11	0.17	0.986	Eq. 4

Triassic Boreal Delta [i]	Triassic	20000000	0.3	0.0000552	17.9	2.11E+14	0.0187	1	Eq. 4
Guadalope-Matarranya Fan	Miocene	4000000	0.25	0.00126	0.481	6.05E+11	0.00998	0.33	Eq. 4

Table 5.2—Data used to calculate Intermittency factor for sedimentary deposits.

[a]Eq. 11. [b]Eq. 14.[c]Eq. 15.[d]Trabucco and Zomer (2018). [e]Durations and volumes from LADPW & LACFCD (2013), D_{50} from Psomas (2018), bankfull depth from estimated from Modrick and Georgekakos (2014), sediment flux from Eq. 17. [f]durations and volumes from Roberts et al. (1997), D_{50} from Shaw et al. (2013), bankfull depth from Wax Lake Outlet in Arcement (1980), sediment flux from Eq. 13. [g]Durations and volumes from Galloway et al. (2011), D_{50} assumed to match data from the Mississippi River (Chitale, 1970), bankfull depth from channel belt data in Milliken et al. (2018) and Eq. 4, sediment flux from Eq. 13. [h]Durations and volumes from Bhattacharya et al. (2019), D_{50} from Chitale (1970), bankfull depth from channel belt data in Milliken et al. (2018) and Eq. 4, sediment flux from Eq. 13. [i]Durations and volumes from Klausen et al. (2019)), D_{50} assumed to match data from the Mississippi River (Chitale, 1970), bankfull depth from channel belt data in Klausen et al. (2019) and Eq. 4, sediment flux from Eq. 13